



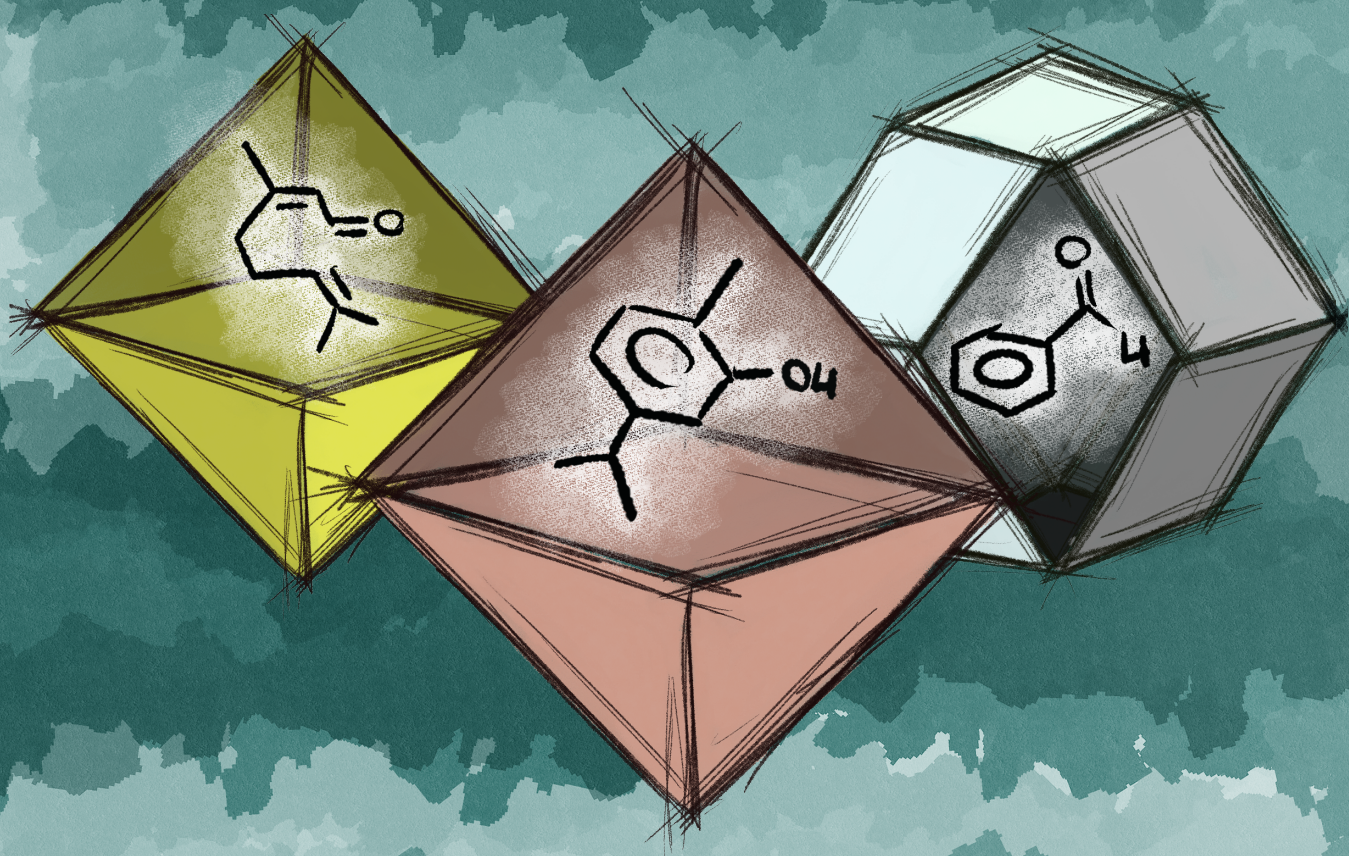
VNIVERSITAT
ID VALÈNCIA

ICMOL

Metal-organic frameworks as non-innocent scaffolds for the encapsulation of active biomolecules

PhD Thesis in Nanoscience and Nanotechnology

Katia Caamaño Chico



Supervised by
Dr. Mónica Giménez Marqués

June 2023

Metal-organic frameworks as non-innocent scaffolds
for the encapsulation of active biomolecules



VNIVERSITAT DE VALÈNCIA

Instituto de Ciencia Molecular (ICMol)

Memoria presentada por Katia Caamaño Chico para aspirar al
título de Doctora en Nanociencia y Nanotecnología

Dirigida por:

Dra. Mónica Giménez Marqués

Junio 2023

Dña. Mónica Giménez Marqués, doctora por la Universitat de València y actualmente investigadora del Instituto de Ciencia Molecular, de la Universitat de València

CERTIFICA:

Que la presente memoria, titulada “Metal-organic frameworks as non-innocent scaffolds for the encapsulation of active biomolecules”, corresponde al trabajo realizado bajo su dirección por Dña. Katia Caamaño Chico, para su presentación como Tesis Doctoral en el Programa de Doctorado en Nanociencia y Nanotecnología Molecular de la Universitat de València.

Y para que conste firma el presente certificado en Valencia, a 10 de julio de 2023.

Fdo. Mónica Giménez Marqués

Acknowledgements

Han pasado más de 6 años desde que en la reunión de inicio del máster Eugenio Coronado me dijese “ya sé con quién te voy a poner”. Durante este tiempo, han pasado muchas cosas, y he conocido a mucha gente sin la cual esta tesis no habría sido posible, con lo cual debo agradecer a muchas personas. María, prepara los pañuelos que se viene.

En primer lugar, me gustaría agradecer al director del ICMol, Eugenio Coronado, el haberme dado la oportunidad de entrar al UIMM durante el máster y haberme permitido quedarme para iniciar mi tesis doctoral.

A mi directora de tesis, Mónica Giménez, gracias, por tanto. Por estar ahí, trabajando conmigo desde el principio del máster hasta el final de la tesis, iniciando cada línea con ilusión y llorando con cada deadline, que por supuesto nos pillaba siempre (ojalá no fuésemos la misma persona). Gracias por ser mi mentora dentro y fuera del laboratorio. Ha sido un placer que me acompañases durante esta etapa científica y personal, y ver también como crecías como científica y líder. Y, aunque a veces te pitasen los oídos tras nuestras reuniones, las ganas de quererte siempre han superado a las de matarte, jeje. Gracias también a Guillermo Mínguez, un investigador impecable, pero mejor persona si cabe. Con el esfuerzo de ambos habéis conseguido fundar un grupo increíble de personas con ganas de hacer la mejor ciencia con ilusión y muchísimo buen ambiente en el laboratorio.

Sin mis compañeros del CEL no me gustaría tanto estar en el laboratorio: Euge, uno de mis mayores apoyos desde el primer día, cerrando el ICMol y también discotecas de vez en cuando. Sonicar nanopartículas ya no mola tanto si tú no estás al lado haciendo una columna. Gracias por acompañarme en momentos críticos de mi vida... siempre nos quedará el Marieta. Luis (el jefe, the boss, el líder, nuestra luz de guía en el laboratorio), nunca dejes de tener la ilusión y el interés por la investigación que tienes. Siempre es un placer hablar de ciencia contigo. Sergio, como futuro pringado jefe y digno

sucesor mío, mantente fuerte y no dejes que reine el caos en el laboratorio. Jesús, el creador de one-liners definitivo. Cualquier conversación gana muchísimo en cuanto tú formas parte de ella. Isa, gracias por explicarme los TGA una y otra vez sin perder la paciencia, por hacerme apreciar el NMR y por estar siempre ahí para contarnos nuestras cosas. Gracias también a Bea, Jana, Eduardo, Thibaut, Gerardo y Christian.

Alicia y Rosa, gracias por ser seres de luz y siempre sacarme una sonrisa con nuestras charlas de pasillo. Sois geniales.

Al resto de compañeros de la segunda planta, que siempre están ahí para echar una mano con cualquier experimento, o para tomar un café y simplemente charlar cuando el estrés o el agobio lo pide: Camilo, Bea, Edurne, Marta, Matteo, Pau, Javi (tenemos una celebración conjunta de cumpleaños pendiente, ve preparando el disfraz). A Silvia y Carla que, aunque vivan en otra planta o en Nueva Caledonia, también cuentan como segunda planta en nuestros corazones.

Al personal técnico y administrativo del ICMol, no sé qué haría sin vosotros: Paco, sin ti no soy nada. Siento haberte costado tanto de criar. Gracias por hacer que entregue todos los documentos a tiempo, sin ti no habría tesis. Alejandra, eres excepcional. Mantienes el ICMol a flote. Chema y Gloria, no hay tartas en el mundo que paguen lo pesada que he sido siempre y lo bien que me habéis tratado. Ruth, gracias por tus habilidades de gestión y nuestras conversaciones sobre el método *curly*. Pascu, gracias por apagar todos mis fuegos siempre con una sonrisa y gentiles palabras. No nos dejes nunca. Cristian, gracias por echarme una mano con los montajes mil veces, aunque no te hiciese un parte. Estela, gracias por tu paciencia cuando no me entero de los trámites o las convocatorias. Xavi y Juanjo, gracias por vuestra pasión y por promover la vida social del instituto, que es muy importante para el estrechamiento de lazos y el fomento de las colaboraciones. O, en otras palabras, gracias por organizar las cenas de empresa.

A Paqui y a Pilar, que cada mañana nos reciben a todos con algo bonito que decir, y oye, qué bonito es sonreír por la mañana gracias a vosotras.

A toda la gente del Edificio Blanco (a día de hoy, sigo buscando en Google cómo se escribe *SCSIE*), pero sobre todo a Salomé, Eva y Ade. Gracias por siempre ayudarme en todo lo que estaba en vuestra mano y tratarme con muchísimo cariño.

A todos los que han leído la tesis y siguen su camino (científico o no), pero que me han acompañado durante muchos de estos años: JoseNa (al final las biocosas no eran tan terribles), José Alberto (que seas muy feliz siendo profe, estoy segura de que tus alumnos te adoran), Jorge (¿has visto? Al final la tesis no era de bromi), Néstor (gracias por ser una abuela con los postres, un cierra bares y un mentor en el laboratorio, pero, sobre todo, por ser un gran amigo), Miguel (aunque seas posdoc desde ayer, te toca ir en este párrafo, siento que seas tan mayor... pero que sepas que estoy muy orgullosa de ti y de todo lo que has luchado, me congratula haber recogido tu testigo), Javi Castells (ahora los dos seremos amigos doctores), Javi López, Samuel, Michelle, Vero, Yan, Ana, Dani P., Marc... Gracias por haber compartido vuestro tiempo conmigo.

A Vic (mi bailarín favorito, y el químico sintético definitivo para el que nada es un problema) y Alejandro (rey de los haters, gracias por entenderme tanto) sois lo mejor que me llevo del máster. Os quiero muchísimo.

Roger, ha llegado tu momento. Te lo mereces todo (sobre todo, te mereces tu propio párrafo, y más largo que el de Ramón). Por ser una maravillosa persona, el más maduro y trabajador y, desgraciadamente, también el más pringado. Gracias por enseñarme tantas cosas en el lab y fuera de él. Los cafés no saben igual sin ti.

Ramón, no te lo mereces, desgraciado, pero que sepas que te quiero mucho. Gracias por todos los buenos momentos, por haber estado siempre ahí. Pero que no se te suba a la cabeza.

A Carmen (miña Carmiña), organizadora no oficial de cenas de ICMol y persona encantadora donde las haya. Gracias por siempre escucharme y aconsejarme. Estoy deseando volver a cantar el himno contigo cuando celebremos esto. A Galle, gracias por ser como eres. Te queda la importante misión de representar a Galicia en el ICMol, cumpíela con orgullo. José (Cuñao), aunque no daba un duro por ti al principio, te he cogido mucho cariño. Eres un digno heredero de Vic, llegarás lejos.

A Ximo. Pocas veces he decidido que alguien iba a ser mi nuevo mejor amigo tan rápido como contigo. Gracias por tu sentido del humor, por compartir tu sabiduría y por siempre tener algo que aportar a cualquier discusión. Pero, sobre todo, gracias por haberte puesto al día con One Piece para que podamos comentar (aunque igual eso deberías agradecermelo tú a mí, por la cuenta que te trae... jajaja).

A Isaac, gracias por no perder la sonrisa ni cuando te han tocado los jardines más difíciles de podar. Nunca nadie ha comentado mejor las películas de sábado por la tarde. Y no preferiría a nadie más como otra mitad del dúo dinámico de los técnicos, ojalá nuestro sueño se haga realidad.

Iván, aunque siento haber sido partícipe de que sintieras la llamada de la ciencia, no puedo arrepentirme de que hayas estado conmigo durante la mayor parte de mi tesis... Al menos nos hemos reído mucho, eso no se puede negar. Nuestras conversaciones con los ojos nunca serán superadas por nada que se pueda decir con palabras. No podré volver a usar el Excel sin acordarme de ti, y creo que eso es bonito.

Va, María, no estés mal que ya te toca a ti. Como diría la gran Toñi Moreno, eres una persona MA-RA-VI-LLO-SA. El ICMol no tendría sentido sin ti. Estoy orgullosísima de ti, de todo lo que has conseguido, y de todo lo que

conseguirás en tu camino hacia convertirte en cristalera legendaria. Porque de la tesis se sale, María, y si no te lo crees, mira todo este libraco... jajaja. Y si no, siempre nos quedarán las paellas por el mundo. Donde tú me digas, me voy contigo. Siempre me vas a tener ahí, no importa si es una conversación a las 4 de la mañana sobre cuánto nos queremos, o una lloradita en el sonicador porque la ciencia no sale y a seguir. Que nadie nos quite esto, porque lo mejor que nos podría pasar a las dos ha sido encontrarnos (con lo de quemar el ICMol no tendremos tanta suerte). Te mereces una tesis entera de dedicatoria. La quiero mucho, señora.

A Jonathan. Te lo he dicho muchas veces, pero no deja de ser verdad. Si no fuese por ti, probablemente no habría ningún documento que leer. Gracias por haberme levantado cuando más abajo he estado. Gracias por decirme lo que necesitaba escuchar y no lo que quería oír. Gracias por haberme devuelto la ilusión por el lab, aunque a veces se me olvide (y por muchas otras cosas). Gracias por creer en mí. Te voy a estar agradecida toda la vida.

También hay gente a la que he conocido antes de mi periplo por el ICMol, pero sin la cual nada de esto habría sido posible tampoco:

A mis compañeros JM, Lore, Emi, Sabela, Santi, Miwi... que sigamos encontrándonos en bodas, retrasemos lo de encontrarnos en los funerales. Gracias por seguir ahí después de todos estos años, por hacer que cada vez que os veo sienta que no ha pasado ni un día desde que éramos unos pipiolos en la facultad. Patri, Fer, Leyre, ¡lo conseguí!

A Rouse, Iago, Luis, Fran, Laura, Adriana, Nacho, Soraya, Alejandra, Cris... gracias por hacer que pasar el día entero en la facultad no fuese tan doloroso. Rocío, de noite as luces brillan más se penso en ti. Habéis crecido muchísimo desde que os dejaba mis libretas de prácticas de inorgánica, jajaja. Estoy muy orgullosa de todos vosotros.

A Cris. Gracias por llevar 20 años (madre mía, 20 ya) a mi lado. Aunque sea una desaparecida durante meses y luego vuelva a casa hablando con un acento raro, gracias por recibirme cada vez con los brazos abiertos. Por otros 20 años más, y hasta que seamos viejitas. Te quiero.

Para o final, os máis importantes de todos. Os da casa. A miña nai. A meu tío. A meus padriños. A Beni. Se non fora por vós nin siquiera estaría aquí. Despois de todos estes anos, xa vou ter por fin o papeliño! Podedes ensinar esto cando vos pregunten que qué fajo. Gracias por aturarme. Espero que estedes orgullosos de min. Quérovos moitísimo.

Y por qué no, a mí. Porque he sido valiente. Porque he llegado hasta el final, a pesar de todo. Porque he podido. Y de eso estoy muy orgullosa.

Espero no haberme dejado a nadie por nombrar, pero quiero que este párrafo sirva para darle las gracias a todas y cada una de las personas que me he cruzado en los pasillos del ICMol porque, de una manera u otra, todos habéis contribuido a que haya llegado hasta aquí. Así que, a todos, GRACIAS.

Index

Index

Summary and organization	XIX
Resumen en castellano	XXI
Abbreviations	XXXIX
CHAPTER 1	41
1.1. Metal-Organic Framework materials.....	43
1.1.1. Metal-Organic Frameworks as carrier agents.....	46
1.1.2. Metal-Organic Frameworks and Food Industry	49
1.2. Essential oils for food safety	52
1.3. Nanostructured MOF candidates for biomolecule encapsulation.....	57
1.3.1 MIL-100(Fe)	58
1.3.2. ZIF-8	60
1.3.3. UiO-66 and UiO-66-NH ₂	62
1.3.4. MUV-2	64
1.4. References	66
OBJECTIVES.....	75
CHAPTER 2	79
2.1. Introduction.....	81
2.2. Results and discussion	85
2.2.1. Encapsulation methodology.....	85
2.2.2. Physicochemical characterization of carvacrol@MOF composites	86
2.2.2.1. Infrared Spectroscopy.....	87
2.2.2.2. Powder X-ray diffraction.....	95
2.2.2.3. Thermogravimetric Analysis.....	97
2.2.2.4. N ₂ sorption isotherms at 77 K.....	102

2.3. Summary and conclusions.....	110
2.4. Methods.....	111
2.5. References.....	115
CHAPTER 3	117
3.1. Introduction.....	119
3.2. Results and discussion.....	123
3.2.1. Optimisation of carvacrol encapsulation in MIL-100(Fe).....	123
3.2.2. Advanced characterization of carvacrol@MIL-100(Fe) material	126
3.2.3. Theoretical calculations.....	134
3.2.4. Kinetics of carvacrol release from MIL-100 supported on films	137
3.2.5. Microbiology studies – Microatmosphere tests.	139
3.2.5. Cell viability studies.....	145
3.3. Summary and conclusions.....	146
3.4. Methods.....	147
3.5. Supporting Information.....	153
3.6. References.....	160
CHAPTER 4	167
4.1. Introduction.....	169
4.2. Results and discussion.....	173
4.2.1. Encapsulation kinetics.....	173
4.2.2. Physicochemical characterization of the biomolecule@ZIF-8 composite materials	175
4.2.4. <i>In vitro</i> evaluation of antifungal activity.....	190
4.3. Summary and conclusions.....	194
4.4. Methods.....	195
4.5. Supporting information.....	199
4.6. References.....	200

CHAPTER 5	203
5.1. Introduction.....	205
5.2. Results and discussion	210
5.2.1. <i>Standard</i> synthesis of mixed metal MUV-2 derivatives.....	210
5.2.2. Physical characterization of the materials.....	211
5.2.2. Chemical and thermal stability – Powder X-ray Diffraction	216
5.2.3. Magnetic Properties.....	220
5.2.4. Single-gas sorption studies.....	223
5.2.5. <i>Green</i> synthesis and Lysozyme encapsulation	229
5.3. Summary and conclusions.....	240
5.4. Methods	241
5.5. Supporting Information.....	244
5.6. References	246

Summary and organization

Ensuring the safety and quality of food is one of the main focuses of the field of food industry. Different active materials are currently studied to extend the useful life of food products. Metal–Organic Framework (MOF) materials have emerged in the last years as a promising alternative owing to their excellent porosity, high loading capacity, controlled release ability and ease of surface modification. The main motivation of this Thesis is to evaluate the possible use of different MOFs as encapsulation agents of active biomolecules to develop smart composite materials that can be employed in food industry applications.

The Thesis is divided into five chapters. *Chapter 1* corresponds to a general introduction to the field of MOFs and their biorelated applications, from drug delivery and biomedicine to food industry, presenting the importance of essential oils and its derivatives in this later field. *Chapter 2* presents a systematic study in which the suitability of MOFs as essential oil encapsulating agents is determined. After selecting the best performing scaffolds, in *Chapter 3* the implementation of a biomolecule@MOF composite into biopolymeric films and its antibacterial activity are studied, thoroughly elucidating the chemical interactions between the guest molecule and the host framework. *Chapter 4* concerns the obtention of a series of biomolecule@MOF composites with enhanced antifungal properties. Finally, in *Chapter 5*, the encapsulation of macrobiomolecules is targeted by synthesizing two mixed-metal hierarchical mesoporous MOFs following a *green chemistry* route.

The work described in this Thesis has given rise to the following publications:

“Exploiting the Redox Activity of MIL-100(Fe) Carrier Enables Prolonged Carvacrol Antimicrobial Activity” K. Caamaño, R. Heras-Mozos, J. Calbo, J. Cases-Díaz, B.J.C. Vieira, J.C. Waerenborgh, P.M. Hernández-Muñoz, R. Gavara, M. Giménez-Marqués. *ACS Appl. Mater. Interfaces*, **2022** 14, 8, 10758–10768.

“ZIF-8-based Biocomposites with Enhanced Antifungal Properties” K. Caamaño, G. López-Carballo, J. Glatz, P.M. Hernández-Muñoz, R. Gavara, M. Giménez-Marqués. *In preparation*.

“Protein Encapsulation within Hierarchical Mesoporous Tetrathiafulvalene-based Mixed-Metal Metal-Organic Frameworks” K. Caamaño, M. Vicent-Morales, G. Mínguez Espallargas, M. Giménez-Marqués, *In preparation*.

Other publication to which the author has contributed during her PhD work:

“A thermally/chemically robust and easily regenerable anilato-based ultramicroporous 3D MOF for CO₂ uptake and separation”. N. Monni, E. Andres-Garcia, K. Caamaño, V. García-López, J.M. Clemente-Juan, M. Giménez-Marqués, M. Oggianu, E. Cadoni, G. Mínguez Espallargas, M. Clemente-León, M.L. Mercuri, E. Coronado. *Journal of Materials Chemistry A*, **2021** 9, 25189-25195.

Resumen de la Tesis en castellano

Actualmente, el uso de diferentes materiales activos para alargar la vida útil de los productos alimenticios es uno de los principales focos del campo de la industria alimentaria. Las redes metal-orgánicas (MOF) han surgido en los últimos años como una prometedora alternativa para garantizar la seguridad y calidad de los alimentos debido a su excelente porosidad y alta capacidad de carga, poseyendo además la habilidad de proporcionar una liberación controlada de agentes activos y una superficie modificable.

La principal motivación de esta tesis es evaluar el posible uso de diferentes MOFs como agentes de encapsulación de biomoléculas activas para desarrollar materiales híbridos inteligentes que puedan emplearse en la industria alimentaria.

Los objetivos de la tesis se resumen en cuatro puntos:

1. Estudio sistemático de la idoneidad de una serie de nanoMOFs como agentes encapsulantes de derivados de aceites esenciales que podrían ser empleados en la industria alimentaria, siguiendo una metodología directa y sencilla como es el método de impregnación.
2. Incorporación de un material híbrido “biomolécula@MOF” en films biopoliméricos y evaluación de la habilidad del MOF para estabilizar y dirigir la liberación de la molécula bioactiva, así como la actividad antimicrobiana del film tras la implementación del material inteligente.
3. Obtención de una serie de compuestos “biomolécula@MOF” y estudio de su efecto fungicida tras su integración en películas bio-poliméricas.
4. Síntesis y caracterización de análogos de MUV-2 de metales mixtos (MM-MUV-2), así como determinación de la idoneidad de dichos materiales como transportadores de macrobiomoléculas.

La tesis se divide en cinco capítulos. El *Capítulo 1* corresponde a una introducción general al campo de los MOF y sus aplicaciones relacionadas con la biología, desde la administración de fármacos y la biomedicina hasta la industria alimentaria, presentando la importancia de los aceites esenciales y sus derivados en este último campo.

Debido a su síntesis basada en “bloques de construcción”, los materiales MOF se caracterizan por una gran versatilidad química que permite un control fino con respecto a la naturaleza del poro, tanto en términos de forma como de tamaño. Estas propiedades químicas modulares han facilitado su aplicación en muchos campos diferentes, como la catálisis, el almacenamiento de energía, la separación de gases y campos relacionados con la biología, como la administración de fármacos y la encapsulación de biomoléculas. En particular, la miniaturización controlada de los MOF resulta de gran interés para la integración de estos materiales en aplicaciones como la detección o la administración de fármacos. El campo de la biomedicina se beneficia particularmente de la nano-estructuración de los MOF, ya que el tamaño de las partículas es un factor limitante para algunas vías de administración donde se requieren tamaños muy precisos. Al considerar el uso de nanoMOF como agentes portadores, su amplia área superficial puede permitir una modificación efectiva de la superficie de las partículas, lo que mejoraría la estabilidad química y coloidal y facilitaría el procesamiento del material al mismo tiempo que promovería una bioactividad mejorada. Los beneficios de las metodologías de encapsulación en el campo de la biomedicina y la industria cosmética también se pueden traducir a la industria alimentaria, recibiendo una amplia atención de investigación, ya que el desarrollo de técnicas confiables y precisas para garantizar la calidad y seguridad de los alimentos siempre es beneficioso para la industria. Se pueden encontrar más de 90000 artículos de investigación en la literatura

sobre MOF para fines de la industria alimentaria en las últimas dos décadas, lo que refleja cómo la comunidad de investigación se ha interesado en esta aplicación potencial. Se pueden encontrar muchos estudios en la literatura sobre el uso de MOF en la eliminación de contaminantes de las fuentes de producción, envasado de alimentos, conservación de alimentos, así como en la detección y monitoreo de contaminantes en productos alimenticios. La investigación sobre MOFs relacionada con las aplicaciones antibacterianas también se puede emplear en la conservación de alimentos, incluida la administración de antibióticos de liberación lenta, el recubrimiento antibacteriano con polímeros y los ingredientes antibacterianos combinados con nanopartículas. Muchas moléculas activas antibacterianas son susceptibles de ser encapsuladas en estas estructuras porosas, pero, en particular, los compuestos bioactivos naturales (BAC, por sus siglas en inglés) resultan de gran interés para la industria alimentaria. Este tipo de moléculas activas (por ejemplo, antioxidantes, vitaminas, polifenoles) se utilizan eficazmente como agentes aromatizantes y/o conservantes de alimentos para inhibir el crecimiento microbiano.

Los componentes activos naturales como los aceites esenciales (en inglés, EO) son ampliamente preferidos en comparación con los aditivos artificiales cuando se considera su uso en aplicaciones relacionadas con la industria alimentaria como conservantes, envases innovadores y la lucha contra los patógenos que causan intoxicación alimentaria. Los EO son líquidos concentrados extraídos de plantas aromáticas. Como productos naturales, a sus interesantes características fisicoquímicas y actividad biológica se le suma un bajo impacto ambiental. Por su compleja composición química, los EO tienen un amplio espectro de actividad biológica y antimicrobiana (presentando actividad antibacteriana, antifúngica, antiviral, contra el control de plagas o como repelentes de insectos). A pesar de exhibir estas

propiedades bioactivas, el uso a gran escala de estos compuestos se ve obstaculizado por su naturaleza volátil e insoluble, su susceptibilidad a diversas condiciones ambientales y de procesamiento y su fuerte aroma característico. Estos frágiles compuestos pueden degradarse fácilmente (por oxidación, volatilización, calentamiento o exposición a la luz) si no se protegen de factores intrínsecos y extrínsecos como el pH, la actividad del agua, la degradación enzimática, la temperatura, la humedad relativa y el entorno de almacenamiento. Por estas razones, la encapsulación de conservantes volátiles en materiales portadores ha sido ampliamente investigada en la industria alimentaria y el campo biomédico como una solución plausible para optimizar su actividad. Ejemplos típicos de encapsulación utilizando nano y micro emulsiones, nanopartículas lipídicas o liposomas, han demostrado aumentar sustancialmente la estabilidad de los EO, a menudo obteniendo como resultado una acción prolongada. El proceso de encapsulación reduce la reactividad con el medio ambiente (factores como el agua, el oxígeno o la luz), disminuye la evaporación o la tasa de transferencia al medio ambiente exterior, enmascara el sabor y mejora la estabilidad coloidal para lograr una distribución uniforme en el producto final.

Con una eficacia demostrada como agentes encapsulantes inteligentes capaces de i) alojar moléculas activas con cargas útiles elevadas con un proceso de carga fácil, ii) preservar la actividad a largo plazo y iii) dirigir la liberación ante estímulos, los MOF se proponen en esta tesis como bioactivos se investigan los transportadores de moléculas y su uso potencial en aplicaciones relacionadas con los alimentos.

El *Capítulo 2* presenta un estudio sistemático en el que se determina la idoneidad de los MOF como agentes de encapsulación de aceites esenciales. Cuatro MOFs arquetípicos se proponen como agentes encapsulantes: MIL-100(Fe), ZIF-8, UiO-66 y su derivado aminado, UiO-66-NH₂. La selección de estos materiales se justifica por su conocida capacidad como agentes encapsulantes de fármacos y su baja citotoxicidad reportada.

El MIL-100(Fe) es uno de los MOF más estudiados en aplicaciones de administración de fármacos. Las características de la estructura de MIL-100(Fe) permiten formar sitios de hierro coordinativamente insaturados (CUS), modificando fuertemente las interacciones preferidas con las moléculas huésped. Esto abre la posibilidad de cargar las moléculas seleccionadas no solo por fisisorción sino también por quimisorción, a través de la coordinación entre los cationes Fe^{III} y la molécula huésped. Una de las principales ventajas de MIL-100(Fe) es la viabilidad de la miniaturización de la estructura, lo que mejora su estabilidad química y coloidal, facilitando así el procesamiento del material. Esencialmente, las nanopartículas de MIL-100(Fe) se obtienen mediante síntesis solvotermal asistida por microondas (MW). Esta síntesis presenta importantes ventajas sobre los métodos clásicos, como el calentamiento homogéneo a lo largo del reactor, tiempos de reacción más rápidos y menor polidispersidad, junto con mayores rendimientos sintéticos. Además, la síntesis asistida por MW permite la implementación de solventes verdes como el agua, que es especialmente adecuado para aplicaciones en la industria alimentaria.

El MOF zeolítico conocido como ZIF-8 posee una estructura similar a las zeolitas de aluminosilicatos convencionales con una topología de sodalita. Este material exhibe porosidad permanente, alta capacidad de carga y degradación sensible al pH, así como una óptima estabilidad térmica y química. El ZIF-8 puede encapsular fármacos hidrófobos, hidrófilos y

anfílicos y, como consecuencia, se ha empleado en diversas aplicaciones relacionadas con la administración de fármacos: fármacos anticancerosos, agentes fototérmicos, agentes fotodinámicos, terapia quimiodinámica, encapsulación de proteínas y terapia genómica. De manera análoga al MIL-100 (Fe), el tamaño de la molécula es la única limitación para la infiltración de moléculas activas en la estructura porosa. A diferencia del MOF basado en Fe^{III} , la red de ZIF-8 no presenta ningún CUS, por lo que la interacción entre el ZIF-8 huésped y las moléculas encapsuladas estaría, en principio, limitada a procesos de fisisorción en los poros. Sin embargo, la estructura dinámica del ZIF-8 puede adaptarse a la presencia de moléculas huésped debido a los ligandos imidazol que pueden rotar, dando lugar a un efecto de “apertura de puerta” que permitiría una mejor acomodación de las moléculas activas alojadas en los poros.

Finalmente, el UiO-66 es una red interesante para muchas aplicaciones debido a su combinación de alta estabilidad térmica y química y su importante porosidad. La combinación de una red robusta con la toxicidad relativamente baja del zirconio convierte este material en un candidato interesante para el transporte de biomoléculas. Además, la posible funcionalización del poro del UiO-66 cambia significativamente sus propiedades: por ejemplo, la capacidad de adsorción y la selectividad de UiO-66 para gases estratégicos como CO_2 y CH_4 pueden modificarse, y el impacto de la funcionalización del MOF en su actividad en también se ha estudiado en la encapsulación de fármacos. En particular, la presencia del grupo amino en el derivado UiO-66- NH_2 abre la posibilidad de diferentes interacciones con las moléculas activas encapsuladas, permitiendo la posibilidad de utilizar la funcionalidad adicional de la red como grupos de anclaje. Por lo tanto, el desempeño del derivado UiO-66- NH_2 MOF se estudia en comparación con el UiO-66 original.

A su vez, se seleccionan tres moléculas activas componentes de aceites esenciales como *moléculas tipo* en este estudio: carvacrol (un monoterpeno aromático presente en el aceite esencial extraído del orégano, principalmente), citral (un aldehído monoterpénico acíclico presente en los aceites de varias plantas, incluido el mirto, la hierba limón o el árbol del té) y benzaldehído (componente principal del aceite de almendras amargas). Estas moléculas activas poseen un amplio espectro de actividad antimicrobiana demostrada y están reconocidas generalmente como seguras para su uso en industria alimentaria (GRAS, por sus siglas en inglés) por la Administración de Alimentos y Medicamentos estadounidense. Habitualmente se emplean como aditivos o conservantes, y son utilizadas como componentes de envases innovadores para la lucha contra los patógenos que provocan intoxicaciones alimentarias.

Se establece también en este capítulo el diseño de un método de encapsulación siguiendo un enfoque directo de impregnación de las partículas de MOF en una suspensión que contiene la molécula activa, manteniendo esta mezcla en contacto durante un período de tiempo y caracterizando los materiales antes y después de aplicar la metodología de encapsulación descrita. Durante el desarrollo de la metodología de infiltración se encontró que la encapsulación de biomoléculas se ve favorecida bajo mezclas hidroalcohólicas (en las que estas moléculas son poco solubles), resultando clave este parámetro para obtener una encapsulación exitosa.

Con respecto a los métodos de caracterización fisicoquímica de estos materiales, los medios más significativos para la caracterización de MOFs y los materiales híbridos que se derivan de ellos incluyen técnicas de caracterización química general, como:

i) la difracción de rayos X (XRD) de monocristal, que proporciona información estructural absoluta sobre el MOF, ii) la difracción de rayos X de polvo (PXRD) para establecer la cristalinidad y la pureza de fase del producto; iii) análisis elemental; iv) análisis termogravimétrico (TGA) para la determinación de la estabilidad térmica y la pureza del MOF, evidenciando la presencia de defectos en la estructura; v) espectroscopia infrarroja (IR) para determinar la presencia o ausencia de grupos funcionales activo en IR en las estructuras; y vi) Microscopías electrónicas de transmisión (TEM) y de barrido (SEM), que proporcionan información sobre el tamaño y la morfología de las partículas. Esta última técnica puede combinarse con la espectroscopia de rayos X de dispersión de energía (EDX) y dar información sobre la composición del material. Además, habitualmente se lleva a cabo un análisis de adsorción específico con gases, que típicamente incluyen las isothermas de adsorción de N₂ típicas a 77 K. Esta medida del área superficial proporciona información sobre la capacidad de un material poroso para adsorber moléculas de gas, y también permite analizar la distribución del tamaño de los poros. De manera general, la mayoría de las técnicas de caracterización descritas, a las que se suman algunas otras más específicas en determinados apartados del trabajo descrito, son empleadas durante toda tesis para establecer la viabilidad de los MOFs como agentes encapsulantes, cuantificar la carga de biomolécula en los materiales híbridos obtenidos y elucidar las interacciones químicas que se producen entre la molécula y el agente encapsulante.

En total, durante el trabajo descrito en el *Capítulo 2* se obtuvieron y caracterizaron doce nuevos biocompuestos, evidenciando la presencia de las biomoléculas activas en los materiales obtenidos para cada producto de encapsulación. La carga de carvacrol fue particularmente efectiva en todos los casos, siendo exitosamente difundida a través de las estructuras porosas debido a su tamaño relativamente pequeño, mostrando resultados excepcionalmente atractivos en combinación con MIL-100(Fe) por coordinación con los centros de Fe^{III}. La interacción citral con el MOF UiO-66-NH₂ mostró interesantes resultados, apuntando en la dirección de la funcionalización del ligando BDC-NH₂. La encapsulación de benzaldehído resultó notablemente efectiva en ZIF-8, con valores de carga mucho más altos que el resto de los MOF propuestos.

Teniendo en cuenta todos los resultados analizados, MIL-100(Fe) y ZIF-8 se presentan como los agentes portadores más prometedores por su gran capacidad de carga, la asequibilidad y disponibilidad de sus precursores y su protocolo sintético más ecológico. En particular, se propone el estudio más a fondo de la capacidad de MIL-100(Fe) para interactuar coordinadamente con las biomoléculas huésped. Si bien UiO-66 y UiO-66-NH₂ mostraron resultados prometedores en combinación con carvacrol y citral, los resultados obtenidos no son tan notables como para justificar los materiales de partida más costosos para su síntesis, o el uso de N,N-dimetilformamida (DMF) y el protocolo de lavado posterior para eliminarla por completo para que sean materiales aptos para aplicaciones industriales.

Después de seleccionar los materiales que presentan las mejores características como agentes encapsulantes, en el *Capítulo 3* se estudia la implementación de un compuesto “biomolécula@MOF” en películas biopoliméricas y su actividad antibacteriana, estudiando profundamente las interacciones químicas entre la molécula acogida y el agente encapsulante.

Gracias a la metodología de impregnación directa implementada en el *Capítulo 2*, se prepara en este capítulo un compuesto biocompatible carvacrol@MIL-100(Fe) que contiene cargas útiles considerables del agente activo. El análisis de las técnicas de caracterización cotidianas explicadas anteriormente apunta en la dirección de una interacción entre las moléculas de carvacrol y la red de MIL-100(Fe), que se estudia más profundamente por medio de técnicas como por ejemplo la espectroscopia de Mössbauer. Gracias a esta técnica es posible elucidar que, mediante una activación térmica, se produce la formación reversible de un trímero de valencia mixta en el material híbrido con retención de las moléculas de carvacrol coordinadas a los centros de Fe^{III}. En experimentos de EPR se observa la aparición de una señal radical característica tras la activación del compuesto, lo que sugiere un mecanismo mediado por radicales para esta coordinación de carvacrol a los centros de Fe^{III}. Esta afirmación se ve respaldada también por cálculos teóricos que, además, confirman que la sustitución de una de las moléculas de agua coordinadas a los cationes Fe^{III} por una molécula de carvacrol está favorecida energéticamente y que el proceso de activación térmica provoca la desprotonación de dicha molécula. Mediante un proceso de transferencia de carga, esta desprotonación y formación de una especie radicalaria provoca a su vez la reducción de uno de los centros Fe^{III} a Fe^{II}, generándose así el trímero de valencia mixta.

Además de proporcionar estabilidad química a la molécula activa, la red de MIL-100(Fe) habilita una liberación sostenida notable y retenida sin precedentes del agente antimicrobiano cuando se procesa en biopelículas poliméricas, debido a su capacidad de respuesta redox única que promueve interacciones efectivas con el agente activo, produciéndose una liberación de carvacrol en dos fases que no se da cuando el agente antimicrobiano se embebe directamente en el biofilm. Este comportamiento único se puede

explicar atribuyendo cada máximo de liberación en el perfil a diferentes interacciones entre las moléculas de carvacrol y el MIL-100(Fe). La primera liberación que ocurre durante las primeras 20 h de estudio se atribuye a la liberación de moléculas de carvacrol que interactúan débilmente con el MIL-100(Fe), mientras que se requieren hasta dos días de condiciones de alta humedad relativa para desencadenar la liberación de las moléculas quimisorbidas a los centros metálicos de hierro disponibles en los poros de la red. En los estudios de microbiología llevados a cabo con dichos films, la dosis de carvacrol liberada fue suficiente para combatir los patógenos bacterianos, con una actividad mejorada contra *E. Coli* y *L. innocua* en comparación con una dosis de carvacrol "libre" equivalente.

En conclusión, la combinación de una preparación directa, el procesamiento fácil y el rendimiento de entrega mediada por andamios que permite una actividad bactericida de carvacrol prolongada, hacen que el compuesto carvacrol@MIL-100(Fe) obtenido sea un candidato prometedor para aplicaciones de envasado de alimentos.

El *Capítulo 4* se refiere a la obtención de una serie de compuestos "biomolécula@MOF" con propiedades fungicidas potenciadas.

La contaminación por hongos en los alimentos conduce a un gran deterioro y a una serie de problemas de seguridad alimentaria. Los efectos de estos microorganismos están relacionados con el crecimiento celular, lo que puede producir metabolitos secundarios tóxicos (micotoxinas), que además de los efectos tóxicos, frecuentemente tienen efectos degenerativos, toxicogénicos o cancerígenos. Los hongos también pueden producir coloración o puntos negros, no aceptados por la mayoría de los consumidores. El potencial antifúngico de los aceites esenciales ha sido ampliamente reportado en la literatura: los estudios demuestran que, en contacto con aceites esenciales,

las células fúngicas sufren daños severos en la pared celular, la membrana y los orgánulos celulares. En otros casos, la alta concentración fungistática de EO puede provocar la autólisis completa de la célula. Cuatro moléculas activas con propiedades fungicidas se emplean en este capítulo: benzaldehído, salicilaldehído, (componente principal del aceite esencial de *Filipendula vulgaris*, una especie de la familia de las rosáceas nativa de Europa), antranilato de metilo (se puede encontrar naturalmente la uva, y es el componente responsable de su aroma y su sabor) y guayacol (presente en aceites esenciales de semillas de apio, hojas de tabaco, hojas de naranja y cáscaras de limón, que se emplea también como precursor de muchos agentes aromatizantes, como la vainillina). Todos ellos son aditivos alimentarios permitidos para la adición directa a alimentos para consumo humano por la FDA.

Tras establecer la tanto viabilidad de ZIF-8 como portador de aceite esencial en el *Capítulo 2* de esta tesis, como la efectividad de la metodología de encapsulación desarrollada, se propone en este Capítulo la obtención de cuatro biocompuestos basados en ZIF-8 que contienen benzaldehído (Bz), salicilaldehído (SA), antranilato de metilo (MA) o guayacol (Gua), adaptando el método de infiltración directa previamente expuesto.

En primer lugar, se evalúa la cinética de encapsulación. Se seleccionan benzaldehído y antranilato de metilo como moléculas modelo y se analiza su concentración en el sobrenadante de encapsulación desde el primer minuto hasta siete días. El resultado apunta en la dirección de un proceso de encapsulación sorprendentemente rápido, donde la infiltración de la biomolécula ocurre casi inmediatamente con cargas efectivas de aproximadamente un 20-30 %. Los resultados de la caracterización fisicoquímica de estos materiales sugieren que el proceso de encapsulación afecta a la estructura de la red de ZIF-8, encontrándose nuevos picos de

difracción en los difractogramas de los materiales encapsulados. No se puede descartar una modificación menor de la red tras el proceso de infiltración, ya que se puede lograr la sustitución del ligando imidazol en el ZIF-8 con relativa facilidad. Esta afirmación se confirma también tras analizar los perfiles de adsorción de N₂ a 77 K de los materiales híbridos: el ZIF-8 muestra flexibilidad durante la adsorción de gas gracias a la rotación de los ligandos imidazol, generando un efecto de “apertura de puerta”. Sin embargo, para todos los materiales compuestos, el comportamiento de apertura de puerta característico de los microporos del ZIF-8 se pierde por completo con la infiltración de biomoléculas, lo que implica que la reorientación de los ligandos durante la adsorción de gas no es posible. Este resultado implicaría también la posible sustitución de ligandos en los materiales compuestos.

De los cuatro compuestos obtenidos, Bz@ZIF-8 y MA@ZIF-8 se emplean en ensayos de actividad antifúngica por presentar la mayor carga de molécula activa. La dosis liberada de benzaldehído y antranilato de metilo fue suficiente para oponerse al crecimiento fúngico, con una actividad mejorada contra *Penicilium expansum* en después de la integración en películas biopoliméricas, reflejando un efecto fungistático y fungicida más eficaz que la molécula libre en ambos casos.

Como conclusión, los compuestos “biomolécula@ZIF-8” preparados en este Capítulo son opciones potenciales para aplicaciones de envasado de alimentos debido a su preparación directa y procesamiento simple, y una actuación mediada por la red metalorgánica que permite una acción antifúngica mejorada.

Finalmente, en el *Capítulo 5*, la encapsulación de macrobiomoléculas se enfoca mediante la síntesis de dos MOF mesoporosos jerárquicos de metales mixtos siguiendo una ruta de química verde.

Como se discute a lo largo de esta Tesis, la encapsulación de moléculas activas en MOFs tras un procedimiento de impregnación es una metodología términos de carga efectiva, preservación y liberación controlada. Este método de infiltración directa presenta la ventaja de utilizar los MOFs preformados, sin modificar el procedimiento sintético y evitando la funcionalización post-sintética. Sin embargo, este método de infiltración está limitado por las dimensiones de la molécula seleccionada, que debe ajustarse al tamaño de poro de la estructura y no exceder la ventana del poro. Por lo tanto, la selección de una estructura mesoporosa, que presente una porosidad prominente y grandes ventanas de poros accesibles, puede ser una estrategia viable para superar esta limitación de tamaño. Entre los pocos MOF jerárquicos mesoporosos reportados hasta la fecha, nuestro grupo ha reportado un MOF basado en tetratiafulvaleno (TTF) llamado MUV-2. Este MOF se propone como un candidato prometedor para la encapsulación de moléculas bioactivas debido a su alta porosidad y su comportamiento flexible, revelando una variación de aproximadamente un 40 % en el tamaño de poro al exponerse a diferentes disolventes. Este interesante comportamiento hace que el MUV-2 sea una selección viable para superar las limitaciones de la metodología de infiltración en cuanto al tamaño de biomolécula, ampliando el espectro de posibles moléculas activas para acomodar en su estructura porosa en comparación con los MOFs discutidos anteriormente.

Una posibilidad de ampliar aún más la gama de aplicaciones de MUV-2 y expandir su química se basa en la modificación de la red. Esencialmente, al reemplazar uno de los centros de hierro en la estructura con un metal

divalente, se obtiene un MOF de metal mixto (MM-MOF) con propiedades ajustables que retiene la estructura mesoporosa. En comparación con los MOFs homometálicos, los MM-MOF pueden aprovechar la complejidad y la sinergia derivadas de la presencia de varios iones metálicos en la estructura del MOF, y pueden exhibir una mayor estabilidad y un rendimiento mejorado en varias aplicaciones, particularmente en almacenamiento y separación de gases, catálisis, sensado y construcción de materiales fotoactivos.

En este Capítulo 5 se persiguen dos objetivos principales. Por un lado, se apunta a la obtención de análogos mixtos de MUV-2 (MM-MUV-2). Por otro lado, también se explorará la elusiva síntesis por vía de *química verde* de MUV-2(Fe) y sus derivados, sustituyendo el DMF de la síntesis reportada por el menos dañino isopropanol. A continuación, se evaluará la idoneidad de los materiales verdes como portadores de biomoléculas de mayor tamaño mediante encapsulación de lisozima siguiendo una metodología de impregnación directa.

Se sintetizan así dos nuevos derivados MOF de metales mixtos de MUV-2 con fórmula empírica $(\text{TTFTB})_3[(\text{Fe}_2\text{M}^{\text{II}}\text{O})(\text{H}_2\text{O})_2]_2$ ($\text{M} = \text{Co}, \text{Ni}$). Estos derivados se caracterizan exhaustivamente mediante diferentes técnicas como IR, TGA, PXRD, ICP-MS, SEM, EDX medidas magnéticas y de adsorción de gases. Los materiales sintetizados son isoestructurales con el MUV-2(Fe) cristalino (tal y como lo confirman sus patrones de difracción) y presentan un comportamiento flexible análogo tras su exposición a disolventes.

El desarrollo de un enfoque de *síntesis verde* reemplaza el nocivo disolvente DMF previamente empleado con el objetivo de avanzar hacia metodologías respetuosas con el medio ambiente y procesos escalables. Se realizan esfuerzos significativos para reproducir la síntesis de MUV-2(Fe) a través de *química verde*, es decir, empleando disolventes menos nocivos como los alcoholes, sin obtener los resultados esperados. Sin embargo, la

síntesis verde de los derivados de MM-MUV-2 se logra siguiendo las condiciones de síntesis estándar, pero sustituyendo el disolvente DMF por isopropanol. Con este protocolo de síntesis, la aplicación de estos materiales en la encapsulación de biomacromoléculas se puede realizar de forma directa, evitando pasos de lavado adicionales. Consecuentemente, aprovechando la naturaleza mesoporosa jerárquica de la red, se evalúa el desempeño de estos materiales mixtos *verdes* como agentes encapsulantes de moléculas bioactivas más grandes mediante la encapsulación de lisozima. La lisozima es una enzima obtenida de la clara de huevo de gallina con actividades bacteriolíticas y bactericidas que pueden integrarse en películas antimicrobianas para la conservación de alimentos.

Siguiendo la cinética de encapsulación, el mayor contenido de lisozima se logra a las 24 horas de encapsulado, alcanzando altos valores de carga estimados (aproximadamente 50 %), y presentando una disminución a las 72 horas. Esto puede sugerir que la encapsulación tiene lugar mediante un intercambio entre el exceso de ligando en los poros de la estructura de los MM-MUV-2 (consecuencia de la poca solubilidad del TTFTB en alcoholes, quedando atrapado en los poros durante el proceso de síntesis) y las moléculas de lisozima, y que una vez se alcanza el equilibrio, la enzima puede liberarse en el medio de encapsulación. Se evalúa también el efecto de la concentración inicial de lisozima, y como era de esperar, el empleo de una concentración inicial de lisozima de $50 \text{ mg}\cdot\text{mL}^{-1}$ genera valores de carga más altos que la concentración de partida de $10 \text{ mg}\cdot\text{mL}^{-1}$, respaldando las condiciones de sobresaturación de biomoléculas en el medio de encapsulación explotadas en la metodología de encapsulación diseñada a lo largo de esta Tesis.

Los resultados preliminares muestran compuestos con altas cargas estimadas de lisozima (hasta un 40 %) siguiendo la metodología de infiltración desarrollada y un tiempo de impregnación de 24 horas, sin que ello afecte a la integridad estructural de las redes. Esencialmente, las redes de MM-MUV-2 pueden acomodar cómodamente una cantidad competitiva de moléculas de lisozima cargadas sin ninguna distorsión en los canales mesoporosos, lo que confirma la idoneidad de estos materiales como portadores de biomoléculas más grandes empleando una metodología de impregnación fácil y directa.

Como trabajo futuro, se debe evaluar la cinética de liberación de lisozima y la actividad antimicrobiana de los compuestos obtenidos.

Abbreviations

antisym	Antisymmetric
ar	Aromatic
BAC	Bioactive Compounds
BCA	Bicinchoninic Acid
BDC	1,4-benzenedicarboxylate
BET	Brunauer-Emmett-Teller
BSA	Bovine Serum Albumin
BTC	Benzene-1,3,5-tricarboxylate
Bz	Benzaldehyde
CFU	Colony-forming Units
CP	Coordination Polymer
CUS	Coordinatively Unsaturated Sites
D.B.	Dry Base
DFT	Density functional theory
DMF	Dimethylformamide
EDX	Energy Dispersive X-ray spectroscopy
EO	Essential Oil
EPR	Electron paramagnetic resonance
EtOH	Ethanol
EVOH	Ethylene vinyl alcohol
FDA	US Food and Drug Administration
FTIR	Fourier-Transform Infrared spectroscopy
GRAS	Generally Recognized As Safe
GS-MS	Gas chromatography–mass spectrometry
Gua	Guaiacol
HPLC	High-Performance Liquid Chromatography
ICP-MS	Inductively Coupled Plasma Mass Spectrometry
LRV	Log Reduction Value
Ly	Lysozyme
MA	Methyl Anthranilate
MHB	Mueller Hinton Broth
MM	Mixed-metal
MOF	Metal-Organic Framework

MW	Microwave
NP	Nanoparticle
oop	Out-of-plane
PDA	Potato Dextrose Agar
PDB	Protein Database
POP	Persistent Organic Pollutants
PSD	Pore-Size Distribution
PTFE	Polytetrafluoroethylene
PXRD	Powder X-Ray Diffraction
RH	Relative Humidity
SA	Salicylaldehyde
SBU	Secondary Building Unit
SEM	Scanning Electron Microscopy
SOD	Sodalite
sym	Symmetric
TEM	Transmission Electron Microscopy
TGA	Thermogravimetric Analysis
TSA	Tryptone Soy Agar
TSB	Tryptone Soy Broth
TTFTB	Tetra-thiafulvalenetetrabenzoate
XRD	X-Ray Diffraction

CHAPTER 1

General Introduction

1.1. Metal-Organic Framework materials

Coordination polymers (CPs) are coordination compounds with repeating coordination entities that extend in one, two, or three dimensions. These CP compounds comprise metal centres connected by organic ligands, generating extended networks. Among all the structures comprised by this definition, a Metal–Organic Framework (MOF) is a coordination network with organic ligands containing potential or permanent voids (**Figure 1.1.1**). This definition takes into account the fact that many systems are dynamic, and changes in structure may occur depending on temperature, pressure, or other external stimuli, thus modifying the potential porosity of the framework due to solvent and/or guest-filled voids.¹

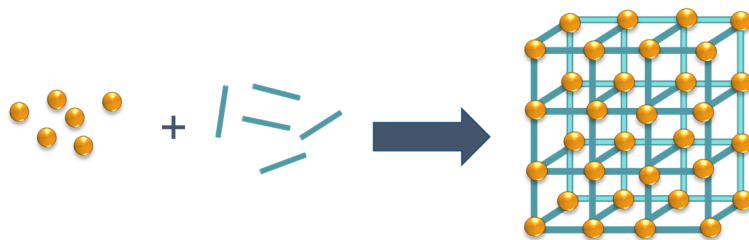


Figure 1.1.1. Schematic representation of the self-assembly between metal ions or metallic clusters (golden spheres) and organic linkers (blue shapes) to constitute a Metal-Organic Framework material.

The work published by Hoskins and Robson in 1989 can be considered the origin of the field of MOFs. They envisioned that a new and potentially extensive class of solid polymeric materials could be afforded by linking together metallic centres with organic ligands, thus generating a regular array of cavities interconnected by windows, and reported the combination of a 4-connected organic linker with Cu^{I} centres, resulting in a three-dimensional framework.² The term MOF was later coined by Yaghi and co-workers with the publication of a porous hybrid network denoted $\text{Cu}(4,4'\text{-bpy})_{1.5}\cdot\text{NO}_3(\text{H}_2\text{O})_{1.25}$ in 1995.³ Since then, this research field, situated at the

interface between molecular coordination chemistry and materials science, has grown at an almost unprecedented rate since the 1990s,⁴ with currently over 90000 MOFs reported and over 500000 structures predicted.⁵

The wide variety of combinations between organic linkers and metals brands MOFs as materials with a very rich chemistry based on reticular synthesis, a conceptual approach that requires the use of secondary building units (SBU) to direct the assembly of ordered frameworks yielding materials designed to have predetermined structures, compositions, and properties. The term “secondary building unit” refers to the geometry of the units defined by the points of extension (such as the carboxylate C atoms in most carboxylate MOFs).⁶ First row transition metals are often the more common choice for MOF synthesis, but examples of cations from every group of the periodic table can be found in MOF research.⁷ Regarding the organic linkers, almost any organic moiety of choice could be selected. Carboxylate, N-heterocyclic, phosphonate, hydroxy- and amino- linkers are typically employed in MOF production.

Historically, when coordination chemists focused on the assembly of organic and inorganic building blocks to produce porous structures in the early 1990s, mild reaction conditions were utilized due to the expectation of weak contacts between the building blocks. However, chemists with experience in zeolite-related materials began to consider the use of organic molecules not only as structure-directing agents, but also as reactants that could be incorporated into the framework structure.⁸ The use of high reaction temperatures, long reaction periods, and solvents with high boiling temperatures is the consequence of this later approach. These distinct scientific foundations explain the various synthetic approaches used in MOF synthesis today.⁹ Nowadays, MOFs can be obtained using many synthetic procedures that range from more “classical” approaches such as slow

diffusion, solvent evaporation hydro- or solvothermal, electrochemical, or mechanochemical synthetic methods, as well as more innovative synthetic approaches like spray drying and flow chemistry synthesis, even permitting larger scale production.^{10,11} A temporal representation of the emergence of these methodologies in the field is depicted in **Figure 1.1.2**.

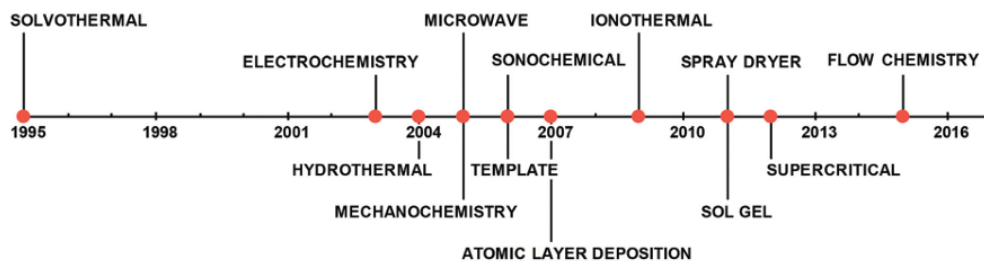


Figure 1.1.2. Timeline of the most common synthetic approaches patented for the synthesis of MOFs. Reproduced from reference 10.

Regarding the physicochemical characterization of these materials, the most significant means for MOF characterisation include general chemical characterization techniques such as i) single crystal X-ray diffraction (XRD), which provides absolute structural information about the MOF; ii) powder X-ray diffraction (PXRD) to establish crystallinity and phase purity of the bulk product; iii) elemental analysis to ensure phase purity of the material; iv) thermogravimetric analysis (TGA) for the determination of the thermal stability and the purity of the MOF, evidencing the presence of defects in the structure; v) infrared spectroscopy (IR) to determine the presence or absence of IR active functional group in the frameworks; and vi) transmission (TEM) and scanning (SEM) electron microscopies, which provide information about particle size and morphology. This latter technique can be coupled with energy dispersive X-ray spectroscopy (EDX) and give information about the composition of the material. In addition, specific sorption analysis with gases is carried out, including typically N₂

sorption isotherms at 77 K. This surface area measurement provides information about the capability of a porous material for gas uptake, whereas pore size distribution can also be analysed.

Due to their “building block”-based synthesis, MOFs are characterized by a large chemical versatility that permits fine control with respect to the nature of the pores, both in terms of shape and size. These modular chemical properties have facilitated their application in many different fields such as catalysis,¹² storage of energy,¹³ gas separation¹⁴ and biologically related fields, such as drug delivery¹⁵ and biomolecule encapsulation.¹⁶

In addition, a controlled miniaturization of MOFs results of great interest for the integration of these materials in applications like sensing or drug delivery. The field of biomedicine particularly benefits from MOF nanostructuring, since particle size is a limiting factor for some administration routes where very precise sizes are required.¹⁷ Thus, combining the intrinsic properties of porous materials with the benefits of nanostructures, MOF nanoparticles (NPs), or nanoMOFs, are expected to improve in some cases the performances of classical bulk crystalline MOFs. When considering the use of nanoMOFs as carriers, their vast surface area may allow for effective surface modification, which would improve the chemical and colloidal stability and facilitate material processing while promoting an enhanced bioactivity.¹⁸

1.1.1. Metal-Organic Frameworks as carrier agents

A crucial effort is devoted in the field of medicine to the development of methods to control drug release in order to achieve a prolonged and better control of drug administration. Two currents have been traditionally explored: the “organic route”, employing biocompatible macromolecules or

polymers,^{19,20} and the “inorganic route”, in which the hosts are inorganic porous solids, such as zeolites²¹ or mesoporous silicate materials.²²

In the first scenario, a wide array of pharmaceuticals can be encapsulated, but regulated drug release is difficult to achieve due to the lack of a well-defined porosity. In the second example, this release is accomplished by grafting organic molecules onto the pore walls, but it results in drug-loading capacity reduction. With the publication in 2006 by Serre, Férey and co-workers on the encapsulation of the model drug ibuprofen into MIL-100 and MIL-101 frameworks,¹⁵ extending later the work to other active molecules and frameworks,^{23–25} the use of MOFs as drug-delivery systems was presented as a third “hybrid route”, combining high and regular porosity with the presence of organic groups within the framework. With these conditions, a high drug loading and a controlled release was achieved, thus improving the performance of classical carrier agents and offering the possibility to tune the uptake and delivery of guest molecules by the appropriate selection of the MOF scaffold. **Figure 1.1.3** summarises the advantages of using MOFs as carrier agents in comparison with classical carriers.



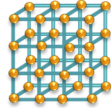
	 Mesoporous materials (SiO ₂)	 Liposomes	 nanoMOFs
Specific surface area	~1000 m ² /g	~100 m ² /g	Up to 7000 m²/g
Adsorption capacity	Up to 0,2 g/g	0,1 g/g	> 1.4 g/g
	Size tunability Surface functionalization	Flexibility Biodegradability	Chemical versatility High stability Guest molecule interaction Controlled delivery

Figure 1.1.3. Comparison of some physico-chemical properties of nanoMOFs versus classical carrier agents.

The tunable porosity and versatile composition of nanoMOFs appoints them as particularly attractive candidates to allocate a wide amount of various guest molecules. Furthermore, the active molecules (drugs, cosmetics, biologically active gases, proteins, or nucleic acids) can be entrapped within the MOF cavities by encapsulation or mineralization, or even be incorporated as a constitutive part of the MOF's structure to be released upon framework degradation.²⁶

The immersion method is the most commonly used protocol for biomolecule encapsulation in MOFs. The general experimental procedure consists in dissolving or suspending the biomolecule in a suitable solvent first to form a mixture with an appropriate active ingredient concentration. Then, the biomolecule solution is added to the MOF particles, and the mixture is stirred for a period of time and heated if needed. After collecting the encapsulation product (usually by centrifugation) and drying, the bioactive-loaded MOF can be obtained. A very important prerequisite for the guest molecule to be infiltrated is that its size and shape need to fit the MOF pores, and then it can be fixed in the confined space of the host framework through π - π interaction, hydrogen bonding, coulombic forces, van der Waals forces, coordination bonds, etc.

These MOF-based composites present high performance in biomedical applications, such as cargo delivery systems for cancer therapy, bioimaging, biosensing, and biocatalysis.²⁷

The cosmetic field is another interesting area that benefits enormously from biomolecule encapsulation. The application of many cosmetic molecules is hindered by their instability, poor solubility, or low bioavailability. MOF encapsulation is presented as a plausible solution for the application of cosmetic molecules with industrial interest. This is the case of active molecules such as the liporeductor caffeine, where MOF encapsulation

overcame its high tendency to crystallize, improving drug loadings as well as controlling the molecule release.^{23,24} The benefits of MOF encapsulation are not limited to skin care products in the cosmetic field, but this methodology can also be applied to encapsulate and release fragrances in a controlled manner.²⁸

1.1.2. Metal-Organic Frameworks in the Food Industry

The benefits of the encapsulation methodologies can also be translated to the food industry, receiving extensive research attention since the developing of reliable and accurate techniques to ensure food quality and safety it is always beneficial to the industry. More than 90000 research articles can be found in the literature regarding MOFs for food industry purposes in the last two decades, reflecting how the research community has taken interest in this potential application (**Figure 1.1.4**).²⁹

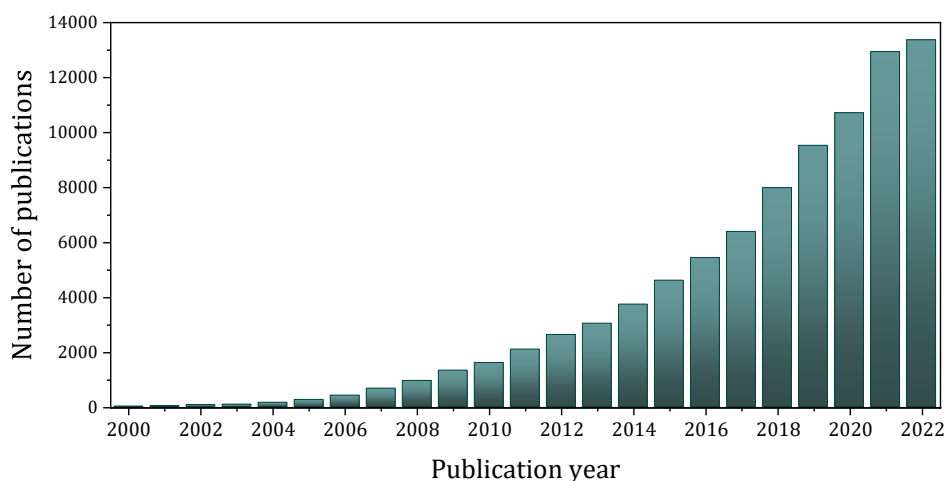


Figure 1.1.4. Number of publications per year of MOFs related with food industry. Data extracted from Web of Science on 21/04/2023.

Controlled MOF-based release systems originated from the drug industry have emerged as an innovative technique to ensure the shelf-life of food

products. Indeed, MOFs have been lately postulated as promising cargo delivering nanocarriers in the research fields of agricultural³⁰ and food chemistry owing to their excellent porosity, high loading capacity, controlled release ability, and ease of surface modification.³¹ In some cases, MOF biocompatibility, processability, and large-scale production have fulfilled industrial requirements and their potential biorelated uses have been investigated.³²

The principal interest of employing MOFs in the food industry relies on the ability of metal-organic frameworks to encapsulate either active molecules or hazardous substances. In the following, examples of MOF uses for food safety applications will be discussed for a better understanding of the field.

Many studies can be found in the literature regarding the use of MOFs in the removal of contaminants from production sources,³³ food packaging,³⁴ food preservation,^{35,36} the detection and monitoring of contaminants in food products.³⁷ For example, these porous materials can be employed in fluorescence sensors for the detection of risky small molecules, ions, and food-borne pathogens in food, yielding facile and sensitive analysis methods for *in situ* and real-time sensing.³⁹

Owing to their high surface areas, MOFs can also be used as adsorbents for the development of sample preparation techniques for food matrices prior to their analysis using chromatographic and spectrometric techniques with excellent performance in the analysis of complex food samples, such as beverages, fruits and vegetables, or meat.³⁸

Environmental pollution has also become one of the major problems affecting food safety and thus affects human health. Once these hazardous substances are introduced into the environment, they can enter the food chain at multiple points and accumulate in organisms. Many MOF-based materials have been successfully applied for the removal of unsafe

components in water and soil, such as herbicides, antibiotics, heavy metal toxic ions, persistent organic pollutants (POPs), and dyes.^{40,41}

Though there have been few reports of MOFs materials in food packaging, MOFs have great potential to be developed into advanced and environmentally friendly materials for food packaging as oxygen or ethylene scavengers, and moisture absorbers.⁴²

MOFs research related to antibacterial applications can also be employed in food preservation, including slow-release antibiotic delivery, antibacterial coating with high-polymer materials, and high-efficiency antibacterial materials combined with nanoparticles.³¹ Many antibacterial active molecules can be encapsulated into the porous frameworks but, in particular, naturally occurring bioactive compounds (BAC) result of great interest for the food industry. These type of active molecules (e.g., antioxidants, vitamins, polyphenols) are effectively used as food flavouring agents and/or preservatives to inhibit microbial growth.

1.2. Essential oils for food safety

Natural active components such as essential oils (EOs) are largely preferred as compared to artificial additives when considering applications in the food industry as preservatives, innovative packaging and the fight against pathogens that cause food poisoning.⁴³ EOs are concentrated liquids extracted from aromatic plant materials. As natural products, a low environmental impact is added to their interesting physicochemical characteristics and biological activity.

Due to their complex chemical composition, EOs have a broad biological and antimicrobial activity spectrum (antibacterial, antifungal, antimould, antiviral, pest control, insect repellents).^{44,45} Numerous studies have highlighted EOs antimicrobial effects even against multi-resistant bacteria. The phenolic components are predominantly responsible for the antibacterial properties of EOs, and have also attracted attention due to their antioxidant and antitumour activity.⁴⁶ **Table 1.2.1** summarizes a selection EOs which have been shown to exert antibacterial properties *in vitro* or in food models, while **Figure 1.2.1** showcases the structural formulas of selected components of EOs with antibacterial and antifungal properties.

Table 1.2.1. Major components of selected EOs that exhibit antibacterial properties. Data extracted from reference 43.

EO common name	Latin name of plant source	Major components	Approximate composition
Cilantro	<i>Coriandrum sativum</i> (immature leaves)	Linalool	26%
		E-2-decanal	20%
Coriander	<i>Coriandrum sativum</i> (seeds)	Linalool	70%
Cinnamon	<i>Cinnamomum zeylandicum</i>	Trans-cinnamaldehyde	65%
Oregano	<i>Origanum vulgare</i>	Carvacrol	Trace-80%
		Thymol	Trace-64%
		γ -Terpinene	2-52%
		p-Cymene	Trace-52%
Rosemary	<i>Rosmarinus officinalis</i>	α -pinene	2-25%
		Bornyl acetate	0-17%
		Camphor	2-14%
		1,8-cineole	3-89%
Sage	<i>Salvia officinalis</i> L.	Camphor	6-15%
		α -Pinene	4-5%
		β -pinene	2-10%
		1,8-cineole	6-14%
		α -tujone	20-42%
Clove (bud)	<i>Syzygium aromaticum</i>	Eugenol	75-85%
		Eugenyl acetate	8-15%
		Thymol	10-64%
Thyme	<i>Thymus vulgaris</i>	Carvacrol	2-11%
		γ -Terpinene	2-31%
		p-Cymene	10-56%

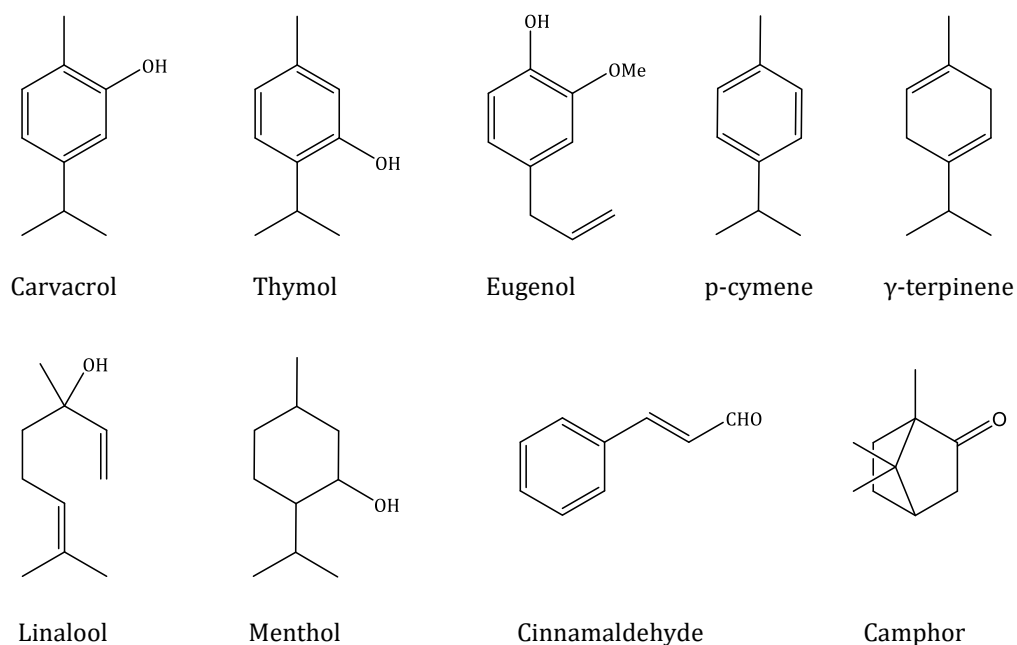


Figure 1.2.1. Structural formulas of selected components of EOs with antibacterial and antifungal activity.

The antimicrobial activity of essential oils cannot be attributed to one specific mechanism, contemplating the vast sum of different chemical compounds present in these biological products. Thus, the mode of action of each EO compound may vary, as some act on the outer membrane of bacteria and some act on the membrane proteins' efflux system.⁴⁷ Although the detailed mechanisms are not yet fully elucidated, key principles have been reported for representative EOs. The primary mechanism by which essential oils disrupt many cellular processes, including membrane-coupled energy production, membrane transport, toxin secretion, and other metabolic regulatory functions, is by destabilizing the cellular architecture. This results in the breakdown of membrane integrity and an increased permeability. Due to their lipophilic nature, EOs are able to permeate bacterial cell wall, which breaks the cell barrier, provoking the release of their essential intracellular components, and stopping the targeted pathogens' cellular metabolism and enzyme kinetics (**Figure 1.2.2**). When the integrity of the membrane is

disrupted, it loses its ability to serve as a barrier, an enzyme matrix, and an energy converter.⁴⁸

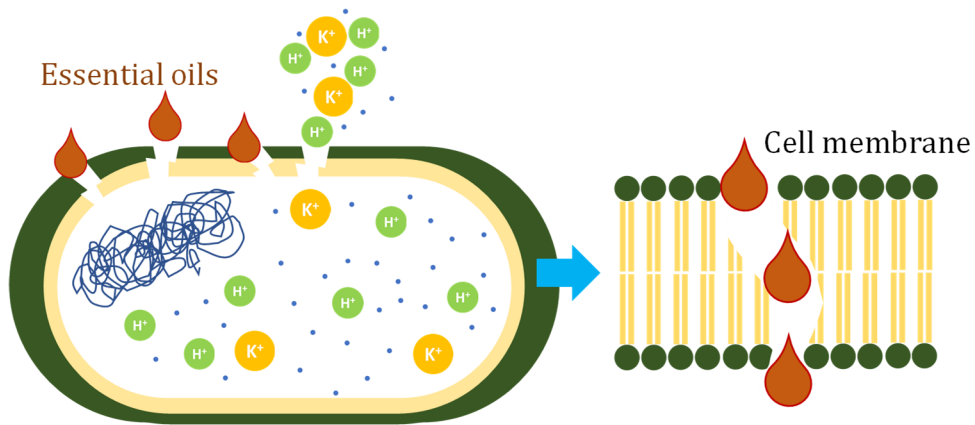


Figure 1.2.2. Membrane disruption in a bacterial cell leading to the leakage of cellular components and loss of ions caused by essential oils.

The food industry presents a growing demand for EOs because of their important applications as food preservatives, innovation in food packaging and the fight against pathogens generating dangerous food poisoning (*Listeria monocytogenes*, *Salmonella typhimurium*, *Clostridium perfringens*, *Pseudomonas putida* and *staphylococcus aureus*). Numerous studies have demonstrated the efficiency of EOs in low doses in the fight against bacterial pathogens encountered in food industry and meat products.⁴⁹

Despite exhibiting these bioactive properties, a desired large-scale use of these compounds is hampered by their volatile and insoluble nature, their susceptibility to various environmental and processing conditions, and their characteristic strong aroma. These fragile compounds could be degraded easily (by oxidation, volatilization, heating, or light exposure) if they are not protected from intrinsic and extrinsic factors such as pH, water activity, enzymatic degradation, temperature, relative humidity, and storage environment.⁵⁰ For these reasons, the encapsulation of volatile preservatives into carrier materials has been widely investigated in the food industry and

biomedical field as a plausible solution to optimize their activity.^{51,52} Typical encapsulation examples using nano- and micro-emulsions,⁵³ lipid nanoparticles⁵⁴ or liposomes,⁵⁵ have shown to substantially increase EOs stability, often ensuing a prolonged action (**Figure 1.2.2**).⁵⁰ The encapsulation process reduces reactivity with the environment (water, oxygen, light), decreases the evaporation or the transfer rate to the outside environment, promotes handling ability, masks taste, and enhances dilution to achieve a uniform distribution in the final product when used in very small amounts.⁵⁶

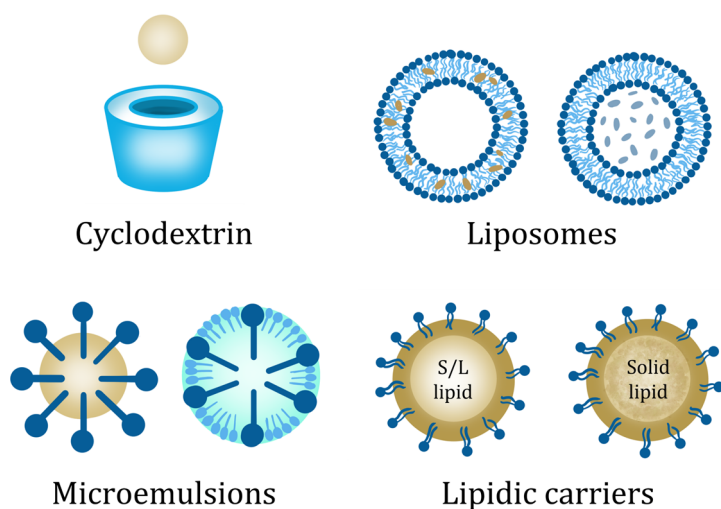


Figure 1.2.3. Schematic representation of the typical EO encapsulation agents used in the food industry and in cosmetics.

With a demonstrated efficiency as smart capsules capable of i) encapsulating active molecules with high payloads with a facile loading process, ii) preserving the activity in the long-term, and iii) directing the release upon stimuli, MOFs are proposed in this thesis as bioactive molecule carriers and their potential use in food related applications is investigated.

1.3. Nanostructured MOF candidates for biomolecule encapsulation

As discussed in the previous sections, the use of MOFs in the food area requires a biocompatible composition, should the consumption of the MOF or any of its components occur. For this, it must be considered to use metals that exhibit an acceptable toxicity such as Ca, Mg, Zn, Fe, Ti, or Zr to be absorbed by the body. The organic counterpart should be excreted from the body – linkers like terephthalic and trimesic acid, or methylimidazole should be easily removed under physiological conditions due to their high polarity.¹⁷ The cytotoxicity of most of the nanoMOFs employed in this Thesis, among others, has been extensively studied in the literature (see **Table 1.3.1**), indicating low toxicity values similar to those of other currently commercialised nanostructured materials.^{18,57} Taking this into consideration, and based on their physico-chemical performance, four nanostructured MOF materials will be tested in this Thesis, mainly MIL-100(Fe), ZIF-8, UiO-66 and UiO-66-NH₂. Furthermore, the viability of the less explored mesoporous MUV-2 material as active molecule carrier will be explored.

Table 1.3.1. Percentages of the ‘Top 10 MOFs’ analysed in toxicity studies. Data extracted from reference 57.

Material	Percentage
MIL-100(Fe)	27 %
UiO-66(Zr)	14 %
ZIF-8(Zn)	14 %
MIL-88B(Fe, Cr)	11 %
MIL-101(Fe, Cr)	11 %
MIL-88A(Fe)	8 %
MOF-74(Co, Ni, Mg, Cu, Mn, Zn)	6 %
MOF-5(Zn)	2 %
UiO-67(Zr)	2 %

1.3.1 MIL-100(Fe)

Among the possible MOFs to be used as encapsulating agents, the mesoporous Fe^{III} trimesate nanoMOF MIL-100(Fe)⁵⁸ (MIL: Materials of Institute Lavoisier) offers unique possibilities since is biocompatible and can be produced through green synthesis⁵⁹ in optimal scales.^{58,60} This Fe^{III} carboxylate MOF is built from trimers of iron octahedra sharing a common vertex $\mu_3\text{-O}$ (**Figure 1.3.1a**). The trimers are then linked by the benzene-1,3,5-tricarboxylate (BTC) moieties (**Figure 1.3.1b**) leading to the formation of hybrid supertetrahedra (**Figure 1.3.1c**) which further assemble into a zeolitic architecture (**Figure 1.3.1d**).

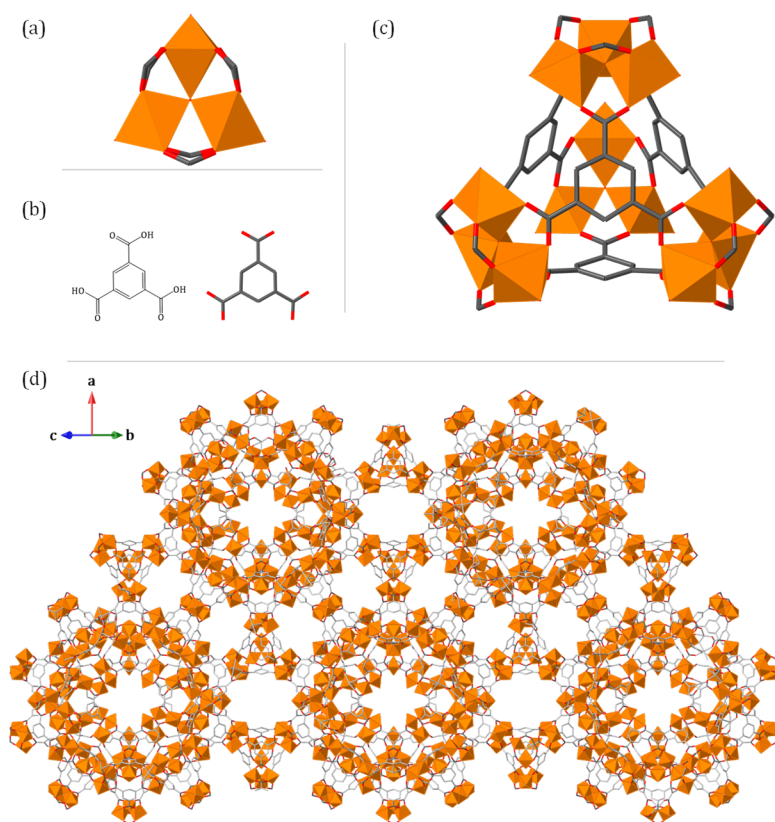


Figure 1.3.1. (a) $[\text{Fe}_3(\mu_3\text{-O})(\text{COO})_6]$ cluster. (b) Benzene-1,3,5-tricarboxylate chemical structure. (c) Supertetrahedra entities assemblies of iron trimers and BTC linkers. (d) View of MIL-100(Fe) structure in the $[0\ 0\ 1]$ direction. Iron, carbon, and oxygen are represented in orange, grey and red, respectively.

The structure of MIL-100(Fe) is delimited by two types of mesoporous cages with pores of *ca.* 25 and 29 Å, accessible through microporous windows of *ca.* 5.5 and 8.6 Å (**Figure 1.3.2**).⁵⁸ The porous framework presents a Surface Area of $\sim 2000 \text{ m}^2 \cdot \text{g}^{-1}$.

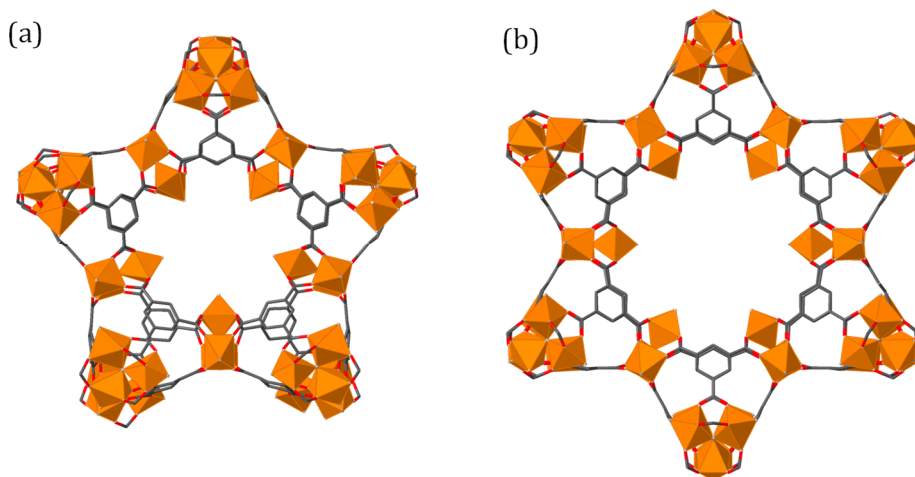


Figure 1.3.2. Pentagonal (a) and hexagonal (b) windows in the MIL-100(Fe) structure. Iron, carbon, and oxygen are represented in orange, grey and red, respectively.

MIL-100(Fe) is one of the most studied MOF in drug delivery applications.⁶¹ The size of the cages is the only limitation to the loading of biomolecules into the pores of MIL-100(Fe). In principle, any molecule with dimensions lower than those of the cages is susceptible to be loaded inside the porous framework. In addition, the structure characteristics of MIL-100(Fe) permit to form accessible coordinatively unsaturated iron sites (CUS) upon induced reducibility on the framework, strongly modifying the preferred interactions with guest molecules.⁶² In the as-synthesized form, the terminal molecules on two of the three iron octahedra are two H_2O molecules, and depending on the synthesis conditions and washing protocol, either F^- or OH^- anions are present on the third iron. This opens the possibility of not only loading the selected molecules by physisorption but also by chemisorption, through coordination between the Fe^{III} cations and the guest molecule.

One of the main advantages of MIL-100(Fe) is the feasibility on miniaturisation. The nano-structuration of the framework improves its chemical and colloidal stability, thus facilitating the processing of the material for immediate applications like its integration in films.¹⁸ Essentially, nanoparticles of MIL-100(Fe) are obtained by microwave-assisted (MW) solvothermal synthesis.⁵⁹ MW-assisted synthesis presents important advantages over classic methods like solvothermal, such as homogeneous heating along the reactor, faster reaction times and lower polydispersity together with higher synthetic yields. Fast crystal growth and small particle size are boosted due to a fast increase of temperature and pressure, which promotes the formation of numerous nucleation sites over crystal growing. Furthermore, MW-assisted synthesis allows the implementation of green solvents like water, which is especially suitable for food industry applications.⁶³

1.3.2. ZIF-8

The zeolitic MOF known as ZIF-8 (ZIF: Zeolitic Imidazolate Framework), comprised by Zn^{II} metal centres tetrahedrally coordinated to 2-methylimidazolate ligands (**Figures 1.3.3a** and **1.3.3b**, respectively), possesses a similar structure as conventional aluminosilicate zeolites with a SOD (sodalite) topology (**Figure 1.3.3c**).⁶⁴ The metal centre is solely coordinated by the N atoms of four 2-methylimidazolate ligands to give an overall neutral framework. The five-membered imidazole ring serves as the bridging unit between the Zn^{II} centres and imparts angle of *ca.* 145° throughout the structure via coordinating N atoms in the 1,3-positions of the ring, providing for organically lined cages and channels rather than a silicate oxide surface as in zeolites. A 11.6 Å micropore is accessible in this framework through 3.4 Å apertures. This material exhibits permanent porosity (Surface Area $\sim 1600 \text{ m}^2 \cdot \text{g}^{-1}$), high loading capacity and pH-sensitive

degradation, as well as optimal thermal and chemical stability. ZIF-8 can encapsulate hydrophobic, hydrophilic and amphiphilic drugs,^{65–67} and consequently, has been employed in various applications related with drug delivery: anticancer drugs, photothermal agents, photodynamic agents, chemodynamic therapy, protein encapsulation and genome therapy.⁶⁸

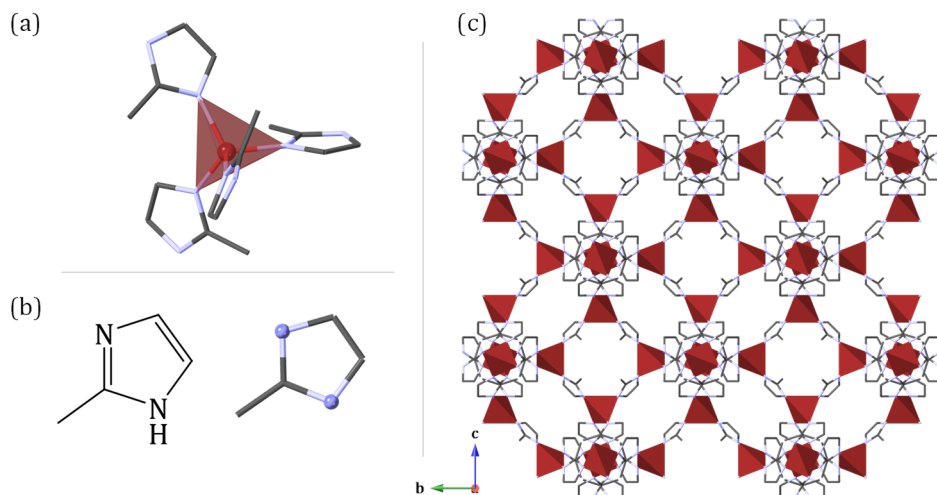


Figure 1.3.3. (a) Zn^{II} metal centre (red tetrahedra) coordinated to four 2-methylimidazole ligands. (b) 2-methylimidazole chemical structure. (c) View of ZIF-8 structure along the *a* axis. Zinc, carbon, and nitrogen are represented in red, grey, and blue, respectively.

Analogous to MIL-100(Fe), the molecule size is the only limitation for active molecule infiltration into the porous structure. Contrary to the Fe^{III} based MOF, ZIF-8 framework does not present any CUS, so the interaction between the host ZIF-8 and the guest molecules would be, in principle, limited to physisorption processes into the pores. However, the dynamic structure of ZIF-8 structure can adapt to the presence of guest molecules due to the rotating imidazolite linkers, giving rise to a gate-opening effect (going from a 3.4 to a 6 Å window diameter) that would allow a better accommodation of the active molecules allocated in the pores.^{69,70}

1.3.3. UiO-66 and UiO-66-NH₂

The following archetypal MOF employed is UiO-66 (UiO: University of Oslo), constituted by Zr^{IV} oxoclusters (**Figure 1.3.4a**) connected through 1,4-benzenedicarboxylate (BDC) linkers (**Figure 1.3.4b**), allowing for 12 extension points for coordination.⁷¹ The SBU in this MOF is constituted by an inner Zr₆O₄(OH)₄ cluster in which the triangular faces of the Zr₆-octahedron are alternatively capped by μ₃-O and μ₃-OH groups. All of the polyhedron edges are bridged by carboxylates originating from the terephthalic acids forming a Zr₆O₄(OH)₄(CO₂)₁₂ cluster. Each zirconium atom is eight-coordinated forming a square-antiprismatic coordination consisting of eight oxygen atoms. One square face is formed by oxygen atoms supplied by carboxylates while the second square face is formed by oxygen atoms coming from the μ₃-O and μ₃-OH groups.

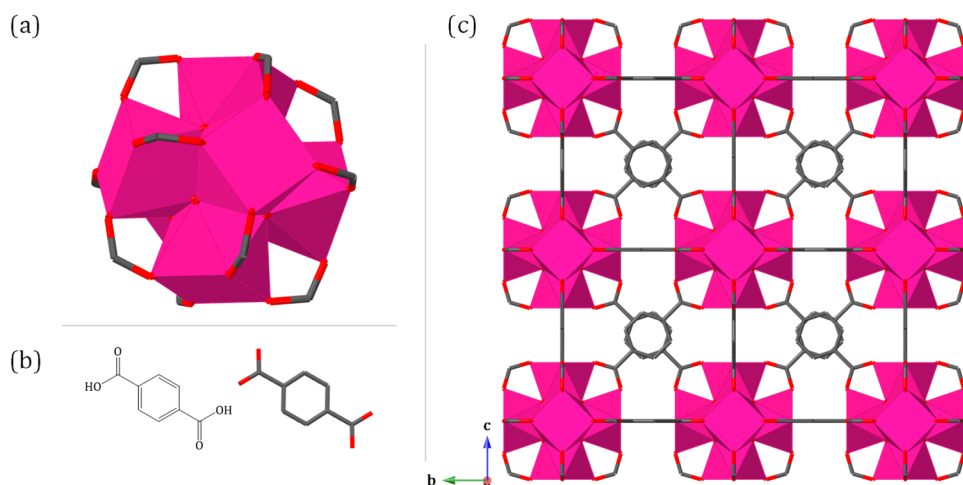


Figure 1.3.4. (a) Zr₆O₄(OH)₄(CO₂)₁₂ cluster. (b) 1,4-benzenedicarboxylate structure (c) View of UiO-66 structure along the *a* axis. Zirconium, carbon, and oxygen are represented in pink, grey, and red, respectively.

The UiO-66 framework is constituted by tetrahedral and octahedral cavities of 7.5 and 12 Å, respectively (**Figure 1.3.5**). Access to the pores is restricted by triangular windows of 6 Å.

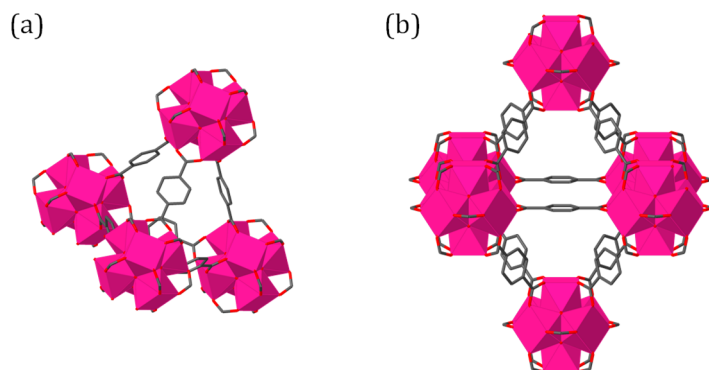


Figure 1.3.5. Tetrahedral (a) and octahedral (b) cavities observed in the UiO-66 framework. Zirconium, carbon, and oxygen are represented in pink, grey, and red, respectively.

UiO-66 is an attractive framework for many applications due to its combination of high thermal and chemical stability and its significant porosity (Surface Area $\sim 1200 \text{ m}^2 \cdot \text{g}^{-1}$).⁷² Its stability can be attributed to the cuboctahedral metal oxide node, since 12-coordination is characteristic of metal atoms in closed packed metal structures. The combination of a robust framework with the relatively low toxicity of zirconium makes this material an interesting candidate for biomolecule carrying. Moreover, functionalizing the pore wall of the UiO-66 framework significantly changes its properties: the adsorption capacity and the selectivity of UiO-66 for strategic gases such as CO_2 and CH_4 can be modified,⁷³ and the impact of the functionalization of the MOF on its drug encapsulation performance has been studied as well.²³

In particular, the presence of the amino group in UiO-66- NH_2 , synthesized using 2-aminobenzene-1,4-dicarboxylic acid, opens the possibility of different interactions with the encapsulated active molecules and enables the possibility to use the additional functionality of the framework as anchoring groups. Therefore, related UiO-66- NH_2 MOF material will be studied in comparison with the parent UiO-66 nanoMOF.

1.3.4. MUV-2

MUV-2 (MUV: Materials of the University of Valencia) is a highly stable tetra-thiafulvalenetetrabenzoate-based MOF with a unique non-interpenetrated hierarchical crystal structure.

MUV-2 consists of 6-connected $[\text{Fe}_3(\mu_3\text{-O})(\text{COO})_6]$ SBUs (**Figure 1.3.6a**) and tetra-thiafulvalenetetrabenzoate (TTFTB) ligands (**Figure 1.3.6b**). Considering each TTFTB ligand as a four-connected node and each $\text{Fe}_3\text{O}(\text{COO})_6$ unit as a six-connected node, MUV-2 can be simplified as a 4,6-connected network with ttp topology. The crystal structure contains large hexagonal mesoporous channels of *ca.* 3 nm along the *c*-axis, which are formed by six TTFTB ligands and six $[\text{Fe}_3(\mu_3\text{-O})(\text{COO})_6]$ clusters (**Figure 1.3.6c**) and are orthogonal to the microporous channels.⁷⁴

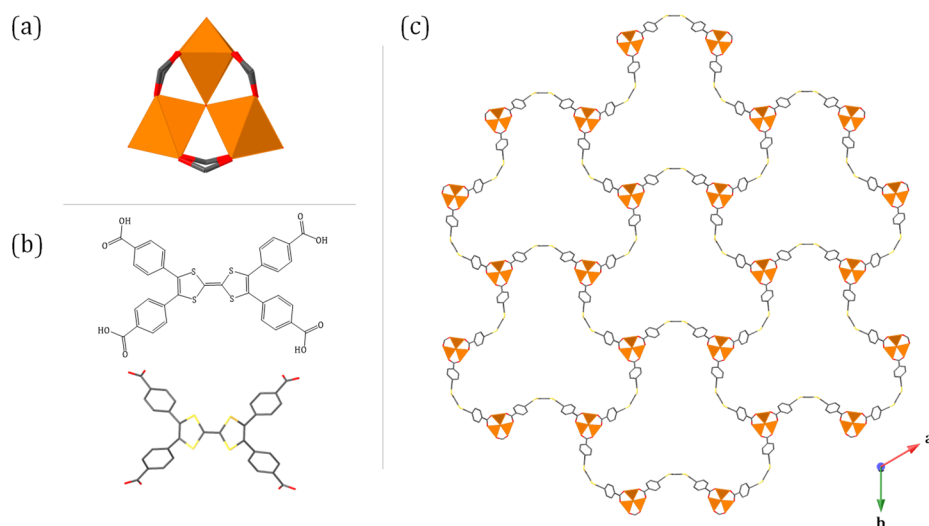


Figure 1.3.6. (a) $[\text{Fe}_3(\mu_3\text{-O})(\text{COO})_6]$ cluster. (b) Tetra-thiafulvalenetetrabenzoate structure. (c) View of MUV-2 structure along the *c* axis. Iron, carbon, sulphur, and oxygen are represented in orange, grey, yellow, and red, respectively.

Although its biocompatibility is currently being tested in our group, MUV-2 results a promising candidate for bioactive molecule encapsulation due its high porosity (Surface Area $\sim 1200 \text{ m}^2\cdot\text{g}^{-1}$) and its breathing behaviour

(**Figure 1.3.7**), revealing a swelling of *ca.* 40 % in pore size upon solvent exposure.⁷⁵ This interesting characteristic makes MUV-2 a viable selection to overcome the limitations of the infiltration methodology in regards of biomolecule size, broadening the spectrum of possible active molecules to accommodate in its porous structure in comparison with the previously discussed MOFs.

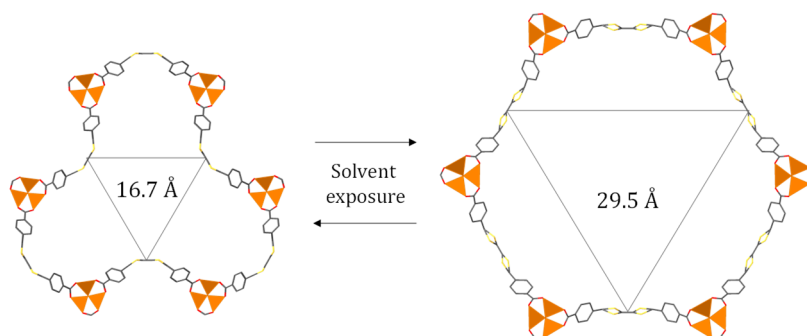


Figure 1.3.7. Breathing behaviour of MUV-2 upon solvent exposure, showcasing the pore size variation between its closed (left) and open form (right).

Furthermore, the performance of MUV-2 incorporating guest molecules has been demonstrated by the encapsulation of fullerenes (C_{60}) without compromising the mesoporosity of the MOF and improving the conductivity performance of the material due to charge transfer donor–acceptor ($TTF \rightarrow C_{60}$) interactions.⁷⁶

1.4. References

- (1) Batten, S. R.; Champness, N. R.; Chen, X.-M.; Garcia-Martinez, J.; Kitagawa, S.; Öhrström, L.; O’Keeffe, M.; Paik Suh, M.; Reedijk, J. Terminology of Metal–Organic Frameworks and Coordination Polymers (IUPAC Recommendations 2013). *Pure Appl. Chem.* **2013**, *85* (8), 1715–1724.
- (2) Hoskins, B. F.; Robson, R. Infinite Polymeric Frameworks Consisting of Three Dimensionally Linked Rod-like Segments. *J. Am. Chem. Soc.* **1989**, *111*, 5962–5964.
- (3) Yaghi, O. M.; Li, H. Hydrothermal Synthesis of a Metal-Organic Framework Containing Large Rectangular Channels. *J. Am. Chem. Soc.* **1995**, *117*, 10401–10402.
- (4) Zhou, H. C. J.; Kitagawa, S. Metal-Organic Frameworks (MOFs). *Chem. Soc. Rev.* **2014**, *43* (16), 5415–5418.
- (5) Moosavi, S. M.; Nandy, A.; Jablonka, K. M.; Ongari, D.; Janet, J. P.; Boyd, P. G.; Lee, Y.; Smit, B.; Kulik, H. J. Understanding the Diversity of the Metal-Organic Framework Ecosystem. *Nat. Commun.* **2020**, *11* (1), 1–10.
- (6) Yaghi, O. M.; O’Keeffe, M.; Ockwig, N. W.; Chae, H. K.; Eddaoudi, M.; Kim, J. Reticular Synthesis and the Design of New Materials. *Nature* **2003**, *423* (6941), 705–714.
- (7) Griffin, S. L.; Champness, N. R. A Periodic Table of Metal-Organic Frameworks. *Coord. Chem. Rev.* **2020**, *414*, 213295.
- (8) Cheetham, A. K.; Férey, G.; Loiseau, T. New Materials Try to Emulate Nature’s Open Frameworks. *Angew. Chemie Int. Ed.* **1999**, *38*, 3269.
- (9) Stock, N.; Biswas, S. Synthesis of Metal-Organic Frameworks (MOFs): Routes to Various MOF Topologies, Morphologies, and Composites. *Chem. Rev.* **2012**, *112* (2), 933–969.
- (10) Ren, J.; Dyosiba, X.; Musyoka, N. M.; Langmi, H. W.; Mathe, M.; Liao, S. Review on the Current Practices and Efforts towards Pilot-Scale Production of Metal-Organic Frameworks (MOFs). *Coord. Chem. Rev.* **2017**, *352*, 187–219.

- (11) Rubio-Martinez, M.; Avci-Camur, C.; Thornton, A. W.; Imaz, I.; Maspoch, D.; Hill, M. R. New Synthetic Routes towards MOF Production at Scale. *Chem. Soc. Rev.* **2017**, *46* (11), 3453–3480.
- (12) Farrusseng, D.; Aguado, S.; Pinel, C. Metal-Organic Frameworks: Opportunities for Catalysis. *Angew. Chemie - Int. Ed.* **2009**, *48* (41), 7502–7513.
- (13) Xu, G.; Nie, P.; Dou, H.; Ding, B.; Li, L.; Zhang, X. Exploring Metal Organic Frameworks for Energy Storage in Batteries and Supercapacitors. *Mater. Today* **2017**, *20* (4), 191–209.
- (14) Lin, R. B.; Xiang, S.; Xing, H.; Zhou, W.; Chen, B. Exploration of Porous Metal–Organic Frameworks for Gas Separation and Purification. *Coord. Chem. Rev.* **2019**, *378*, 87–103.
- (15) Horcajada, P.; Serre, C.; Vallet-Regí, M.; Sebban, M.; Taulelle, F.; Férey, G. Metal-Organic Frameworks as Efficient Materials for Drug Delivery. *Angew. Chemie - Int. Ed.* **2006**, *45* (36), 5974–5978.
- (16) Juan-Alcañiz, J.; Gascon, J.; Kapteijn, F. Metal-Organic Frameworks as Scaffolds for the Encapsulation of Active Species: State of the Art and Future Perspectives. *J. Mater. Chem.* **2012**, *22* (20), 10102–10119.
- (17) Horcajada, P.; Gref, R.; Baati, T.; Allan, P. K.; Maurin, G.; Couvreur, P.; Férey, G.; Morris, R. E.; Serre, C. Metal-Organic Frameworks in Biomedicine. *Chem. Rev.* **2012**, *112* (2), 1232–1268.
- (18) Giménez-Marqués, M.; Hidalgo, T.; Serre, C.; Horcajada, P. Nanostructured Metal-Organic Frameworks and Their Bio-Related Applications. *Coord. Chem. Rev.* **2016**, *307*, 342–360.
- (19) Freiberg, S.; Zhu, X. X. Polymer Microspheres for Controlled Drug Release. *Int. J. Pharm.* **2004**, *282* (1–2), 1–18.
- (20) Chevalier, M. T.; Gonzalez, J.; Alvarez, V. Biodegradable Polymeric Microparticles as Drug Delivery Devices. *IFMBE Proc.* **2015**, *49*, 187–190.
- (21) Servatan, M.; Zarrintaj, P.; Mahmodi, G.; Kim, S. J.; Ganjali, M. R.; Saeb, M. R.; Mozafari, M. Zeolites in Drug Delivery: Progress, Challenges and Opportunities. *Drug Discov. Today* **2020**, *25* (4), 642–656.

- (22) Vallet-Regi, M.; Rámila, A.; Del Real, R. P.; Pérez-Pariente, J. A New Property of MCM-41: Drug Delivery System. *Chem. Mater.* **2001**, *13* (2), 308–311.
- (23) Cunha, D.; Gaudin, C.; Colinet, I.; Horcajada, P.; Maurin, G.; Serre, C. Rationalization of the Entrapping of Bioactive Molecules into a Series of Functionalized Porous Zirconium Terephthalate MOFs. *J. Mater. Chem. B* **2013**, *1* (8), 1101–1108.
- (24) Cunha, D.; Ben Yahia, M.; Hall, S.; Miller, S. R.; Chevreau, H.; Elkaim, E.; Maurin, G.; Horcajada, P.; Serre, C. Rationale of Drug Encapsulation and Release from Biocompatible Porous Metal-Organic Frameworks. *Chem. Mater.* **2013**, *25* (14), 2767–2776.
- (25) Horcajada, P.; Serre, C.; Maurin, G.; Ramsahye, N. A.; Balas, F.; Vallet-Regí, M.; Sebban, M.; Taulelle, F.; Férey, G. Flexible Porous Metal-Organic Frameworks for a Controlled Drug Delivery. *J. Am. Chem. Soc.* **2008**, *130* (21), 6774–6780.
- (26) McKinlay, A. C.; Morris, R. E.; Horcajada, P.; Férey, G.; Gref, R.; Couvreur, P.; Serre, C. BioMOFs: Metal-Organic Frameworks for Biological and Medical Applications. *Angew. Chemie - Int. Ed.* **2010**, *49* (36), 6260–6266.
- (27) Yang, J.; Yang, Y. W. Metal–Organic Frameworks for Biomedical Applications. *Small* **2020**, *16* (10), 1–24.
- (28) Vaughn, J.; Wu, H.; Efremovska, B.; Olson, D. H.; Mattai, J.; Ortiz, C.; Puchalski, A.; Li, J.; Pan, L. Encapsulated Recyclable Porous Materials: An Effective Moisture-Triggered Fragrance Release System. *Chem. Commun.* **2013**, *49* (51), 5724–5726.
- (29) Magri, A.; Petriccione, M.; Gutiérrez, T. J. Metal-Organic Frameworks for Food Applications: A Review. *Food Chem.* **2021**, *354* (January).
- (30) Rojas, S.; Rodríguez-Diéguez, A.; Horcajada, P. Metal-Organic Frameworks in Agriculture. *ACS Appl. Mater. Interfaces* **2022**, *14* (15), 16983–17007.
- (31) Shen, M.; Forghani, F.; Kong, X.; Liu, D.; Ye, X.; Chen, S.; Ding, T. Antibacterial Applications of Metal–Organic Frameworks and Their Composites. *Compr. Rev. Food Sci. Food Saf.* **2020**, *19* (4), 1397–1419.

- (32) Pettinari, C.; Pettinari, R.; Di Nicola, C.; Tombesi, A.; Scuri, S.; Marchetti, F. Antimicrobial MOFs. *Coord. Chem. Rev.* **2021**, *446*, 214121.
- (33) Gao, Q.; Xu, J.; Bu, X. H. Recent Advances about Metal–Organic Frameworks in the Removal of Pollutants from Wastewater. *Coord. Chem. Rev.* **2019**, *378*, 17–31.
- (34) Chopra, S.; Dhumal, S.; Abeli, P.; Beaudry, R.; Almenar, E. Metal-Organic Frameworks Have Utility in Adsorption and Release of Ethylene and 1-Methylcyclopropene in Fresh Produce Packaging. *Postharvest Biol. Technol.* **2017**, *130* (January), 48–55.
- (35) Wyszogrodzka, G.; Marszałek, B.; Gil, B.; Dorożyński, P. Metal-Organic Frameworks: Mechanisms of Antibacterial Action and Potential Applications. *Drug Discov. Today* **2016**, *21* (6), 1009–1018.
- (36) Wu, Y.; Luo, Y.; Zhou, B.; Mei, L.; Wang, Q.; Zhang, B. Porous Metal-Organic Framework (MOF) Carrier for Incorporation of Volatile Antimicrobial Essential Oil. *Food Control* **2019**, *98*, 174–178..
- (37) Yao, C. X.; Zhao, N.; Liu, J. C.; Chen, L. J.; Liu, J. M.; Fang, G. Z.; Wang, S. Recent Progress on Luminescent Metal-Organic Framework-Involved Hybrid Materials for Rapid Determination of Contaminants in Environment and Food. *Polymers (Basel)*. **2020**, *12* (3), 1–29.
- (38) Manousi, N.; Zachariadis, G. A.; Deliyanni, E. A.; Samanidou, V. F. Applications of Metal-Organic Frameworks in Food Sample Preparation. *Molecules* **2018**, *23* (11), 1–21.
- (39) Dou, X.; Sun, K.; Chen, H.; Jiang, Y.; Wu, L.; Mei, J.; Ding, Z.; Xie, J. Nanoscale Metal-Organic Frameworks as Fluorescence Sensors for Food Safety. *Antibiotics* **2021**, *10* (4).
- (40) Rojas, S.; Horcajada, P. Metal-Organic Frameworks for the Removal of Emerging Organic Contaminants in Water. *Chem. Rev.* **2020**, *120* (16), 8378–8415.
- (41) Wang, P.-L.; Xie, L.-H.; Joseph, E. A.; Li, J.-R.; Su, X.-O.; Zhou, H.-C. Metal–Organic Frameworks for Food Safety. *Chem. Rev.* **2019**, *119* (18), 10638–10690.

- (42) Sultana, A.; Kathuria, A.; Gaikwad, K. K. Metal–Organic Frameworks for Active Food Packaging. A Review. *Environ. Chem. Lett.* **2022**, *20* (2), 1479–1495.
- (43) Burt, S. Essential Oils: Their Antibacterial Properties and Potential Applications in Foods - A Review. *Int. J. Food Microbiol.* **2004**, *94* (3), 223–253.
- (44) Mayaud, L.; Carricajo, A.; Zhiri, A.; Aubert, G. Comparison of Bacteriostatic and Bactericidal Activity of 13 Essential Oils against Strains with Varying Sensitivity to Antibiotics. *Lett. Appl. Microbiol.* **2008**, *47* (3), 167–173.
- (45) Kalemba, D.; Kunicka, A. Antibacterial and Antifungal Properties of Essential Oils. *Curr. Med. Chem.* **2005**, *10* (10), 813–829.
- (46) Mukherjee, A.; Basu, S.; Sarkar, N.; Ghosh, A. Advances in Cancer Therapy with Plant Based Natural Products. *Curr. Med. Chem.* **2012**, *8* (12), 1467–1486.
- (47) Aljaafari, M. N.; Alali, A. O.; Baqais, L.; Alqubaisy, M.; Alali, M.; Molouki, A.; Ong-Abdullah, J.; Abushelaibi, A.; Lai, K. S.; Lim, S. H. E. An Overview of the Potential Therapeutic Applications of Essential Oils. *Molecules* **2021**, *26* (3).
- (48) Cristani, M.; D'Arrigo, M.; Mandalari, G.; Castelli, F.; Sarpietro, M. G.; Micieli, D.; Venuti, V.; Bisignano, G.; Saija, A.; Trombetta, D. Interaction of Four Monoterpenes Contained in Essential Oils with Model Membranes: Implications for Their Antibacterial Activity. *J. Agric. Food Chem.* **2007**, *55* (15), 6300–6308.
- (49) Oussalah, M.; Caillet, S.; Saucier, L.; Lacroix, M. Inhibitory Effects of Selected Plant Essential Oils on the Growth of Four Pathogenic Bacteria: E. Coli O157:H7, Salmonella Typhimurium, Staphylococcus Aureus and Listeria Monocytogenes. *Food Control* **2007**, *18* (5), 414–420.
- (50) Prakash, B.; Kujur, A.; Yadav, A.; Kumar, A.; Singh, P. P.; Dubey, N. K. Nanoencapsulation: An Efficient Technology to Boost the Antimicrobial Potential of Plant Essential Oils in Food System. *Food Control* **2018**, *89*, 1–11.

- (51) Asbahani, A. El; Miladi, K.; Badri, W.; Sala, M.; Addi, E. H. A.; Casabianca, H.; Mousadik, A. El; Hartmann, D.; Jilale, A.; Renaud, F. N. R.; et al. Essential Oils: From Extraction to Encapsulation. *Int. J. Pharm.* **2015**, *483* (1–2), 220–243.
- (52) Pateiro, M.; Gómez, B.; Munekata, P. E. S.; Barba, F. J.; Putnik, P.; Kovačević, D. B.; Lorenzo, J. M. Nanoencapsulation of Promising Bioactive Compounds to Improve Their Absorption, Stability, Functionality and the Appearance of the Final Food Products. *Molecules* **2021**, *26*, 1547.
- (53) Raffaella, C.; Casettari, L.; Fagioli, L.; Cespi, M.; Bonacucina, G.; Baffone, W. Activity of Essential Oil-Based Microemulsions against *Staphylococcus Aureus* Biofilms Developed on Stainless Steel Surface in Different Culture Media and Growth Conditions. *Int. J. Food Microbiol.* **2017**, *241*, 132–140.
- (54) Saporito, F.; Sandri, G.; Bonferoni, M. C.; Rossi, S.; Boselli, C.; Cornaglia, A. I.; Mannucci, B.; Grisoli, P.; Vigani, B.; Ferrari, F. Essential Oil-Loaded Lipid Nanoparticles for Wound Healing. *Int. J. Nanomedicine* **2018**, *13*, 175–186.
- (55) Sherry, M.; Charcosset, C.; Fessi, H.; Greige-Gerges, H. Essential Oils Encapsulated in Liposomes: A Review. *J. Liposome Res.* **2013**, *23* (4), 268–275.
- (56) Gibbs, B. F.; Kermasha, S.; Alli, I.; Mulligan, C. N. Encapsulation in the Food Industry: A Review. *Int. J. Food Sci. Nutr.* **1999**, *50* (3), 213–224.
- (57) Ettlinger, R.; Lächelt, U.; Gref, R.; Horcajada, P.; Lammers, T.; Serre, C.; Couvreur, P.; Morris, R. E.; Wuttke, S. Toxicity of Metal-Organic Framework Nanoparticles: From Essential Analyses to Potential Applications. *Chem. Soc. Rev.* **2022**, *51* (2), 464–484.
- (58) Horcajada, P.; Surblé, S.; Serre, C.; Hong, D.-Y.; Seo, Y.-K.; Chang, J.-S.; Grenèche, J.-M.; Margiolaki, I.; Férey, G. Synthesis and Catalytic Properties of MIL-100(Fe), an Iron(III) Carboxylate with Large Pores. *Chem. Commun.* **2007**, *100* (27), 2820–2822.

- (59) García Márquez, A.; Demessence, A.; Platero-Prats, A. E.; Heurtaux, D.; Horcajada, P.; Serre, C.; Chang, J. S.; Férey, G.; De La Peña-O'Shea, V. A.; Boissière, C.; et al. Green Microwave Synthesis of MIL-100(Al, Cr, Fe) Nanoparticles for Thin-Film Elaboration. *Eur. J. Inorg. Chem.* **2012**, *100* (32), 5165–5174.
- (60) Grall, R.; Hidalgo, T.; Delic, J.; Garcia-Marquez, A.; Chevillard, S.; Horcajada, P. *In Vitro* Biocompatibility of Mesoporous Metal (III; Fe, Al, Cr) Trimesate MOF Nanocarriers. *J. Mater. Chem. B* **2015**, *3* (42), 8279–8292.
- (61) Rafael, C.; Lima, C.; Silva, C.; Carolina, R.; Frem, R.; Chorilli, M. Application of MIL-100 (Fe) in Drug Delivery and Biomedicine. *J. Drug Deliv. Sci. Technol.* **2021**, *61* (August 2020), 102217.
- (62) Yoon, J. W.; Seo, Y. K.; Hwang, Y. K.; Chang, J. S.; Leclerc, H.; Wuttke, S.; Bazin, P.; Vimont, A.; Daturi, M.; Bloch, E.; et al. Controlled Reducibility of a Metal-Organic Framework with Coordinatively Unsaturated Sites for Preferential Gas Sorption. *Angew. Chemie - Int. Ed.* **2010**, *49* (34), 5949–5952.
- (63) Willaime, H.; Gref, R.; Horcajada, P.; Couvreur, P.; Rodriguez-Ruiz, V.; Agostoni, V.; Serre, C. 'Green' Fluorine-Free Mesoporous Iron(III) Trimesate Nanoparticles for Drug Delivery. *Green Mater.* **2013**, *1* (4), 209–217.
- (64) Park, K. S.; Ni, Z.; Cote, A. P.; Choi, J. Y.; Huang, R.; Uribe-Romo, F. J.; Chae, H. K.; O'Keeffe, M.; Yaghi, O. M. Exceptional Chemical and Thermal Stability of Zeolitic Imidazolate Frameworks. *Proc. Natl. Acad. Sci.* **2006**, *103* (27), 10186–10191.
- (65) Liédana, N.; Galve, A.; Rubio, C.; Téllez, C.; Coronas, J. CAF@ZIF-8: One-Step Encapsulation of Caffeine in MOF. *ACS Appl. Mater. Interfaces* **2012**, *4*, 5016–5021.
- (66) Soomro, N. A.; Wu, Q.; Amur, S. A.; Liang, H.; Rahman, A. U.; Yuan, Q. Natural Drug Physcion Encapsulated Zeolitic Imidazolate Framework, and Their Application as Antimicrobial Agent. *Colloids Surfaces B Biointerfaces* **2019**, *182* (April), 110364.

- (67) Duan, Y.; Ye, F.; Huang, Y.; Qin, Y.; He, C.; Zhao, S. One-Pot Synthesis of a Metal-Organic Framework-Based Drug Carrier for Intelligent Glucose-Responsive Insulin Delivery. *Chem. Commun.* **2018**, *54* (42), 5377–5380.
- (68) Feng, S.; Zhang, X.; Shi, D.; Wang, Z. Zeolitic Imidazolate Framework-8 (ZIF-8) for Drug Delivery : A Critical Review. *Front. Chem. Sci. Eng.* **2021**, *15* (2), 221–237.
- (69) Fairen-Jimenez, D.; Moggach, S. A.; Wharmby, M. T.; Wright, P. A.; Parsons, S.; Düren, T. Opening the Gate: Framework Flexibility in ZIF-8 Explored by Experiments and Simulations. *J. Am. Chem. Soc.* **2011**, *133* (23), 8900–8902.
- (70) Hobday, C. L.; Woodall, C. H.; Lennox, M. J.; Frost, M.; Kamenev, K.; Düren, T.; Morrison, C. A.; Moggach, S. A. Understanding the Adsorption Process in ZIF-8 Using High Pressure Crystallography and Computational Modelling. *Nat. Commun.* **2018**, *9* (1), 1–9.
- (71) Cavka, J. H.; Jakobsen, S.; Olsbye, U.; Guillou, N.; Lamberti, C.; Bordiga, S.; Lillerud, K. P. A New Zirconium Inorganic Building Brick Forming Metal Organic Frameworks with Exceptional Stability. *J. Am. Chem. Soc.* **2008**, *130* (42), 13850.
- (72) Winarta, J.; Shan, B.; McIntyre, S. M.; Ye, L.; Wang, C.; Liu, J.; Mu, B. A Decade of UiO-66 Research: A Historic Review of Dynamic Structure, Synthesis Mechanisms, and Characterization Techniques of an Archetypal Metal-Organic Framework. *Cryst. Growth Des.* **2020**, *20* (2), 1347–1362.
- (73) Yang, Q.; Guillerm, V.; Ragon, F.; Wiersum, A. D.; Llewellyn, P. L.; Zhong, C.; Devic, T.; Serre, C.; Maurin, G. CH₄ Storage and CO₂ Capture in Highly Porous Zirconium Oxide Based Metal–Organic Frameworks. *Chem. Commun.* **2012**, *48* (79), 9831–9833.
- (74) Souto, M.; Santiago-Portillo, A.; Palomino, M.; Vitórica-Yrezábal, I. J.; Vieira, B. J. C.; Waerenborgh, J. C.; Valencia, S.; Navalón, S.; Rey, F.; García, H.; et al. A Highly Stable and Hierarchical Tetrathiafulvalene-Based Metal-Organic Framework with Improved Performance as a Solid Catalyst. *Chem. Sci.* **2018**, *9* (9), 2413–2418.

- (75) Souto, M.; Romero, J.; Calbo, J.; Vitórica-Yrezábal, I. J.; Zafra, J. L.; Casado, J.; Ortí, E.; Walsh, A.; Mínguez Espallargas, G. Breathing-Dependent Redox Activity in a Tetrathiafulvalene-Based Metal-Organic Framework. *J. Am. Chem. Soc.* **2018**, *140* (33), 10562–10569.
- (76) Souto, M.; Calbo, J.; Mañas-Valero, S.; Walsh, A.; Espallargas, G. M. Charge-Transfer Interactions between Fullerenes and a Mesoporous Tetrathiafulvalene-Based Metal-Organic Framework. *Beilstein J. Nanotechnol.* **2019**, *10*, 1883–1893.

OBJECTIVES

The objectives of this Thesis are summarized in four points:

1. Systematic evaluation of the feasibility of nanoMOFs as essential oil carrier agents following a direct impregnation methodology.
2. Incorporation of a composite biomolecule@MOF material into biopolymeric films and evaluation of the MOF ability to stabilize and govern the release of the bioactive molecule.
3. Obtention of a series of biomolecule@MOF biocomposites and study of their fungicidal effect after integration into biopolymeric films.
4. Synthesis and characterization of Mixed-Metal MUV-2 analogues (MM-MUV-2), as well as suitability determination of the materials as macrobiomolecule carriers.

CHAPTER 2

Essential oil encapsulation into metal-organic
framework nanoparticles

2.1. Introduction

As discussed in Chapter 1, natural occurring active components are very appreciated in the food industry for their potential use as preservatives and in innovative packaging. However, an optimal implementation of these chemically unstable molecules requires their previous protection. In this context, encapsulation has been largely proposed for active biomolecule processing. The selection of an appropriate carrier with i) high loading capacity, ii) chemical and thermal stability, and most importantly iii) the ability to provide a controlled release of active components is fundamental for an improved natural BAC encapsulation.

Among the plausible carriers available, MOF materials are presented as candidates to achieve this improvement. Essentially, the chemical control that the MOF chemistry provides is a potential way to design carrier materials for programmed release of multiple natural occurring active ingredients occurring upon certain physical (light, temperature, humidity) or chemical stimuli (pH, chelating agents).¹ As a particular example in the field of food safety, Lashkari and co-workers determined that water vapor at high concentration can act as an effective trigger to release allyl isothiocyanate molecules from RPM6-Zn, HKUST-1 and MOF-74(Zn).^{2,3}

Furthermore, the study of the interaction between the MOF functional groups and guest molecules is fundamental for the design of smart carriers.⁴ Balestri and co-workers recently studied the processes occurring inside the MOF when different guests compete for settling in the pores by following the exchange of dimethylformamide (DMF) with eugenol in a PUM168 single crystal.⁵

However, the use of toxic solvents like DMF and in some cases the lack of biocompatibility studies of the MOF hinders the immediate applications of these materials in the food industry, demanding a more profound analysis.

A thorough study of the host-guest interactions between biocompatible and processable MOFs and encapsulated active molecules is necessary in order to develop smart composite materials in which the carrier agent i) preserves the physicochemical characteristics of the active molecules, ii) promotes an increase in their action duration, and iii) provides a controlled release, that can be of interest in active antimicrobial systems.

In particular three active molecules derived from essential oils will be explored: carvacrol, benzaldehyde and citral (see **Table 2.1.1.**). These molecules were selected taking into account their optimal performance in food industry. All of them are Generally Recognized As Safe (GRAS) by the US Food and Drug Administration (FDA).

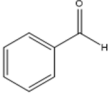
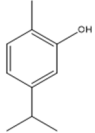
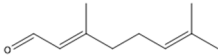
Carvacrol or 2-methyl-5-(1-methylethyl)-phenol, is an aromatic monoterpene present in the essential oil extracted mostly from oregano. It is regularly used in products as a flavouring and/or as an antimicrobial agent, showing a broad-spectrum of effectiveness against bacteria, yeasts and fungi.^{6,7}

Benzaldehyde is the main constituent of bitter almond oil. This molecule is commonly employed as an almond flavouring agent to foods and scented products. This active molecule presents insecticidal, antimicrobial, and antioxidant activity.⁸

Citral (3,7-dimethyl-2,6-octadienal), is an acyclic monoterpene aldehyde present in the oils of several plants, including lemon myrtle, lemongrass, or lemon tea-tree. The term citral covers two geometric isomers: the *E*-isomer geranial (*trans*-citral, citral A), and the *Z*-isomer neral (*cis*-citral, citral B). Citral has a strong citrus scent and is used as an aroma compound in

perfumery and as a food additive. Citral is known to present appreciable antimicrobial activity against Gram-positive and Gram-negative bacteria, as well as fungi.^{9,10}

Table 2.1.1. Physical properties of the bioactive molecules employed in this chapter.

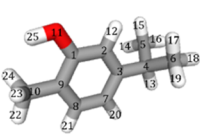
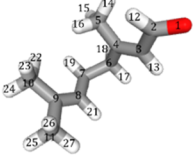
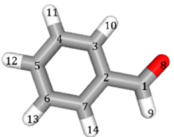
Molecule	Benzaldehyde	Carvacrol	Citral
Structure			
Molecular weight / g·mol ⁻¹	106.124	150.221	152.237
Density / g·cm ⁻³	1.044	0.976	0.894
Boiling point / °C	178	237	229
λ _{max} / nm	260	273	288

We propose four nanoMOF candidates for the encapsulation of active molecules derived from essential oils: MIL-100(Fe), ZIF-8, UiO-66 and UiO-66-NH₂, all of them previously described as agent carriers in Chapter 1 of this manuscript. **Tables 2.1.2** and **2.1.3** summarize the dimensions of the molecules and the pore size of the plausible carrier agents.

Table 2.1.2. Summary of the different pore size and accessible apertures of the nanoMOF candidates for active molecule encapsulation.

nanoMOF	Pore size	Accessible windows	Characteristics
MIL-100 (Fe)	25 and 29 Å	5.5 and 8.6 Å	Hydrophilic, C.U.S.
ZIF-8	11.6 Å	3.4 Å	Hydrophobic
UiO-66	7.5 and 12 Å	6 Å	Hydrophobic
UiO-66-NH ₂	6 Å	6 Å	Hydrophilic, Ligand functionalization

Table 2.1.3 Largest distances in the chemical structure (as calculated by ChemDraw V.19.0 software) of the three active molecules employed in this chapter. First row of the table showcases the numbered atoms for reference.

	Carvacrol	Citral	Benzaldehyde
			
Molecule	Carvacrol	Citral	Benzaldehyde
Largest distances	H23··H14 7.9 Å H25··H18 7.5 Å	H25··H14 9.0 Å O1··H27 6.9 Å	O8··H12 5.94 Å O8··H11 5.61 Å

The main goal of this Chapter 2 is to systematically evaluate the feasibility of MOFs as EO carrier agents. With this aim, the four archetypal MOFs are combined with carvacrol, citral and benzaldehyde solutions to obtain a composite material. Through systematic characterization, the chemical interaction between the MOF and the guest biomolecules will be analysed, as well as the different biomolecule loading of the frameworks and how the encapsulation process affects the net porosity of the materials.

2.2. Results and discussion

Synthesis of archetypal nanoMOFs. MOF nanoparticles were synthesized following previously reported methods.

MIL-100(Fe) nanoparticles were synthesized by MW-assisted hydrothermal reaction of a mixture of Fe^{III} chloride and trimesic acid solutions.¹¹ The use of high MW power and short reaction times favours the nucleation process, yielding smaller size particles. This synthetic methodology also produces a high yield in minutes-long reaction times.

ZIF-8 nanoparticles were synthesized by solvothermal reaction of Zn^{II} nitrate and 2-methylimidazole methanolic solutions for 1h.¹²

UiO-66 and **UiO-66-NH₂** nanoparticles were obtained by solvothermal synthesis of zirconyl chloride and terephthalic or 2-aminoterephthalic acid, respectively, in N,N-dimethylformamide.¹³ To ensure the complete removal of DMF, and obtain a suitable material for food-related applications, the materials were washed by stirring in hot EtOH. This solvent exchange was applied every 24h for two weeks before drying the nanostructured MOFs at air and store them.

2.2.1. Encapsulation methodology

In a typical procedure, nanostructured MOFs were incubated for a period of time in a specific solution of EOs (carvacrol, benzaldehyde and citral). Ethanol was first selected as the solvent due to the optimal biomolecule solubility in this medium. Different biomolecule/MOF molar ratios, mainly 1/1, 3/1 and 5/1, were explored. Evaluation of the encapsulation efficiency during the infiltration process was first attempted by analysing the molecule concentration in the ethanolic medium by means of UV-Vis spectroscopy.

However, due to the volatile nature of the biomolecules and their exceptional solubility in ethanol this characterization was not reproducible.

Attempts with different solvents were then explored, obtaining best results in H₂O:EtOH (4:1) mixture of solvents. It is important to remark that by using this mixture a white emulsion is obtained due to the poor aqueous solubility of the active molecules, which also hinders the collection of aliquots of supernatant for UV-Vis monitoring. Consequently, encapsulation efficiency was addressed by characterization of the solid recovered after centrifugation. The established encapsulation parameters were the use of EtOH:H₂O as encapsulation medium, with a 5/1 molecule/MOF molar ratio and during 5 days of infiltration. The use of a high molecule concentration in the encapsulation medium and a long incubation time was employed as a strategy to ensure an intense contact between the active molecules and the carrier frameworks.

All four archetypal MOFs (MIL-100(Fe), ZIF-8, UiO-66 and UiO-66-NH₂) were combined with carvacrol, citral and benzaldehyde solutions using the above-mentioned encapsulation parameters, obtaining in total twelve composite materials that will be analysed.

2.2.2. Physicochemical characterization of carvacrol@MOF composites

The following sections comprise the physicochemical characterization of the biomolecule@MOF composites obtained. This systematic study has served to determine the feasibility of the porous materials as carrier agents for each BAC.

2.2.2.1. Infrared Spectroscopy

All composite materials were firstly characterized by means of infrared spectroscopy to discern the presence of biomolecule bands in the composite spectrum. **Tables 2.2.2.1** and **2.2.2.2** summarize the most characteristic bands of the pristine MOFs and the encapsulated molecules.

Table 2.2.2.1. Position and assignation of the principal bands of the three active molecules employed in this study.

Active molecule	Band position / cm^{-1}	Assignment
Carvacrol	3361	VO-H
	2958 and 2869	sym and antisym $\nu_{\text{C-H}}$
	1301	isopropylic $\delta_{\text{C-H}}$
	1178-811	ar $\gamma_{\text{C-C}}$ and oop $\delta_{\text{C-H}}$
Citral	2962, 2919 and 2855	$\nu_{\text{C-H}}$
	1400-1100	oop $\delta(\text{C}=\text{C}-\text{H})$, $\delta(\text{C}-(\text{CH}_3)_2)$ and $\delta(\text{CH}_2)$.
	1672	aldehyde $\nu_{\text{C=O}}$
Benzaldehyde	3064	aromatic $\nu_{\text{C-H}}$
	2816 and 2734	aldehyde-related $\nu_{\text{C-H}}$
	1696	aldehyde $\nu_{\text{C=O}}$
	1595 and 1583	aromatic $\nu_{\text{C=C}}$
	1454	aldehyde $\delta_{\text{C-H}}$

Table 2.2.2.2. Position and assignment of the principal bands of the four archetypal MOFs employed in this study.

MOF	Band position / cm ⁻¹	Assignment
MIL-100 (Fe)	1620 and 1570	$\nu_{\text{as}}(\text{COO}^-)$
	1445 and 1370	$\nu_{\text{s}}(\text{COO}^-)$
	3500-3000	H-bonding of H ₂ O adsorbates
	618	$\nu_{\text{as}}(\text{Fe}_3\text{O})$
ZIF-8	3135 and 2929	aromatic and aliphatic $\nu_{\text{as}}(\text{C-H})$
	1583	$\nu_{\text{C=N}}$
	1460–1309	skeletal vibration of the imidazolate ring
	1180 and 1146	aromatic $\nu_{\text{C-N}}$
	995 and 760	$\delta_{\text{C-N}}$ and $\delta_{\text{C-H}}$
	420	$\nu_{\text{Zn-N}}$
UiO-66	1569 and 1390	symmetric and asymmetric $\nu_{\text{C=O}}$
	1503	$\nu_{\text{C=C}}$ in the benzene ring
	879 and 811	aromatic $\gamma_{\text{C-C}}$ and oop $\delta_{\text{C-H}}$
	745	$\nu_{\text{Zr-O}}$ (Zr-O)
	650	$\nu_{\text{Zr-O}}$ (Zr- μ_3 -O)
	471	$\nu_{\text{Zr-O}}$ (O-Zr-O)
UiO-66-NH ₂	3471 and 3345	symmetric and asymmetric ν_{NH}
	1375 and 1247	ν_{CN} (aromatic amines)
	1556 and 1431	symmetric and asymmetric $\nu_{\text{C=O}}$
	1495	$\delta(\text{NH}_2)$
	760	$\nu_{\text{Zr-O}}$ (Zr-O)
	650	$\nu_{\text{Zr-O}}$ (Zr- μ_3 -O)
	474	$\nu_{\text{Zr-O}}$ (O-Zr-O)

MIL-100(Fe) composites. Analysis of the FTIR spectra of the impregnated biomolecule@MIL-100(Fe) materials (**Figures 2.2.2.1 to 2.2.2.3**) revealed the appearance of the most remarkable bands of each encapsulated active molecule while retaining the typical bands corresponding to the Fe^{III} trimesate MOF. Interestingly, it can be noticed that the $\nu_{\text{as}}(\text{Fe}_3\text{O})$ vibration at 618 cm^{-1} , characteristic of the Fe^{III} oxo-trimeric core in MIL-100(Fe),¹⁴ appears shifted in the composite materials. This suggests an effective interaction between the active molecules and the accessible Fe^{III} sites, as previously described for the binding of different molecules.^{15,16}

In the case of carvacrol@MIL-100(Fe) (**Figure 2.2.2.1**), this band shifts to 628 cm^{-1} . For Citral@MIL-100(Fe) spectrum (**Figure 2.2.2.2**), the $\nu_{\text{as}}(\text{Fe}_3\text{O})$ vibration at 618 cm^{-1} , appears shifted to 622 cm^{-1} . Interestingly, the citral aldehyde-related band appears in low intensity, as a shoulder to the most intense $\nu_{\text{C}=\text{O}}$ associated to the coordinated BTC carboxylate in MIL-100(Fe). Benzaldehyde@MIL-100(Fe) IR spectrum (**Figure 2.2.2.3**) presents with more intensity the aldehyde-related $\nu_{\text{C}=\text{O}}$ band in comparison with citral@MIL-100(Fe), whereas the $\nu_{\text{as}}(\text{Fe}_3\text{O})$ vibration appears shifted to 623 cm^{-1} in this composite spectrum.

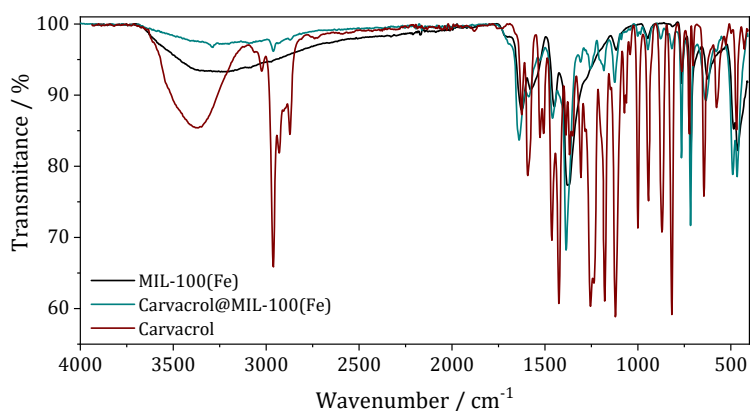


Figure 2.2.2.1. FT-IR spectra of carvacrol@MIL-100(Fe) composite (teal) as compared with pristine MIL-100(Fe) (black) and carvacrol (red).

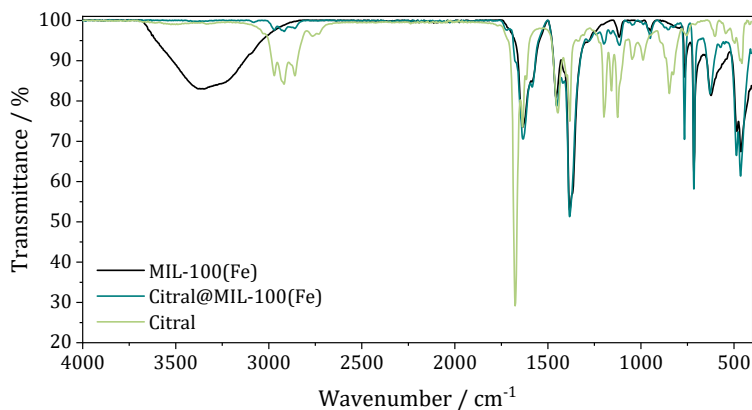


Figure 2.2.2.2. FT-IR spectra of citral@MIL-100(Fe) composite (teal) as compared with pristine MIL-100(Fe) (black) and citral (green).

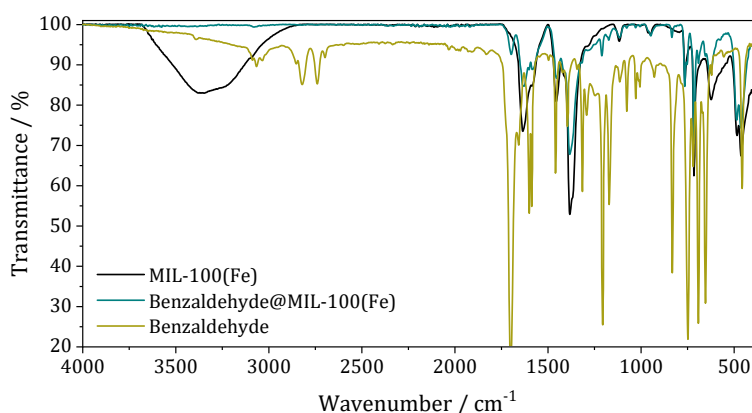


Figure 2.2.2.3. FT-IR spectra of benzaldehyde@MIL-100(Fe) composite (teal) as compared with pristine MIL-100(Fe) (black) and benzaldehyde (yellow).

ZIF-8 composites. FT-IR spectra of all the biomolecule@ZIF-8 composites (**Figures 2.2.2.4 to 2.2.2.6**) present characteristic bands of each molecule as well as maintain the typical bands of ZIF-8. In general, in the IR spectra of ZIF-8 composites spectra all the biomolecule related bands are present with much more intensity that in the case of MIL-100(Fe) composites. The absence of CUS in the ZIF-8 framework, and thus lack of chemical interaction between the MOF host and the guest molecules, prevents the shifting of any vibration band in the composites spectra.

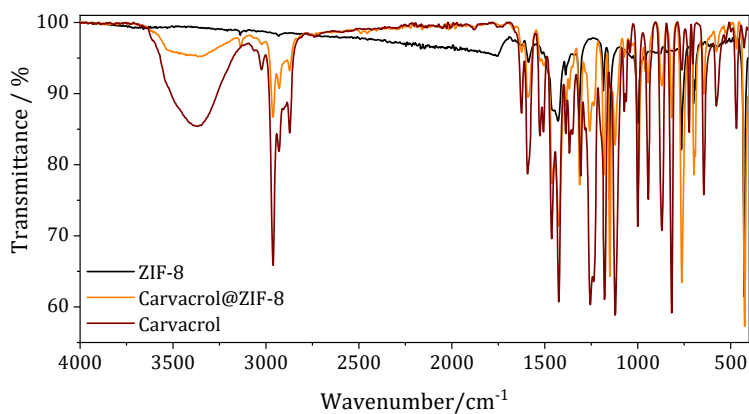


Figure 2.2.2.4. FT-IR spectra of carvacrol@ZIF-8 composite (orange) as compared with pristine ZIF-8 (black) and carvacrol (red).

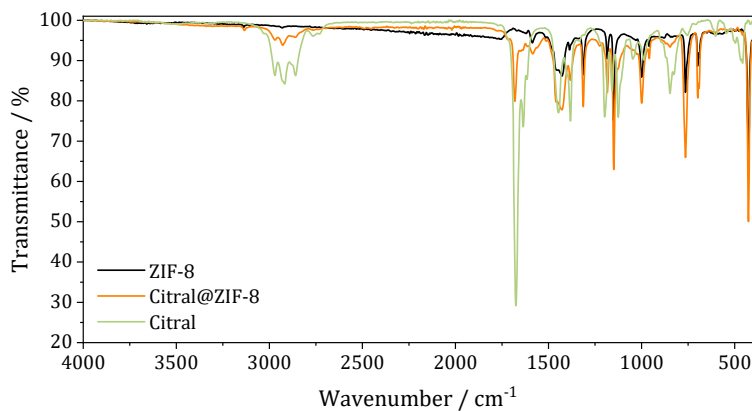


Figure 2.2.2.5. FT-IR spectra of citral@ZIF-8 composite (orange) as compared with pristine ZIF-8 (black) and citral (green).

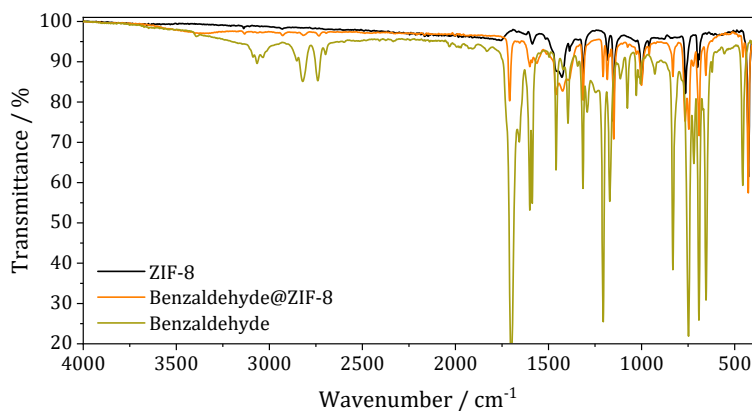


Figure 2.2.2.6. FT-IR spectra of benzaldehyde@ZIF-8 composite (orange) as compared with pristine ZIF-8 (black) and benzaldehyde (yellow).

UiO-66 composites. In UiO-66 IR spectrum, the three lowest frequencies at 745, 650, and 471 cm^{-1} are assigned to $\nu_{\text{Zr-O}}$ vibrations: (Zr-O), (Zr- μ_3 -O) and (O-Zr-O), respectively. Carvacrol@UiO-66 spectrum (**Figure 2.2.2.7**) presents very intense carvacrol-related bands $\nu_{\text{O-H}}$ and $\nu_{\text{C-H}}$. In a similar behaviour to carvacrol@MIL-100(Fe), $\nu_{\text{Zr-O}}$ vibrations corresponding to (Zr- μ_3 -O) and (O-Zr-O) in carvacrol@UiO-66 shift after the encapsulation, moving from 650 and 471 cm^{-1} to 642 and 465 respectively. In the case of citral@UiO-66, only a shoulder at 1652 cm^{-1} that can be linked with the aldehyde functional group can be observed (**Figure 2.2.2.8**) while $\nu_{\text{Zr-O}}$ bands are not shifted in this composite spectrum. Benzaldehyde@UiO-66 spectrum (**Figure 2.2.2.9**) presents few benzaldehyde related bands. The aldehyde $\nu_{\text{C=O}}$ band appears shifted to lower wavenumber values, being located at 1687 cm^{-1} . Moreover, the three Zr-O associated bands appear shifted in this composite spectrum to 741, 647 and 741 cm^{-1} , respectively. This shifting to lower frequencies suggests the possible interaction of carvacrol and benzaldehyde to the Zr^{IV} centres of the UiO-66 clusters.

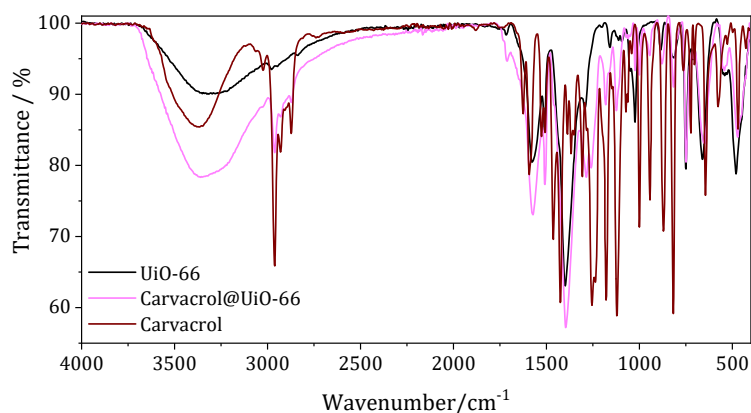


Figure 2.2.2.7. FT-IR spectra of carvacrol@UiO-66 composite (pink) as compared with pristine UiO-66 (black) and carvacrol (red).

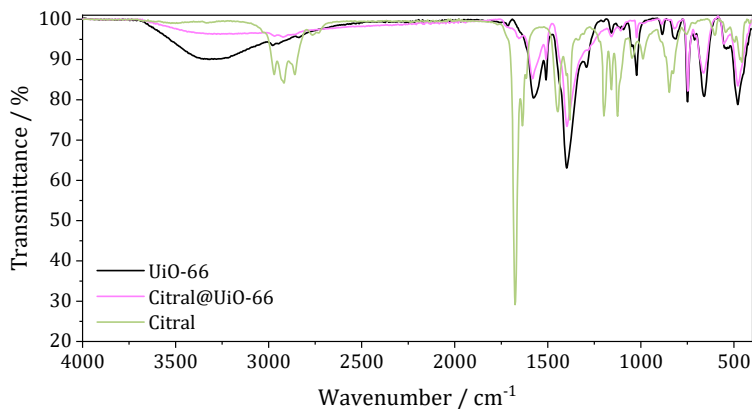


Figure 2.2.2.8. FT-IR spectra of citral@UiO-66 composite (pink) as compared with pristine UiO-66 (black) and citral (green).

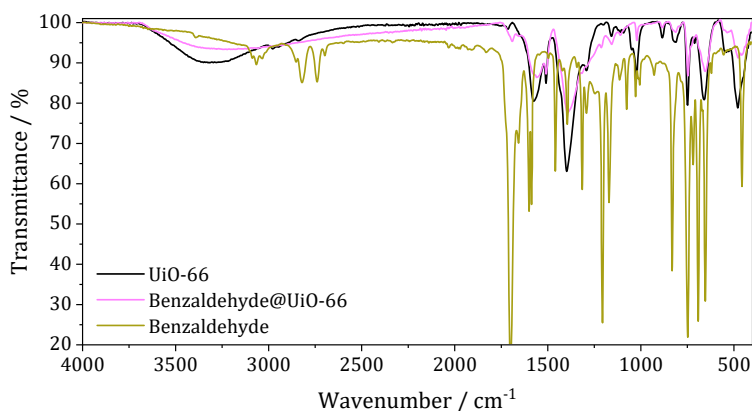


Figure 2.2.2.9. FT-IR spectra of benzaldehyde@UiO-66 composite (pink) as compared with pristine UiO-66 (black) and benzaldehyde (yellow).

UiO-66-NH₂ composites. All composite materials retain the characteristic UiO-66-NH₂ bands. In addition, carvacrol@UiO-66-NH₂ composite (**Figure 2.2.2.10**) present all the characteristic carvacrol bands. Neither citral@UiO-66-NH₂ nor benzaldehyde@UiO-66-NH₂ spectra (**Figures 2.2.2.11** and **2.2.2.12**) present any biomolecule related bands and the Zr-O related bands are not shifted in any of the obtained composites, pointing in the direction of a poorly effective encapsulation.

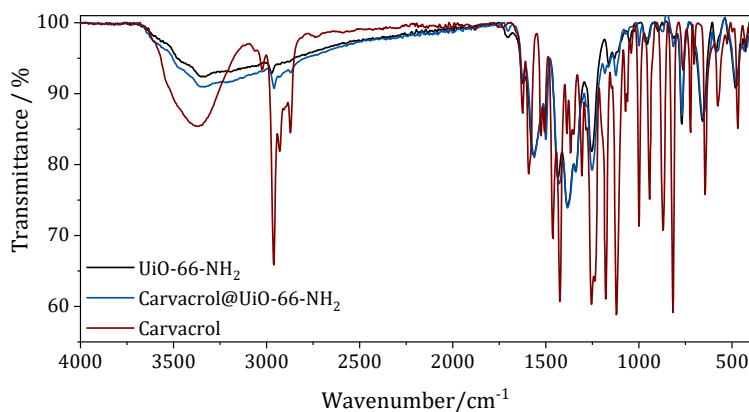


Figure 2.2.2.10. FT-IR spectra of carvacrol@UiO-66-NH₂ composite (blue) as compared with pristine UiO-66-NH₂ (black) and carvacrol (red).

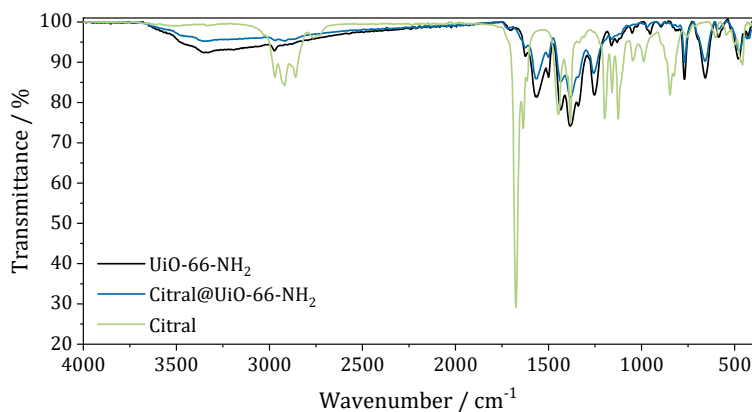


Figure 2.2.2.11. FT-IR spectra of citral@UiO-66-NH₂ composite (blue) as compared with pristine UiO-66-NH₂ (black) and citral (green).

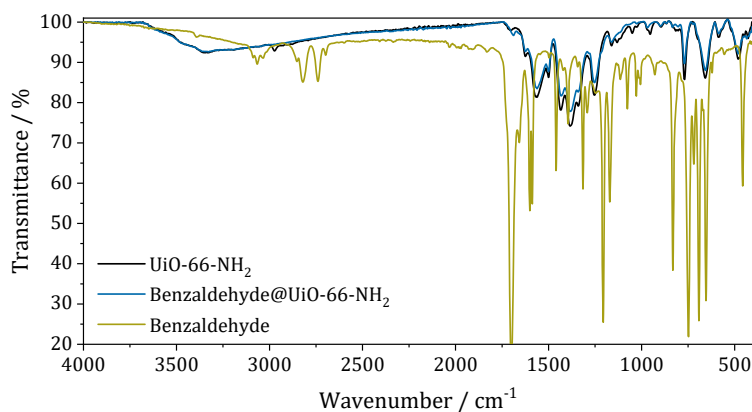


Figure 2.2.2.12. FT-IR spectra of benzaldehyde@UiO-66-NH₂ composite (blue) as compared with pristine UiO-66-NH₂ (black) and benzaldehyde (yellow).

2.2.2.2. Powder X-ray diffraction

Powder X-ray diffraction (PXRD) measurements of all the biomolecule@MOF composites were performed to evaluate the crystal integrity after molecule infiltration. With this aim, PXRD analysis were performed before and after the encapsulation processes. In the case of the MIL-100(Fe) framework (**Figure 2.2.2.13a**) the crystal structure is maintained after biomolecule loading, as all the MIL-100(Fe) diffraction peaks are present in the three obtained composites. The same conclusion can be drawn in the case of ZIF-8 composites (**Figure 2.2.2.13b**). The diffraction pattern of all composites retains ZIF-8 diffraction peaks, but a sharp decrease in the (011) associated peak located at $2\theta = 7.3^\circ$ can be observed, directly related with the increase of electronic density due to infiltration of the active molecules into the ZIF-8 pores. Furthermore, for carvacrol@ZIF-8 and citral@ZIF-8, a new diffraction peak at $2\theta = 11.0^\circ$ can be observed. As can be seen at the bottom of the diffraction pattern, the reflection list of ZIF-8 does not depict any systematic absence to which this diffraction peak could be attributed, thus pointing in the direction of possible defects in the framework as a consequence of the infiltration process, perhaps due to a ligand exchange between the imidazolate ligands and the encapsulated molecules. UiO-66 and UiO-66-NH₂ composites (**Figures 2.2.2.13c** and **2.2.2.13d**, respectively) reveal a powder pattern with low crystallinity, which is directly related with the low dimensions of the of the pristine MOF NPs.

The integrity of the frameworks is not compromised after infiltration in any case except for benzaldehyde@UiO-66, where the intensity of all the diffraction peaks seems to be reduced in the PXRD pattern. However, the general low crystallinity of the particles deters further elucidation.

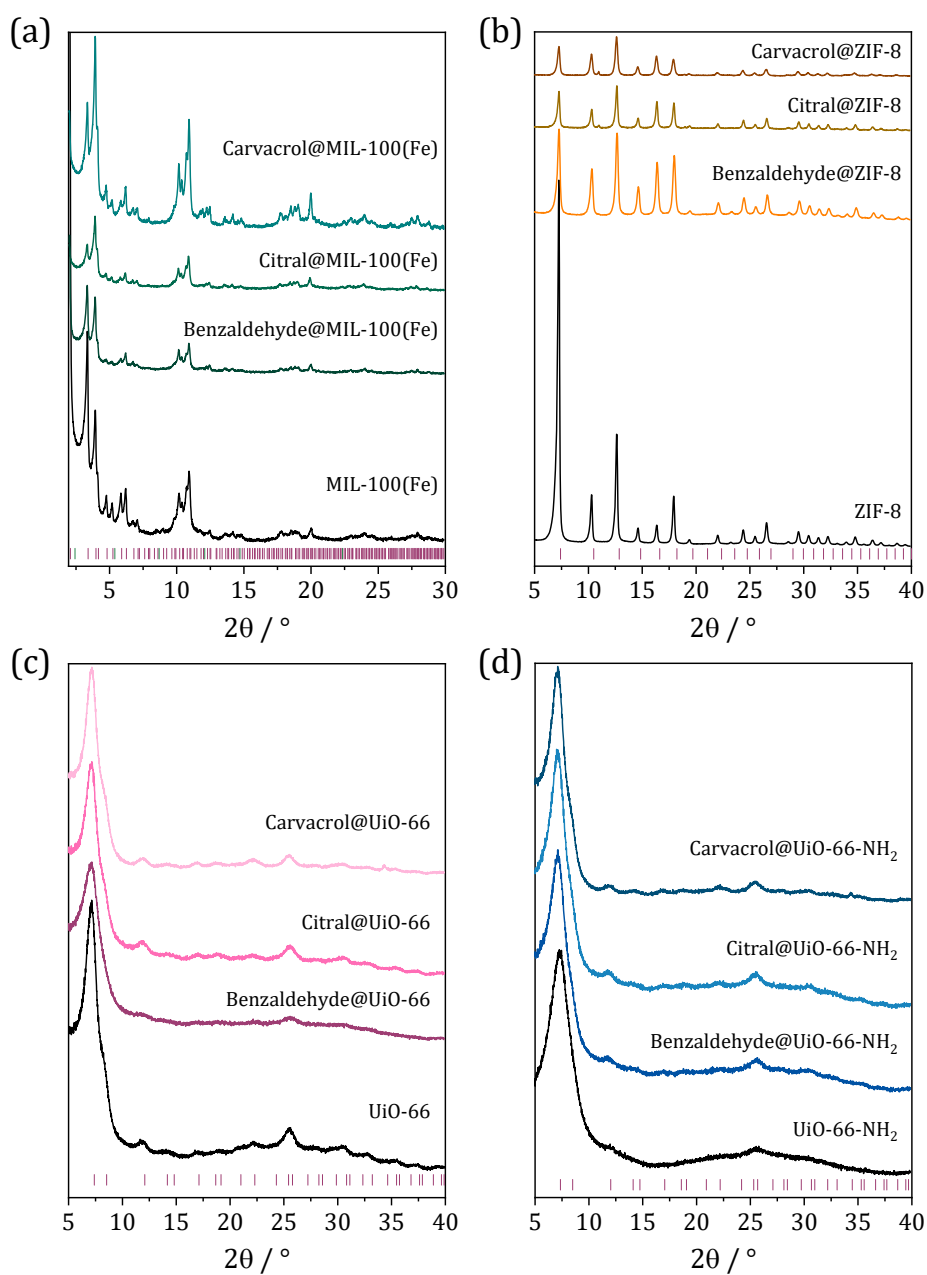


Figure 2.2.2.13. XRPD pattern of the twelve obtained biomolecule@MOF composites in comparison with the corresponding pristine MOFs. The (h, k, l) reflection list of each pristine MOF unit cell, obtained from crystallographic data, is depicted at the bottom of each diffractogram.

2.2.2.3. Thermogravimetric Analysis

Once the crystallinity of the composites was addressed, thermogravimetric analysis were carried out to investigate their thermal stability and estimate the biomolecule content. **Table 2.2.2.3** summarizes the inorganic residue content of all the composite materials, as compared to their control empty MOFs and related theoretical values (theo). In addition, the estimated loaded molecule is provided. 120 °C is established as dry base (D.B.) temperature.

Table 2.2.2.3. Thermogravimetric analysis summary.

	Solvent % (w/w)	Ligand decom. T / °C	Inorganic residue (D.B.) % (w/w)	Encapsulated molecule % (w/w)
MIL-100(Fe) theo	-	-	35.8	-
MIL-100(Fe) exp	30.6	350	35.7	-
Carvacrol@MIL-100(Fe)	8.0	300	22.3	37.7
Citral@MIL-100(Fe)	11.7	295	21.7	39.4
Benzaldehyde@MIL- 100(Fe)	21.14	310	31.4	12.3
ZIF-8 theo	-	-	36.0	-
ZIF-8 exp	-	400	36.1	-
Carvacrol@ZIF-8	5.5	350	27.5	23.6
Citral@ZIF-8	-	350	29.1	19.2
Benzaldehyde@ZIF-8	-	400	27.4	23.9

	Solvent % (w/w)	Ligand decom. T / °C	Inorganic residue (D.B.) % (w/w)	Encapsulated molecule % (w/w)
UiO-66 theo	-	-	44.0	-
UiO-66 exp	14.3	475	50.8	-
Carvacrol@UiO-66	13.8	336	37.1	27.0
Citral@UiO-66	12.2	325	40.2	20.8
Benzaldehyde@UiO-66	10.0	490	46.6	9.6
UiO-66-NH ₂ theo	-	-	42.0	-
UiO-66-NH ₂ exp	14.4	336	47.7	-
Carvacrol@UiO-66-NH ₂	6.6	320	37.0	22.4
Citral@UiO-66-NH ₂	11.4	330	35.3	26.0
Benzaldehyde@UiO-66- NH ₂	13.1	320	45.2	5.3

MIL-100(Fe) composites. MIL-100(Fe) thermal profile follows the expected behaviour with a 35.7 % (D.B.) inorganic residue at 700 °C after ligand decomposition, in good agreement with the expected 35.8 % considering MIL-100(Fe) molecular formula. On the other hand, carvacrol@MIL-100(Fe) thermal profile (**Figure 2.2.2.14a**) presents two separated mass losses in the 120-180 °C interval and at 230 °C, which translates into a carvacrol content of 37.7 %. This separation in carvacrol decomposition points out the release of carvacrol molecules differently interacting with the framework (*i.e.* physisorption vs chemisorption). Thermal profile of citral@MIL-100 (**Figure 2.2.2.14b**) presents a 39.4 % (D.B.) mass loss attributed to citral with a more gradual decomposition in

comparison with the carvacrol combustion. Thermal profile of benzaldehyde@MIL-100(Fe) (**Figure 2.2.2.14c**) presents a 12.3 % (D.B.) mass loss that can be associated with benzaldehyde encapsulated molecules. As a general trend, the stability of the composite materials after volatiles release is in all three cases lower than in pristine MIL-100(Fe) likely due to the abrupt removal of the encapsulated molecules.

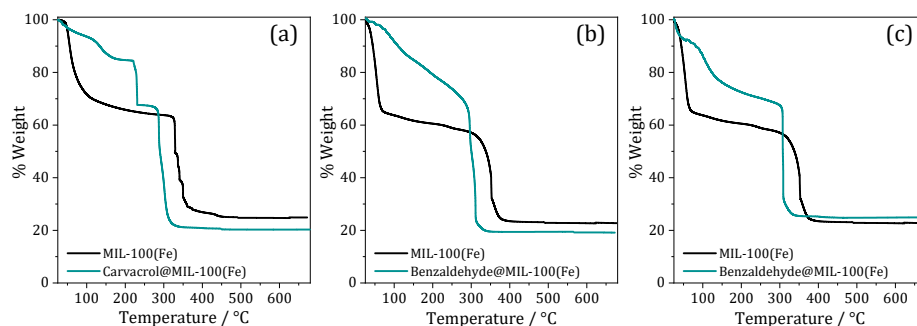


Figure 2.2.2.14. Thermal decomposition profiles of the three obtained biomolecule@MIL-100(Fe) composites (teal) in comparison with pristine MIL-100(Fe) (black): (a) carvacrol@MIL-100(Fe), (b) citral@MIL-100(Fe), and (c) benzaldehyde@MIL-100 (Fe).

ZIF-8 composites. The thermal profile of pristine ZIF-8 follows the expected trend with a 36.1 % of inorganic content (D.B.) at 700 °C, in good agreement with the expected 36.0 % value considering ZIF-8 molecular formula. Carvacrol@ZIF-8 thermal profile (**Figure 2.2.2.15a**) presents a 23.6 % mass loss (D.B.) attributed to carvacrol loading. Ligand decomposition occurs at 350 °C, presenting a similar thermal stability decrease to what was observed in MIL-100(Fe) composites due to the biomolecule removal and collapsing of the structure. In the case of citral@ZIF-8 and benzaldehyde@ZIF-8, thermal profile (**Figures 2.2.2.15b** and **2.2.2.15c**), the thermal decomposition of these composites follows

similar thermal profile as the pristine MOF, with an estimated biomolecule loading of a 19.2 % and 23.9 %, respectively.

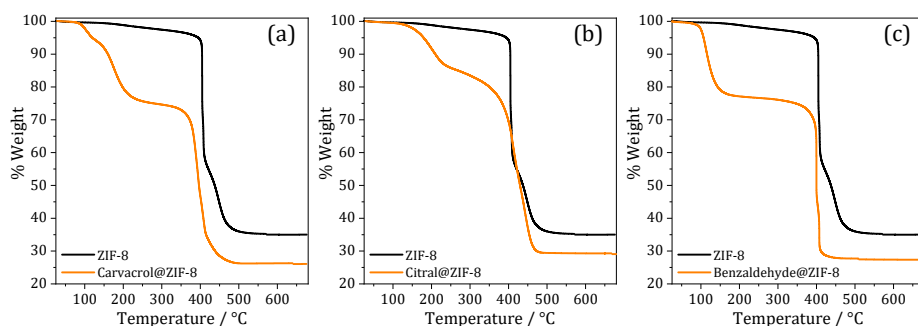


Figure 2.2.2.15. Thermal decomposition profiles of the three obtained biomolecule@ZIF-8 composites (orange) in comparison with pristine ZIF-8 (black): (a) carvacrol@ZIF-8, (b) citral@ZIF-8, and (c) benzaldehyde@ZIF-8.

UiO-66 composites. UiO-66 thermal profile presents a continuous mass drop up until ligand decomposition at 475 °C. The inorganic content after ligand decomposition in the pristine NPs is 50.8 %, higher than expected when considering UiO-66 molecular formula (theoretical inorganic residue is 44 %). This increased inorganic content could be explained by BDC defects in the structure due to the low dimensionality of the nanoparticles, or possible zirconium oxide presence. Ligand decomposition of carvacrol@UiO-66 composite (**Figure 2.2.2.16a**) occurs at a much lower temperature and a more gradual and soft decomposition than the pristine UiO-66 profile. There is a 27.0 % (D.B.) mass loss attributed to encapsulated carvacrol molecules. The lower thermal stability of the composite material could be prompted by the removal of carvacrol molecules coordinated to Zr centres (as suggested by the IR shift in the Zr-O bands previously discussed), causing a premature disruption of the framework. Citral loading corresponds to a 20.8 % (D.B.) in the case of thermal profile of citral@UiO-66 (**Figure 2.2.2.16b**), where the ligand decomposition takes place between 325 and

570 °C with a gradual two-step mass drop. Benzaldehyde@UiO-66 (**Figure 2.2.2.16c**) exhibits a similar thermal profile to the pristine MOF. A decrease in mass of only 9.6 % (D.B.) can be related to encapsulated benzaldehyde, lower than expected considering the interactions with the Zr^{IV} clusters predicted during IR spectroscopy analysis.

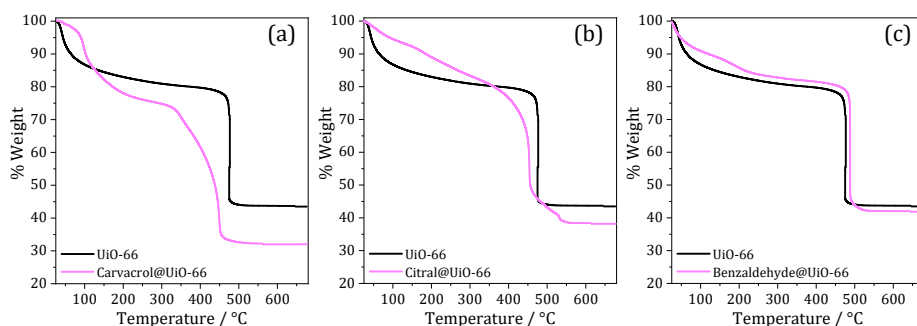


Figure 2.2.2.16. Thermal decomposition profiles of the three obtained biomolecule@UiO-66 composites (pink) in comparison with pristine UiO-66 (black): (a) carvacrol@UiO-66, (b) citral@UiO-66, and (c) benzaldehyde@UiO-66.

UiO-66-NH₂ composites. The obtained inorganic content in UiO-66-NH₂ thermal profile corresponds to a 47.7 %, a higher value than expected considering UiO-66-NH₂ molecular formula (theoretical inorganic residue of 42 %). Analogous to UiO-66, BDC-NH₂ defects in the structure or oxide presence could explain this higher inorganic content in the material. Carvacrol@UiO-NH₂ and benzaldehyde@UiO-66-NH₂ thermal profiles (**Figures 2.2.2.17a** and **2.2.2.17c**) present a similar trend as the pristine nanoMOF, with a 22.4 % (D.B.) and 5.3 % (D.B.) estimated biomolecule content, respectively. The almost identical thermal profile of this latter composite to the pristine MOF, combined with the absence of benzaldehyde-related vibration bands observed in the FT-IR spectrum previously discussed, further points in the direction of an unsuccessful

encapsulation. Thermal profile of citral@UiO-66-NH₂ (**Figure 2.2.2.17b**) presents a citral-related mass loss of 14.3 % (D.B.). Ligand decomposition occurs in a very soft and gradual step, seeming to increase the thermal stability of the composite in comparison with the pristine UiO-66-NH₂ NPs.

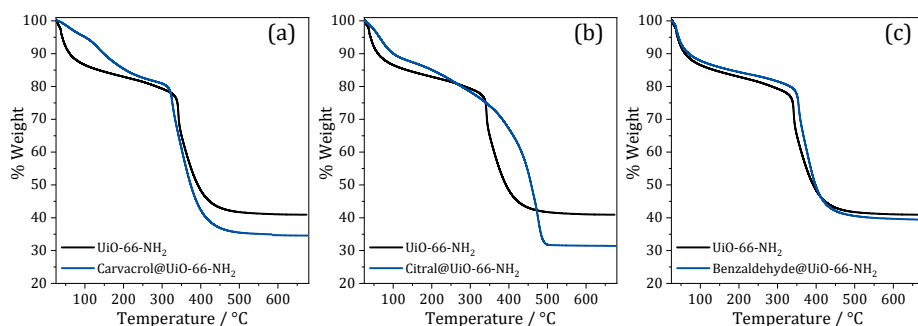


Figure 2.2.2.17. Thermal decomposition profiles of the three obtained biomolecule@UiO-66-NH₂ composites (blue) in comparison with pristine UiO-66-NH₂ (black): (a) carvacrol@UiO-66-NH₂, (b) citral@UiO-66-NH₂, and (c) benzaldehyde@UiO-66-NH₂.

2.2.2.4. N₂ sorption isotherms at 77 K

N₂ sorption studies at 77 K were carried out to identify the resulting porous nature of the composite materials. To compare the porosity of the materials, the well-known Brunauer-Emmett-Teller (BET) surface area analysis is employed.^{17,18} Prior analysis, all samples were thermally activated at 100 °C under vacuum for 3h. **Table 2.2.2.4** summarizes the MOF porosity decrease after the infiltration process, comparing the S_{BET} values of the pristine MOFs vs the encapsulation products.

Table 2.2.2.4. N₂ sorption measurements summary.

Composite	S _{BET} pristine MOF / m ² ·g ⁻¹	S _{BET} composite / m ² ·g ⁻¹	S _{BET} reduction / %
Carvacrol@MIL-100(Fe)	1303	99	92
Citral@MIL-100(Fe)	1153	57	95
Benzaldehyde@MIL-100(Fe)	1153	217	81
Carvacrol@ZIF-8	1566	94	94
Citral@ZIF-8	1603	652	60
Benzaldehyde@ZIF-8	1566	282	82
Carvacrol@UiO-66	695	171	75
Citral@UiO-66	695	219	68
Benzaldehyde@UiO-66	695	287	59
Carvacrol@UiO-66-NH ₂	519	188	64
Citral@UiO-66-NH ₂	519	64	88
Benzaldehyde@UiO-66-NH ₂	519	292	44

MIL-100(Fe) composites. MIL-100 (Fe) exhibits a characteristic type I behaviour isotherm. The abrupt increase of N₂ uptake in the 0-0.1 relative pressure region is concordant with the microporosity of the material. A significant decrease (*ca.* 90 %) in the porous surface was evidenced after biomolecule encapsulation in all three composites(**Figure 2.2.2.18**), which is consistent with an effective biomolecule loading, although window-blocking phenomena should be also considered to some extent (especially in the case of benzaldehyde@MIL-100(Fe), which presents an estimated biomolecule loading of less than half than the other two composites).

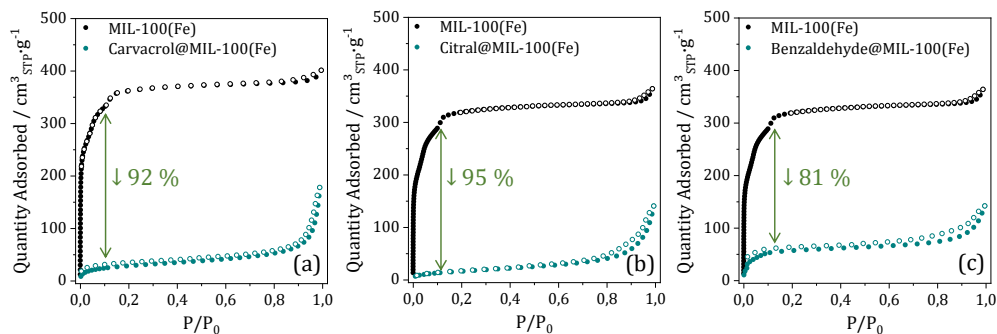


Figure 2.2.2.18. N_2 sorption studies at 77 K (solid symbols for adsorption and open ones for desorption) of the three obtained biomolecule@MIL-100(Fe) composites (teal) in comparison with pristine MIL-100(Fe) (black): (a) carvacrol@MIL-100(Fe), (b) citral@MIL-100(Fe), and (c) benzaldehyde@MIL-100(Fe).

ZIF-8 composites. Control ZIF-8 material presents a typical type I isotherm (**Figure 2.2.2.19**). The porosity decrease in this set of composites follows the expected trend considering the estimated biomolecule loading values, with Carvacrol@ZIF-8 and benzaldehyde@ZIF-8 presenting a more drastic reduction than citral@ZIF-8, which exhibits a decrease in BET surface of *ca.* 60 %.

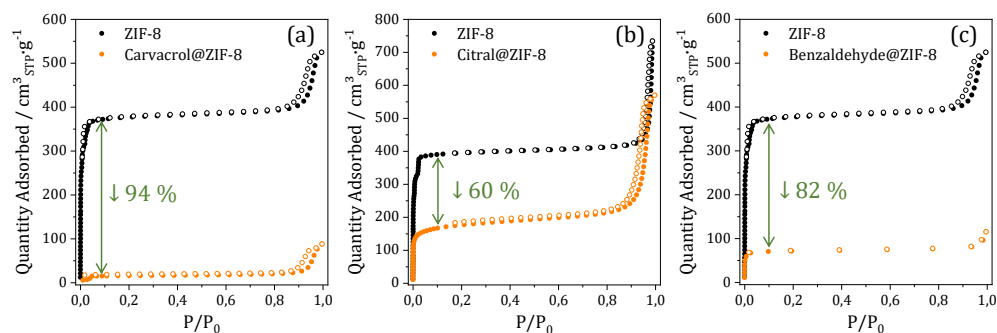


Figure 2.2.2.19. N_2 sorption studies at 77 K (solid symbols for adsorption and open ones for desorption) of the three obtained biomolecule@ZIF-8 composites (orange) in comparison with pristine ZIF-8 (black): (a) carvacrol@ZIF-8, (b) citral@ZIF-8, and (c) benzaldehyde@ZIF-8.

UiO-66 composites. UiO-66 presents a type IV N₂ sorption isotherm. In carvacrol@UiO-66 sorption profile (**Figure 2.2.2.20a**), the hysteretic behaviour of the pristine material is increased after the molecule loading, occurring between 0.4 to 0.9 relative pressure region, in contrast with the 0.4-0.7 range of UiO-66. Considering the analysis of the IR spectrum of the composite, the binding of carvacrol molecules to the zirconium clusters of the nanoMOF could have led to the formation of mesopores in the structure by displacing the terephthalic ligand. This effect could also be related with the observed thermal behaviour of the composite. A substantial decrease in the BET surface is also observed for this material. N₂ sorption studies in citral@UiO-66 (**Figure 2.2.2.20b**) show a smaller decrease in the BET surface evidencing a slightly poorer interaction between citral and the framework compared to carvacrol@UiO-66 composite. In the case of benzaldehyde@UiO-66 (**Figure 2.2.2.20c**), the hysteretic behaviour of the pristine material is completely lost after the molecule loading, which could be related to some extent with the possible decrease in crystallinity in the nanoMOF observed in PXRD measurements. The decrease in the BET surface is not too far from the values obtained for the other two composites, which considering the low quantity of encapsulated molecule estimated by means of TGA would point in the direction of the collapsing of the structure rather than effective benzaldehyde loading.

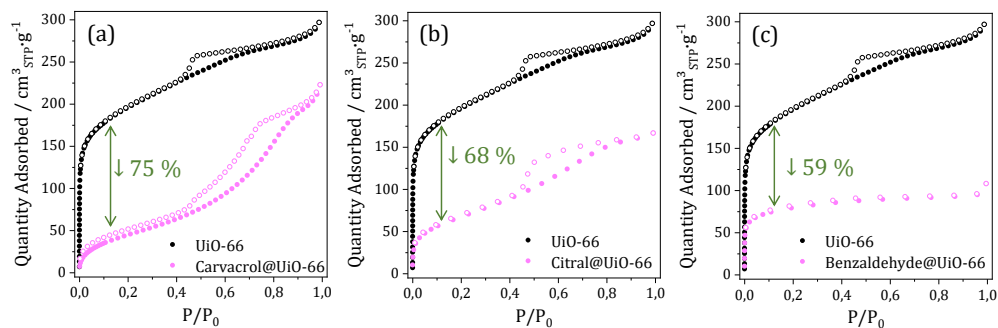


Figure 2.2.2.20. N_2 sorption studies at 77 K (solid symbols for adsorption and open ones for desorption) of the three obtained biomolecule@UiO-66 composites (pink) in comparison with pristine UiO-66 (black): (a) carvacrol@UiO-66, (b) citral@UiO-66, and (c) benzaldehyde@UiO-66.

UiO-66-NH₂ composites. UiO-66-NH₂ thermal profile presents a type IV sorption isotherm. Carvacrol@UiO-66 presents a *ca.* 64 % BET surface reduction compared with the pristine nanoMOF (**Figure 2.2.2.21a**), an expected behaviour taking into account the estimated 22 % loading. Citral@UiO-66-NH₂ presents a substantial *ca.* 88 % BET surface reduction after citral loading (**Figure 2.2.2.21b**). In general, the combination of citral with this nanoMOF yielded interesting results: in view of the broad range of temperature that the ligand decomposition comprises, surpassing by more than 100 °C the thermal stability of the pristine MOF, the interaction between the aldehyde group of citral and the amine of aminoterephthalic acid should not be discarded. However, this interaction should give rise to an imine formation, and the FT-IR spectrum of citral@UiO-66-NH₂ did not evidence the appearance of a new band in the 1690-1640 cm^{-1} region even if $\nu(\text{C}=\text{N})$ bands are not particularly intense, many vibration bands of citral and UiO-66-NH₂ are overlapped, and the overall intensity of the IR spectrum of UiO-66-NH₂ is very low. The functionalization of the BDC-NH₂ ligand in some of the framework pores could also explain the drastic decrease in the porous

capacity of the composite. Interestingly, even if the estimated benzaldehyde loading in benzaldehyde@UiO-66-NH₂ is only a 5 % according to its thermal profile, the composite presents a *ca.* 44 % BET surface reduction (**Figure 2.2.2.21c**) compared with pristine UiO-66-NH₂, suggesting that the modest amount of benzaldehyde molecules trapped in the porous network is enough to block the window pore of the nanoMOF.

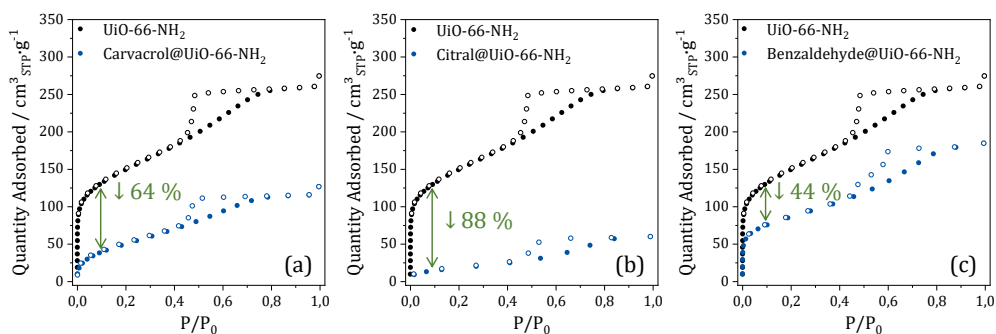


Figure 2.2.2.21. N₂ sorption studies at 77 K (solid symbols for adsorption and open ones for desorption) of the three obtained biomolecule@UiO-66-NH₂ composites (blue) in comparison with pristine UiO-66-NH₂ (black): (a) carvacrol@UiO-66-NH₂, (b) citral@UiO-66-NH₂, and (c) benzaldehyde@UiO-66-NH₂.

2.2.3. Encapsulation Summary

Considering the obtained results throughout this Chapter 2 (see **Table 2.2.3.1**), MIL-100(Fe) is presented as a very adequate carrier for carvacrol and citral, presenting estimated loadings of almost 40 %, and a drastic decrease in the sorption capacity of the nanoMOF. The shifting of the Fe-O related bands observed in IR spectroscopy after the encapsulation suggests the binding of the active molecules to the Fe^{III} clusters in the three obtained composites.

The absence of CUS in the ZIF-8 structure prevents a further chemical interaction with the molecules, but the estimated loadings of around 20 %

for the three physisorbed molecules place this nanoMOF as a suitable carrier in all three cases. This is especially remarkable for benzaldehyde, since ZIF-8 not only presents the higher loading values, but it is also the only nanoMOF that reaches loading values over 20 %, doubling the benzaldehyde loading capacity of the second-best benzaldehyde carrier, MIL-100(Fe).

Comparing the performance of the two Zr-based materials, the estimated biomolecule loading values extracted from their thermal profiles are very similar in all cases, with best results for the combination of carvacrol@UiO-66 and citral@UiO-66-NH₂, but their best performance does not reach the loading values of MIL-100(Fe).

Furthermore, the presence of the amino group in UiO-66-NH₂ seems to hinder the biomolecule diffusion into the framework and prevents the direct interaction of the molecules to the Zr^{IV} centres, since the consequential shifting of Zr-O related bands in the composites IR spectra only occurs for UiO-66. However, interesting results were also obtained regarding the study of the chemical interactions between the active molecules and the framework: carvacrol infiltration into UiO-66 porous structure produced and increased hysteretic behaviour in the N₂ sorption isotherms, pointing in the direction of mesopore formation due to the coordination of carvacrol to the Zr^{IV} clusters observed by means of IR spectroscopy. Interestingly, the interaction of citral with the amino functionalised linker of UiO-66-NH₂ gave rise to an increase of thermal stability of 100 °C in the composite compared with the pristine nanoMOF. The relatively high 26 % estimated citral loading is also surprising, considering the absence of citral-related bands in the composite IR spectrum.

Table 2.2.3.1 Summary of the encapsulation results obtained by different techniques in this chapter.

Composite	IR: Presence of biomolecule bands	TGA: Estimated molecule loading / % (w/w)	N₂ sorption: Porosity (BET) decrease / %
Carvacrol@MIL-100(Fe)	Yes	37.7	92
Citral@MIL-100(Fe)	Yes	37.4	95
Benzaldehyde@MIL-100(Fe)	Yes	12.3	81
Binding to Fe ^{III} centres in all cases			
Carvacrol@ZIF-8	Yes	23.6	94
Citral@ZIF-8	Yes	19.2	60
Benzaldehyde@ZIF-8	Yes	23.9	82
High physisorbed molecule loading in all cases			
Carvacrol@UiO-66	Yes	27.0	75
Citral@UiO-66	Yes	20.8	68
Benzaldehyde@UiO-66	Yes	9.6	59
Carvacrol and benzaldehyde binding to the Zr ^{IV} centres			
Carvacrol@UiO-66-NH ₂	Yes	22.4	64
Citral@UiO-66-NH ₂	No	26.0	88
Benzaldehyde@UiO-66-NH ₂	No	5.3	44
Ligand functionalization seems to hinder molecule interaction with the metallic clusters			

2.3. Summary and conclusions

In this Chapter 2, a systematic study was performed to an array of archetypal MOFs to evaluate their performance as natural BAC carriers for their potential application in food industry. Furthermore, a direct impregnation method was developed, where it was found that biomolecule encapsulation was favoured under aqueous-alcoholic mixtures (in which these molecules are poorly soluble), this parameter resulting key for a successful encapsulation.

In total, twelve new biocomposites were obtained and analysed. The presence of the biomolecules in the composites was evidenced for each encapsulation product. **Carvacrol** loading was particularly effective in all cases, being successfully diffused through the porous frameworks due to its relatively small size, showing exceptionally attractive results in combination with MIL-100(Fe) by coordination with the Fe^{III} centres. **Citral** interaction with UiO-66-NH₂ showed interesting results, pointing in the direction of the functionalization of the BDC-NH₂ ligand. **Benzaldehyde** encapsulation was remarkably effective in ZIF-8, with much higher loading values than the rest of the nanoMOF candidates.

Considering all the analysed results, **MIL-100(Fe)** and **ZIF-8** are presented as the most promising carrier agents for their great loading capacity, the affordability and availability of their precursors, and their *greener* synthetic protocol. In particular, the ability of MIL-100(Fe) to coordinatively interact with the guest biomolecules will be more thoroughly studied. Even though UiO-66 and UiO-66-NH₂ showcased promising results in combination with carvacrol and citral, the afforded results are not so remarkable to justify the more expensive starting materials for their synthesis, or the use of DMF and the subsequential washing protocol to completely remove it in order to be suitable materials for industrial applications.

2.4. Methods

Synthesis of nanoMOF particles

MIL-100(Fe) nanoparticles were synthesized following the procedure described by García Márquez and co-workers,¹¹ by a microwave-assisted method. $\text{FeCl}_3 \cdot 6\text{H}_2\text{O}$ (2.43 g, 6.01 mmol) and H_3BTC (0.84 g, 4.00 mmol) were dissolved in 20 mL of miliQ water. The reaction was suddenly heated to 130 °C in 30 s at 1600 W, then maintained at this temperature for 5 min 30 s. The reacting mixture was placed in an ice bath to cool down and centrifuged (10000 rpm, 25 min, room temperature), then washed 6 times with H_2O and EtOH. The as-synthesized material was treated in a KF 0.1M solution for 2h and washed with H_2O to remove excess of reagents. The particles were collected by centrifugation (10000 rpm, 20 min, room temperature) and stored humid. Yield $\sim 50\%$ after washing protocol due to the loss of the smaller NPs during the several washing steps.

ZIF-8 nanoparticles were synthesized adapting the protocol of Langner and co-workers.¹² A solution of $\text{Zn}(\text{NO}_3)_2 \cdot 6\text{H}_2\text{O}$ (1.476 g, 5 mmol) in 100 mL of methanol at 40 °C was rapidly added to a solution of 2-methylimidazole (3.286 g, 40 mmol) in methanol (50 mL) at the same temperature. The mixture was heated at 65 °C and stirred for 1 h at this temperature before placing the flask in an ice bath to stop the reaction. The precipitate was isolated by centrifugation (8000 rpm, 30 min, room temperature), washed with methanol three times, and dried in air overnight. Yield: $\sim 80\%$.

UiO-66 and **UiO-66-NH₂** nanoparticles were synthesized adapting the protocol of Cavka and co-workers.¹³ 25 mmol (8.06 g) of $\text{ZrOCl}_2 \cdot 8\text{H}_2\text{O}$ and 25 mmol of dicarboxylic linker (terephthalic acid – H_2BDC , 4.16 g; or 2-aminoterephthalic acid – $\text{H}_2\text{BDC-NH}_2$, 4.53 g) were dispersed in 250 mL of N,N-dimethylformamide (DMF), and heated for 6 h at 90 °C in a round bottom flask. The product was recovered by centrifugation (5000 rpm, 30 min, room temperature), washed one time with DMF and 6 more times with

EtOH. Further washing of the materials was carried out by stirring them in hot EtOH and exchanging the solvent every 24 h for two weeks to ensure the removal of DMF. The nanostructured MOFs were dried at air and stored. Yield $\sim 30\%$ for both materials, due to the several washing steps of the protocol.

Method for molecule encapsulation: (i) Ethanolic encapsulations

Calibration solutions were prepared to ascertain that the encapsulation kinetics could be followed by UV-Vis spectroscopy, monitoring the biomolecule concentration remanent in the encapsulation medium.

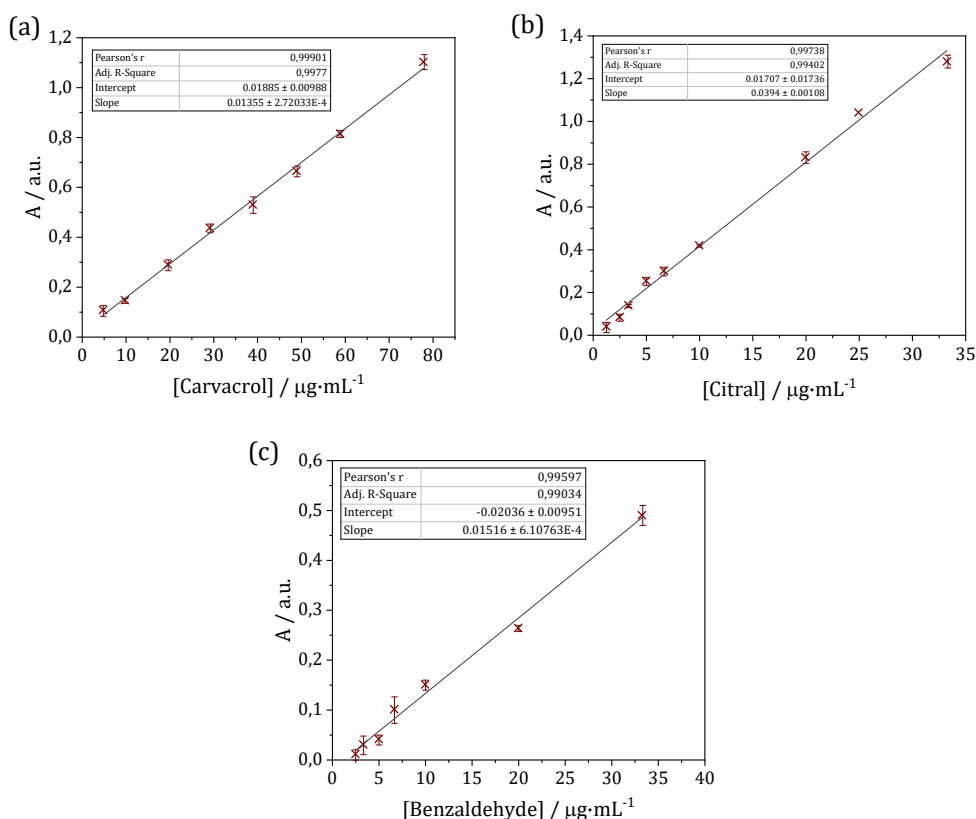


Figure 2.4.1. UV-Vis calibration curves of (a) carvacrol, (b) citral, and (c) benzaldehyde in EtOH. All samples were prepared by triplicate.

(ii) H₂O:EtOH (4:1) mixture encapsulations

Composite biomolecule@MOF materials were obtained following a direct impregnation method. A certain amount of biomolecule emulsion prepared in a H₂O:EtOH (4:1) mixture was directly added to MOF nanoparticles (weighted humid and corresponding to 200 mg of dried MOF in the case of MIL-100(Fe), dry product for the rest of the pristine MOFs), ensuring that the biomolecule/MOF molar ratio is 5/1. **Table 2.4.1** summarizes the exact volume values in each case. After 5 days stirring in a 360° rotating shaker, the biomolecule@MOF material was retrieved by centrifugation (10000 rpm, 20 min, room temperature) and dried at air overnight.

Table 2.4.1. Biomolecule emulsion added volume for each encapsulation.

nanoMOF	Added Volume / mL		
	Carvacrol	Benzaldehyde	Citral
MIL-100(Fe)	23.0	8.1	11.7
ZIF-8*	33.0	11.7	33.5
UiO-66	8.6	3.2	4.6
UiO-66-NH ₂	9.0	3.0	4.3

* ZIF-8 encapsulations are performed by duplicate using 100 mg of dry MOF for better processability.

Characterization of biomolecule@MOF composite materials

X-ray powder diffraction experiments were acquired in an X-ray diffractometer (PANalytical Empyrean) with copper as a radiation source (Cu-K α , 1.5418 Å). Infrared spectroscopy spectra were registered employing an ALPHA II FTIR spectrometer (Bruker). Thermogravimetric analyses were carried out with TGA 550 (TA Instruments) in high-resolution mode (Ramp: 20.0 °C/min to 680.00 °C; Res 4 Sensitivity 3). N₂ adsorption isotherms were obtained using a TRISTAR II apparatus (Micromeritics) at -196 °C. All samples were activated at 100 °C under vacuum for 3h before measurement.

The porosity of the materials is compared by means of the Brunauer-Emmett-Teller (BET) surface area analysis: this method consists in the multi-point measurement of an analyte's specific surface area ($\text{m}^2\cdot\text{g}^{-1}$) through gas adsorption analysis, where nitrogen gas is continuously flowed over a solid sample. Due to weak Van der Waals forces, N_2 molecules adsorb to the solid substrate and its porous features, generating an adsorbed gas monolayer. The specific surface area of a solid in the micropore region can be calculated using this monomolecular layer and the rate of adsorption.

2.5. References

- (1) Katsoulidis, A. P.; Antypov, D.; Whitehead, G. F. S.; Carrington, E. J.; Adams, D. J.; Berry, N. G.; Darling, G. R.; Dyer, M. S.; Rosseinsky, M. J. Chemical Control of Structure and Guest Uptake by a Conformationally Mobile Porous Material. *Nature* **2019**, *565* (7738), 213–217.
- (2) Wang, H.; Lashkari, E.; Lim, H.; Zheng, C.; Emge, T. J.; Gong, Q.; Yam, K.; Li, J. The Moisture-Triggered Controlled Release of a Natural Food Preservative from a Microporous Metal-Organic Framework. *Chem. Commun.* **2016**, *52* (10), 2129–2132.
- (3) Lashkari, E.; Wang, H.; Liu, L.; Li, J.; Yam, K. Innovative Application of Metal-Organic Frameworks for Encapsulation and Controlled Release of Allyl Isothiocyanate. *Food Chem.* **2017**, *221*, 926–935.
- (4) Dong, Z.; Sun, Y.; Chu, J.; Zhang, X.; Deng, H. Multivariate Metal-Organic Frameworks for Dialing-in the Binding and Programming the Release of Drug Molecules. *J. Am. Chem. Soc.* **2017**, *139* (40), 14209–14216.
- (5) Balestri, D.; Mazzeo, P. P.; Perrone, R.; Fornari, F.; Bianchi, F.; Careri, M.; Bacchi, A.; Pelagatti, P. Deciphering the Supramolecular Organization of Multiple Guests Inside a Microporous MOF to Understand Their Release Profile. *Angew. Chemie - Int. Ed.* **2021**, 10194–10202.
- (6) Ramos, M.; Jiménez, A.; Peltzer, M.; Garrigós, M. C. Characterization and Antimicrobial Activity Studies of Polypropylene Films with Carvacrol and Thymol for Active Packaging. *J. Food Eng.* **2012**, *109* (3), 513–519.
- (7) Kamimura, J. A.; Santos, E. H.; Hill, L. E.; Gomes, C. L. Antimicrobial and Antioxidant Activities of Carvacrol Microencapsulated in Hydroxypropyl-Beta-Cyclodextrin. *LWT - Food Sci. Technol.* **2014**, *57* (2), 701–709.
- (8) Ullah, I.; Khan, A. L.; Ali, L.; Khan, A. R.; Waqas, M.; Hussain, J.; Lee, I. J.; Shin, J. H. Benzaldehyde as an Insecticidal, Antimicrobial, and Antioxidant Compound Produced by *Photorhabdus Temperata* M1021. *J. Microbiol.* **2015**, *53* (2), 127–133.
- (9) Saddiq, A. A.; Khayyat, S. A. Chemical and Antimicrobial Studies of Monoterpene: Citral. *Pestic. Biochem. Physiol.* **2010**, *98* (1), 89–93.

- (10) Thielmann, J.; Theobald, M.; Wutz, A.; Krolo, T.; Buergey, A.; Niederhofer, J.; Welle, F.; Muranyi, P. Litsea Cubeba Fruit Essential Oil and Its Major Constituent Citral as Volatile Agents in an Antimicrobial Packaging Material. *Food Microbiol.* **2021**, *96* (December 2020), 103725.
- (11) García Márquez, A.; Demessence, A.; Platero-Prats, A. E.; Heurtaux, D.; Horcajada, P.; Serre, C.; Chang, J. S.; Férey, G.; De La Peña-O'Shea, V. A.; Boissière, C.; et al. Green Microwave Synthesis of MIL-100(Al, Cr, Fe) Nanoparticles for Thin-Film Elaboration. *Eur. J. Inorg. Chem.* **2012**, *100* (32), 5165–5174.
- (12) Tsai, C. W.; Langner, E. H. G. The Effect of Synthesis Temperature on the Particle Size of Nano-ZIF-8. *Microporous Mesoporous Mater.* **2016**, *221*, 8–13.
- (13) Cavka, J. H.; Jakobsen, S.; Olsbye, U.; Guillou, N.; Lamberti, C.; Bordiga, S.; Lillerud, K. P. A New Zirconium Inorganic Building Brick Forming Metal Organic Frameworks with Exceptional Stability. *J. Am. Chem. Soc.* **2008**, *130* (42), 13850–13851.
- (14) Leclerc, H.; Vimont, A.; Lavalley, J. C.; Daturi, M.; Wiersum, A. D.; Llwellyn, P. L.; Horcajada, P.; Férey, G.; Serre, C. Infrared Study of the Influence of Reducible Iron(III) Metal Sites on the Adsorption of CO, CO₂, Propane, Propene and Propyne in the Mesoporous Metal-Organic Framework MIL-100. *Phys. Chem. Chem. Phys.* **2011**, *13* (24), 11748–11756.
- (15) Bellido, E.; Hidalgo, T.; Lozano, M. V.; Guillevic, M.; Simón-Vázquez, R.; Santander-Ortega, M. J.; González-Fernández, Á.; Serre, C.; Alonso, M. J.; Horcajada, P. Heparin-Engineered Mesoporous Iron Metal-Organic Framework Nanoparticles: Toward Stealth Drug Nanocarriers. *Adv. Healthc. Mater.* **2015**, *4* (8), 1246–1257.
- (16) Hidalgo, T.; Alonso-Nocelo, M.; Bouzo, B. L.; Reimondez-Troitiño, S.; Abuin-Redondo, C.; De La Fuente, M.; Horcajada, P. Biocompatible Iron(III) Carboxylate Metal-Organic Frameworks as Promising RNA Nanocarriers. *Nanoscale* **2020**, *12* (8), 4839–4845.
- (17) Brunauer, S.; Emmett, P. H.; Teller, E. In *Multimolecular*. *J. Am. Chem. Soc.* **1938**, *60* (2), 309–319.
- (18) Walton, K. S.; Snurr, R. Q. Applicability of the BET Method for Determining Surface Areas of Microporous Metal-Organic Frameworks. *J. Am. Chem. Soc.* **2007**, *129* (27), 8552–8556.

CHAPTER 3

Implementation of carvacrol@MIL-100(Fe) as
active agent for smart packaging

3.1. Introduction

In an effort to meet the needs of consumers, fresh food production, processing, and marketing have undergone significant experimentation over the past few decades. However, product spoilage waste and processing residue waste are becoming a serious economic and environmental problem.¹ Classically, plastic materials employed in food industry are prepared by condensation polymerization process or polymerization of hydrocarbon or hydrocarbon-like monomers from different raw materials originating from the petrochemical industry. Consequently, they are non-biodegradable and non-renewable products and nowadays contribute to aggravate one of the major societal global challenges which is climate change.

As a result, efforts are being directed toward improving and optimizing food packaging systems from both researchers and the food industry. For instance, the use of biopolymers offers different advantages including abundant availability in nature, reasonable mechanical properties, and biodegradability. Examples of these biopolymers include starch, chitosan, gelatine, and cellulose, which are widely applied in food packaging.² Furthermore, the development of edible films, for instance, has developed rapidly in the recent years, due to the increasing consumer interest in health, nutrition, food safety, and environmental issues.³

A particularly interesting renewable polymeric material employed in this Thesis is zein. This biopolymer consists of prolamins, a group of alcohol-soluble proteins from corn, which have thermoplastic properties and very low solubility in water. The main advantage of films derived from zein is their desirable heat seal characteristics, suitable for packaging applications (**Figure 3.1.1**).⁴ This corn protein is Generally Recognized As Safe (GRAS) by the FDA for the film coating of pharmaceuticals, and has been used to develop biodegradable films and plastics.⁵ Finally, the design of antimicrobial zein

films with carvacrol can be found in the literature,⁶ as well as with other active biomolecules such as lysozyme.⁷

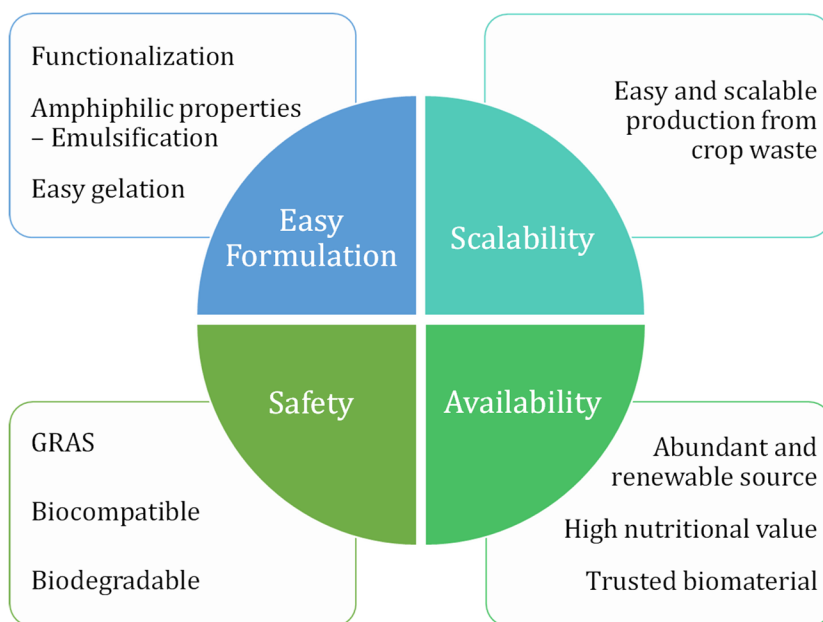


Figure 3.1.1. Main advantages of employing zein protein for biomedical and food-related applications. Adapted from reference 4.

Extending shelf life of food products is another appealing policy to reduce food waste. For this reason, the implementation of antimicrobial agents in packaging has arisen as a creative method to maintain the quality and safety of food. The main motivation is that their later progressive release into the packaged product or the head-space of the package causes an inhibitory effect against food-borne pathogens.⁸

This incorporation of EOs in various types of biopolymer films, has a promising outlook for *greener* food-packaging applications.^{9,10} Two main routes can be employed to incorporate these natural BACs into polymeric matrixes: i) the direct incorporation of the natural ingredients into the polymer material and ii) using encapsulation technologies.

As previously described in Chapter 2, successful direct incorporation of EOs within active packaging is limited due to their volatile nature, low

solubility, and their susceptibility to oxidation. For example, Neira and co-workers reported antioxidant and antibacterial fish gelatine edible films with improved moisture resistance and water vapor barrier after the incorporation of carvacrol. However, the sustainable loss of carvacrol over time dropped significantly the *in vitro* antibacterial and antioxidant efficiency under storage conditions.¹¹

On the other hand, the use of carrier agents presents numerous advantages compared with the direct film incorporation route: encapsulation techniques can increase EOs stability against oxidation, light-induced reactions, humidity, and high temperatures, or providing a controlled release of the compound from the encapsulating agent.¹² The implementation of MOF-based composite materials can be a promising strategy to greatly enhance the stability of the BACs and promote a controlled delivery of the active molecules after its film integration.

The selected molecule in this study is carvacrol, one of the most studied EO derivatives in food industry due to its broad-spectrum antimicrobial activity against foodborne bacteria which has been shown to be effective in the vapor phase. This feature makes it a promising antimicrobial agent to be released from the film into the headspace of a food package.¹³ Carvacrol can be either directly integrated in polymeric films like soy protein¹⁴ or chitosan,¹⁵ or encapsulated in carrier agents like β -cyclodextrins,¹⁶ nanofibres,¹⁷ or nanoemulsions.¹⁸

For all this, after determination of MIL-100(Fe) as a feasible carvacrol carrier in Chapter 2, the aim of this Chapter 3 is to incorporate the obtained composite carvacrol@MIL-100(Fe) material into biopolymeric films and evaluate the MOF ability to stabilize and govern the release of the bioactive molecule. Furthermore, an extensive physicochemical characterization of the hybrid material will lead to further understand the electronic interactions between the Fe^{III} centres and the bioactive molecule. Finally, the performance of the composite after integration into biopolymeric films will be assessed, to establish if the MOF scaffold promotes a durable or improved antimicrobial effect, resulting of interest for food industry uses (**Figure 3.1.2**).

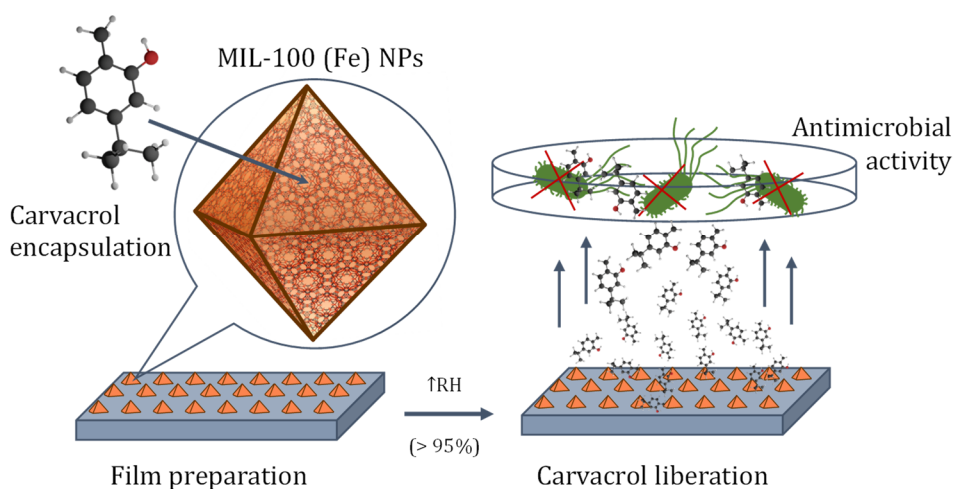


Figure 3.1.2. Schematic representation of the encapsulation process and the implementation in polymeric films, showcasing the antimicrobial properties of the liberated carvacrol molecules.

3.2. Results and discussion

3.2.1. Optimisation of carvacrol encapsulation in MIL-100(Fe)

After the systematic study performed in Chapter 2, evaluating the EO loading capacity of four archetypal MOFs, carvacrol@MIL-100(Fe) composite material was selected for further study as a promising carvacrol encapsulating agent for its integration in biopolymeric films.

Encapsulation kinetics. Preliminary studies developed in achieved carvacrol loading by soaking MIL-100(Fe) nanoparticles into a 10 mg·mL⁻¹ carvacrol ethanolic solution (20 %) with a 5/1 carvacrol/MIL-100(Fe) molar ratio. To evaluate the highest plausible carvacrol loading, infiltration kinetics were further analysed by means of thermic desorption Gas Chromatography. It was observed that after 5 days of encapsulation saturation was reached (**Figure 3.2.1a**) with no further loading occurring up to 10 days. Once the encapsulation time was optimized, the effect of the carvacrol concentration in the loading kinetics was also analysed. Different carvacrol/MIL-100(Fe) molar ratios ranging from 1/1 to 10/1 were studied up to 5-days encapsulations (**Figure 3.2.1b**). The parameters evaluated for optimal encapsulation including time and different concentration conditions are listed in **Table 3.2.1**, whereas initial carvacrol concentration details are summarized in **Table 3.2.2**. Carvacrol loading and encapsulation efficiency are defined according to the equations:

$$\text{Carvacrol loading \%} = \frac{\text{mass of carvacrol}}{\text{mass of composite}} \times 100$$

$$\text{Encapsulation Efficiency \%} = \frac{\text{mass of loaded carvacrol}}{\text{mass of initial carvacrol}} \times 100$$

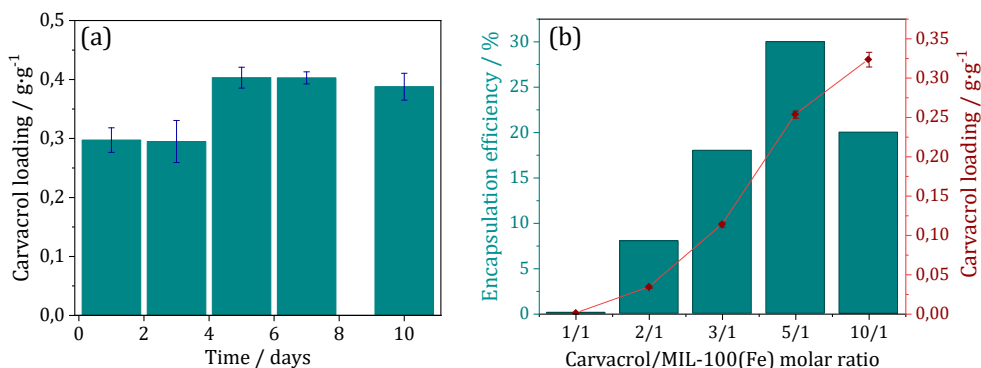
Table 3.2.1: Evaluated parameters in the optimization of the encapsulation protocol.

Solvent	Carvacrol/MIL-100(Fe) molar ratio	Encapsulation time (days)
H ₂ O/EtOH (4/1)	5/1	1, 3, 5, 7, 10
	1/1	
	2/1	
	3/1	5
	5/1	
	10/1	

Table 3.2.2. Initial carvacrol concentration in the encapsulation media for the different molar ratios with their corresponding encapsulation efficiency.

Carvacrol/MIL-100(Fe) molar ratio	1/1	2/1	3/1	5/1	10/1
[Carvacrol] ₀ / mg·mL ⁻¹	2	4	6	10	20
Encapsulation efficiency / %	0.1	8	18	30	20

As **Figure 3.2.1b** showcases, even if the carvacrol content in the obtained composites increases with the carvacrol/MIL-100(Fe) molar ratio employed in the encapsulation process, the higher encapsulation efficiency is obtained for a 5/1 carvacrol/MIL-100(Fe) ratio.

**Figure 3.2.1.** (a) Carvacrol content in the composite as a function of time of incubation. (b) Encapsulation efficiency as a function of carvacrol/MIL-100(Fe) molar ratio

Encapsulation temperature was also evaluated by performing two 5-day encapsulations with a molar ratio of 5/1 at room temperature and 37 °C in parallel, with no differences observed in encapsulation efficiency.

Summarizing the obtained data upon monitoring of the carvacrol sorption equilibrium over time in the collected composite material by gas chromatography, a maximum carvacrol loading of 42 % was reached after 5 days of immersion and resulted in an encapsulation efficiency of 58 %. This payload is, to the best of our knowledge, the highest carvacrol uptake onto a MOF obtained in a liquid-phase encapsulation, surpassing the considerable 34% of carvacrol loading achieved in MIL-53(Al) by supercritical CO₂ encapsulation reported by He and coworkers.¹⁹ In addition, as compared to other classical carrier agents, the obtained carvacrol@MIL-100(Fe) composite is in a competitive position in terms of carvacrol loading, only being surpassed by carvacrol-loaded human serum albumin nanoparticles. For a better comparison, these loadings and encapsulation efficiencies is summarized in **Table 3.2.3**.²⁰

Table 3.2.3: Carvacrol encapsulation efficiency of the composite in comparison with classical carriers.

Encapsulation agent	Encapsulation efficiency / %	Carvacrol loading / %
This work	58	42
Chitosan NPs ²¹	14–31	3–21
Poly(DL-lactide-co-glycolide) (PLGA) NPs ²²	26	21
Hydroxypropyl-beta-cyclodextrin microcapsule ²³	83, 91	-
Human serum albumin NPs ²⁰	48	45
Bovine serum albumin NPs ²⁴	68	27
Polyhydroxy butyrate NPs ²⁵	21	13
Attapulgate (zeolite) ²⁶	76*	23

* Extracted from experimental data in published work.

3.2.2. Advanced characterization of carvacrol@MIL-100(Fe) material

On top of the already discussed characterisation in Chapter 2 of this Thesis, the obtained nanostructured carvacrol@MIL-100(Fe) composite was further characterised.

First evidence of effective carvacrol loading was noticed by a colour change in the powder from orange to dark brown, respectively for bare MIL-100(Fe) and the collected carvacrol@MIL-100(Fe) composite (**Figure 3.2.2**).



Figure 3.2.2. Colour difference between the pristine MIL-100(Fe) (left) and the final biocomposite (right) after the encapsulation process.

Interestingly, a more drastic colour change to dark took place during a thermal treatment used for activation of the composite prior N₂ sorption studies (**Figure 3.2.3**). In a more detailed observation, the material evolves to dark grey under vacuum for one hour and appears completely black upon heating at 100 °C for 3 hours. This black colour is retained after the gas sorption measurement is finished.

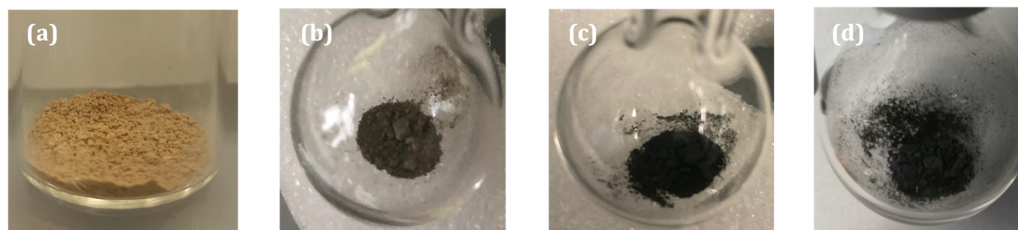


Figure 3.2.3. Colour evolution of carvacrol@MIL-100(Fe) composite during the N₂ adsorption measurements: (a) Before activation. (b) Under vacuum. (c) After thermal treatment (100 °C, 3h) under vacuum. (d) After measurement.

PXRD measurements were carried out to ascertain retention of crystalline phase. As depicted in **Figure 3.2.4** the diffraction pattern of carvacrol@MIL-100(Fe) does not change before and after thermal treatment.

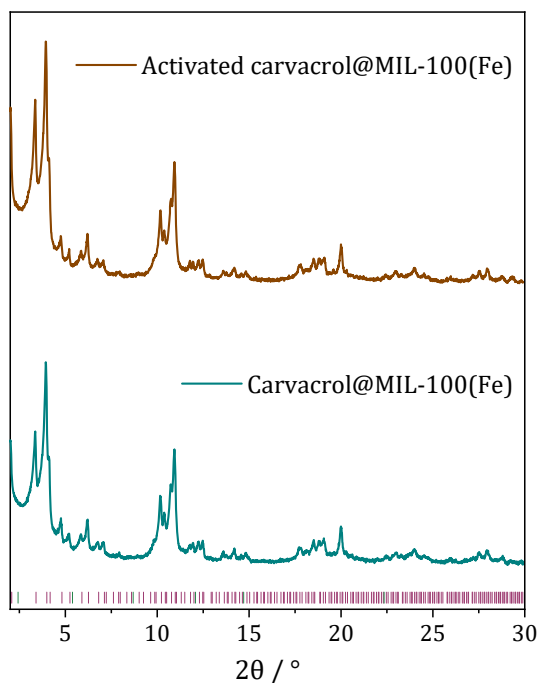


Figure 3.2.4. PXRD pattern of the encapsulation product carvacrol@MIL-100(Fe) before (teal) and after (brown) thermal treatment at 100 °C for 3 hours under vacuum. On the bottom, reflection list of the MIL-100(Fe) unit cell obtained from crystallographic data.

Particle integrity. Scanning Electron Microscopy (SEM) and Transmission Electron Microscopy (TEM) studies reveal a distribution of particle size ranging between 100 and 200 nm, with a non-regular octahedral morphology that remains unaffected by the encapsulation process (**Figure 3.2.5**).

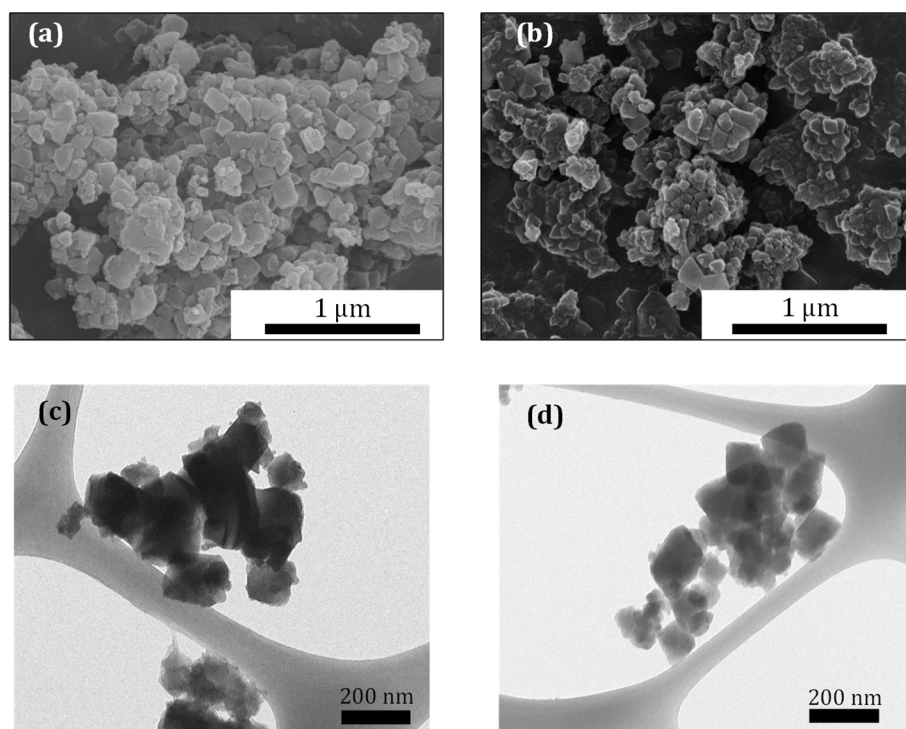


Figure 3.2.5. SEM images of MIL-100(Fe) particles before (a) and after (b) encapsulation. TEM images of the MOF before (c) and after (d) the encapsulation process.

Infrared spectroscopy. As previously discussed in Chapter 2, the $\nu_{\text{as}}(\text{Fe}_3\text{O})$ vibration band related with the Fe^{III} oxo-trimeric core in MIL-100(Fe) at 618 cm^{-1} appears shifted to 628 cm^{-1} in the composite material obtained after carvacrol loading. In an attempt to investigate the nature of this shift, the composite and the control empty material were exposed to thermal treatment under vacuum for 2 hours. Thermal activation ($250\text{ }^\circ\text{C}$) has been previously shown to induce the generation of coordinatively unsaturated iron sites (CUS) with mixed valence $\text{Fe}^{\text{II}}/\text{Fe}^{\text{III}}$ trimers in MIL-100(Fe), manifested by a shifting of the $\nu_{\text{as}}(\text{Fe}_3\text{O})$ band located at 618 cm^{-1} to 597 cm^{-1} in IR spectroscopy studies.^{27,28} In a similar study, the high temperature activation was limited to $190\text{ }^\circ\text{C}$ in order to remain below the carvacrol boiling point. Exposing MIL-100(Fe) control to this thermal activation leads to a reduced shifting in the $\nu_{\text{as}}(\text{Fe}_3\text{O})$ from 618

to 611 cm^{-1} recovering the original value upon 1 min of air exposure (**Figure 3.2.6a**). This band evolution reflects a reversible partial loss of coordinated water molecules as compared to the reported material, as may be expected for lower activation temperature and lack of sample isolation from ambient conditions. In case of carvacrol@MIL-100(Fe) treated at $190\text{ }^{\circ}\text{C}$ under vacuum, a shifting in the $\nu_{\text{as}}(\text{Fe}_3\text{O})$ band from 628 to 605 cm^{-1} is observed, and the original value is recovered after 1 min of air exposure (**Figure 3.2.6b**). The large shifting of the $\nu_{\text{as}}(\text{Fe}_3\text{O})$ band observed in the case of the activated composite is in good agreement with the displacement reported in the mixed valence $\text{Fe}^{\text{II}}/\text{Fe}^{\text{III}}$ MIL-100(Fe) spectrum (23 vs 21 cm^{-1} , respectively).

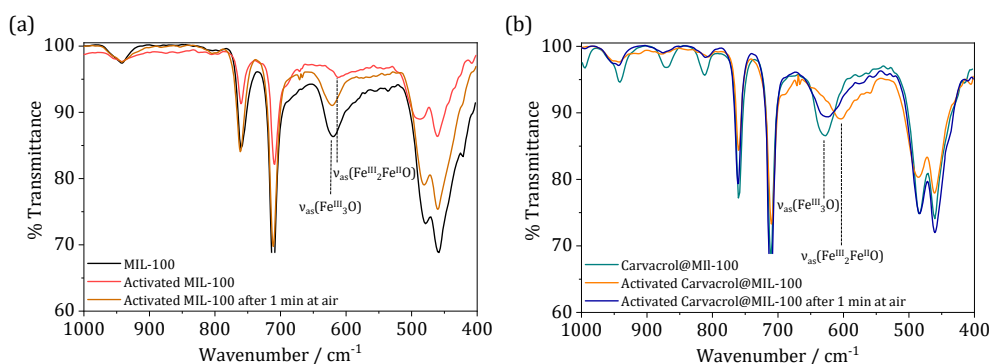


Figure 3.2.6. Infrared spectra comparison in the $1000\text{--}400\text{ cm}^{-1}$ region of the materials (a) pristine MIL-100(Fe) and (b) carvacrol@MIL-100(Fe) before activation, after thermal treatment under vacuum ($190\text{ }^{\circ}\text{C}$ for 2 hours) and upon air exposure for 1 minute.

In addition to the vibrational changes, the solid undergoes drastic colour changes similar to those observed during activation that are depicted in **Figure 3.2.7**. Upon thermal treatment, the original brown composite evolves to an intense black carbon-like colour, and this colour is recovered to some extent upon exposure to air. It is worth mentioning that crystallinity was preserved during this process, as denoted by maintenance of the PXRD patterns in the material (**Figure 3.2.8**).

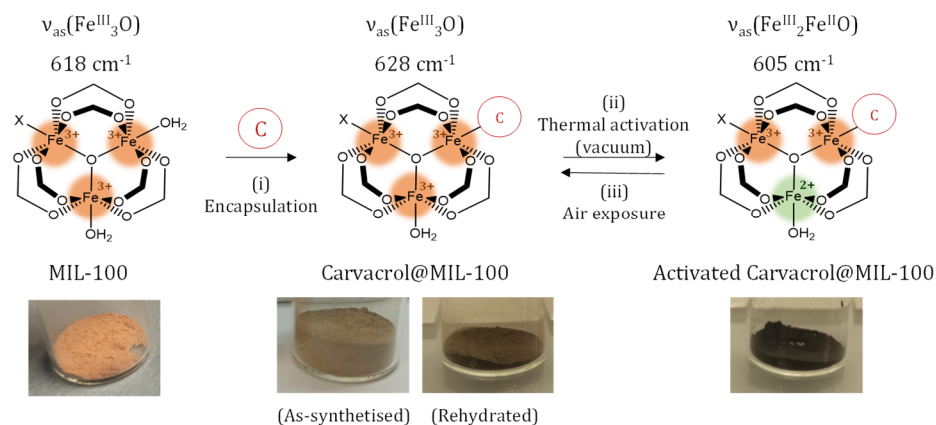


Figure 3.2.7. Scheme of (i) encapsulation, (ii) thermal activation under vacuum and (iii) reversible air exposure processes, with the corresponding colour change in each step. Position of the IR asymmetric stretching bands of the iron trimeric unit is highlighted.

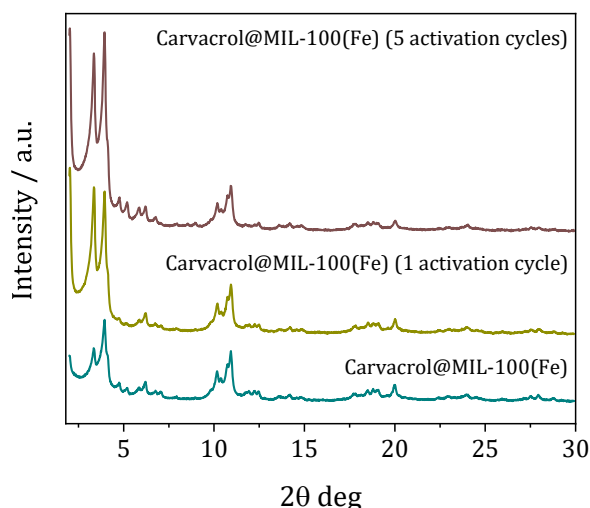


Figure 3.2.8. X-ray powder diffractograms of the encapsulation product before (teal) and after activation (green), and after 5 cycles of thermal treatment (brown).

Mössbauer and EPR spectroscopies. In order to evaluate the effect of carvacrol loading in the MIL-100(Fe) electronic structure, Mössbauer spectroscopy experiments were carried out in collaboration João C. Waerenborgh, and Bruno J. Vieira from the Center for Nuclear Sciences and Technologies (C2TN) (Instituto Superior Técnico - Universidade de Lisboa).

In all cases, spectra were collected at 80K. Control experiments in the as synthesized MIL-100(Fe) and carvacrol@MIL-100(Fe) loaded materials revealed spectra with two broad peaks fitted to distributions of quadrupole doublets (**Figure 3.2.9**). **Table 3.2.4** summarises the calculated isomer shift (IS) values as well as the temperature independent quadrupole splitting (QS), which are consistent with high-spin Fe^{III} ($S = 5/2$) in both samples.²⁹⁻³²

In case of the carvacrol@MIL-100(Fe) composite, a lower QS of Fe^{III} can be detected, which suggests a different Fe^{III} environment in the composite. This difference may arise from the replacement of one of the water molecules coordinated to the Fe^{III} centres by one molecule of carvacrol, in agreement with the shifting of the $\nu_{\text{as}}(\text{Fe}_3\text{O})$ band observed in IR measurements.

Studies on the activated compounds were then performed, after exposing MIL-100(Fe) and carvacrol@MIL-100(Fe) samples to thermal treatment (190 °C) under vacuum for 6 hours and quenching the samples in liquid nitrogen for analysis.

As expected, activated MIL-100(Fe) spectrum obtained at 80 K (**Figure 3.2.9, left**) showed significantly higher average QS as compared to the pristine sample. This is consistent with a more distorted Fe^{III} environment becoming 5-coordinated due to the loss of coordinated water molecules.²⁷ Once the sample was brought back to room temperature in air, the spectrum of the untreated sample was recovered, confirming the reversibility of the desolvation process.

Similar analysis performed on activated carvacrol@MIL-100(Fe) spectrum (**Figure 3.2.9, right**) indicates that approximately 24% of the Fe is reduced to high-spin Fe^{II}, with the estimated IS and QS suggesting that both Fe^{II} and Fe^{III} are 6-coordinated.²⁹ Then, the initial carvacrol@MIL-100(Fe) spectrum is recovered after exposing the activated sample in air and at room temperature for a few hours. These observations are in good agreement with

IR experiments and denote the effective reversible formation of the mixed valence trimer in the composite material with retention of the carvacrol molecules coordinated to the Fe^{III} centres.

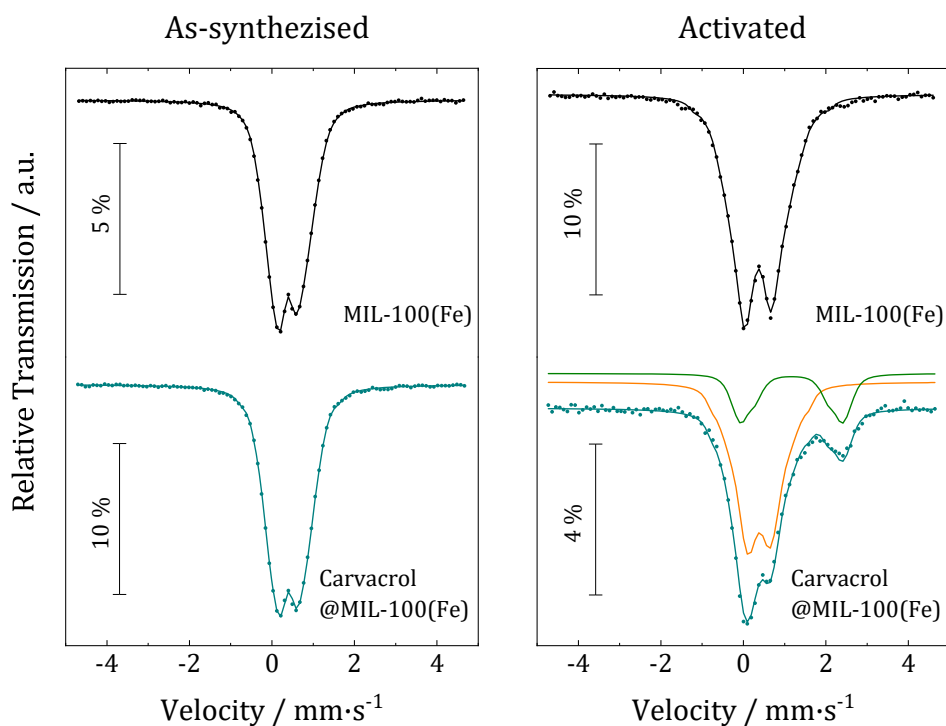


Figure 3.2.9. Mössbauer spectra recorded at 80 K of MIL-100(Fe) (black) and carvacrol@MIL-100(Fe) (teal) measured as-synthesized (left) and after activation (right). The solid lines over the experimental points are the fitted distribution of quadrupole doublets. The sum of two distributions of quadrupole doublets due to Fe^{III} and Fe^{II} , is shown slightly shifted for clarity in orange and green, respectively.

Table 3.2.4: Estimated parameters from the Mössbauer spectra of the MIL-100(Fe) and carvacrol@MIL-100(Fe) samples collected at 80 K.

Sample	T	IS (mm/s)	QS (mm/s)	I	Fe coordination number
MIL-100(Fe)	80 K	0.53	0.72	100%	Fe ^{III} CN=6
Activated MIL-100(Fe)	80 K	0.52	0.96	100%	Fe ^{III} CN=6 and CN=5
Carvacrol@MIL-100(Fe)	80 K	0.53	0.61	100%	Fe ^{III} CN=6
Activated Carvacrol@MIL-100(Fe)	80 K	0.54	0.83	76%	Fe ^{III} CN=6
		1.33	2.30	24%	Fe ^{II} CN=6

IS average isomer shift relative to metallic α -Fe at 295 K; QS average quadrupole splitting; I estimated relative area. Estimated errors are $\leq 0.04 \text{ mm}\cdot\text{s}^{-1}$ for IS and QS and $\leq 3 \%$ for I.

To further investigate the coordination between carvacrol and MIL-100(Fe), EPR experiments were conducted. Spectra recorded at room temperature revealed similar signals for the as-synthesized materials before and after encapsulation (**Figure 3.2.10**), whereas the appearance of a characteristic radical signal ($g = 2.005$) was observed upon activation of the composite (190 °C under vacuum for 2 h), suggesting a radical-mediated mechanism for the carvacrol coordination to the Fe^{III} centres. Interestingly, the radical remains stable, as long as the material is isolated from air.

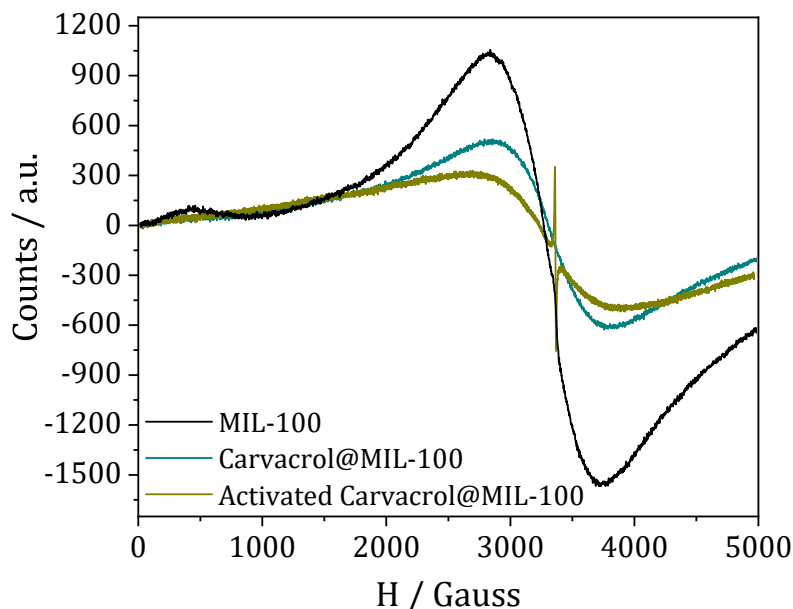


Figure 3.2.10. EPR spectra of Carvacrol@MIL-100(Fe) before (teal) and after activation (green), in comparison with pristine MIL-100(Fe) (black). All measurements are performed at 300K.

3.2.3. Theoretical calculations

Density functional theory calculations were performed to shed light into the coordination process between carvacrol and the Fe^{III} oxo-trimeric core and the formation of the mixed-valence Fe^{II}/Fe^{III} MIL-100(Fe) upon thermal activation. Theoretical calculations were performed by Joaquín Calbo from the Theoretical Chemistry Group (ICMol - Universidad de Valencia). Additional description of this section can be found in the Supporting Information section of this chapter.

An oxo-centred tri-metallic cluster model with six benzoate ligands was extracted from the crystal structure of MIL-100(Fe), bearing two water molecules and a fluoride anion in the coordination environment of Fe^{III} atoms for charge neutrality, and was optimized at the B3LYP/6-31G(d,p) level of theory in a high-spin configuration (**Figure S3.1**). A preliminary

evaluation of the thermodynamics of Fe^{III} coordination bonds, indicates that insertion of carvacrol in MIL-100(Fe) is expected to occur by replacing a coordinative water molecule (**Figure S3.2**), where the overall substitution process is energetically favoured ($\Delta E = -16.15 \text{ kcal}\cdot\text{mol}^{-1}$) (**Figure 3.2.11**).

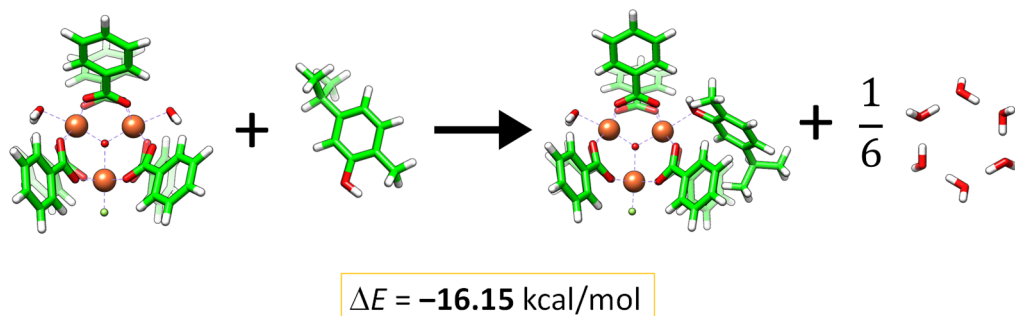


Figure 3.2.11. Bottom: Energy difference for the substitution of a coordinated water molecule by carvacrol system calculated at the B3LYP-D3/6-31G(d,p) level.

In a more complex analysis, a bigger cluster consisting of the pentagonal gate of MIL-100(Fe) was modelled to support the structural and stability properties predicted for the coordination of carvacrol. After geometry optimization, a carvacrol molecule was placed inside the pentagonal window to replace a coordinating water molecule (**Figure S3.5**). Theoretical calculations at the B3LYP/6-31G(d,p) level indicate that the coordination of carvacrol is significantly more stable than with water ($\Delta E = -11.23 \text{ kcal}\cdot\text{mol}^{-1}$ for the reaction of replacing a coordinating water by carvacrol), in good accord with that predicted for the smaller cluster model and in line with the experimental evidence.

Moreover, spin density contours indicate that coordinated carvacrol, in its neutral protonated form, does not show a radical character (oxidized state) that could explain the reduction of one Fe^{III} to engender a mixed-valence Fe^{II}/Fe^{III} system (**Figure 3.2.12a**). Accumulated charges confirm the closed-shell nature of carvacrol moiety, which is barely charged (+0.08e; **Figure 3.2.13**), similar to that calculated for the coordinated water molecule

(+0.09e). On the other hand, time-dependent DFT calculations predict low-lying singlet electronic transitions in the range of 2.2–2.6 eV from the carvacrol system to the Fe-d orbitals (**Figure S3.7**), supporting its electron-donor character compared to the tri-metallic cluster of MIL-100(Fe). Spontaneous one-electron carvacrol oxidation and MIL-100(Fe) reduction was hypothesized to origin upon deprotonation of the relatively acid hydroxy group of carvacrol when coordinated. Theoretical calculations show that proton transfer to other entities is energetically feasible (for example, proton transfer to a coordinating fluoride and water exchange is calculated $< 10 \text{ kcal}\cdot\text{mol}^{-1}$; **Figure S3.8**).

Upon carvacrol deprotonation, the excess of charge in carvacrol moiety is partially withdrawn by the oxo-centred cluster, especially in one of the iron atoms, thus supporting the formation of a mixed-valence $\text{Fe}^{\text{II}}/\text{Fe}^{\text{III}}$ tri-metallic system (showcased in **Figure 3.2.13**). This leads to the formation of a carvacrol radical, which is confirmed by the spin density contours (**Figure 3.2.12b**). The radical carvacrol species coordinated to MIL-100(Fe) is predicted to exhibit several low-lying singlet excited states of charge-transfer nature, with a moderate intensity, and extending over the full visible region of the absorption spectrum (**Figure S3.9**). These results are in good agreement with the black carbon-like colour displayed by carvacrol@MIL-100(Fe) upon thermal activation.

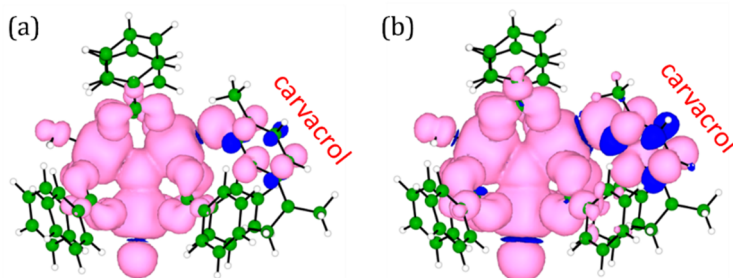


Figure 3.2.12. Spin density contours (isovalue = 0.001 au) calculated for the representative tri-metallic MIL-100(Fe) cluster with coordination of (a) carvacrol molecule or (b) deprotonated carvacrol (radical) system.

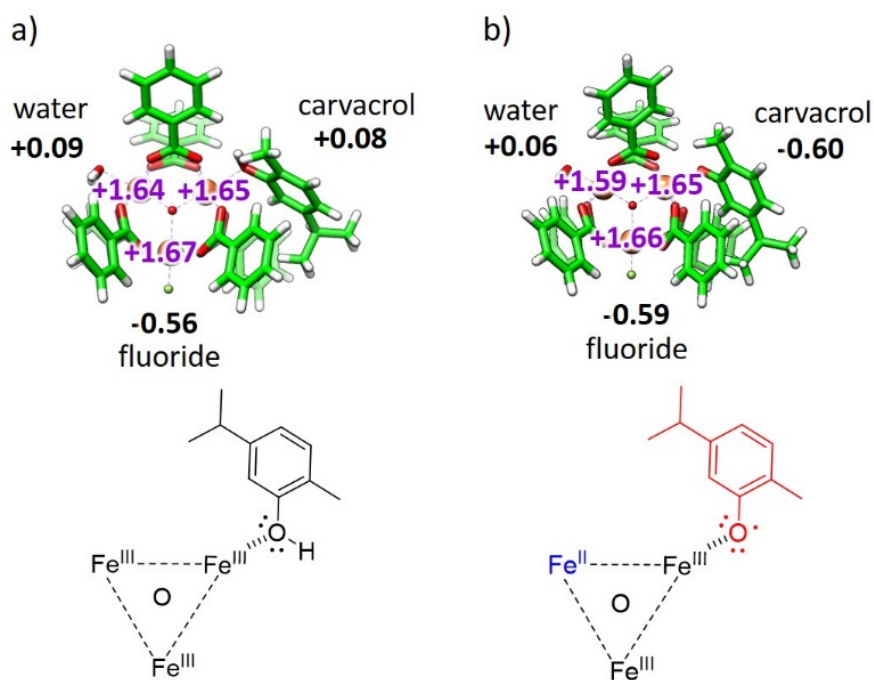


Figure 3.2.13. Natural population analysis (NPA) charges calculated at the B3LYP-D3/6-31G(d,p) level for the coordination of carvacrol molecule (a) and deprotonated carvacrol (b) in the tri-metallic cluster model of MIL-100(Fe). The corresponding chemical structure representation is drawn at the bottom

3.2.4. Kinetics of carvacrol release from MIL-100 supported on films

Once evidenced the effective interaction of carvacrol guest molecules with the MOF, the following step consisted of interrogating the MOF scaffold influence in the release of carvacrol. With this aim, the incorporation of the MOF composite into polymeric films was first targeted. Carvacrol liberation was studied after the incorporation of the composite in a Zein polymeric matrix simulating fresh food environmental conditions. This section was carried out in collaboration with Pilar Hernández-Muñoz and Rafael Gavara from Instituto de Agroquímica y Tecnología de Alimentos, IATA-CSIC.

Zein is relatively hydrophobic, non-soluble in water but soluble in aqueous ethanol solutions. In contrast to films derived from other proteins, films

derived from zein possess desirable heat seal characteristics suitable for packaging applications due to their thermoplastic capacity, presenting the ability to resist high temperatures (thermal degradation point 320 °C).³³ To analyse the how the encapsulation into MIL-100(Fe) affects the kinetics of the liberation of carvacrol molecules compared with the free molecule after bio film integration, two zein films were prepared from an 80 % hydroalcoholic solution containing 15 % weight of zein. Two fractions of this solution were separated: Carvacrol@MIL-100(Fe) composite was added to the first one, whereas the corresponding amount of free carvacrol was directly added to the second fraction. The mixtures were spread on a flat surface of PTFE and dried in an open oven to obtain the biofilm.

Figure 3.2.14 shows the results of carvacrol liberation from the composite-containing film as compared to a control film containing free carvacrol in the same concentration. Control free carvacrol release profile is characterized by a direct continuous delivery with a maximum corresponding to a 4 % of the total liberated carvacrol at 20 h followed by an exponential decay, which corresponds with a delivery governed by diffusion until agent depletion. A drastically different profile is observed in the composite-containing film, which is described with a significant carvacrol retention of *ca.* 5 hours occurring before the liberation starts. After 5 h, two clearly different delivery phases are observed that are ascribed to the occurrence of sequential fast and slow desorption processes reflected in a first maximum of delivered carvacrol corresponding to 10 % of the total liberated carvacrol at 20 h, followed by an additional second maximum corresponding to 70 % at 66 h. This unique behaviour can be explained by attributing each maximum to different host-guest interactions between the carvacrol molecules and the MIL-100(Fe) framework. The first liberation occurring over 20 h may correspond to the release of weakly interacting carvacrol molecules, whereas up to two days of high relative humidity

conditions are required to trigger the liberation of the chemisorbed molecules. In conclusion, the two-step release profile mediated by the MOF scaffold represents a clear improvement to deliver carvacrol at prolonged times as compared to the same amount of free molecule in the polymeric film, evidencing the unique MOF performance.

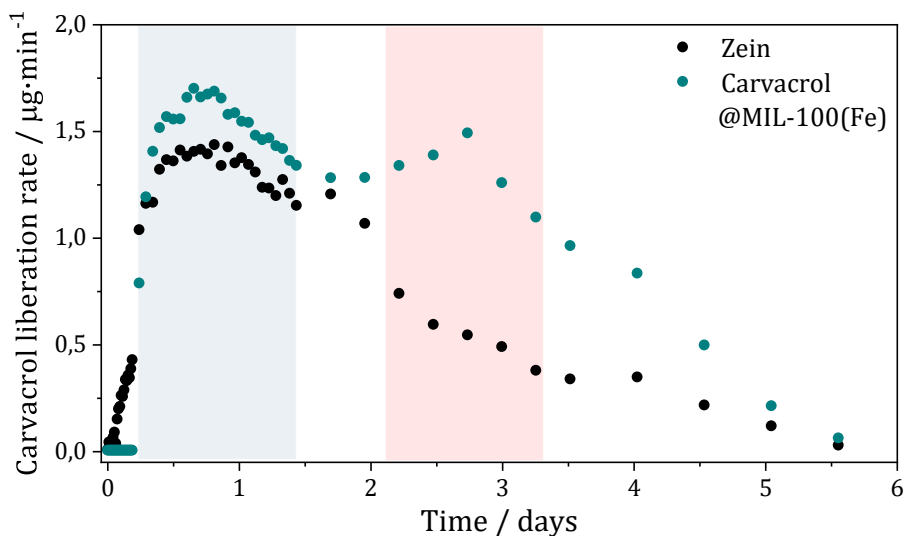


Figure 3.2.14. Relative cumulative release profiles ($\mu\text{g}\cdot\text{min}^{-1}$) in 1 g of zein film containing carvacrol@MIL-100(Fe) composite and 1 g of zein film containing the equivalent amount of free carvacrol.

3.2.5. Microbiology studies – Microatmosphere tests.

In view of the unique release profile evidenced in the carvacrol@MIL-100(Fe) composite when supported into zein polymeric films, its biocide capacity was investigated, also in collaboration with P. Hernández-Muñoz and R. Gavara. In particular, microbiology studies were conducted to determine the efficiency of the obtained composite against *E. coli* and *L. innocua* (as subrogate for *L. monocytogenes*). These different species have been selected considering the antibacterial mechanism of phenolic carvacrol molecules, which are known to interact with the lipid bilayer that constitute the cytoplasmic bacterium membrane, with the

subsequent increase of its permeability.³⁴ To analyse the antimicrobial effect of the volatile agent in the vapor phase, the microatmosphere method reported by Gavara and co-workers was employed.³⁵ This method consists on producing a bacterial background lawn on the surface of the agar and evaluate the inhibition effect of the vapor delivered from the film on the density of this lawn. Three dishes were seeded with each bacterium, one containing a film of the carvacrol@MIL-100(Fe) composite, the second containing a zein film with the same concentration of free carvacrol, and the third one as a control. It is important to note that a high concentration of bacteria (10^7 CFU·mL⁻¹, where CFU stands for colony-forming units) is needed in order to obtain an adequate bacterial lawn. The agar inoculated medium was then aseptically removed and homogenized to recover bacteria and count. The optimum time and incubation temperature allowed the microbial growth to reach 9 log in control samples.

Figures 3.2.15 and **3.2.16** reveal a clear reduction of the grass density occurring on the samples with carvacrol, corroborating the antimicrobial effect of the active films, an effect that is particularly more evident with the film containing the carvacrol@MIL-100(Fe) composite. **Table 3.2.5** summarizes the quantitative effects of the active films against *E. coli* and *L. innocua* bacteria. In case of *E. coli*, a clear Log Reduction Value (LRV) of 1.02 and 1.76 was respectively obtained for free and MOF-encapsulated carvacrol films, which translates into an 82 % increase in the carvacrol antimicrobial effect upon encapsulation into MIL-100(Fe). This effect was also evidenced in *L. innocua* bacteria, where free carvacrol was able to reach a CFU reduction of 0.40 whilst the CFU reduction of carvacrol@MIL-100(Fe) was 1.57, achieving a 93 % increase of antimicrobial effect as compared with the free carvacrol in the film. This effectiveness against *L. innocua* is particularly relevant provided the demonstrated reduced activity of carvacrol against Gram positive bacteria.⁴⁹

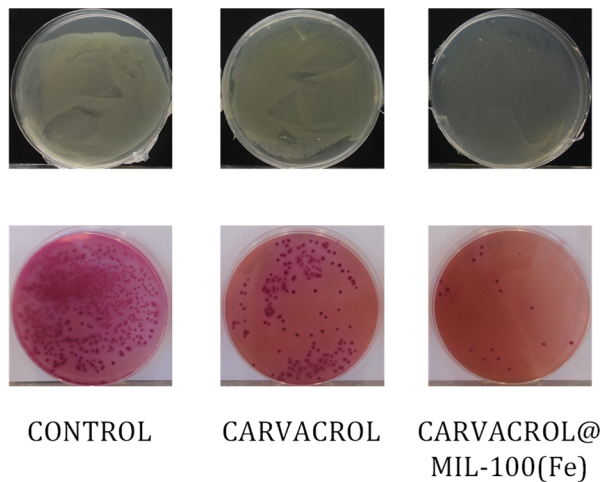


Figure 3.2.15. Images of the microatmosphere test carried out to determine the activity of films against *E. coli*: On the top, images of the Petri dishes showing the grass density generated by bacteria after the incubation for control (left), carvacrol film (middle) and carvacrol@MIL-100(Fe) containing film (right). On the bottom, images of the Petri dishes with Brilliant green agar after the 5th decimal dilution.

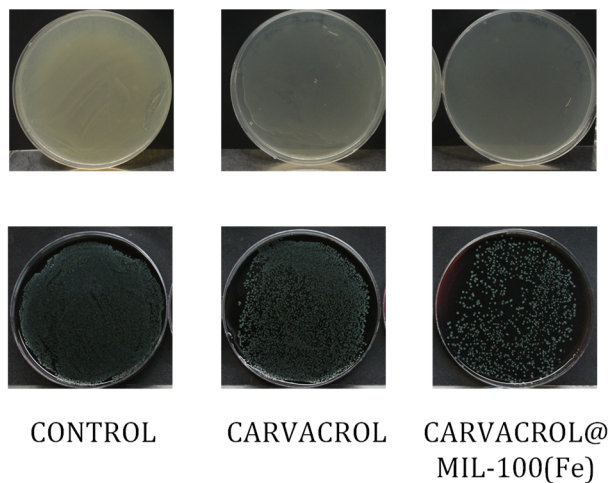


Figure 3.2.16. Images of the microatmosphere test carried out to determine the activity of films against *L. innocua*: On the top, images of the Petri dishes showing the grass density generated by bacteria after the incubation for control (left), carvacrol film (middle) and carvacrol@MIL-100(Fe) containing film (right). On the bottom, images of the Petri dishes with Palcam agar after the 3rd decimal dilution.

Table 3.2.5. Antimicrobial activity of films (80 mm diameter surface) against *E. coli* and *L. innocua*. Data are showed as log (colony forming units·mL⁻¹) and log reduction value (LRV) observed after incubation in Petri dishes without film (control), free carvacrol film and carvacrol@MIL-100 (Fe) composite.

Sample	<i>E. coli</i>	LRV	<i>L. innocua</i>	LRV
Control	9.04 ± 0.12		9.21 ± 0.15	
Free carvacrol film	8.02 ± 0.21	1.02	8.81 ± 0.14	0.40
Carvacrol@MIL-100(Fe) composite film	7.28 ± 0.11	1.76	7.64 ± 0.87	1.57

This greater antibacterial effect observed in the film with encapsulated carvacrol is potentially bounded to two significant effects: i) a larger content of carvacrol and ii) the different release from the film in the composite material. The first effect matches with the fact that, despite initially incorporating an equivalent carvacrol amount in the control and composite samples, the final content of carvacrol was *ca.* 20 % greater in the carvacrol@MIL-100(Fe) film. This carvacrol difference may be produced during film drying, which highlights the capacity of the nanoMOF to retain the carvacrol molecules. It should be also noticed that the Petri dish is not a hermetic container since bacteria need to breath. Under these conditions, different carvacrol losses through the openings between dish and lid and by scalping on the dish matrix (made of polystyrene) may also contribute to some extent to differences in the final content of carvacrol. Considering the other effect of different release, a fast release is observed in the samples with free carvacrol, with an initial high concentration of carvacrol that rapidly decreases. On the contrary, encapsulated carvacrol@MIL-100(Fe) retains carvacrol up to 5 h and then releases it at a slower pace, providing a sustained antibacterial effect along the assay period. This effect constitutes an advantage over other carriers, since the abrupt initial release of active

molecule in the first hours may not be required under specific uses such in fresh product preservation, provided that bacterial growth has not started yet. Both properties, larger carvacrol content and delayed sustained release are unique characteristics of the obtained carvacrol@MIL-100(Fe) composite that result in a more efficient antimicrobial effect of carvacrol against *E. coli* and *L. innocua*.

Lysozyme co-encapsulation. To further enhance the antimicrobial activity of the carvacrol@MIL-100(Fe) composite, a co-encapsulation strategy was carried out employing lysozyme as a bactericide agent. Lysozyme, an enzyme obtained from hen egg white, has bacteriolytic and bactericidal activities, mainly against Gram-positive bacteria. Lysozyme is typically integrated in antimicrobial films for food conservation.^{36,37} For this study, a general *in situ* strategy to form protein@MIL-100(Fe) biocomposites previously reported by Cases and co-workers was employed,³⁸ obtaining ly/MIL-100(Fe) composites as the carvacrol carrier agent. The incorporation of ly/carcvacrol@MIL-100(Fe) into the polymeric films was carried out following a similar extrusion protocol as the one employed with carvacrol@MIL-100(Fe) composites.

The activity of the films was tested in 10 mL of MHB liquid medium against microorganisms in exponential phase (10^5 CFU·mL⁻¹). Two films containing different ly/carcvacrol@MIL-100(Fe) loadings – 0.15 and 0.25 g – were tested. As summarized in **Figure 3.2.17** and **Table 3.2.6**, all the films containing either carvacrol@MIL-100(Fe) or lys/carcvacrol@MIL-100(Fe) materials reduce the *L. innocua* growth in approximately 1 log, independently of the film quantity employed. For *E. coli*, a greater efficiency is observed when both antimicrobial agents are combined, and a larger amount of film is employed. However, it can be concluded that these

differences are not significant enough to justify the co-encapsulation approach.

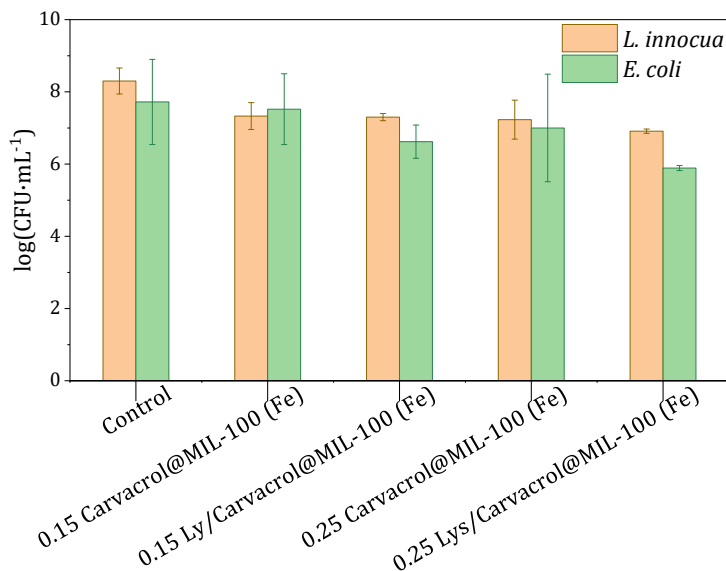


Figure 3.2.17. Antimicrobial activity of active films against *E. coli* and *L. innocua* after incubation in Petri dishes without film (control), containing 0.15 g of carvacrol@MIL-100 (Fe) or ly/carcvacrol@MIL-100(Fe) within the film, and containing 0.25 g of carvacrol@MIL-100 (Fe) or ly/carcvacrol@MIL-100 (Fe) composites.

Table 3.2.6. Antimicrobial activity of films (80 mm diameter surface) against *E. coli* and *L. innocua*. Data are showed as log (colony forming units·mL⁻¹) and log reduction value (LRV) observed after incubation in Petri dishes without film (control), with 0.15 g of carvacrol@MIL-100(Fe) or ly/carcvacrol@MIL-100(Fe) film, and with 0.25 g of carvacrol@MIL-100(Fe) or ly/carcvacrol@MIL-100(Fe) composites.

Sample	<i>E. coli</i>	LRV	<i>L. innocua</i>	LRV
Control	7.72 ± 1.18		8.30 ± 0.36	
0.15 Carvacrol@MIL-100(Fe)	7.52 ± 0.98	0.20	7.33 ± 0.37	0.97
0.15 Ly/Carvacrol@MIL-100(Fe)	6.62 ± 0.46	1.11	7.30 ± 0.10	0.99
0.25 Carvacrol@MIL-100(Fe)	7.00 ± 1.49	0.73	7.23 ± 0.54	1.07
0.25 Ly/Carvacrol@MIL-100(Fe)	5.89 ± 0.07	1.83	6.91 ± 0.06	1.38

3.2.5. Cell viability studies

Cell viability studies were performed by our group to study the cellular toxicity after prolonged exposure to carvacrol@MIL-100(Fe) composite. HEK293 human embryonic kidney cells were used in these cell viability assays at concentrations up to $200 \mu\text{g}\cdot\text{mL}^{-1}$ (**Figure 3.2.18**). As expected, the use of free carvacrol reduces cell viability by 40% at concentrations of $200 \mu\text{g}\cdot\text{mL}^{-1}$, which is consistent with reported data showcasing cellular death if carvacrol concentration surpasses $100 \mu\text{g}\cdot\text{mL}^{-1}$.³⁹ On the contrary, carvacrol@MIL-100(Fe) exhibits biocompatibility over a significantly wider range, observing that 100% of the cells were viable after exposure of carvacrol@MIL-100(Fe) containing a $200 \mu\text{g}\cdot\text{mL}^{-1}$ equivalent carvacrol amount for 24h. Thus, the obtained biocomposite exerts a protective effect as compared with free carvacrol due to its ability to retain the carvacrol molecules, and therefore preventing o exert their associated toxicity.

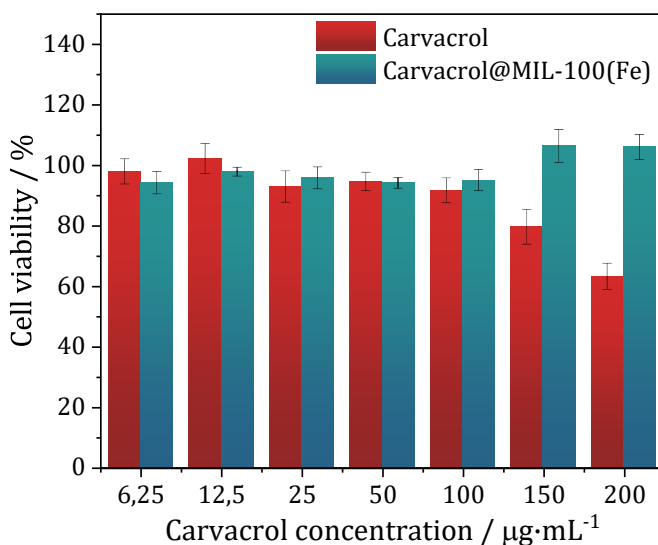


Figure 3.2.18. Cell viability of HEK293 cells in contact with free carvacrol (red) and carvacrol@MIL-100(Fe) biocomposite (green) at carvacrol concentrations between 6.25 and $200 \mu\text{g}\cdot\text{mL}^{-1}$ for 24 h. The percent viable cells were calculated in comparison to untreated cells taken as 100%.

3.3. Summary and conclusions

In this Chapter 3, a carvacrol@MIL-100(Fe) biocompatible composite containing considerable payloads of active agent was prepared following a direct impregnation method. In addition to provide chemical stability to the active molecule, MIL-100(Fe) scaffold endorses an unprecedented retained and remarkable sustained delivery of the antimicrobial agent when processed in polymeric biofilms, because of its unique redox responsiveness that promotes effective interactions with the active agent.

Mossbauer spectroscopy supported by theoretical calculations revealed a successful reversible interaction of the carvacrol molecules with the redox-active MIL-100(Fe) scaffold, thus enabling a prolonged delivery. The released carvacrol dose was enough to fight bacterial pathogens, with an improved activity against *E. Coli* and *L. innocua* in comparison with an equivalent “free” carvacrol dosage.

The combination of a direct preparation, the facile processing and the scaffold-mediated delivery performance that enables prolonged carvacrol bactericide activity, make the obtained carvacrol@MIL-100(Fe) composite a promising candidate for food packaging applications.

3.4. Methods

Synthesis of MIL-100(Fe) nanoparticles. As previously discussed in Chapter 2 of this Thesis, MIL-100(Fe) nanoparticles were synthesized following the procedure described by García Márquez and coworkers,³² by a microwave-assisted method. The as-synthesized material was treated in a KF 0.1 M solution for 2 h and washed with H₂O to remove excess of reagents. The particles were collected by centrifugation (9900 rpm, 20 min, room temperature) and stored.

Preparation of carvacrol@MIL-100(Fe) composite material. Composite carvacrol@MIL-100(Fe) material was obtained following a direct impregnation method. 23 mL from a 10 mg·mL⁻¹ carvacrol emulsion prepared in a H₂O:EtOH (4:1) mixture was directly added to MIL-100(Fe) nanoparticles (weighted humid and corresponding to 200 mg of dried MOF). After 5 days stirring in a 360° rotating shaker, the carvacrol@MIL-100(Fe) material was retrieved by centrifugation (10000 rpm, 20 min, room temperature) and dried at air overnight resulting in a dark-brown powder.

Synthesis of ly/carcacrol@MIL-100(Fe) Biocomposites. The synthesis of ly/MIL-100(Fe) biocomposite followed the *in situ* biocompatible procedure developed previously by our group.³⁸ In a general procedure, a 12 mL aqueous solution of Fe^{III} chloride (40 mM) and Fe^{II} chloride (40 mM) and 12 mL of a benzene 1,3,5-tricarboxylic acid (40 mM) buffered aqueous solution (Tris 200 mM, pH 7.5) were simultaneously added at a constant rate of 12 mL·h⁻¹ to 24 mg of lysozyme dissolved in 20 mL of water. Biocomposite formation was immediately initiated upon the addition of both solutions and detected by the formation of suspended particles. Reaction completion was achieved in 1 h and the particles were collected by centrifugation (5000 rpm, 2 min, room temperature) and washed two times with water (9000 rpm, 5

min, room temperature) to obtain the ly/MIL-100(Fe) composite. After the washing protocol, carvacrol encapsulation in ly/MIL-100(Fe) was carried out following the same impregnation method described for MIL-100(Fe) nanoparticles.

Carvacrol quantification. Carvacrol content in the obtained composites was determined by thermic desorption Gas Chromatography, using a HP 7890B equipped with a HP5 column of 30 m, 320 μm of diameter and 0.25 μm of thickness. The thermic gradient employed was: 40 $^{\circ}\text{C}$ (3 min), 10 $^{\circ}\text{C}\cdot\text{min}^{-1}$ ramp until 200 $^{\circ}\text{C}$ and 15 min isotherm. Injector heats on ballistic ramp ($600\text{ }^{\circ}\text{C}\cdot\text{min}^{-1}$) from 40 to 200 $^{\circ}\text{C}$ and 4 min isotherm.

Characterization of carvacrol@MIL-100(Fe) composite material. Scanning electron microscopy images were acquired using a Hitachi S4800 microscope. For transmission electron microscopy, a JEM 1010 (JEOL) microscope was employed. X-ray powder diffraction experiments were acquired in an X-ray diffractometer (PANalytical Empyrean) with copper as a radiation source ($\text{Cu-K}\alpha$, 1.5418 \AA). Infrared spectroscopy spectra were registered employing an ALPHA II FTIR spectrometer (Bruker). Mössbauer spectra were collected using a conventional constant acceleration spectrometer and a ^{57}Co (Rh) source. The velocity scale was calibrated with an α -Fe foil. Low-temperature measurements were performed with the samples immersed in He exchange gas in a bath cryostat. The spectra were fitted to distributions of quadrupole doublets according to the histogram method.⁴⁰ Electron paramagnetic resonance spectra were recorded with a Bruker ELEXYS E580 spectrometer operating in the X-band (9.47 GHz). Sweep width 4960.0 G, time constant 2.56 ms, modulation frequency 100 kHz, modulation width 1 G, microwave power 19.82 mW.

Preparation of polymeric films. Two zein films were prepared from an 80 % hydroalcoholic solution containing 15 % weight of zein. Two fractions were separated: to the first one 0.125 g Carvacrol@MIL-100(Fe) composite was added per g of zein, whereas the corresponding amount of free carvacrol was directly added in a concentration of 0.05 g·g⁻¹ zein to the second fraction. The mixtures were spread on a flat surface of PTFE using a 200 µm coating rod and dried in an open oven at 75 °C for 10 min. The films obtained were stored in PP/met envelopes until further characterisation. The residual content of carvacrol in both films was analysed. For this, samples were cut from both films, introduced into a micro vial, and tested by thermal desorption and gas chromatography obtaining a final concentration of carvacrol of 0.059 ± 0.008 g·g⁻¹ in the encapsulated film and 0.050 ± 0.001 g·g⁻¹ in the film with pure carvacrol.

Evaluation of carvacrol release from the films. Relative cumulative release profiles were measured by monitoring the carvacrol release from the polymeric films at 23 ± 1 °C and 95 ± 3 % RH (simulating the exposure to fresh food). A piece sample of film was placed on a desorption tube where a humid 15 mL·min⁻¹ stream of He hauled the released product to a gas chromatograph. The carvacrol release flow was determined using a HP5890 gas chromatograph with a 200-µL automatic injection valve and a HP5 column of 30 m, 320 µm of diameter and 0.25 µm of thickness. Thermal conditions were: 80 °C at the injection valve, 200 °C at the injection port, 220 °C at the flame ionization detector, and 100 °C at the column oven. Film samples were exposed to high humidity conditions with a He stream that.

Antimicrobial Properties of the Films. Bacterial strain *Escherichia coli* CECT 434 (ATCC 25922) and *Listeria innocua* CECT 910 (ATCC 33090), as surrogate strain for *Listeria monocytogenes*, were obtained from the Spanish Type Culture Collection (Valencia, Spain). These strains were chosen because of its relevance in Food Industry as a Gram-negative and Gram-positive model, respectively. They were stored in liquid medium Tryptone Soy Broth (TSB) supplied from Scharlab (Barcelona, Spain) with 20 % glycerol at $-80\text{ }^{\circ}\text{C}$ until needed. The stock cultures were maintained by periodic subculture on agar Tryptone Soy Agar (TSA) from Scharlab (Barcelona, Spain) slants at $4\text{ }^{\circ}\text{C}$ and transferred monthly. To test antimicrobial effect of active films, the microatmosphere method, in which the volatile active compound released from the film to the headspace of the Petri dish interacts with the microorganisms, was carried out. In this method, $100\text{ }\mu\text{L}$ of a bacteria suspension containing approximately 10^7 colony forming units (CFU)·mL⁻¹ were spread over the 15 mL of TSA surface, and a disk of the antimicrobial films (80 mm in diameter) was adhered to the lid of the Petri dish, without direct contact with the microorganism, sealed with Parafilm and incubated at $37\text{ }^{\circ}\text{C}$ for 24 – 48 h. After the incubation period, the diameter of the resulting inhibition zone in the bacterial growth was measured.³⁵ Controls without films and control films with free carvacrol were also tested. Finally, the inoculated Petri dishes were employed to count the colony forming units (CFU) and log reduction value (LRV). For that, agar medium was aseptically removed from the Petri dishes and homogenized in a sterile BagPage with 100 mL of peptone water for 2 min with a Stomacher. Serial dilutions were made with peptone water and plated in Petri dishes with 15 mL of selective agar medium: Brilliant Green agar for *E. coli* and supplemented Palcam agar for *L. innocua* respectively, (Scharlab, Barcelona, Spain). Plates were incubated at $37\text{ }^{\circ}\text{C}$ for 24 – 48 h. Results were expressed as log CFU·mL⁻¹. LRV was calculated by comparison between control sample

and samples with film ($LRV = (\text{Control log CFU}\cdot\text{mL}^{-1}) - (\text{Film log CFU}\cdot\text{mL}^{-1})$). The experiments were carried out in triplicate.

Cell culture. HEK293 human embryonic kidney cells were obtained from the American Type Culture Collection (ATCC), cultured in DMEM supplemented with 10 % Fetal Bovine Serum (FBS, Gibco), 1 % penicillin/streptomycin (Sigma) and 0.1 % Amphotericin B (Gibco) and maintained in 20 % O₂ and 5 % CO₂ at 37 °C. Cells were routinely tested for Mycoplasma using the universal mycoplasma detection kit (ATCC).

Cell viability studies. HEK293 cells were plated in a 96-well plate (8,000 and 20,000 cells per well, respectively) and allowed to adhere to the wells. At 24 h post-seeding, the cells were incubated with varying concentrations of carvacrol and carvacrol@MIL-100(Fe) for 24 h. Cell viability was evaluated using the CellTiter 96® Aqueous One Solution Cell Proliferation Assay (Promega). Absorbance was recorded at 450 and 570 nm 1 hour later with a 96-well plate reader (Thermo Forma Fisher, Multiscan).

Computational Details. Theoretical calculations were performed under the density functional theory (DFT) framework by means of the Gaussian-16.A03 suite of programs.⁴¹ Minimum-energy geometry structures were obtained upon atom relaxation at the B3LYP/6-31G(d,p) level of theory^{42,43} including dispersion corrections by means of the Grimme's D3 (Becke-Johnson damping function) protocol.^{44,45} To maintain the topology of the cluster models as in the corresponding MOF, the terminal hydrogen atoms were frozen during the optimization procedure. Non-covalent interaction (NCI) surfaces were obtained under the NCIPLOT-3.0 program⁴⁶ and visualized through the VMD software⁴⁷ with standard thresholds of 0.3 and 0.04 a.u. for the reduced density gradient and density, respectively. Time-

dependent DFT calculations were performed on the lowest-lying singlet excited states at the B3LYP/6-31G(d,p) level. Charge analysis was performed through the natural bond order (NBO) approach by means of the NBO version 3 as implemented in Gaussian-16.A03. Spin density contours were plotted through the Chemcraft software.⁴⁸

3.5. Supporting Information

Theoretical calculations

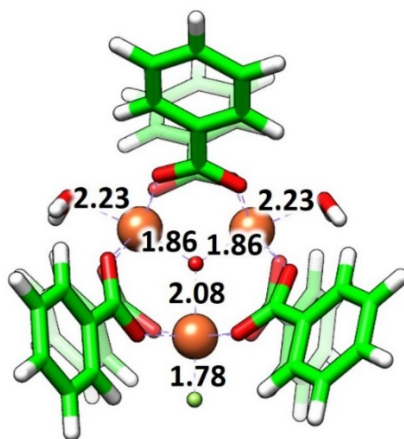


Figure S3.1. Minimum-energy structure calculated at the B3LYP-D3/6-31G(d,p) level of theory for the oxo-centered tri-metallic cluster of MIL-100(Fe) in a high-spin configuration for iron atoms. Relevant coordination distances are indicated in Å.

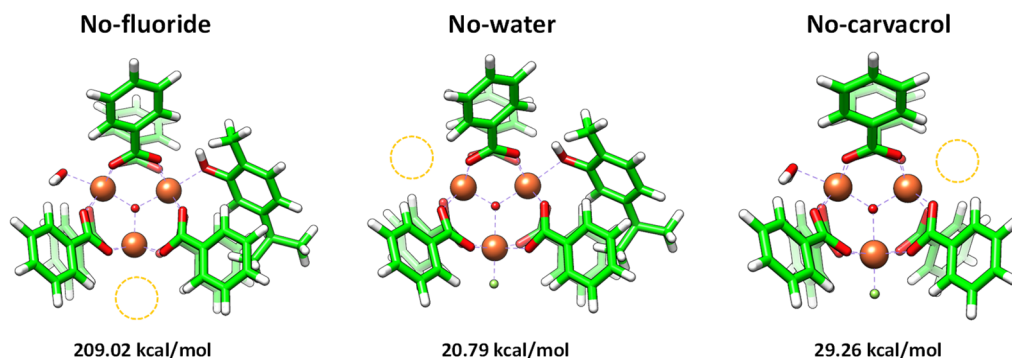


Figure S3.2: Top: Energy required to detach a coordinated fluoride, water and carvacrol moiety from the tri-metallic cluster model of MIL-100(Fe) at the B3LYP-D3/6-31G(d,p) level.

The minimum-energy structure of the oxo-centred trimetallic cluster indicates that the hydroxy group of carvacrol effectively coordinates with an Fe^{III} atom, displaying a small interatomic distance of 2.29 Å (**Figure S3.3a**), similar to that calculated for a coordinating water molecule (2.25 Å).

Non-covalent index (NCI) surfaces evidence a large number of weak but stabilizing dispersion interactions between the carvacrol moiety and the benzoate units of the cluster (green surfaces in **Figure S3.3b**), whereas the strong coordination bond between the hydroxy group of carvacrol and one Fe^{III} is revealed as a localized bluish NCI surface (**Figure S3.3b** inset and **Figure S3.4**).

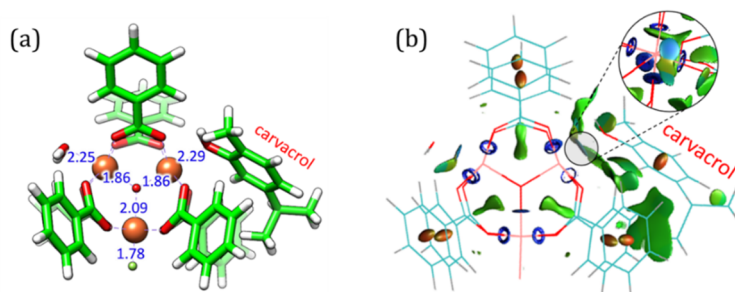


Figure S3.3. (a) Minimum-energy structure for the representative cluster of MIL-100(Fe) upon carvacrol inclusion. Relevant coordination distances are indicated in Å. Colour coding: C in green, O in red, H in white and Fe in orange. (b) Non-covalent index (NCI) surface showing the large amount of dispersion interactions that stabilize the chemisorption of carvacrol into the MIL-100(Fe) cluster.

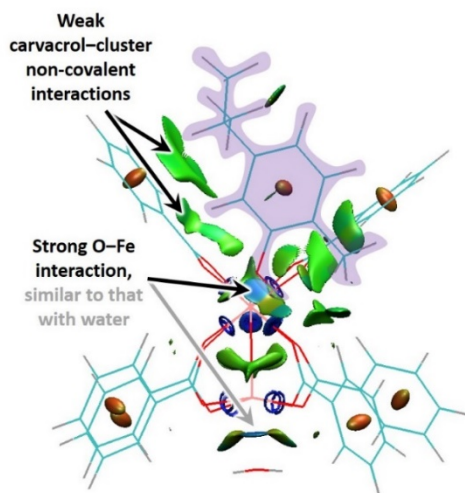


Figure S3.4. Non-covalent interaction (NCI) surfaces calculated for the trimetallic cluster model upon carvacrol coordination. Green surfaces indicate weak non-covalent interactions whereas bluish surfaces represent stronger coordinative bonds.

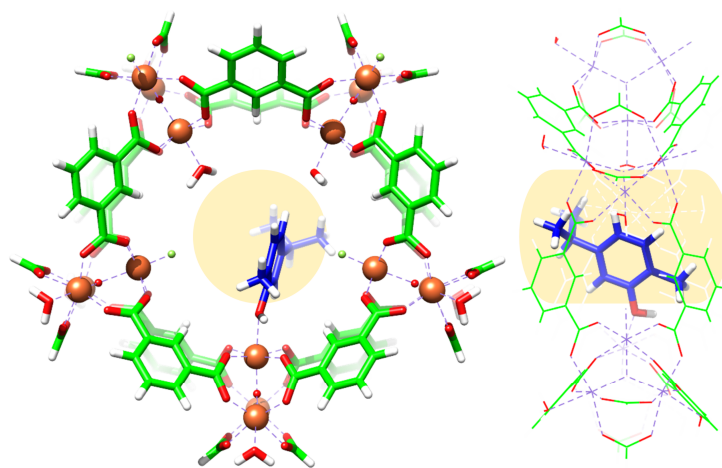


Figure S3.5. Front (left) and side (right) views of the minimum-energy structure calculated for the MIL-100(Fe) pentagonal window upon carvacrol complexation. Carvacrol carbon atoms are coloured in blue for better viewing. The window gate is calculated with a diameter of 5.5 Å and coloured in light yellow.

NCI surfaces confirm the presence of a large number of noncovalent interactions between the carvacrol molecule and the framework, along with a strong, localized interaction corresponding to the coordination bond with Fe^{III} (**Figure S3.6**). Note that the pentagonal pore gate is predicted with a diameter of 5.5 Å, which nicely fits the carvacrol size of 5.0 Å calculated without considering the hydroxy group (see light yellow region in **Figure S3.5**). The hexagonal pore gate, which is of about 8.6 Å, is therefore expected to bear and diffuse the carvacrol along the framework easily.

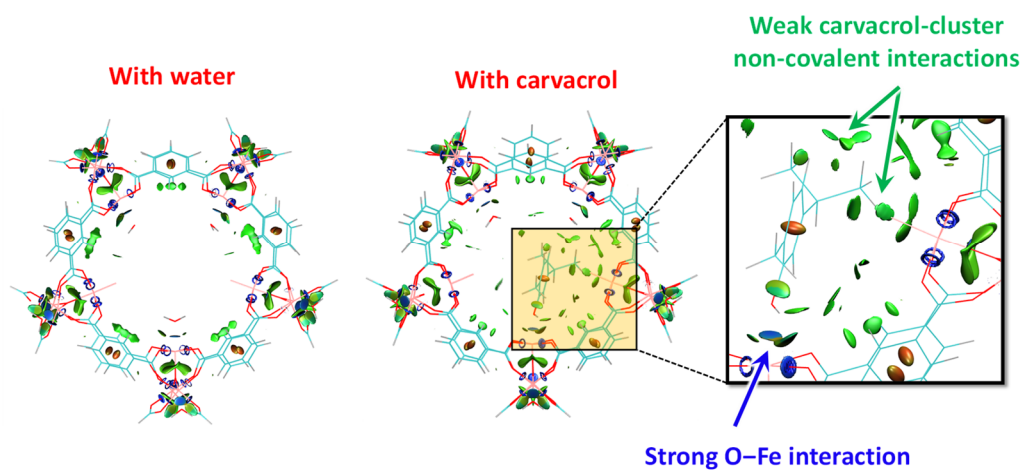


Figure S3.6. Non-covalent interaction (NCI) surfaces calculated for the pentagonal gate window model with coordination of water (left) and carvacrol (right).

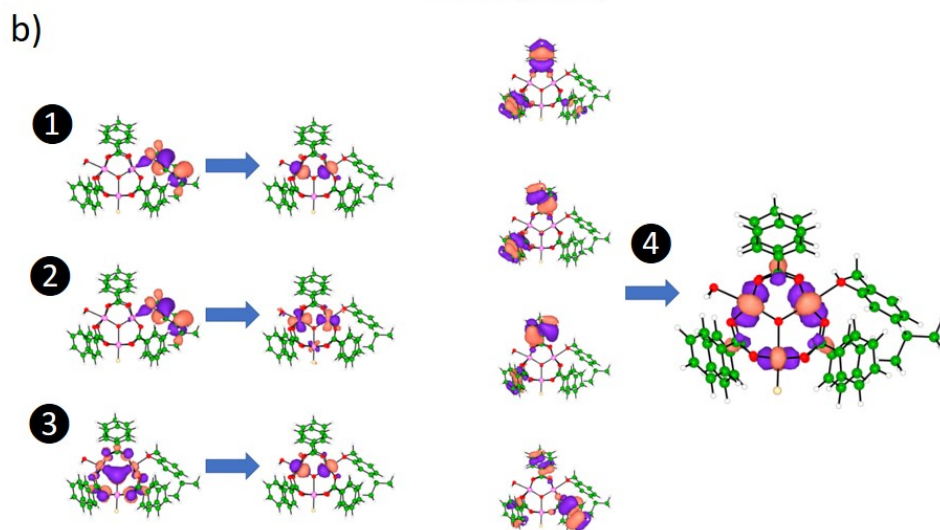
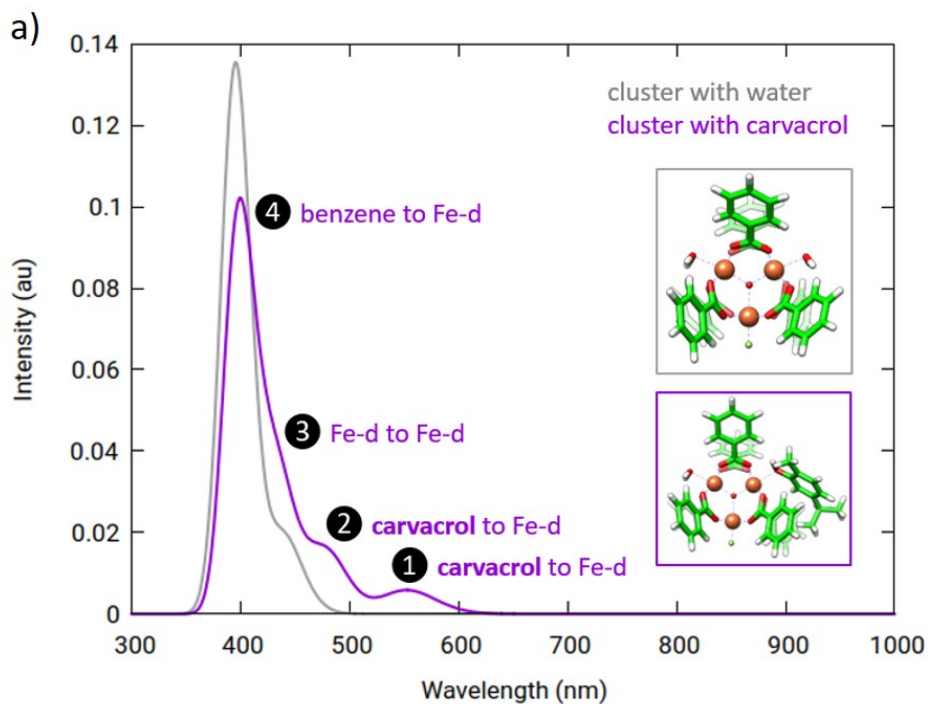


Figure S3.7. (a) Time-dependent DFT absorption spectra calculated for the tri-metallic cluster model with water (gray) and carvacrol (purple) coordination. (b) Monoenergetic excitations that describe the most relevant singlet excited states giving shape to the absorption spectrum of carvacrol@MIL-100(Fe) cluster system.

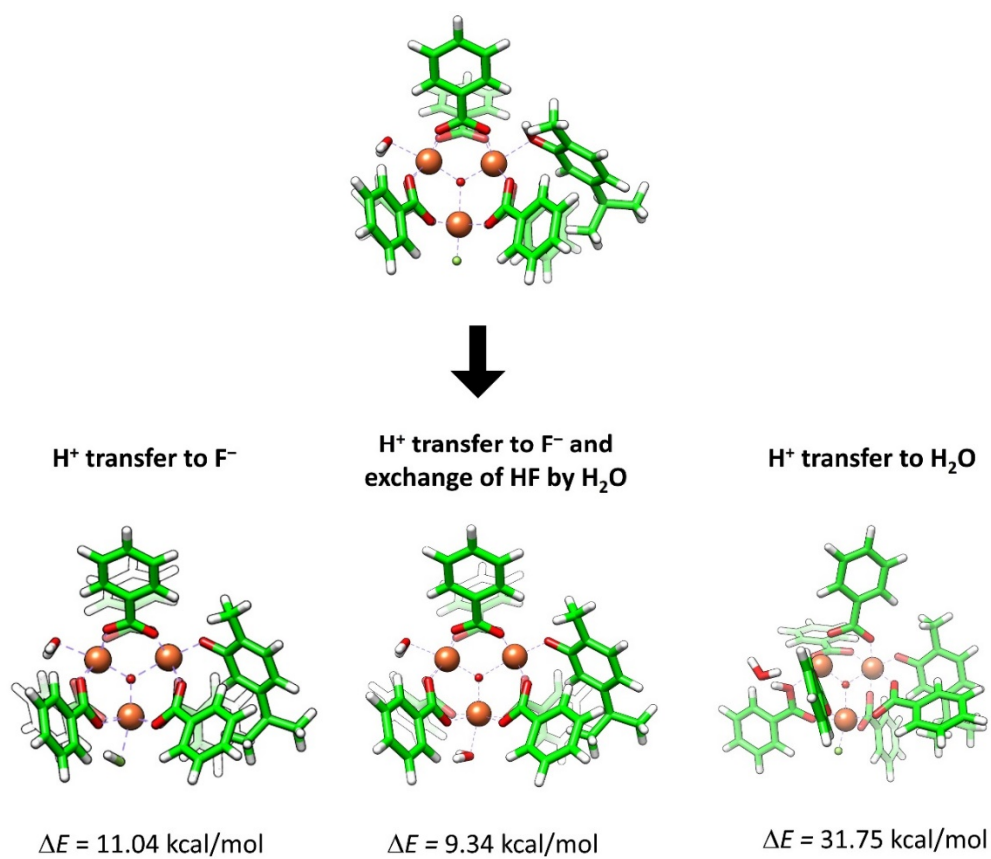


Figure S3.8. Energy penalty for the proton transfer from the hydroxy group of carvacrol to fluoride, to fluoride plus water exchange, or to water.

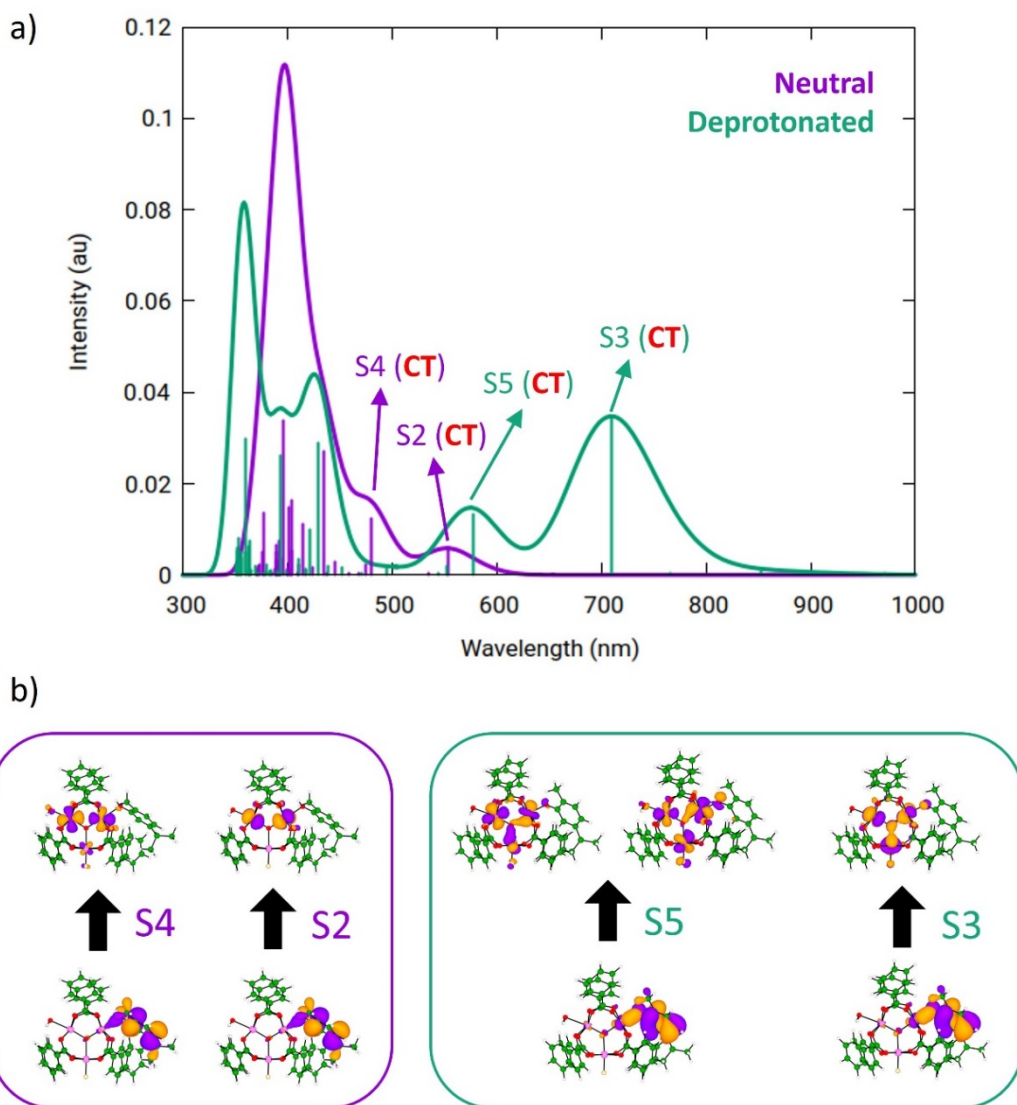


Figure S3.9. (a) Time-dependent DFT absorption spectra calculated for the carvacrol@MIL-100(Fe) cluster model with neutral protonated carvacrol (purple) and deprotonated carvacrol (green). (b) Monoexcited singlet excited states giving shape to the absorption spectra for neutral (left) and deprotonated (right) carvacrol.

3.6. References

- (1) Tubiello, F. N.; Karl, K.; Flammini, A.; Gütschow, J.; Obli-Laryea, G.; Conchedda, G.; Pan, X.; Qi, S. Y.; Halldórudóttir Heiðarsdóttir, H.; Wanner, N.; et al. Pre- and Post-Production Processes Increasingly Dominate Greenhouse Gas Emissions from Agri-Food Systems. *Earth Syst. Sci. Data* **2022**, *14* (4), 1795–1809.
- (2) Khalid, M. Y.; Arif, Z. U. Novel Biopolymer-Based Sustainable Composites for Food Packaging Applications: A Narrative Review. *Food Packag. Shelf Life* **2022**, *33* (April), 100892.
- (3) Espitia, P. J. P.; Du, W. X.; Avena-Bustillos, R. de J.; Soares, N. de F. F.; McHugh, T. H. Edible Films from Pectin: Physical-Mechanical and Antimicrobial Properties - A Review. *Food Hydrocoll.* **2014**, *35*, 287–296.
- (4) Kashiri, M.; Cerisuelo, J. P.; Domínguez, I.; López-Carballo, G.; Muriel-Gallet, V.; Gavara, R.; Hernández-Muñoz, P. Zein Films and Coatings as Carriers and Release Systems of Zataria Multiflora Boiss. Essential Oil for Antimicrobial Food Packaging. *Food Hydrocoll.* **2017**, *70*, 260–268.
- (5) Tortorella, S.; Maturi, M.; Vetri Buratti, V.; Vozzolo, G.; Locatelli, E.; Sambri, L.; Comes Franchini, M. Zein as a Versatile Biopolymer: Different Shapes for Different Biomedical Applications. *RSC Adv.* **2021**, *11* (62), 39004–39026.
- (6) Altan, A.; Çayır, Ö. Encapsulation of Carvacrol into Ultrafine Fibrous Zein Films via Electrospinning for Active Packaging. *Food Packag. Shelf Life* **2020**, *26* (January).
- (7) Arcan, I.; Yemencioğlu, A. Development of Flexible Zein-Wax Composite and Zein-Fatty Acid Blend Films for Controlled Release of Lysozyme. *Food Res. Int.* **2013**, *51* (1), 208–216.
- (8) Aragón-Gutiérrez, A.; Heras-Mozos, R.; Montesinos, A.; Gallur, M.; López, D.; Gavara, R.; Hernández-Muñoz, P. Pilot-Scale Processing and Functional Properties of Antifungal EVOH-Based Films Containing Methyl Anthranilate Intended for Food Packaging Applications. *Polymers (Basel)*. **2022**, *14* (16).
- (9) Ribeiro-Santos, R.; Andrade, M.; Melo, N. R. de; Sanches-Silva, A. Use of Essential Oils in Active Food Packaging: Recent Advances and Future Trends. *Trends Food Sci. Technol.* **2017**, *61*, 132–140.

- (10) Acevedo-Fani, A.; Salvia-Trujillo, L.; Rojas-Graü, M. A.; Martín-Belloso, O. Edible Films from Essential-Oil-Loaded Nanoemulsions: Physicochemical Characterization and Antimicrobial Properties. *Food Hydrocoll.* **2015**, *47*, 168–177.
- (11) Neira, L. M.; Martucci, J. F.; Stejskal, N.; Ruseckaite, R. A. Time-Dependent Evolution of Properties of Fish Gelatin Edible Films Enriched with Carvacrol during Storage. *Food Hydrocoll.* **2019**, *94* (November 2018), 304–310.
- (12) Zanetti, M.; Carniel, T. K.; Dalcanton, F.; dos Anjos, R. S.; Gracher Riella, H.; de Araújo, P. H. H.; de Oliveira, D.; Antônio Fiori, M. Use of Encapsulated Natural Compounds as Antimicrobial Additives in Food Packaging: A Brief Review. *Trends Food Sci. Technol.* **2018**, *81* (May 2017), 51–60.
- (13) López, P.; Sánchez, C.; Batlle, R.; Nerín, C. Vapor-Phase Activities of Cinnamon, Thyme, and Oregano Essential Oils and Key Constituents against Foodborne Microorganisms. *J. Agric. Food Chem.* **2007**, *55* (11), 4348–4356.
- (14) Tao, R.; Sedman, J.; Ismail, A. Characterization and in Vitro Antimicrobial Study of Soy Protein Isolate Films Incorporating Carvacrol. *Food Hydrocoll.* **2022**, *122* (April 2021), 107091.
- (15) Fernández-Pan, I.; Maté, J. I.; Gardrat, C.; Coma, V. Effect of Chitosan Molecular Weight on the Antimicrobial Activity and Release Rate of Carvacrol-Enriched Films. *Food Hydrocoll.* **2015**, *51*, 60–68.
- (16) Buendía-Moreno, L.; Soto-Jover, S.; Ros-Chumillas, M.; Antolinos, V.; Navarro-Segura, L.; Sánchez-Martínez, M. J.; Martínez-Hernández, G. B.; López-Gómez, A. Innovative Cardboard Active Packaging with a Coating Including Encapsulated Essential Oils to Extend Cherry Tomato Shelf Life. *Lwt* **2019**, *116* (September), 108584.
- (17) Tampau, A.; González-Martínez, C.; Chiralt, A. Release Kinetics and Antimicrobial Properties of Carvacrol Encapsulated in Electrospun Poly-(ϵ -Caprolactone) Nanofibres. Application in Starch Multilayer Films. *Food Hydrocoll.* **2018**, *79*, 158–169.
- (18) Tastan, Ö.; Ferrari, G.; Baysal, T.; Donsì, F. Understanding the Effect of Formulation on Functionality of Modified Chitosan Films Containing Carvacrol Nanoemulsions. *Food Hydrocoll.* **2016**, *61*, 756–771.

- (19) Monteagudo-Olivan, R.; Cocero, M. J.; Coronas, J.; Rodríguez-Rojo, S. Supercritical CO₂ Encapsulation of Bioactive Molecules in Carboxylate Based MOFs. *J. CO₂ Util.* **2019**, *30* (December 2018), 38–47.
- (20) Maryam, K.; Shakeri, S.; Kiani, K. Preparation and in Vitro Investigation of Antigastric Cancer Activities of Carvacrol-Loaded Human Serum Albumin Nanoparticles. *IET Nanobiotechnology* **2015**, *9* (5), 294–299.
- (21) Keawchaon, L.; Yoksan, R. Preparation, Characterization and in Vitro Release Study of Carvacrol-Loaded Chitosan Nanoparticles. *Colloids Surfaces B Biointerfaces* **2011**, *84* (1), 163–171.
- (22) Iannitelli, A.; Grande, R.; di Stefano, A.; di Giulio, M.; Sozio, P.; Bessa, L. J.; Laserra, S.; Paolini, C.; Protasi, F.; Cellini, L. Potential Antibacterial Activity of Carvacrol-Loaded Poly(DL-Lactide-Co-Glycolide) (PLGA) Nanoparticles against Microbial Biofilm. *Int. J. Mol. Sci.* **2011**, *12* (8), 5039–5051.
- (23) Santos, E. H.; Kamimura, J. A.; Hill, L. E.; Gomes, C. L. Characterization of Carvacrol Beta-Cyclodextrin Inclusion Complexes as Delivery Systems for Antibacterial and Antioxidant Applications. *LWT - Food Sci. Technol.* **2015**, *60* (1), 583–592.
- (24) Gholijani, N.; Abolmaali, S.-S.; Kalantar, K.; Ravanrooy, M.-H. Therapeutic Effect of Carvacrol-Loaded Albumin Nanoparticles on Arthritic Rats. *Iran. J. Pharm. Res.* **2019**, *0* (January 2019), 312–320.
- (25) Shakeri, F.; Shakeri, S.; Hojjatoleslami, M. Preparation and Characterization of Carvacrol Loaded Polyhydroxybutyrate Nanoparticles by Nanoprecipitation and Dialysis Methods. *J. Food Sci.* **2014**, *79* (4), N697–N705.
- (26) Zhong, H.; Mu, B.; Zhang, M.; Hui, A.; Kang, Y.; Wang, A. Preparation of Effective Carvacrol/Attapulgit Hybrid Antibacterial Materials by Mechanical Milling. *J. Porous Mater.* **2020**, *27* (3), 843–853.
- (27) Yoon, J. W.; Seo, Y. K.; Hwang, Y. K.; Chang, J. S.; Leclerc, H.; Wuttke, S.; Bazin, P.; Vimont, A.; Daturi, M.; Bloch, E.; et al. Controlled Reducibility of a Metal-Organic Framework with Coordinatively Unsaturated Sites for Preferential Gas Sorption. *Angew. Chemie - Int. Ed.* **2010**, *49* (34), 5949–5952.

- (28) Leclerc, H.; Vimont, A.; Lavalley, J. C.; Daturi, M.; Wiersum, A. D.; Llwellyn, P. L.; Horcajada, P.; Férey, G.; Serre, C. Infrared Study of the Influence of Reducible Iron(III) Metal Sites on the Adsorption of CO, CO₂, Propane, Propene and Propyne in the Mesoporous Metal-Organic Framework MIL-100. *Phys. Chem. Chem. Phys.* **2011**, *13* (24), 11748–11756.
- (29) Greenwood, N.N., Gibb, T. C. *Mössbauer Spectroscopy*; Hall, C. and, Ed.; Ltd. Publishers: London, 1971.
- (30) Gavrilenko, K. S.; Vértes, A.; Vanko, G.; Kiss, L. F.; Addison, A. W.; Weyhermüller, T.; Pavlishchuk, V. V. Synthesis, Magnetochemistry, and Spectroscopy of Heterometallic Trinuclear Basic Trifluoroacetates [Fe₂M(μ₃-O)(CF₃COO)₆(H₂O)₃]·H₂O (M = Mn, Co, Ni). *Eur. J. Inorg. Chem.* **2002**, *6* (12), 3347–3355.
- (31) Ramos Silva, M.; Coutinho, J. T.; Pereira, L. C. J.; Martín-Ramos, P.; Waerenborgh, J. C. Synthesis, Structure and Physical Properties of a Low Dimensional Compound. *Spectrochim. Acta - Part A Mol. Biomol. Spectrosc.* **2017**, *172*, 9–13.
- (32) García Márquez, A.; Demessence, A.; Platero-Prats, A. E.; Heurtaux, D.; Horcajada, P.; Serre, C.; Chang, J. S.; Férey, G.; De La Peña-O’Shea, V. A.; Boissière, C.; et al. Green Microwave Synthesis of MIL-100(Al, Cr, Fe) Nanoparticles for Thin-Film Elaboration. *Eur. J. Inorg. Chem.* **2012**, *100* (32), 5165–5174.
- (33) Shukla, R.; Cheryan, M. Zein: The Industrial Protein from Corn. *Ind. Crops Prod.* **2001**, *13* (3), 171–192.
- (34) Muriel-Galet, V.; Cerisuelo, J. P.; López-Carballo, G.; Lara, M.; Gavara, R.; Hernández-Muñoz, P. Development of Antimicrobial Films for Microbiological Control of Packaged Salad. *Int. J. Food Microbiol.* **2012**, *157* (2), 195–201.
- (35) Higuera, L.; López-Carballo, G.; Gavara, R.; Hernández-Muñoz, P. Effect of Hydroxypropyl-β-Cyclodextrin and Coadjuvants on the Sorption Capacity of Hydrophilic Polymer Films for Monoterpene Alcohols. *Carbohydr. Polym.* **2016**, *151*, 1193–1202.
- (36) Bayarri, M.; Oulahal, N.; Degraeve, P.; Gharsallaoui, A. Properties of Lysozyme/Low Methoxyl (LM) Pectin Complexes for Antimicrobial Edible Food Packaging. *J. Food Eng.* **2014**, *131*, 18–25.

- (37) Zhang, W.; Rhim, J. W. Functional Edible Films/Coatings Integrated with Lactoperoxidase and Lysozyme and Their Application in Food Preservation. *Food Control* **2022**, *133* (PB), 108670.
- (38) Cases Díaz, J.; Lozano-Torres, B.; Giménez-Marqués, M. Boosting Protein Encapsulation through Lewis-Acid-Mediated Metal-Organic Framework Mineralization: Toward Effective Intracellular Delivery. *Chem. Mater.* **2022**, *34* (17), 7817–7827.
- (39) Kumari, P.; Mishra, R.; Arora, N.; Chatrath, A.; Gangwar, R.; Roy, P.; Prasad, R. Antifungal and Anti-Biofilm Activity of Essential Oil Active Components against *Cryptococcus Neoformans* and *Cryptococcus Laurentii*. *Front. Microbiol.* **2017**, *8* (NOV), 1–14.
- (40) Hesse, J.; Rubartsch, A. Model Independent Evaluation of Overlapped Mossbauer Spectra. *J. Phys. E.* **1974**, *7* (7), 526–532.
- (41) Gaussian 16, Revision A.03, M. J. Frisch, G. W. Trucks, H. B. Schlegel, G. E. Scuseria, M. A. Robb, J. R. Cheeseman, G. Scalmani, V. Barone, G. A.; Petersson, H. Nakatsuji, X. Li, M. Caricato, A. V. Marenich, J. Bloino, B. G. Janesko, R. Gomperts, B. Mennu, 20. Gaussian 16, Revision A.03. Gaussian, Inc.: Wallingford CT 2016.
- (42) Becke, A. D. Density-Functional Thermochemistry. III. The Role of Exact Exchange. *J. Chem. Phys.* **1993**, *98* (7), 5648–5652.
- (43) Rassolov, V. A.; Ratner, M. A.; Pople, J. A.; Redfern, P. C.; Curtiss, L. A. 6-31G* Basis Set for Third-Row Atoms. *J. Comput. Chem.* **2001**, *22* (9), 976–984.
- (44) Grimme, S.; Antony, J.; Ehrlich, S.; Krieg, H. A Consistent and Accurate Ab Initio Parametrization of Density Functional Dispersion Correction (DFT-D) for the 94 Elements H-Pu. *J. Chem. Phys.* **2010**, *132* (15), 154104.
- (45) Grimme, S.; Ehrlich, S.; Goerigk, L. Effect of the Damping Function in Dispersion Corrected Density Functional Theory. *J. Comput. Chem.* **2011**, *32*, 1456–1465.
- (46) Contreras-García, J.; Johnson, E. R.; Keinan, S.; Chaudret, R.; Piquemal, J. P.; Beratan, D. N.; Yang, W. NCIPLLOT: A Program for Plotting Noncovalent Interaction Regions. *J. Chem. Theory Comput.* **2011**, *7* (3), 625–632.
- (47) Humphrey, W.; Dalke, A.; Schulten, K. VMD: Visual Molecular Dynamics. *J. Mol. Graph.* **1996**, *14* (October 1995), 33–38.

- (48) Chemcraft - graphical software for visualization of quantum chemistry computations <https://www.chemcraftprog.com>.

CHAPTER 4

Synthesis and performances of fungicidal
ZIF-based biocomposites

4.1. Introduction

Fungal contamination in food leads to vast deterioration and a series of food safety problems. The effects of these microorganisms are related to cell growth, which can produce toxic secondary metabolites (mycotoxins), that besides the toxic effects, frequently have degenerative, toxinogenic, or carcinogenic effects. Fungi can also produce coloration or black points, not accepted for most consumers.¹

The difficulty of controlling these undesirable fungi, as well as the growing interest of the consumers by natural products has been forcing the industry to find new alternatives for food conservation. The antifungal potential of EOs has been reported widely.^{2,3} Scientific research regarding the mode of action of EOs on fungal spores and mycelial cells are very scarce, unlike bacteria. However, since a fungal cell has a true nucleus, internal cell structures, and a cell wall (**Figure 4.1.1**), the mode of action of EOs on fungal spores should be analogous to bacterial cells described in section 2.1.1 of this Thesis.

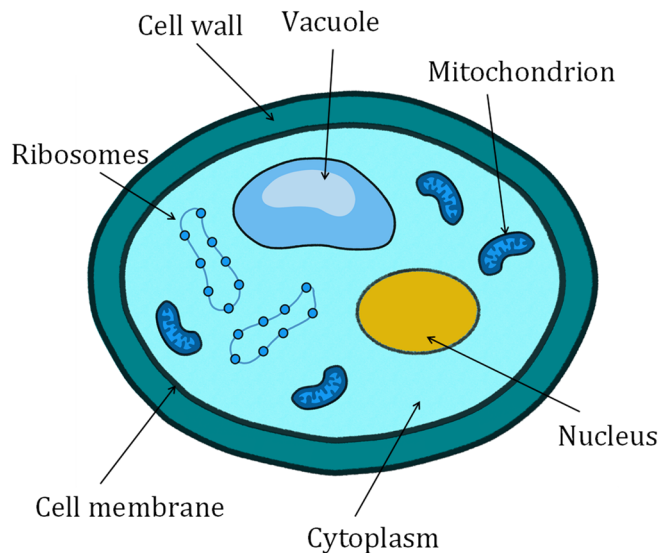


Figure 4.1.1. Scheme of an archetypal fungal cell.

Studies have shown changes in the ultrastructure of fungal cells under the influence of EOs, having observed severe damage to the cell wall, cell membrane and cellular organelle mainly mitochondrial destruction. In other cases, the high fungistatic concentration of EO caused complete autolysis of cell, involving disorganization and depletion of hyphal cytoplasm, and membranous organelles include nuclei, endoplasmic reticulum, and mitochondria.⁴ Four active molecules with fungicidal properties, namely benzaldehyde, salicylaldehyde, methyl anthranilate and guaiacol, are employed in this Chapter. All of them are food additives permitted for direct addition to food for human consumption by the FDA. Their physical properties are summarized in **Table 4.1.1**.

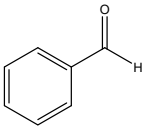
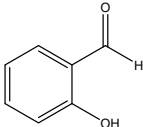
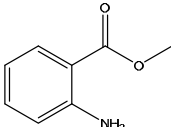
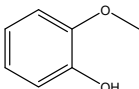
Benzaldehyde. On top of its antimicrobial activity, discussed in section 2.1.1, the fungicidal activity of benzaldehyde and its derivatives has been studied as well,⁵ and has shown promising results for its use in active packaging during the postharvest commercialization of fruits.⁶

Salicylaldehyde (2-hydroxybenzaldehyde) is the main component of *Filipendula vulgaris* essential oil (commonly known as dropwort), which is a perennial herbaceous plant in the family Rosaceae. It is found in dry pastures in Europe and central and northern Asia. Salicylaldehyde presents antifungal, anti-mycotoxigenic and especially as a chemosensitizing agent, proving to be efficient even with pathogenic fungi with resistance to conventional fungicides.^{7,8}

Methyl anthranilate (methyl 2-aminobenzoate) can be naturally found in the Concord and other *Vitis labrusca* grapes, being the responsible component of grape scent and flavour. It has been extensively used as a flavouring agent in food and as a flavour enhancer in drugs. Not only its antifungal activity has been demonstrated,⁹ the molecule has been proven effective after incorporation into active EVOH-based films at pilot scale.¹⁰

Guaiacol (2-methoxyphenol) is usually derived from guaiacum or wood creosote. It is also found in essential oils from celery seeds, tobacco leaves, orange leaves, and lemon peels. Guaiacol is employed also as a precursor to many flavouring agents, such as vanillin. On top of its antifungal activity,¹¹ is more commonly employed as a natural antioxidant pharmaceutical and food preservation applications.

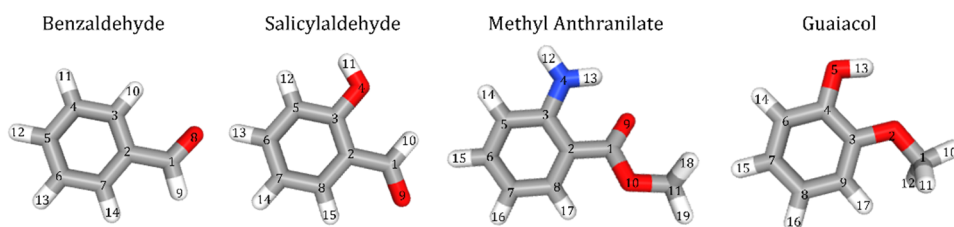
Table 4.1.1. Physical properties of the molecules employed in this chapter.

Molecule	Benzaldehyde	Salicylaldehyde	Methyl Anthranilate	Guaiacol
Structure				
Molecular weight / $\text{g}\cdot\text{mol}^{-1}$	106.124	122.037	151.165	124.139
Density / $\text{g}\cdot\text{cm}^{-3}$	1.044	1.146	1.168	1.112
Boiling point / $^{\circ}\text{C}$	178	196	256	204
λ_{max} / nm	260	85; 110	250; 330	280

The feasibility of ZIF-8 as an essential oil carrier has been previously established in Chapter 2 of this Thesis. The previously designed infiltration method yielded good results for benzaldehyde encapsulation into this porous framework. ZIF-8 has a cavity with a diameter of 11.6 Å, and its hexagonal holes window is 3.3 Å wide, which is not static and due to the rotation of the imidazolate ligands can be expanded to 7.6 Å or greater. **Table 4.1.2** summarises the dimensions of the molecules as calculated by the software ChemDraw V.19.0, evidencing that the active components can fit the limited pore window in the porous framework.

ZIF-8 has been previously utilised for the delivery of fungicidal agents. For example, Liang and co-workers developed a light-triggered pH-responsive nanocomposite using a one-pot method to encapsulate prochloraz and 2,4-dinitrobenzaldehyde in ZIF-8 nanoparticles for the smart control of *S. sclerotiorum*.¹² However, this method involves the degradation of the matrix for the delivery of the active agent. Using the same strategy, Jiao and co-workers prepared an effective antifungal delivery system based on the degradation of ZIF-8 at pH = 5.¹³ The study of ZIF-8 as a drug delivery system in which the degradation of the porous matrix is not involved is scarce in the literature.

Table 4.1.2. Largest distances in the chemical structure (as calculated by ChemDraw V.19.0 software) of the four active molecules employed in this chapter. First row of the table showcases the numbered atoms for reference.



Molecule	Benzaldehyde	Salicylaldehyde	Methyl anthranilate	Guaiacol
Largest distances	O8··H12 5.94 Å O8··H11 5.61 Å	O9··H12 5.61 Å O9··H13 5.94 Å	H18··H15 8.06 Å H18··H16 7.73 Å	H10··H15 6.98 Å H10··H16 5.68 Å

The aim of this Chapter 4 is to obtain a series of biomolecule@ZIF-8 biocomposites. Chemical characterization will be developed with particular emphasis on the established host-guest interactions. Finally, fungicidal effect of the best performing biocomposites will be studied after integration into biopolymeric films.

4.2. Results and discussion

In view of the afforded preliminary results of benzaldehyde@ZIF-8 described in Chapter 2 of this Thesis, nanoZIF-8 was selected as carrier agent for an array of fungicidal biomolecules based on its good performance as a carrier, the affordability of its precursor materials, and its facile synthesis, which also avoids the use of DMF as a solvent in contrast with UiO-66 and UiO-66-NH₂.

Encapsulation of the different fungicidal molecules was carried out following the direct impregnation method previously developed in Chapter 2. In a general synthesis, ZIF-8 nanoparticles were soaked in a 20 mg·mL⁻¹ benzaldehyde (Bz), salicylaldehyde (SA), methyl anthranilate (MA), or guaiacol (Gua) aqueous-ethanol solution in a 4:1 H₂O:EtOH mixture with a 5/1 biomolecule/ZIF-8 molar ratio. Interestingly, an immediate change of colour was observed in the case of SA@ZIF-8, the encapsulation suspension changing from milky white to intense yellow right after being added to the ZIF-8 nanoparticles. No changes were detected for the other biomolecules.

4.2.1. Encapsulation kinetics

The kinetic profile of biomolecule encapsulation was assessed by monitoring the benzaldehyde and methyl anthranilate concentration in the supernatant encapsulation media over time by means of High-Performance Liquid Chromatography (HPLC). Salicylaldehyde presents two absorption maxima in located at $\lambda = 85$ and 110 nm, which are out of the range of the UV-Vis detector. Benzaldehyde and methyl anthranilate were selected as model molecules and their concentration in the encapsulation supernatant was analysed between one minute and seven days. Each encapsulation was performed in triplicate to ensure the reproducibility. A fast encapsulation kinetic profile is exhibited for the two studied molecules, where the

concentration of biomolecule in the supernatant decreases *ca.* 80 % and 70 %, respectively for benzaldehyde and methyl anthranilate after the first minute of contact (**Figure 4.2.1**).

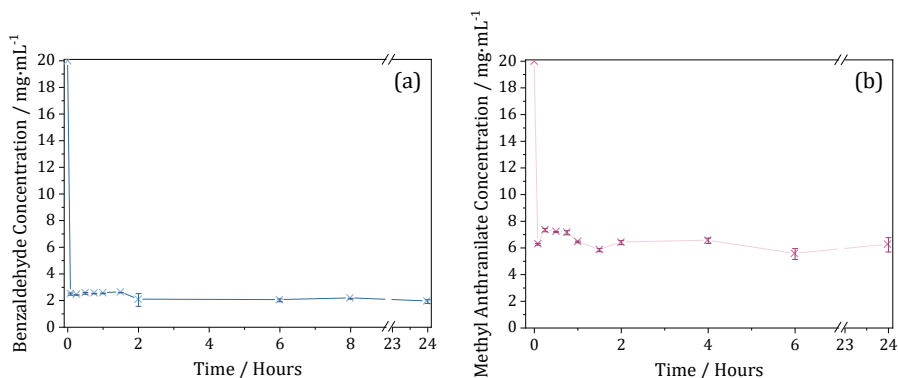


Figure 4.2.1. Benzaldehyde (a) and methyl anthranilate (b) concentration remanent in the encapsulation media after different encapsulation times quantified by means of HPLC.

In view of the rapid encapsulation kinetics, 1 hour was selected as the encapsulation time for all the materials. **Figure 4.2.3** showcases the aspect of the encapsulation products after performing the 1-hour biomolecule infiltration and being left to dry overnight. The recovered SA@ZIF-8 encapsulation product retains the intense yellow colour observed upon adding the biomolecule solution to the ZIF-8 NPs. In the case of MA@ZIF-8, the obtained product presents a gel-like texture, which is difficult to completely dry. The aspect of Bz@ZIF-8 and Gua@ZIF-8 composite materials does not differ significantly from the pristine MOF.

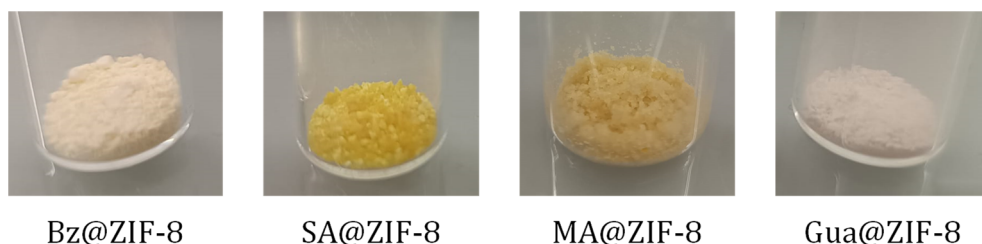


Figure 4.2.3. Image of the encapsulated materials. From left to right: Bz@ZIF-8, SA@ZIF-8, MA@ZIF-8, and Gua@ZIF-8.

4.2.2. Physicochemical characterization of the biomolecule@ZIF-8 composite materials

Successful biomolecule loading was evaluated by thermogravimetric analysis (TGA), Fourier transform infrared (FTIR) spectroscopy, powder X-ray diffraction (PXRD), and N₂ sorption measurements at 77 K.

Infrared Spectroscopy. FTIR comparisons of the spectra of the prepared biomolecule@ZIF-8 composites, ZIF-8 NPs, and the free biomolecules are illustrated in **Figures 4.2.4 to 4.2.7**. **Table 4.2.1** summarizes the most characteristic bands of ZIF-8 and the four encapsulated active molecules, as well as the corresponding vibration mode.

Table 4.2.1. Position and assignation of the principal bands of pristine ZIF-8 and the four active molecules employed in this study.

Compound	Band position / cm ⁻¹	Assignment
ZIF-8	3135 and 2929	aromatic and aliphatic ν _{as} (C-H)
	1583	ν _{C=N}
	1460–1309	skeletal vibration of the imidazolate ring
	1180 and 1146	aromatic ν _{C-N}
	995	δ _{C-N}
	760	δ _{C-H}
	420	ν _{Zn-N}

Compound	Band position / cm^{-1}	Assignment
Benzaldehyde	3064	aromatic $\nu_{\text{C-H}}$
	2816 and 2734	aldehyde-related $\nu_{\text{C-H}}$
	1696	aldehyde $\nu_{\text{C=O}}$
	1595 and 1583	aromatic $\nu_{\text{C=C}}$
	1454	aldehyde $\delta_{\text{C-H}}$
Salicylaldehyde	3180	phenolic $\nu_{\text{O-H}}$
	2845 and 2748	Fermi doublets $\nu_{\text{C-H}}$
	1278	phenolic $\nu_{\text{C-O}}$
	1643, 1621 and 1580	aromatic $\nu_{\text{C=C}}$
	883	out-of-plane $\delta_{\text{C-H}}$
Methyl anthranilate	3479 and 3370	$\nu(\text{NH}_2)$
	2951	$\nu_{\text{C-H}}$
	1612, 848 and 798	$\delta(\text{NH}_2)$
	1685	$\nu_{\text{C=O}}$
	1242	$\nu_{\text{as}}(\text{CO-O})$
	1098	$\nu_{\text{as}}(\text{O-C-C})$
Guaiacol	3543	$\nu_{\text{O-H}}$
	2844	$\nu_{\text{C-H}} (\text{CH}_3)$
	1503	$\nu_{\text{C-C}}$
	739	$\gamma_{\text{C-H}}$ of the benzene ring
	1258, 1224, 1108, 1041 and 1026	$\delta(\text{C-H}) + \nu(\text{C-OH}) + \nu(\text{C-OCH}_3) + \rho(\text{CH}_3) + \delta(\text{COH})$ ¹⁴

In all cases, in addition to the characteristic bands of ZIF-8, the composite materials spectra present the most remarkable bands of each encapsulated molecule, evidencing the presence of the active molecules in the obtained materials. The intensity of the molecule bands is particularly important in the case of MA@ZIF-8 (**Figure 4.2.6**), as expected by the gel appearance of the obtained product.

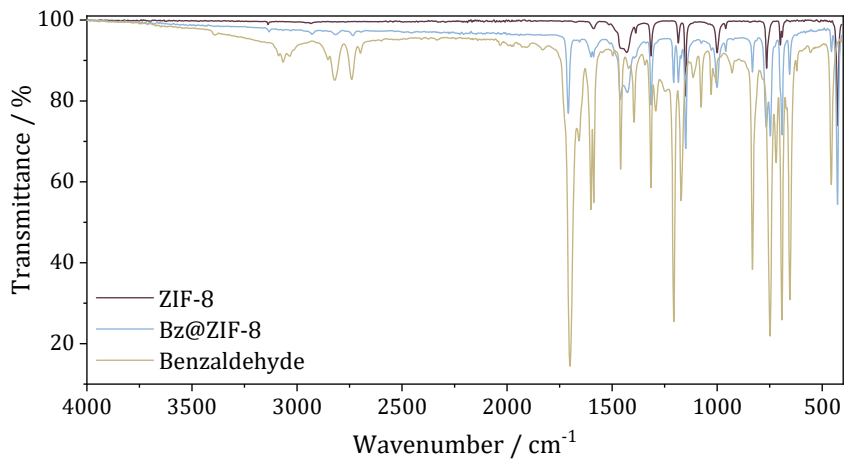


Figure 4.2.4. FTIR spectra of Bz@ZIF-8 (blue) compared with ZIF-8 (purple) and benzaldehyde (yellow).

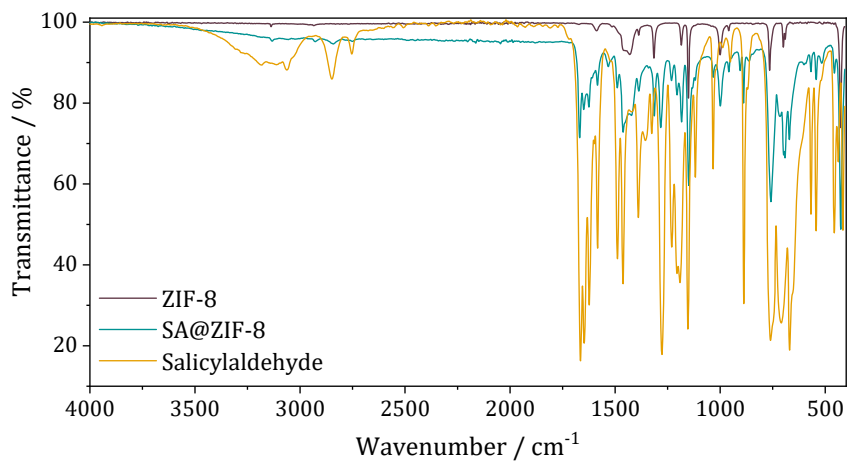


Figure 4.2.5. FTIR spectra of SA@ZIF-8 (teal) compared with ZIF-8 (purple) and salicylaldehyde (yellow).

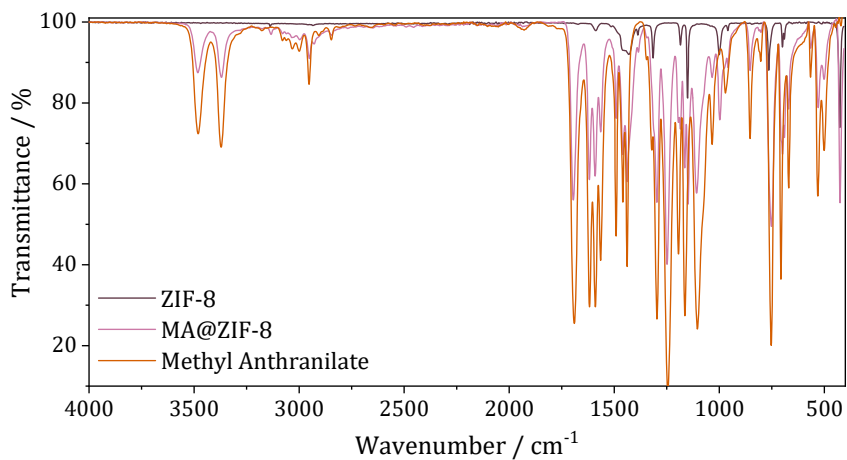


Figure 4.2.6. FTIR spectra MA@ZIF-8 (pink) compared with ZIF-8 (purple) and methyl anthranilate (orange).

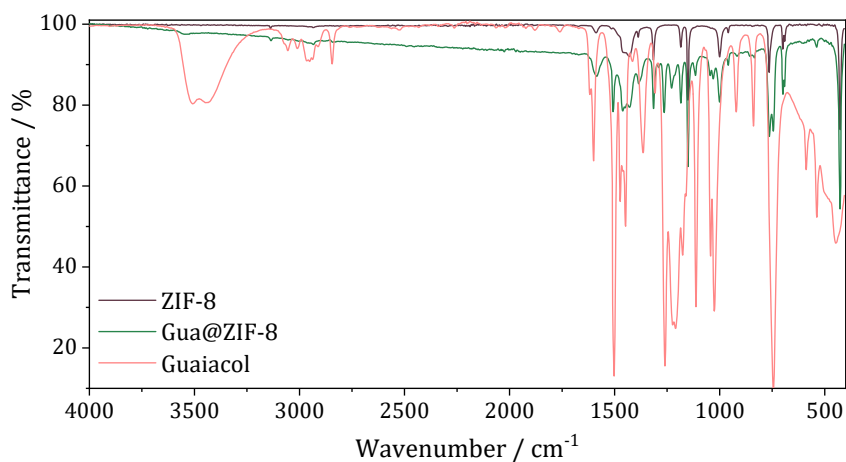


Figure 4.2.7. FTIR spectra of Gua@ZIF-8 (green) compared with ZIF-8 (purple) and guaiacol (red).

Powder X-ray Diffraction. Framework integrity was evaluated after biomolecule infiltration by means of PXRD analysis, performed before and after the encapsulation process (**Figure 4.2.8**), confirming that in all four cases ZIF-8 crystal structure is preserved after loading. PXRD patterns were collected on completely dried powders.

In all cases, the intensity of the first diffraction peak corresponding to the (011) plane decreases, in good agreement with the increase of electronic density due to physisorption of the active molecules into the pores in the framework. However, a small new diffraction peak can be observed at $2\theta = 11.0^\circ$ in Bz@ZIF-8 diffractogram, that also appears in Gua@ZIF-8 diffraction pattern. In the case of SA@ZIF-8 diffraction pattern, a new diffraction peak appears at $2\theta = 6.5^\circ$. For MA@ZIF-8 composite material the diffraction pattern matches perfectly with pristine ZIF-8 NPs and no new diffraction peaks are visible.

ZIF-8 simulated powder diffraction does not present any other possible reflection than the ones exhibited in the typical PXRD pattern of the material. Thus, the new diffraction peaks must be a result of the biomolecule encapsulation. A minor modification of the ZIF-8 framework after the infiltration process cannot be discarded since ligand substitution on ZIF-8 can be achieved with relative facility. In this regard, Lang and co-workers reported a surface ligand exchange to replace methylimidazole with 5,6-dimethylbenzimidazole (DBIM) by simply mixing the ZIF-8 particles with a solution containing the new ligand and heating at 60°C for 5 h, triggering the nucleophilic substitution of methylimidazole with DBIM.¹⁵ The methodology was first reported by Liu and co-workers with the aim of enhancing hydrothermal stability of the ZIF-8 particles,¹⁶ and it is demonstrated to be an efficient protocol to modify the ZIF-8 selectivity in gas separation.¹⁷

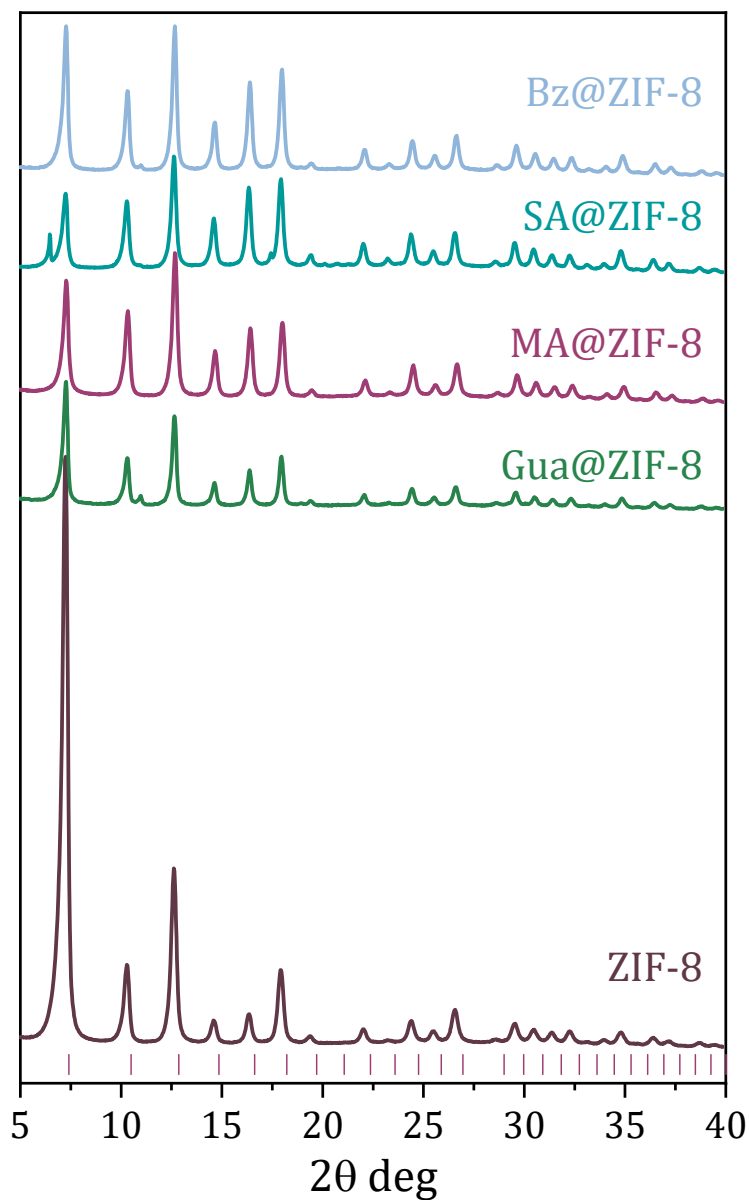


Figure 4.2.8. XRPD pattern of the four obtained biomolecule@ZIF-8 composites in comparison with pristine ZIF-8. The (h, k, l) reflection list of ZIF-8 unit cell, obtained from crystallographic data, is depicted at the bottom.

Thermogravimetric Analysis. Thermal stability of the obtained composite materials was evaluated in comparison with the pristine ZIF-8 nanoMOF. The thermogravimetric analysis of the samples was performed in high-resolution mode, which carries out an isothermal ramp when a mass loss is detected. This feature is very useful to determine the mass loss of volatile molecules inside a porous material, as it allows a better differentiation between the evacuation of the encapsulated molecules and the combustion of the host material. In high-resolution mode, the temperature remains constant during the evacuation process. In this way, the mass loss is more visible and a clean, sharp decrease in the weight can be observed in the thermal profile of the sample. This allows for a simpler interpretation of the thermal profile.

Overnight air-dried materials were measured first. All the composite materials seemed to present different degrees of solvent content due to the interactions between the molecules and the encapsulation media with the ZIF-8 framework. For example, a 50 % mass loss could be observed for MA@ZIF-8 (**Figure S4.1c**) at 80 °C, as expected since the obtained material was in gel form after the infiltration process. In view of the large volatile content in all samples, thermogravimetric analyses were carried out after preliminary thermal treatment. To maximize solvent removal while retaining the active molecules, the pre-treatment consisted of heating at 100 °C for 3 hours (including pristine ZIF-8 NPs). In case of the MA@ZIF-8, this thermal pre-treatment was extended up to 16 hours due to its gel nature. The thermal profile of the activated materials is depicted in **Figure 4.2.9**. **Table 4.2.2** summarizes the inorganic residue content of all the composite materials, as compared to the control empty ZIF-8 and related theoretical value (theo). In addition, the estimated loaded molecule is provided.

Table 4.2.2. Thermogravimetric analysis of the obtained biomolecule@ZIF-8 composites compared with pristine ZIF-8, summarizing the ligand decomposition temperature, inorganic residue value and the estimated molecule loading for each material.

	Ligand decomp. T / °C	Inorganic residue (D.B.) / % (w/w)	Encapsulated molecule / % (w/w)
ZIF-8 (theo)	-	36.0	-
ZIF-8	405	36.1	-
Bz@ZIF-8	410	28.4	21.3
SA@ZIF-8	370 - 540	25.5	29.4
MA@ZIF-8	400	23.9	33.8
Gua@ZIF-8	397	29.2	19.1

Thermal profile of activated ZIF-8 nanoparticles follows the expected decomposition, presenting a 36.1 % of inorganic content, in good agreement with the expected 36 % value considering ZIF-8 molecular formula. **Bz@ZIF-8** composite thermal profile (**Figure 4.2.9a**) presents an additional 21.3 % mass loss at 150 °C that can be related with the removal of benzaldehyde molecules. For **SA@ZIF-8** (**Figure 4.2.9b**), there is a continuous two-step mass loss of 29.4 % between 100 and 300 °C that can be attributed to the encapsulated salicylaldehyde molecules. Ligand decomposition takes place in this case in a multiple step manner between 370 and 540 °C. The smooth and continuous decomposition of the composite points to an effective and differentiated interaction of salicylaldehyde guest molecules with the ZIF-8 host than in the case of the other composites, where this effect is not observed. **MA@ZIF-8** sample was dried at 100 °C for a total of 16 h in order to completely dry the obtained gel after the encapsulation process and obtain a manageable powder. Even after this extended thermal

treatment, the solvent molecules of the encapsulation medium are not completely removed from the sample, as can be seen in **Figure 4.2.9c**. MA@ZIF-8 thermal profile presents a 17.7 % mass loss before 100 °C that can be related to solvent molecules remanent from the encapsulation process. Between this temperature and 260 °C a mass loss of 33.8 % (D.B.) is observed, that can be assigned to the encapsulated methyl anthranilate molecules, and a 23.9 % (DB) inorganic residue is obtained. Finally, **Gua@ZIF-8** thermal profile (**Figure 4.2.9d**) showcases a 19.1 % two-step mass loss between 110 and 300 °C attributed to the guaiacol encapsulated molecules, the lower estimated content of all the composite materials. Inorganic residue corresponds to a 29.2 %.

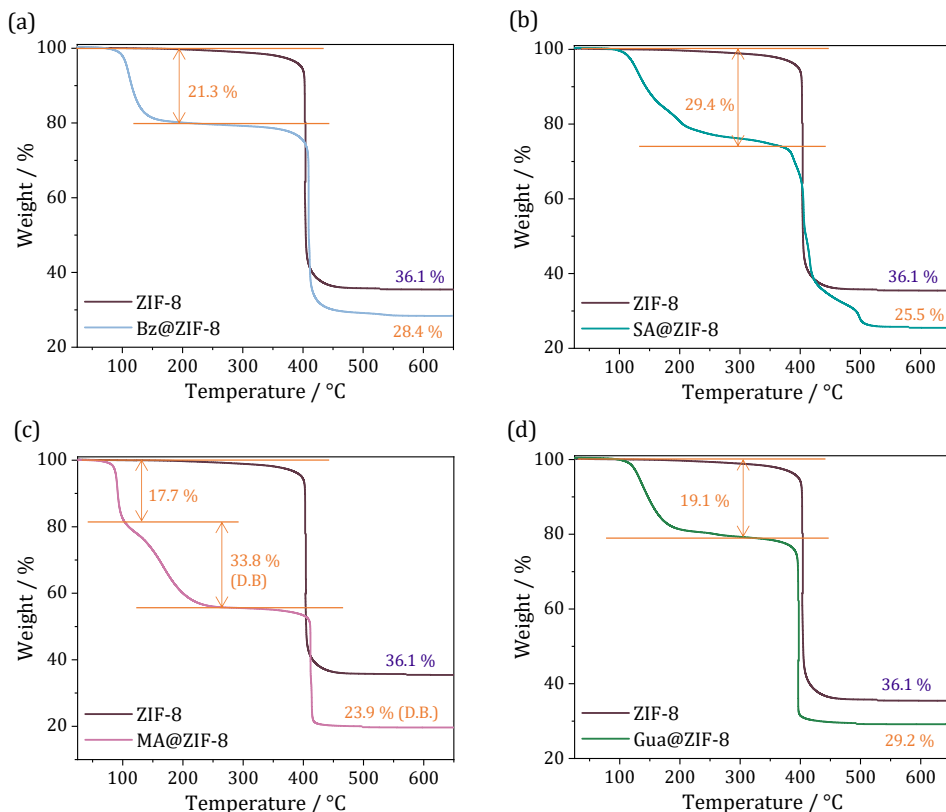


Figure 4.2.9. Thermal profile of Bz@ZIF-8 (a), SA@ZIF-8, MA@ZIF-8 (c), and Gua@ZIF-8 (d), compared with the pristine ZIF-8 nanoparticles. All samples were dried in oven at 100 °C for 3 h before measurement, except MA@ZIF-8 which was dried for 12 h.

N₂ sorption isotherms at 77 K. N₂ sorption studies before and after benzaldehyde encapsulation were carried out to evaluate the porosity of the composite material (**Figure 4.2.10**).

A *ca.* 84 % decrease in the porous surface (**Figure 4.2.10a**) was evidenced after benzaldehyde encapsulation ($S_{\text{BET}} = 1712$ vs. $276 \text{ m}^2\cdot\text{g}^{-1}$, respectively for ZIF-8 and Bz@ZIF-8). This is a similar BET value reduction to the one obtained in the preliminary study discussed in chapter 2, when employing 5-day encapsulations. This result further supports the rapid kinetics of the benzaldehyde infiltration into the ZIF-8 framework. In the case of SA@ZIF-8 (**Figure 4.2.10b**), the BET reduction is *ca.* 94 % ($S_{\text{BET}} = 108 \text{ m}^2\cdot\text{g}^{-1}$ for SA@ZIF-8). Interestingly, SA@ZIF-8 is the only composite which loses its hysteretic behaviour. Also considering the appearance of a diffraction peak at $2\theta = 6.5^\circ$ in the composite diffraction pattern, and its thermal profile, being the only one that presents a ligand decomposition in multiple steps, these results further point in the direction of ligand functionalization or substitution in this composite. MA@ZIF-8 (**Figure 4.2.10c**) presents a BET reduction of *ca.* 90 % ($S_{\text{BET}} = 169 \text{ m}^2\cdot\text{g}^{-1}$ for SA@ZIF-8) showcasing a slight increase in the region affected by the hysteretic behaviour. Gua@ZIF-8 (**Figure 4.2.10d**) presents a BET reduction of *ca.* 61 % ($S_{\text{BET}} = 665 \text{ m}^2\cdot\text{g}^{-1}$ for SA@ZIF-8).

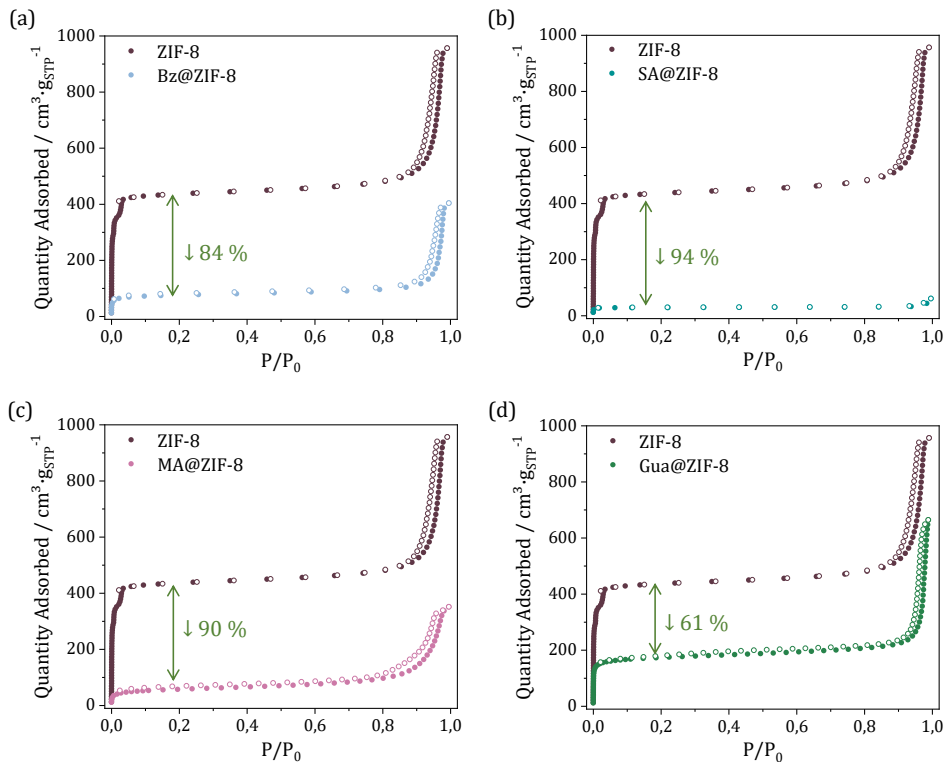


Figure 4.2.10. N₂ sorption isotherms at 77 K of Bz@ZIF-8 (a), SA@ZIF-8 (b), MA@ZIF-8 (c), and Gua@ZIF-8 (d), compared with ZIF-8. Solid symbols for adsorption and open ones for desorption. Samples were activated at 100 °C for 3h before measurement.

ZIF-8 exhibits flexibility upon gas uptake,¹⁸ reflected in slope changes in the 0-0.1 P/P₀ region of the N₂ sorption isotherms. A close inspection of this gate-opening effect is displayed in the logarithmic representation of the N₂ adsorption branch (**Figure 4.2.11**), where three steps can be clearly distinguished. Interestingly, for all composite materials the characteristic gate opening behaviour of the ZIF-8 micropores is completely lost upon biomolecule infiltration, hindering the reorientation of the imidazolate linkers upon gas sorption. This effect can be expected in the case of complete blocking of the pores, being the case of SA@ZIF or MA@ZIF-8 sorption profiles, but not for Bz@ZIF-8 and Gua@ZIF-8 composites, which sorption

profiles manifest available porosity in the micropore region. This result further implies the possible ligand substitution in the composite materials.

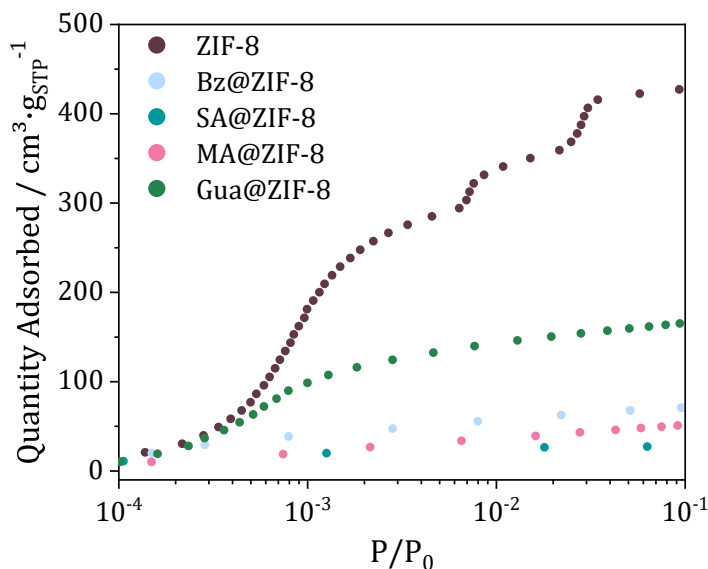


Figure 4.2.11. Logarithmic representation of N_2 adsorption isotherms at 77 K of Bz@ZIF-8, SA@ZIF-8, MA@ZIF-8, and Gua@ZIF-8 compared with ZIF-8 in the micropore region.

Pore distribution analysis was conducted by employing the Horvath-Kawazoe equations for pore-size distribution (PSD). Pristine ZIF-8 NPs present 3 PSD centres. The 5.8 and 7.4 Å PSD sites of ZIF-8 (**Figure 4.2.12a**) are due to the flexible six-membered ring, which arises from the vibrations of the linker: the methyl rotation of the methylimidazolate ligand allows the infiltration of more N_2 molecules, expanding the available volume in the pore. The largest PSD centre of ZIF-8 nanoparticles, of about 9.4 Å, corresponds to the maximum opening available, almost the diameter of the ZIF-8 SOD cage (pore size according to the crystal structure is 11.6 Å).¹⁹ In all the composite materials the PSD drastically changes, and the encapsulation products present only one PSD centre, further evidencing that the distinctive ZIF-8 gate opening upon N_2 uptake is lost. In summary, the retrieved pore width

for the composite materials is: Bz@ZIF-8 (4.9 Å) < Gua@ZIF-8 (5.5 Å) < SA@ZIF-8 (5.9 Å) < MA@ZIF-8 (6.3 Å).

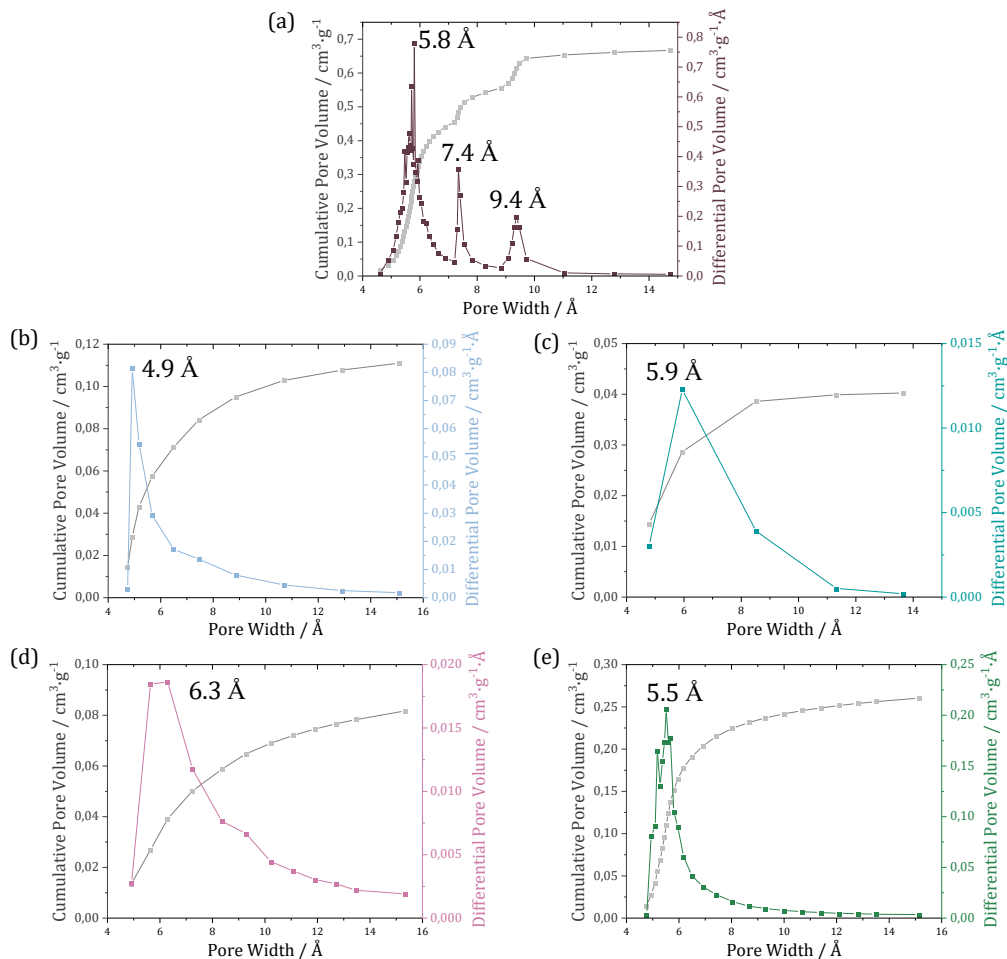


Figure 4.2.12. Pore size distributions obtained employing the Horvath-Kawazoe equations of pristine ZIF-8 NPs (a), Bz@ZIF-8 (b), SA@ZIF-8 (c), MA@ZIF-8 (d), and Gua@ZIF-8 (e).

Biomolecule loading and encapsulation efficiency. Biomolecule loading in the obtained composite materials was quantified by CG-MS, which was employed to calculate the encapsulation efficiency according to the equations described in section 3.2.1 of this Thesis. The obtained results are

summarized in **Table 4.2.3**, where the estimated molecule content determined by TGA is also included for comparison.

Table 4.2.3. Biomolecule loading estimated by TGA and GC, and calculated encapsulation efficiency of the obtained composites.

Sample	Loading (TGA) / % (w/w)	Loading (GC) / % (w/w)	Encapsulation efficiency (E.E.) / %
Bz@ZIF-8	21.3	31.4	20
SA@ZIF-8	29.4	19.0	9
MA@ZIF-8	33.4	36.6	16
Gua@ZIF-8	19.1	15.3	7

The molecule loading values obtained by means of GC and the estimated values attained from TGA are in the same range, but the calculated encapsulation efficiency values may seem low at first sight especially considering the attained results by means of HPLC. The 80 % decrease in benzaldehyde and 70 % decrease in methyl anthranilate concentration in the encapsulation supernatant should translate into exceptionally high loading values in the composite materials. However, two considerations must be contemplated while analysing these results: on the one hand, greatly oversaturated biomolecule mixtures are employed in this procedure to ensure the 5/1 biomolecule/MOF ratio, which implies that a high amount of active molecule would not enter the MOF scaffold during the infiltration process even if all the pores were to be filled. On the other hand, the decrease of molecule concentration in the supernatant is not only a result of the infiltration of the active molecules into the porous framework but also the contribution of molecules attached to the ZIF-8 NPs surface. Due to their volatile nature, the poorly attached molecules are released immediately after encapsulation, during the overnight drying process and the thermal

treatment at 100 °C. Taking these considerations into account, the obtained loading values are acceptable even if the encapsulation efficiency values seem low.

Regarding the biomolecule loading of the composites, **Table 4.2.4** showcases the loading capacity values of other porous frameworks for comparison. In general, considering how the inhibitory concentrations required for antifungal activity in essential oils are usually not very high, the loaded biomolecule content obtained could be appropriate for fungicidal applications in all cases.

Table 4.2.4. Loading capacity of the studied biomolecules in other porous materials.

Carrier	Encapsulated molecule	Loading / %
Nanoporous carbon based on MIL-101 ²⁰	Benzaldehyde	56
γ -cyclodextrin-based MOF ²¹	Benzaldehyde	3
ZIF-8 ²²	Salicylaldehyde	8
NaY zeolite ²³	Methyl anthranilate	34
HKUST-1 ²⁴	Guaiacol	40

After evaluation of the physicochemical characterization of all the four obtained composites, and loading comparison with other active carriers, **Bz@ZIF-8** and **MA@ZIF-8** were selected to be further employed in antifungal activity essays, due to their moderate but greater biomolecule loading.

4.2.4. *In vitro* evaluation of antifungal activity.

Microbiology studies were conducted to determine the efficiency of Bz@ZIF-8 (**Figure 4.2.13**) and MA@ZIF-8 (**Figure 4.2.14**) composites against *Penicillium expansum* after their integration in zein biopolymeric films. This section was carried out in collaboration with Pilar Hernández-Muñoz and Rafael Gavara from Instituto de Agroquímica y Tecnología de Alimentos, IATA-CSIC.

P. expansum is a spoilage organism known to cause blue mold decay of fruit and produces toxic secondary metabolites such as patulin and citrinin. Though primarily known as a disease of apples, this plant pathogen can infect a wide range of hosts, including pears, strawberries, tomatoes, corn, and rice.²⁵

In these experiments, 3 droplets of a suspension containing *P. expansum* spores are placed equidistantly on a PDA plate. Analogously to the protocol discussed in Chapter 3 of this Thesis for the antibacterial activity of carvacrol@MIL-100(Fe), a zein film that contains either the biomolecule@ZIF-8 composite or the equivalent content of free molecule is placed on the inside of the Petri dish lid. The prepared dishes are incubated at 28 °C and the growth of the fungus is monitored visually by measuring the growth halo. After six days of incubation the films are removed, and the plates continue incubating until day 9 to assess if the effect is fungistatic (the spores recover and grow in the absence of the active agent) or fungicidal (no growth occurs even after removing the active agent). The results of this study are showcased in **Figures 4.2.13 to 4.2.15**.

Essentially, the free-benzaldehyde zein film does not present either fungistatic or fungicidal effect, as the presence of the molecule does not prevent fungal growth completely (**Figure 4.2.13, centre**): the three droplets of the fungal suspension present a *ca.* 90 % size of the control after 48 h, even though the growth rate is slower with time reaching a 70 % of

fungus growth compared with the control at day 6. With the removal of the benzaldehyde containing film after 6 days, the fungal growth does not significantly increase, reaching a 75 % of the control. However, the biomolecule encapsulation drastically improves its antifungal activity. No fungal presence can be observed in the dish in contact with the Bz@ZIF-8 containing film after 48 h of incubation (**Figure 4.2.13, right**) nor even after 6 days. After removal of the active layer, at day 9 the fungal growth is still completely prevented (**Figure 4.2.15**). Thus, the film containing Bz@ZIF-8 composite presents both fungistatic and fungicidal effects.

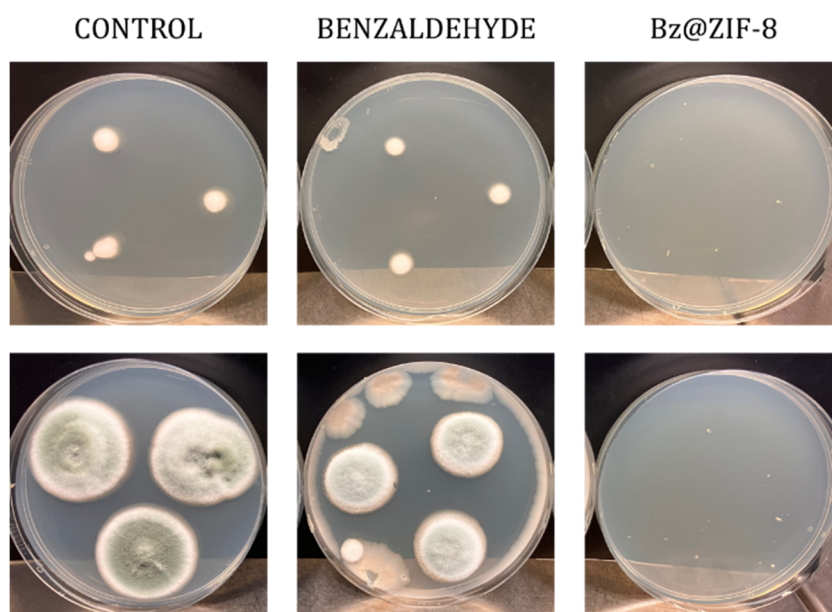


Figure 4.2.13. Images of the microatmosphere test carried out to determine the activity of Bz@ZIF-8 films against *Penicillium expansum*: On the top, images of the Petri dishes showing 3 droplets of the fungal suspension after 48 hours of incubation for control (left), benzaldehyde (middle) and Bz@ZIF-8 (right). On the bottom, images of the Petri dishes after 6 days.

The presence of free methyl anthranilate is already relatively effective in hindering fungal growth, since the dish in presence of the methyl anthranilate film presents a *ca.* 75 % reduced fungal growth when compared

to the control plate (**Figure 4.2.14, centre**) at 48 h, increasing its efficiency up to 85 % after 6 days of incubation and maintaining this effect even after removal of the film. Still, the encapsulation of the bioactive molecule increases its effectiveness, and no fungal presence can be observed in the dish in contact with the MA@ZIF-8 containing film after 48 h of incubation (**Figure 4.2.14, right**). Even after removal of the active film at day 6, the fungal growth is still completely prevented after 9 days (**Figure 4.2.15**). Analogous to the incorporation of Bz@ZIF-8, the film containing MA@ZIF-8 composite also presents both fungistatic and fungicidal effects.

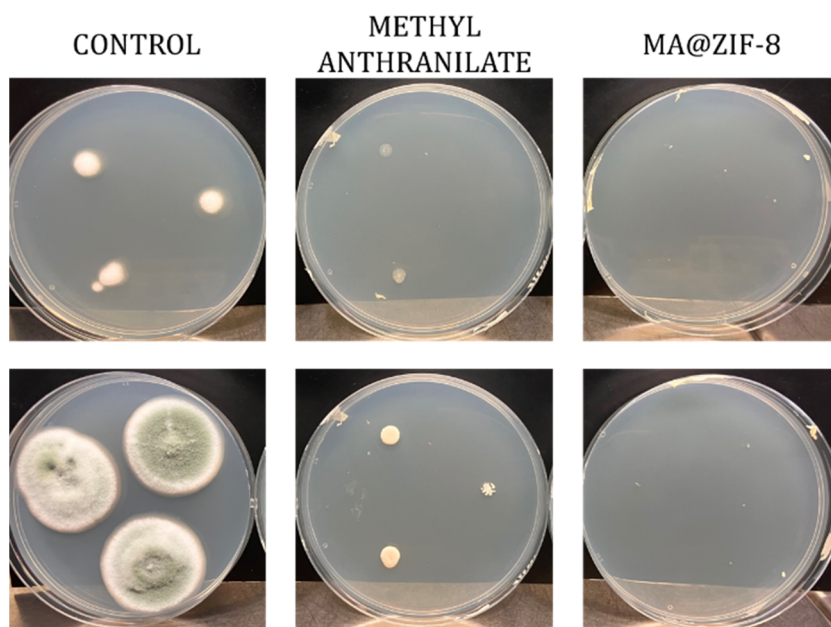


Figure 4.2.14. Images of the microatmosphere test carried out to determine the activity of MA@ZIF-8 films against *Penicillium expansum*: On the top, images of the Petri dishes showing 3 droplets of the fungal suspension after 48 hours of incubation for control (left), methyl anthranilate (middle) and Bz@ZIF-8 (right). On the bottom, images of the Petri dishes after 6 days.

Figure 4.2.15 visually summarizes the discussed fungal growth studies, clearly evidencing the enhancement of the fungicidal activity of the biomolecules upon ZIF-8 encapsulation, especially in the case of benzaldehyde infiltration.

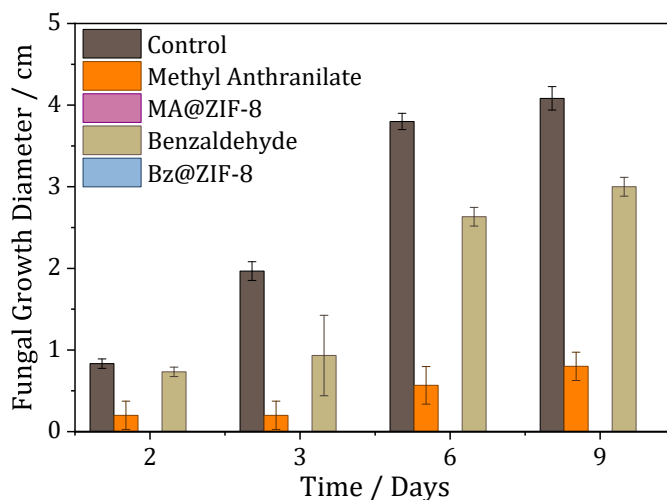


Figure 4.2.15. Fungal growth diameter on the incubated dishes.

4.3. Summary and conclusions

In this chapter, four ZIF-8-based biocomposites containing benzaldehyde, salicylaldehyde, methyl anthranilate or guaiacol, were obtained adapting the direct infiltration method previously developed and described in Chapter 2. The encapsulation kinetics were evaluated, resulting in a surprisingly fast encapsulation process, where the infiltration of the biomolecule occurs almost immediately with effective loadings of *ca.* 20-30 %.

Of the four obtained composites, **Bz@ZIF-8** and **MA@ZIF-8** were employed in antifungal activity essays. The released benzaldehyde and methyl anthranilate dose was enough to oppose fungal growth, with an improved activity against *Penicillium expansum* in comparison with the “free” biomolecule after integration in biopolymeric films.

The prepared biomolecule@ZIF-8 composites are potential options for food packaging applications due to their direct preparation and simple processing, and a scaffold-mediated performance that permits an enhanced antifungal action.

4.4. Methods

Synthesis of ZIF-8 nanoparticles

ZIF-8 nanoparticles were synthesized at 60 °C adapting the procedure described by Langner and coworkers.²⁶ A solution of $\text{Zn}(\text{NO}_3)_2 \cdot 6\text{H}_2\text{O}$ (1.476 g, 5 mmol) in 100 mL of methanol at 40 °C was rapidly added to a solution of 2-methylimidazole (3.286 g, 40 mmol) in methanol (50 mL) at the same temperature. The mixture was heated at 65 °C and stirred for 1 h at this temperature before placing the flask in an ice bath to stop the reaction. The precipitate was isolated by centrifugation (8000 rpm, 30 min, room temperature), washed with methanol three times, and dried in air overnight.

Preparation of biomolecule@ZIF-8 composite materials

Composites benzaldehyde@ZIF-8 and methylanthranilate@ZIF-8 were obtained following a direct impregnation method. 11.65 mL of benzaldehyde, 16.61 mL of methyl anthranilate, 13.41 mL of salicylaldehyde, and 13.64 mL of guaiacol emulsions (20 $\text{mg} \cdot \text{mL}^{-1}$ concentration) prepared in a $\text{H}_2\text{O}:\text{EtOH}$ (4:1) mixture with were directly added to 100 mg of ZIF-8 nanoparticles. After 1h stirring in a 360 ° rotating shaker, the biomolecule@ZIF-8 materials were retrieved by centrifugation (10000 rpm, 20 min) and dried at air overnight. The composites were then additionally dried at 100 °C for 3 hours in oven to ensure the complete ethanol and water removal from the samples.

Determination of encapsulation kinetics

To establish if the encapsulation kinetics could be monitored by HPLC, calibration curves were prepared and measured in a HPLC 1260 Agilent Infinity equipment with UV-Vis detection. Benzaldehyde and methyl anthranilate were selected for the screening test. Benzaldehyde and methyl anthranilate solutions were prepared in acetonitrile in the range of 0.015 to

0.2 and 0.25 to 5 mg·mL⁻¹, respectively. The column used was 150×4.6 mm packed with 4 μm particles of C18 (Agilent) operated at 25°C. To elute the biomolecules, the mobile phase employed was a binary mix of acetonitrile (70 %) and water (30 %). The flow rate of the mixture was 1 mL·min⁻¹, and the injection volume of the samples was 20 μL. The molecules were detected by UV-Vis at λ = 260 nm for benzaldehyde and λ = 250 nm for methyl anthranilate with retention times of 2.04 and 3.55 min, respectively. To ensure the reproducibility, calibration curves were repeated 6 times.

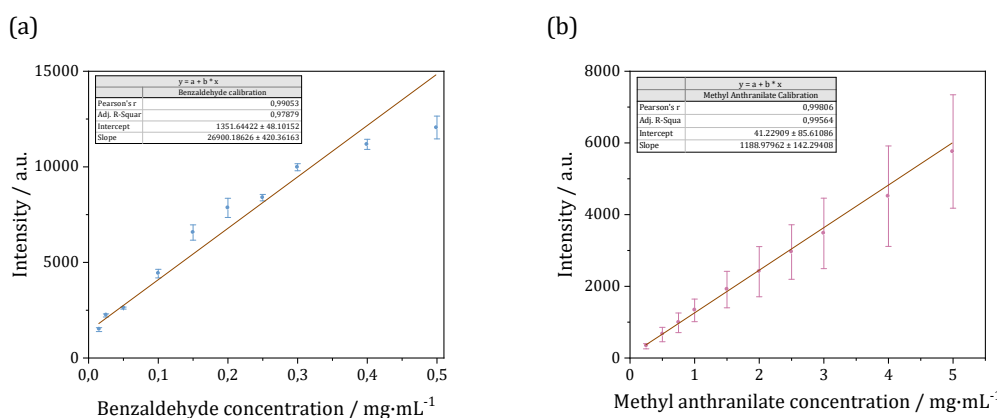


Figure 4.4.1. Calibration curves in acetonitrile of benzaldehyde (a) and methyl anthranilate (b). Statistics table is included in each graph.

For the analysis of the biomolecule content in the supernatant performed by HPLC, encapsulations were carried out by adding the corresponding amount of biomolecule emulsion to 10 mg of dry ZIF-8 NPs in an Eppendorf tube. Each encapsulation was performed by triplicate. The encapsulations were stopped at different times by centrifugation (13400 rpm, 15 min) and a 100 μL aliquot was extracted from each tube, diluted ten times in acetonitrile and injected into HPLC for quantification.

Determination of biomolecule loading and encapsulation efficiency

Bioactive molecule content in the obtained composite was determined by thermic desorption Gas Chromatography, using a HP 7890B equipped with a HP5 column of 30 m, 320 μm of diameter and 0.25 μm of thickness. The thermic gradient employed was: 40 $^{\circ}\text{C}$ (3 min), 10 $^{\circ}\text{C}\cdot\text{min}^{-1}$ ramp until 200 $^{\circ}\text{C}$ and 15 min isotherm. Injector heats on ballistic ramp (600 $^{\circ}\text{C}\cdot\text{min}^{-1}$) from 40 to 200 $^{\circ}\text{C}$ and 4 min isotherm.

Characterization of biomolecule@ZIF-8 composite materials

X-ray powder diffraction experiments were acquired in an X-ray diffractometer (PANalytical Empyrean) with copper as a radiation source (Cu-K α , 1.5418 \AA). Infrared spectroscopy spectra were registered employing an ALPHA II FTIR spectrometer (Bruker). Thermogravimetric analyses were carried out with TGA 550 (TA Instruments) in high-resolution mode (Ramp: 20.0 $^{\circ}\text{C}/\text{min}$ to 700 $^{\circ}\text{C}$; Res 4 Sensitivity 3). All samples were activated at 100 $^{\circ}\text{C}$ 3h before measurement. N₂ sorption isotherms were obtained using a TRISTAR II apparatus (Micromeritics) at -196 $^{\circ}\text{C}$. All samples were activated at 100 $^{\circ}\text{C}$ under vacuum for 3h before measurement.

Determination of fungicidal activity

The strain of *Penicillium expansum* fungus was obtained from the Spanish Collection of Type Cultures (CECT 2278). The fungus is grown on agar before the experiment in PDA (potato dextrose agar) medium which is a solid general fungal growth medium. The fungus takes about seven days to grow at 28 $^{\circ}\text{C}$ occupying the entire plate (90 mm). It is in this phase when the spores are extracted. The extracting protocol consists of the following steps: in a laminar flow cabinet 10 mL of peptone water with Tween 80 (0.05 %) are dropped on the surface of the plate and the mycelium is broken by scraping with the help of a spatula. 5 mL of the formed suspension are shaken

vigorously with a vortex. After serial dilutions a concentration of 10^5 spores/mL is achieved - the spores are counted in an optical microscope with the help of a Neubuer camera. 3 μ L of said suspension are placed equidistantly on the PDA plate. A film that contains either the biomolecule@ZIF-8 composite or the equivalent content of free molecule is placed on the inside of the Petri dish lid. The prepared dishes are incubated at 28 °C and the growth of the fungus is monitored visually by measuring the growth halo. After six days of incubation the films are removed, and the plates continue incubating until day 9.

4.5. Supporting information

Thermogravimetric analysis of the air-dried obtained composites

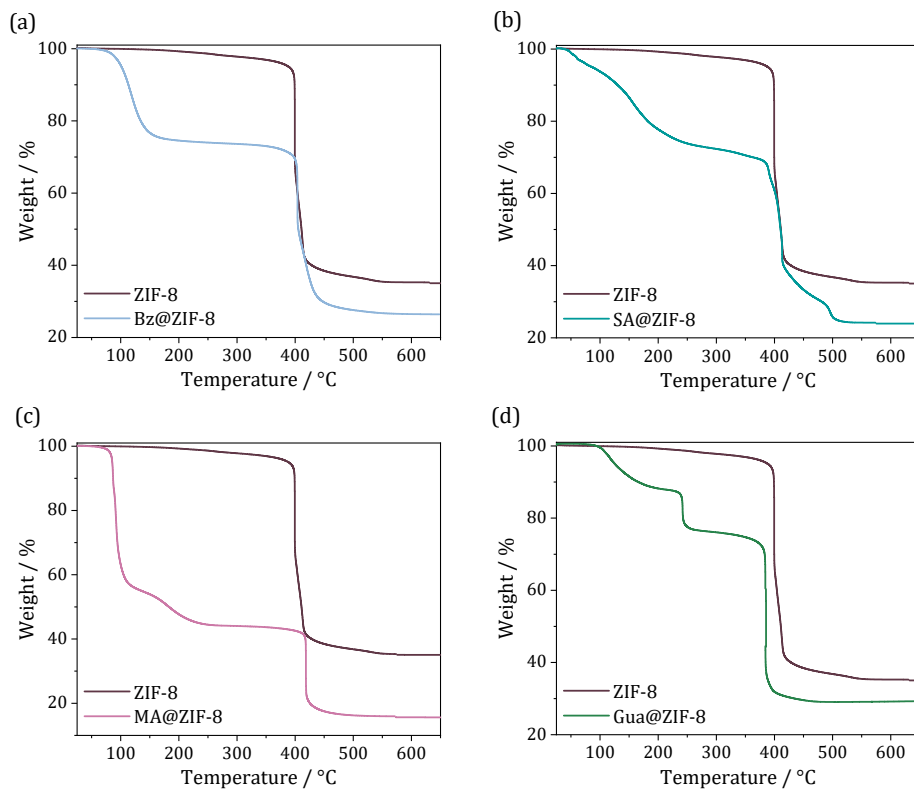


Figure S4.1. Thermal profile of Bz@ZIF-8 (a), SA@ZIF-8, MA@ZIF-8 (c), and Gua@ZIF-8 (d), compared with the pristine ZIF-8 nanoparticles. All the samples were dried at air overnight before measurement.

4.6. References

- (1) Van Long, N. N.; Dantigny, P. *Fungal Contamination in Packaged Foods*; Elsevier Inc., 2016.
- (2) Hu, F.; Tu, X. F.; Thakur, K.; Hu, F.; Li, X. L.; Zhang, Y. S.; Zhang, J. G.; Wei, Z. J. Comparison of Antifungal Activity of Essential Oils from Different Plants against Three Fungi. *Food Chem. Toxicol.* **2019**, *134* (August), 110821.
- (3) MARUZZELLA, J. C.; LIGUORI, L. The in Vitro Antifungal Activity of Essential Oils. *J. Am. Pharm. Assoc. Am. Pharm. Assoc. (Baltim).* **1958**, *47* (4), 250–254.
- (4) Basak, S. A Review on Antifungal Activity and Mode of Action of Essential Oils and Their Delivery as Nano-Sized Oil Droplets in Food System. *J. Food Sci. Technol.* **2018**, *55* (12), 4701–4710.
- (5) Kim, J. H.; Chan, K. L.; Mahoney, N.; Campbell, B. C. Antifungal Activity of Redox-Active Benzaldehydes That Target Cellular Antioxidation. *Ann. Clin. Microbiol. Antimicrob.* **2011**, *10*.
- (6) Calvo, H.; Mendiara, I.; Arias, E.; Gracia, A. P.; Blanco, D.; Venturini, M. E. Antifungal Activity of the Volatile Organic Compounds Produced by *Bacillus Velezensis* Strains against Postharvest Fungal Pathogens. *Postharvest Biol. Technol.* **2020**, *166* (April), 111208.
- (7) Kim, J. H.; Campbell, B. C.; Mahoney, N.; Chan, K. L.; Molyneux, R. J. Chemosensitization of Aflatoxigenic Fungi to Antimycin A and Strobilurin Using Salicylaldehyde, a Volatile Natural Compound Targeting Cellular Antioxidation System. *Mycopathologia* **2011**, *171* (4), 291–298.
- (8) Lee, J. E.; Seo, S. M.; Huh, M. J.; Lee, S. C.; Park, I. K. Reactive Oxygen Species Mediated-Antifungal Activity of Cinnamon Bark (*Cinnamomum Verum*) and Lemongrass (*Cymbopogon Citratus*) Essential Oils and Their Constituents against Two Phytopathogenic Fungi. *Pestic. Biochem. Physiol.* **2020**, *168* (April), 104644.
- (9) Chambers, A. H.; Evans, S. A.; Folta, K. M. Methyl Anthranilate and γ -Decalactone Inhibit Strawberry Pathogen Growth and Achene Germination. *J. Agric. Food Chem.* **2013**, *61* (51), 12625–12633.

- (10) Aragón-Gutiérrez, A.; Heras-Mozos, R.; Montesinos, A.; Gallur, M.; López, D.; Gavara, R.; Hernández-Muñoz, P. Pilot-Scale Processing and Functional Properties of Antifungal EVOH-Based Films Containing Methyl Anthranilate Intended for Food Packaging Applications. *Polymers (Basel)*. **2022**, *14* (16).
- (11) Gao, T.; Zhang, Y.; Shi, J.; Mohamed, S. R.; Xu, J.; Liu, X. The Antioxidant Guaiacol Exerts Fungicidal Activity Against Fungal Growth and Deoxynivalenol Production in *Fusarium Graminearum*. *Front. Microbiol.* **2021**, *12* (November), 1–10.
- (12) Liang, W.; Xie, Z.; Cheng, J.; Xiao, D.; Xiong, Q.; Wang, Q.; Zhao, J.; Gui, W. A Light-Triggered PH-Responsive Metal-Organic Framework for Smart Delivery of Fungicide to Control Sclerotinia Diseases of Oilseed Rape. *ACS Nano* **2021**, *15* (4), 6987–6997.
- (13) Jiao, S.; Li, Y.; Gao, Z.; Chen, R.; Wang, Y.; Zou, Z. The Synthesis of an Antifungal 1,2,4-Triazole Drug and the Establishment of a Drug Delivery System Based on Zeolitic Imidazolate Frameworks. *New J. Chem.* **2019**, *43* (47), 18823–18831.
- (14) Scoullou, E. V.; Hofman, M. S.; Zheng, Y.; Potapenko, D. V.; Tang, Z.; Podkolzin, S. G.; Koel, B. E. Guaiacol Adsorption and Decomposition on Platinum. *J. Phys. Chem. C* **2018**, *122* (51), 29180–29189.
- (15) Lang, L.; Banihashemi, F.; James, J. B.; Miao, J.; Lin, J. Y. S. Enhancing Selectivity of ZIF-8 Membranes by Short-Duration Postsynthetic Ligand-Exchange Modification. *J. Memb. Sci.* **2021**, *619* (July 2020), 118743.
- (16) Liu, X.; Li, Y.; Ban, Y.; Peng, Y.; Jin, H.; Bux, H.; Xu, L.; Caro, J.; Yang, W. Improvement of Hydrothermal Stability of Zeolitic Imidazolate Frameworks. *Chem. Commun.* **2013**, *49* (80), 9140–9142.
- (17) Abraha, Y. W.; Tsai, C. W.; Niemantsverdriet, J. W. H.; Langner, E. H. G. Optimized CO₂ Capture of the Zeolitic Imidazolate Framework ZIF-8 Modified by Solvent-Assisted Ligand Exchange. *ACS Omega* **2021**, *6* (34), 21850–21860.
- (18) Fairen-Jimenez, D.; Moggach, S. A.; Wharmby, M. T.; Wright, P. A.; Parsons, S.; Düren, T. Opening the Gate: Framework Flexibility in ZIF-8 Explored by Experiments and Simulations. *J. Am. Chem. Soc.* **2011**, *133* (23), 8900–8902.

- (19) Mei, X.; Yang, S.; Lu, P.; Zhang, Y.; Zhang, J. Improving the Selectivity of ZIF-8/Polysulfone-Mixed Matrix Membranes by Polydopamine Modification for H₂/CO₂ Separation. *Front. Chem.* **2020**, *8* (July), 1–10.
- (20) Wu, C. J.; Liu, Y. F.; Zhang, W. F.; Zhang, C.; Chai, G. B.; Zhang, Q. D.; Mao, J.; Ahmad, I.; Zhang, S. S.; Xie, J. P. Encapsulation and Controlled Release of Fragrances from MIL-101(Fe)-Based Recyclable Magnetic Nanoporous Carbon. *Colloids Surfaces A Physicochem. Eng. Asp.* **2022**, *640* (December 2021), 128453.
- (21) Zhang, B.; Chen, H.; Hu, Q.; Jiang, L.; Shen, Y.; Zhao, D.; Zhou, Z. CelluMOFs: Green, Facile, and Flexible Metal-Organic Frameworks for Versatile Applications. *Adv. Funct. Mater.* **2021**, *31* (43).
- (22) Xiong, L.; Liu, J.; Yu, M.; Li, S. Improving the Corrosion Protection Properties of PVB Coating by Using Salicylaldehyde@ZIF-8/Graphene Oxide Two-Dimensional Nanocomposites. *Corros. Sci.* **2019**, *146* (February 2018), 70–79.
- (23) Costa, S. P. G.; Soares, O. S. G. P.; Aguiar, C. A.; Neves, I. C. Fragrance Carriers Obtained by Encapsulation of Volatile Aromas into Zeolite Structures. *Ind. Crops Prod.* **2022**, *187* (PA), 115397.
- (24) Chen, Q.; Chen, Q. W.; Zhuang, C.; Tang, P. P.; Lin, N.; Wei, L. Q. Controlled Release of Drug Molecules in Metal-Organic Framework Material HKUST-1. *Inorg. Chem. Commun.* **2017**, *79*, 78–81.
- (25) Yu, L.; Qiao, N.; Zhao, J.; Zhang, H.; Tian, F.; Zhai, Q.; Chen, W. Postharvest Control of *Penicillium expansum* in Fruits: A Review. *Food Biosci.* **2020**, *36* (September 2019), 100633.
- (26) Tsai, C. W.; Langner, E. H. G. The Effect of Synthesis Temperature on the Particle Size of Nano-ZIF-8. *Microporous Mesoporous Mater.* **2016**, *221*, 8–13.

CHAPTER 5

Mixed-metal MUV-2 derivatives

5.1. Introduction

As discussed in previous chapters of this Thesis, the encapsulation of active molecules into MOF scaffolds following an impregnation procedure is a valuable methodology for their loading, preservation, and controlled release. This direct infiltration method presents the advantage of using pre-formed MOFs without modification of the synthetic procedure and avoiding post-synthetic functionalization. A general simple process consists of mixing the pristine porous materials and the biomolecule solution, which results on the desired composite product. However, this infiltration method is limited by the dimensions of the selected molecule, which must fit the pore size of the framework and not exceed the pore window. Therefore, the selection of a mesoporous framework, featuring prominent porosity and large accessible pore windows can be a viable strategy to overcome this size limitation.

Hierarchical mesoporous MOFs with adjustable mesopores (either intrinsic mesopores or introduced mesoporous defects) have shown great potential for the encapsulation of bioactive macromolecules.¹ For example, Chen and co-workers immobilized the peptide hormone insulin in NU-1000 (**Figure 5.1.1**), obtaining a high loading of ~ 40 wt % in only 30 min by simply soaking the MOF particles in an insulin solution. The obtained composite preserved the majority of the insulin activity upon harsh conditions mimicking the stomach environment while releasing the hormone in conditions that imitate the bloodstream.²

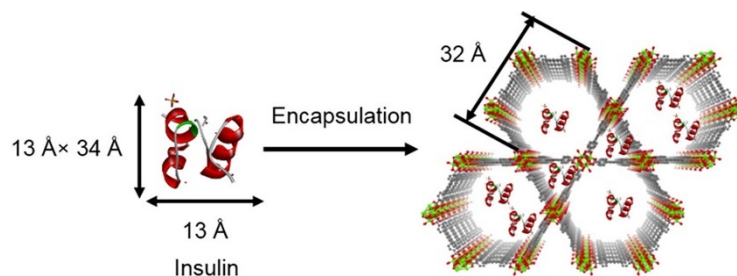


Figure 5.1.1 Schematic representation of insulin encapsulation in the mesopores of NU-1000. Reproduced from reference 2.

Using a flexible framework can be another plausible strategy to encapsulate biomolecules with higher dimensions. Recently, Qi and co-workers encapsulated lysozyme (**Figure 5.1.2**) in MIL-53(Fe) microparticles and incorporated them into polylactic acid polymer using a direct impregnation technique. The successful encapsulation is based on the ability of the MIL-53(Fe) framework to reversibly adapt its pore size upon different stimuli (guest adsorption, temperature, pH).^{3,4} The composite microparticles endowed the film with better lysozyme stability, antibacterial and anti-adhesion properties.⁵

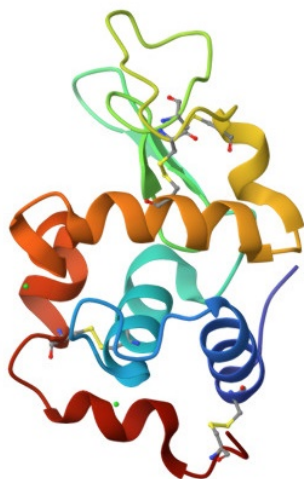


Figure 5.1.2. Tertiary structure of lysozyme (PDB ID-3ZEK).

Since the main advantage of mesoporous MOFs relies in their adsorptive storage ability, the encapsulation of macrobiomolecules for drug delivery is not the only application that can be benefitted from the presence of larger pores. Hierarchical porous materials can result promising candidates for catalysis, separation, and sorption applications.⁶ Particularly, the steady accumulation of carbon dioxide in the atmosphere in the last decades has generated substantial environmental concerns. However, CO₂ is also a recyclable substance with a highly appealing application for the chemical sector as a carbon source, and current carbon capture systems are inefficient,

energy-intensive, and costly. Thus, CO₂ capture systems must be improved, and mesoporous MOFs may present great potential for CO₂ capture due to their increased surface area and enhanced mass diffusion.⁷

Among the few mesoporous hierarchical MOFs reported to date, a tetrathiafulvalene (TTF)-based MOF named MUV-2, has been reported in our group. MUV-2 crystallises in the space group $P\bar{6}2m$ and consists of 6-connected $[\text{Fe}_3(\mu_3\text{-O})(\text{COO})_6]$ SBUs and tetratopic TTFTB ligands, constituting a 4,6-connected network with ttp topology. Microporous channels of *ca.* 1 nm are orthogonal to mesoporous channels of *ca.* 3 nm (**Figure 5.1.3**), leading to a structure with a calculated free volume of *ca.* 82 %, that translates into a reported experimental BET surface for this material of 1200 m²·g⁻¹. MUV-2 is a highly stable material, both thermally (ligand decomposition and structure collapse occurs at *ca.* 350 °C) and chemically (the PXRD pattern of the material is maintained after exposure to aqueous solutions with pH values ranging from 2 to 11 and in different organic solvents for 24 h).⁸

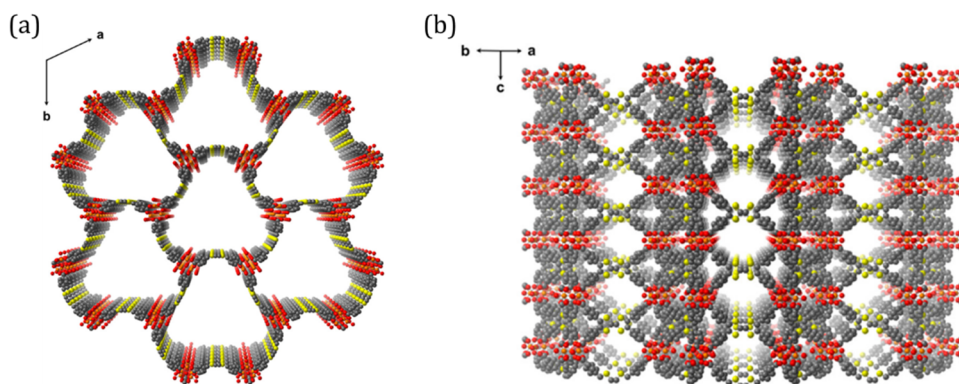


Figure 5.1.3. Overview of the crystal structure of MUV-2 showing the hexagonal mesoporous channels along the *c*-axis (a) and microporous channels orthogonal to the mesoporous ones (b). The grey, yellow, red, and orange colours correspond C, S, O, and Fe, respectively. Reproduced from reference 9.

The remarkable chemical stability of MUV-2 upon solvent exposure gives also rise to a breathing behaviour in the porous structure that is based on the flexibility of the TTFTB ligands, becoming much more planar upon solvent adsorption, and also on the partial rotation of the $\text{Fe}_3\text{O}(\text{COO})_6$ SBUs (**Figure 5.1.4**).⁹

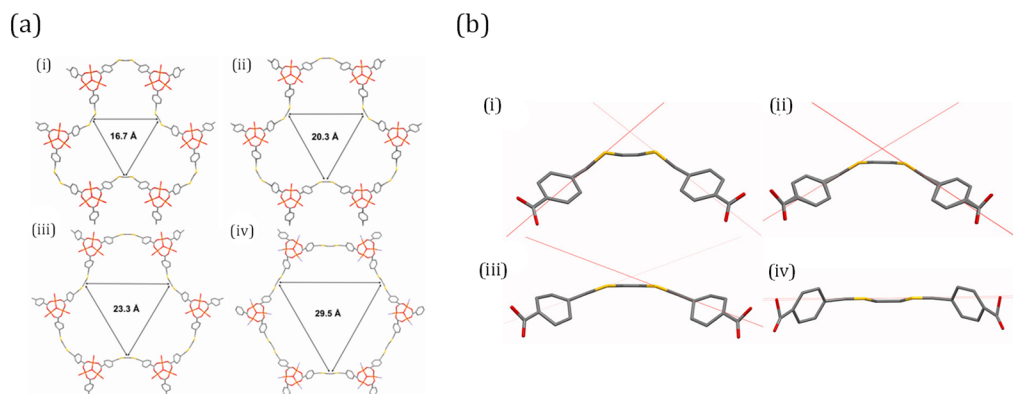


Figure 5.1.4. Crystal view of the pore opening evolution of MUV-2 (a) with the corresponding partial views of the TTFTB ligand for the crystal structures (b) highlighting the dihedral angles between the planes formed by the two dithiol rings ($\theta = 69^\circ, 54^\circ, 41^\circ$, and 9° , for (i), (ii), (iii) and (iv), respectively). Reproduced from reference 9.

The breathing motion of the structure also impacts the electrochemical properties of MUV-2, offering the possibility to tune them by the effect of different solvents. Furthermore, the improved catalytic activity of MUV-2 over the widely utilized MIL family as heterogeneous catalysts has been demonstrated for the aerobic oxidation of dibenzothiophene (DBT) using long chain alkanes as solvents.

As previously discussed, the combination of the mesoporous channels of *ca.* 3 nm of diameter in the structure and its breathing behaviour upon solvent exposure makes MUV-2 an interesting plausible candidate for the encapsulation of larger active molecules. However, the synthesis of this material relies in using harmful DMF as a solvent, and as discussed in Chapter 2 regarding the synthesis of UiO-66 and its aminated derivative, this solvent

is very difficult to exchange. Thus, advances towards greener synthetic routes are an essential step towards the implementation of MUV-2 in specific applications, since more scalable processes can be considered.

One possibility to further extend the array of applications of MUV-2, and expand its chemistry, relies on the modification of its framework. Essentially, by replacing one of the iron centres in the structure with a divalent metal, a mixed-metal MOF (MM-MOF) with tunable properties that retains the mesoporous structure is obtained. By definition, MM-MOFs contain at least 2 different metal ions in any part of their structure.¹⁰ In the literature, the fabrication of MM-MOFs has been conducted following either one-pot synthesis or post-synthesis modification.^{11,12} When compared to homometallic MOFs, MM-MOFs can take advantage of the complexity and synergism obtained from the presence of various metal ions in the structure of MOFs, and may exhibit higher stability and an improved performance in various applications, particularly in gas storage and separation,¹³ catalysis,¹⁴ sensing,¹⁵ and construction of photoactive materials.¹⁶ Particularly in the field of gas storage and separation, mesoporous MM-MOFs would present an advantage for not only possessing high uptake of gases, but also tunable functionality to selectively adsorb different guest molecules.

In this Chapter 5, two main objectives will be pursued. On the one hand, the obtention of Mixed-Metal MUV-2 analogues (MM-MUV-2) will be targeted. On the other hand, the elusive green chemistry synthesis of MUV-2(Fe) and its derivatives will be also explored, substituting DMF by the more convenient isopropanol solvent. The obtained materials will be thoroughly characterized, and their CO₂ uptake capacity will be assessed.

Then, the suitability of the *green* materials as larger biomolecule carriers will be evaluated by means of lysozyme encapsulation following a direct impregnation methodology.

5.2. Results and discussion

5.2.1. Standard synthesis of mixed metal MUV-2 derivatives

A well-known method for the synthesis of mixed-valence oxo-trimer based MOFs consists in replacing, in a controlled manner, some of the constitutive Fe^{III} cations by other octahedrally coordinated metal cations.¹⁷ Following the same protocol, for the synthesis of mixed metal MUV-2 derivatives, the preparation of the heterometallic building block $(\text{Fe}_2\text{M}^{\text{II}}\text{O})(\text{CH}_3\text{COO})_6(\text{H}_2\text{O})_3$ ($\text{M}=\text{Ni}$ or Co) was first carried out by direct mixture of Fe^{III} acetate with an equimolar amount of M^{II} acetate tetrahydrate dissolved in water. The reaction mixture is magnetically stirred at room temperature until the precipitation of a powder is observed - the mixed acetate trimer precipitates due to the insertion of the divalent metal, achieving the electroneutrality of the structure. The obtained $(\text{Fe}_2\text{M}^{\text{II}}\text{O})(\text{CH}_3\text{COO})_6(\text{H}_2\text{O})_3$ is then mixed with H_4TTFTB ligand in DMF to form the corresponding Mixed-Metal MUV-2 with the addition of acetic acid as a modulator in a solvothermal procedure. The resulting dark brown powder was collected by filtration and thoroughly washed before being filtered and left to dry at air. Activation of the samples consisted in thermal treatment at 120 °C for three hours. Light brown crystalline powders were obtained (**Figure 5.2.1**), in contrast with the characteristic black crystalline powder of MUV-2(Fe).



Figure 5.2.1. Image of the obtained MM-MUV-2 derivatives: MUV-2(Fe/Co) (left), MUV-2(Fe/Ni) (centre), in comparison with MUV-2(Fe) crystalline powders (right).

5.2.2. Physical characterization of the materials

To confirm the successful synthesis of MUV-2 mixed metal derivatives, Infrared Spectroscopy (IR), Thermogravimetric Analysis (TGA), Inductively Coupled Plasma Mass Spectrometry (ICP-MS), Energy-Dispersive X-ray Analysis, and Scanning Electron Microscopy (SEM) studies were performed.

Infrared Spectroscopy. **Figure 5.2.2a** compares the FTIR spectra of the iron-based MUV-2 and the mixed-metal analogous materials in the 1800-400 cm^{-1} region. The spectra of all the materials are virtually the same: the characteristic bands in the range of 1655-1400 cm^{-1} correspond to the coordination of the metallic clusters to the carboxylic groups of the ligand. The $\nu_{\text{C=O}}$ band located at 1659 cm^{-1} in the MUV-2(Fe) spectrum evidences the presence of DMF remaining likely in the pores of the framework. **Figure S5.1** exhibits how this 1659 cm^{-1} band is also present in the MM-MUV-2 derivatives in the as-synthesised materials but does not appear after washing and thermal activation of the samples. The main difference in the IR spectra of the materials lies in the asymmetric stretch region (800-400 cm^{-1}). Mainly, the $\nu_{\text{as}}(\text{Fe}_3\text{O})$ vibration band in MUV-2(Fe) is split in two peaks at 632 and 621 cm^{-1} respectively, suggesting a different interaction between the solvent molecules and the accessible Fe^{III} sites. This could be attributed to the binding of DMF molecules to some of the Fe^{III} centres, as discussed previously in Chapter 3 regarding the carvacrol coordination to the iron centres of MIL-100. This effect is much more evident in the case of the MM-MUV-2 derivatives (**Figure 5.2.2b**), as this difference arises mainly due to the insertion of the divalent metal. The trimer-related band shifts to lower wavenumber, as the electronic density of the $\text{M}^{\text{II}}\text{-O}$ bond increases - thus vibrating at lower frequencies. The band split for MUV-2(Fe/Co) is located at 632 and 599 cm^{-1} , whereas the same band appears at 632 and 603 cm^{-1} in MUV-2(Fe/Ni).

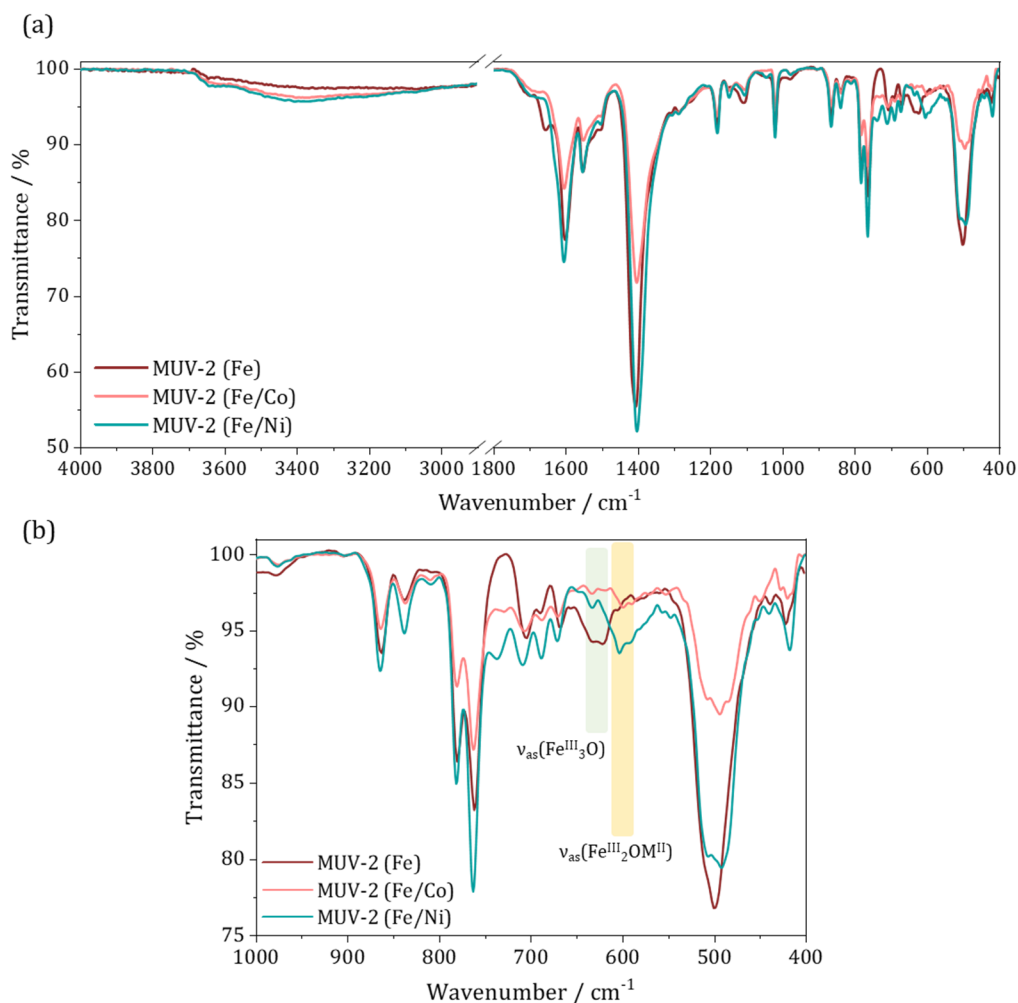


Figure 5.2.2. (a) FT-IR spectra of MUV-2(Fe/Co) (pink) and MUV-2(Fe/Ni) (teal) after DMF/EtOH washing and thermal treatment at 120 °C for 3h, compared with MUV-2(Fe) (red). (b) 1000-400 cm⁻¹ section of the same spectra, focusing on the asymmetric stretching region of the metal trimers.

Thermogravimetric Analysis. Thermal profiles of activated MM-MUV-2 derivatives are illustrated in **Figure 5.2.3**. The comparison of the mixed-valence derivative MOFs and MUV-2(Fe) before and after activation are displayed in **Figure S5.2**, exhibiting an analogous thermal behaviour to MUV-2(Fe). Both materials present similar thermal profiles, with a *ca.* 8 % mass loss between room temperature and 130 °C that can be related with

ambient humidity and ethanol molecules remanent from the washing protocol. Ligand decomposition occurs at *ca.* 320 °C, leaving in both cases an inorganic residue of approximately 19 % of the mass at 700 °C, in good agreement with the proposed $(\text{TTFTB})_3[(\text{Fe}^{\text{III}}_2\text{M}^{\text{II}}\text{O})(\text{H}_2\text{O})_3]_2$ molecular formula (see **Table 5.2.1**).

Table 5.2.1. Thermogravimetric analysis of the obtained MM-MUV-2 materials, summarizing the ligand decomposition temperature and inorganic residue value, in comparison with the theoretical value extracted from the molecular formula.

	Ligand decomp. T / °C	Inorganic residue (D.B.) / % (w/w)
MUV-2(Fe/Co) (theo)	-	19.0
MUV-2(Fe/Co)	320	19.1
MUV-2(Fe/Ni) (theo)	-	19.0
MUV-2(Fe/Ni)	316	19.6

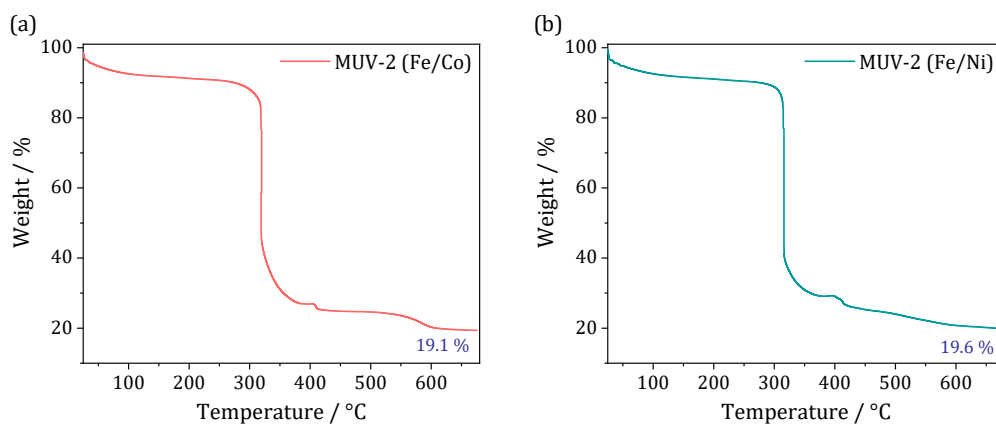


Figure 5.2.3. Thermal decomposition profiles of MUV-2(Fe/Co) (a) and MUV-2(Fe/Ni) (b) from 25 to 700 °C.

Inductively Coupled Plasma Mass Spectrometry. The metallic ratio of the mixed-metal compounds was evaluated by means of ICP-MS after MW-assisted acid digestion of the samples. Analyses of MM-MUV-2 (Fe/Co) revealed a Fe/Co ratio of 2.15/1. For MM-MUV-2 (Fe/Ni), a Fe/Ni ratio of 2.17/1 was obtained, further confirming the proposed $(\text{TTFTB})_3[(\text{Fe}^{\text{III}}_2\text{M}^{\text{II}}\text{O})(\text{H}_2\text{O})_3]_2$ molecular formula. **Table 5.2.2** summarizes the results.

Table 5.2.2. ICP-MS Results.

Sample	Fe / $\text{mg}\cdot\text{g}^{-1}$	M^{II} / $\text{mg}\cdot\text{g}^{-1}$	Fe : M^{II} molar ratio
MUV-2 (Fe/Co)	189.4 ± 0.9	87.9 ± 0.8	2.15 : 1
MUV-2 (Fe/Ni)	195.1 ± 1.3	89.9 ± 0.4	2.17 : 1

Scanning Electron Microscopy. The morphology and dimensions of the particles were assessed with Scanning Electron Microscopy (SEM). As **Figure 5.2.4** showcases, the particles of both materials present a needle-like shape with more well-defined borders in the case of MUV-2(Fe/Co) (**Figures 5.2.4a** and **5.2.4b**), specially for the larger particles. In view of the variety in particle dimensions (from nm to μm), it can be concluded that these synthesis do not provide a controlled size, for any mixed-metal derivative. In comparison, the tendency is for a smaller size in the case of MUV-2(Fe/Ni) (**Figures 5.2.4c** and **5.2.4d**).

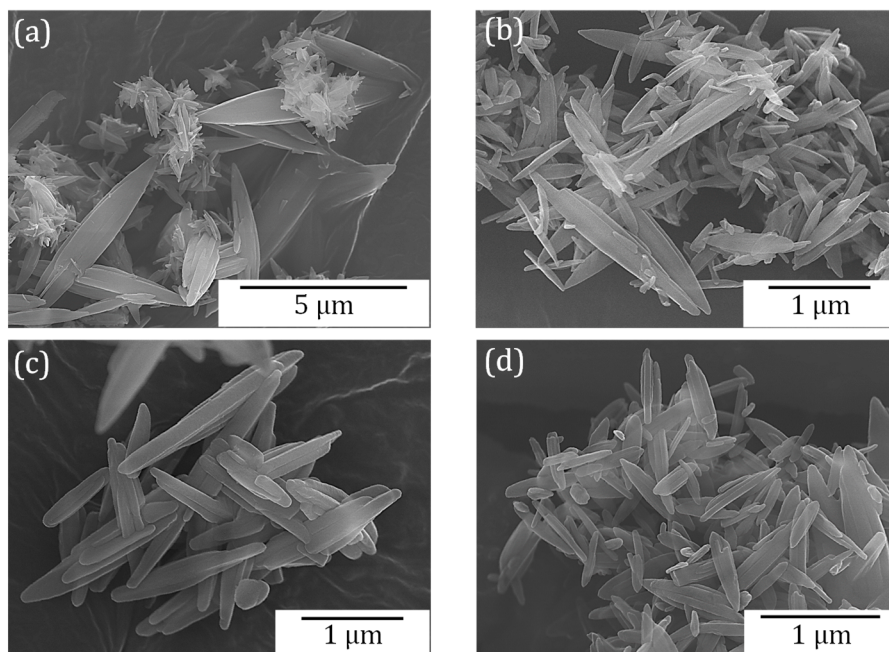


Figure 5.2.4. Scanning Electron Microscopy images of (a, b) MUV-2(Fe/Co) and (c, d) MUV-2(Fe/Ni) particles. Scale bar is 5 μm for image (a) and 1 μm for the rest of images.

Energy-dispersive X-ray spectroscopy. In addition, EDX measurements in both mixed metal materials revealed a S/Fe/M^{II} ratio of 7/2/1, showcasing a higher TTFTB₄⁻⁴ content than expected when compared with the S/Fe ratio of MUV-2, which is 6/3. The absence of ligand contribution in the thermal profile of both washed mixed-metal derivatives, as well as the absence of a free ligand band in their IR spectra discards the presence of free ligand inside the pores. This points in the direction of possible cluster defects in the structure, which is indicative of the chemical robustness of the framework. **Table 5.2.3** summarizes the results.

Table 5.2.3. EDX results.

Sample	% S	% Fe	% M ^{II}
MUV-2 (Fe/Co)	71.3 ± 2.7	20.8 ± 1.8	7.9 ± 0.9
MUV-2 (Fe/Ni)	73.0 ± 0.4	20.7 ± 0.2	6.2 ± 0.3

5.2.2. Chemical and thermal stability – Powder X-ray Diffraction

The crystalline structure of the materials was compared by means of PXRD with MUV-2(Fe).

Figure 5.2.5 displays the diffraction pattern of MUV-2(Fe/Co) and MUV-2(Fe/Ni) samples after washing and thermal treatment at 120 °C for 3 h, as compared with the simulated diffraction pattern of MUV-2(Fe).⁹ It is worth remarking that the main diffraction peak, corresponding to the (1 0 0) reflection, in MUV-2(Fe/Co) and MUV-2(Fe/Ni) appears at $2\theta = 3.35^\circ$ after solvent removal, whereas the contracted MUV-2(Fe) crystal structure presents its (1 0 0) peak at $2\theta = 3.45^\circ$. The (2 -1 0) and (2 0 0) associated reflections with diffraction peaks at $2\theta = 6.0$ and 6.92° also appear shifted in the experimental diffraction pattern, with 2θ values of 5.70 and 6.63° , respectively.

These minor differences in the diffraction peak positions may suggest that the insertion of the divalent metal slightly influences the MUV-2 crystal structure. Nevertheless, the rest of the diffraction pattern of the mixed valence samples matches perfectly with the simulated MUV-2(Fe) reference, confirming that the novel materials are isostructural with the MUV-2 framework after the insertion of the divalent cation into the secondary building unit of the framework, and its crystalline structure is overall maintained.

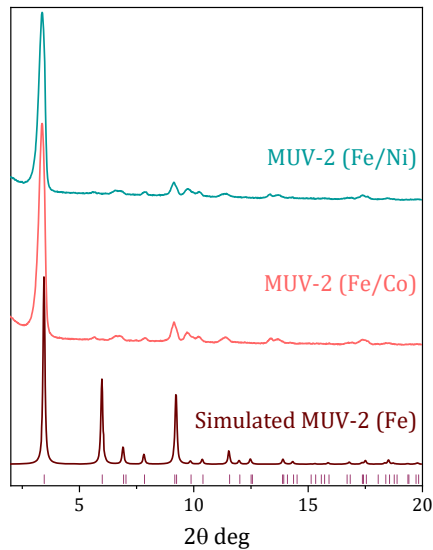


Figure 5.2.5. XRPD pattern of MUV-2 (Fe/Co) (pink) and MUV-2 (Fe/Ni) (teal) after thermal treatment at 120°C for 3h, compared with the simulated diffraction pattern of MUV-2 (Fe) obtained from crystallographic data (red).⁹

PXRD was also employed to evaluate the if the characteristic breathing behaviour of MUV-2(Fe) upon solvent adsorption (**Figure 5.2.6**) is also present in the mixed metal materials.

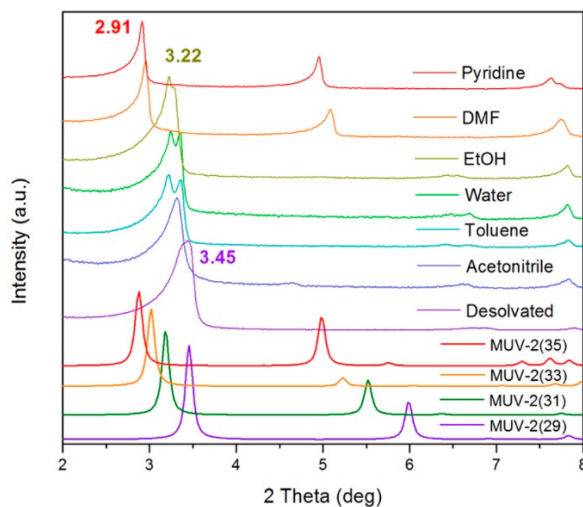


Figure 5.2.6. Evolution of PXRD patterns for MUV-2(Fe) after soaking with various solvents at room temperature, compared with simulated diffraction patterns of MUV-2(Fe) in different states of pore contraction. Reproduced from reference 9.

As featured in **Figures 5.2.7a** and **5.2.7b**, and previously discussed, the characteristic (1 0 0) peak of the mixed-metal MOFs appears at $2\theta = 3.35^\circ$ after solvent removal, whereas the contracted MUV-2(Fe) crystal structure presents its (1 0 0) peak at $2\theta = 3.45^\circ$ after thermal treatment.⁹ This peak shifts toward lower degrees after MM-MUV-2 samples are soaked in different solvents during 2 h. In view of this result, the possibility of MM-MUV-2 to reversibly undergo the same breathing phenomenon that MUV-2(Fe) presents by exposing the material to different solvents was explored. Soaking the materials in pyridine or DMF provokes a shift in the (100) peak to $2\theta = 2.89^\circ$, analogous to MUV-2(Fe) which showcases that peak at $2\theta = 2.91^\circ$. Essentially, pyridine and DMF generate the largest pore opening while exposure to other different solvents (ethanol, water, toluene, and acetonitrile) yields intermediate pore apertures in the mixed-metal derivatives, following the same tendency as the iron-based material.

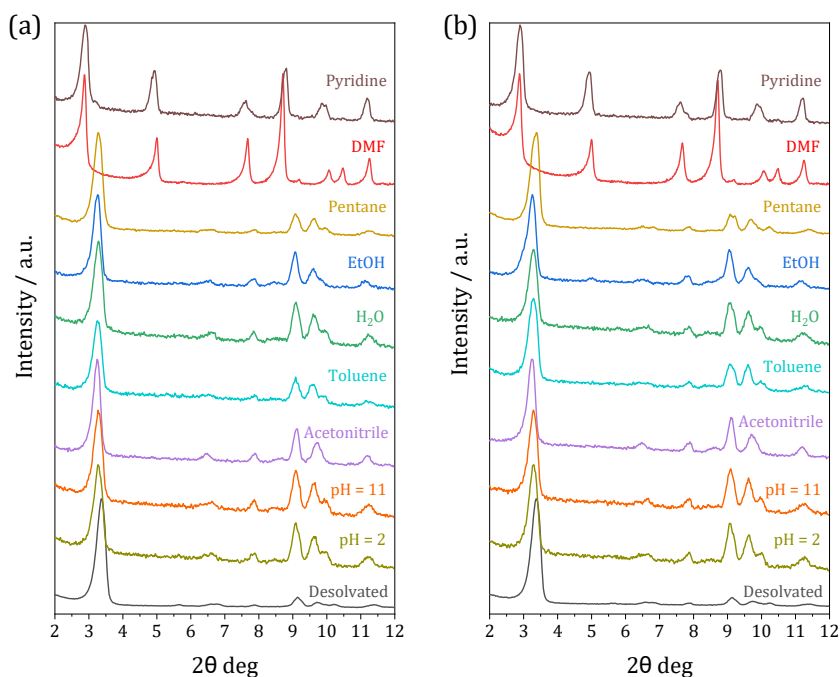


Figure 5.2.7. Evolution of PXRD patterns for MUV-2(Fe/Co) (a) and MUV-2(Fe/Ni) (b) after soaking the samples in various solvents at room temperature for 2h.

This breathing behaviour upon solvent exposure demonstrates that the solvent interactions that the inorganic $\text{Fe}_3\text{O}(\text{COO})_6$ SBUs experience remain unaffected in the case of the heterometallic $\text{Fe}_2\text{M}^{\text{II}}\text{O}(\text{COO})_6$ moieties after the cluster is modified.

The maintenance of the breathing phenomenon was evaluated after thermal treatment at different temperatures (**Figures 5.2.8** and **5.2.9**), and its reversibility was confirmed after soaking the samples in DMF. There is a drastic increase in the intensity of the (1 0 0) peak in all the thermally activated samples in comparison with the as-synthesized material, even when employing a relatively soft activation temperature of 80 °C, that does not further increase with higher temperatures. In both cases, the mixed-metal derivatives present optimal thermal stability up until 150 °C, maintaining their breathing behaviour as revealed by the (1 0 0) peak shift from $2\theta = 3.35^\circ$ to $2\theta = 2.89^\circ$. Upon activation at 200 °C and subsequent DMF exposure, MUV-2(Fe/Co) presents a second peak at $2\theta = 3.15^\circ$ (**Figure 5.2.8b**), suggesting a partial framework response to the DMF soaking.

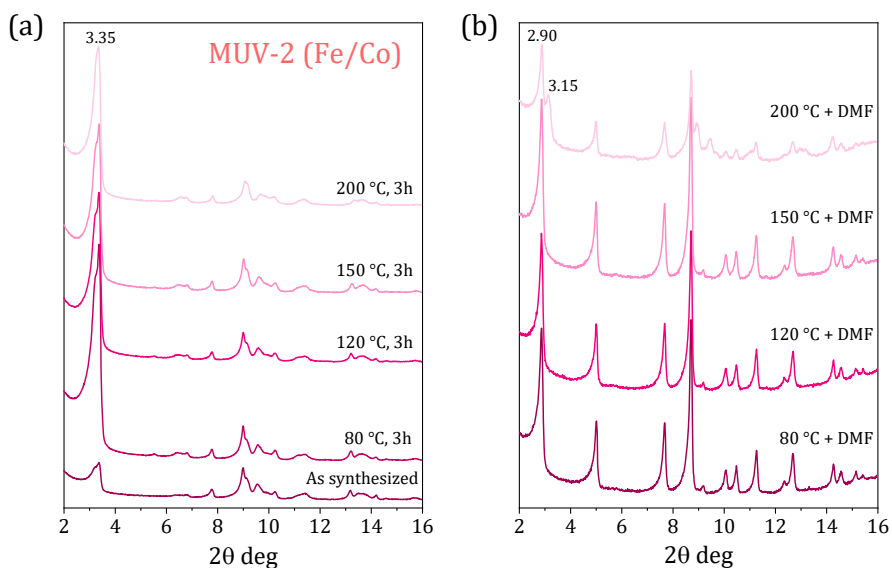


Figure 5.2.8. PXRD pattern of MUV-2(Fe/Co) upon thermal treatment at different temperatures for 3h (a) and upon DMF exposure of each sample (b).

In the case of MUV-2(Fe/Ni), after thermal treatment at 200 °C and DMF exposure, the main peak is located at $2\theta = 3.20^\circ$ (**Figure 5.2.9b**) and the relative intensity of the principal diffraction peak drastically decreases in comparison with the previous activation temperatures, meaning that the high temperature compromises the crystallinity and flexibility of the material to some extent. Upon DMF soaking, the main peak shifts to $2\theta = 3.16^\circ$ indicating the loss of breathing behaviour upon these conditions.

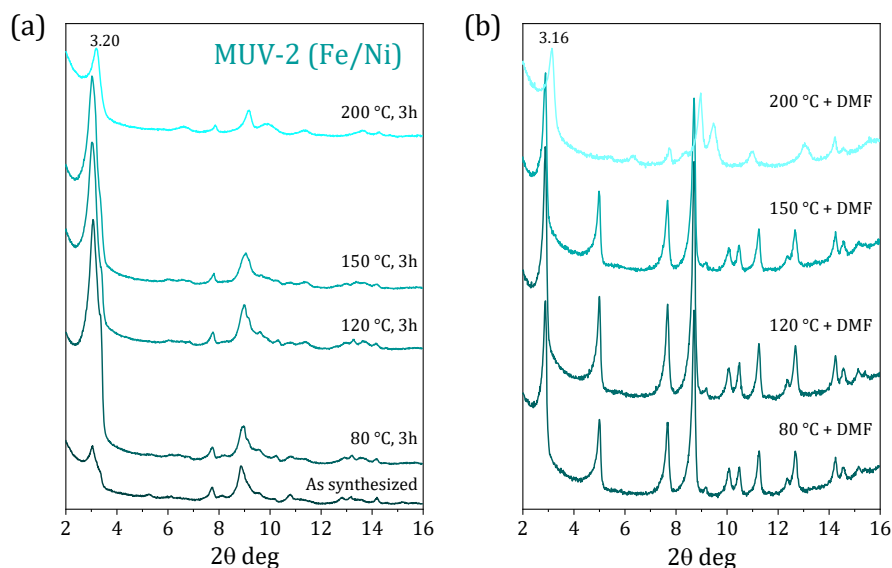


Figure 5.2.9. PXRD pattern of MUV-2(Fe/Ni) upon thermal treatment at different temperatures for 3h (a) and upon DMF exposure of each sample (b).

5.2.3. Magnetic Properties

In order to investigate how the insertion of the divalent cation could influence the magnetic behaviour of the MM-MUV-2 derivatives, magnetic characterization was carried out. The variation of the magnetic susceptibility with the temperature between 2 and 300 K under a 0.1 T magnetic field was measured, as well as the magnetization upon variation of the magnetic field between 7 and -7 T at 2 K. The temperature dependence of the magnetic susceptibility upon increasing magnetic fields is showcased in **Figures S5.3**

and **S5.4**. The reported $\chi_m T$ product of MUV-2 at 300 K ($11.9 \text{ emu}\cdot\text{K}\cdot\text{mol}^{-1}$)⁸ is close to the theoretical expected value for three Fe^{III} non-interacting $S = 5/2$ spins ($\chi_m T = 13.125 \text{ emu}\cdot\text{K}\cdot\text{mol}^{-1}$). Upon cooling, $\chi_m T$ value strongly decreases in agreement with the strong antiferromagnetic $\text{Fe}\cdots\text{Fe}$ coupling within the quasi-isolated Fe^{III} trimers (**Figure 5.2.10**).

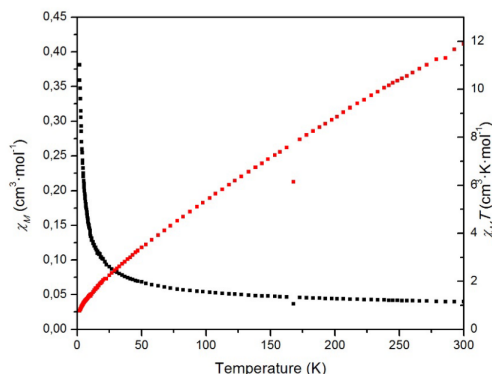


Figure 5.2.10. Magnetic susceptibility χ_m (black line) and $\chi_m T$ (red line) versus temperature variation of MUV-2(Fe) at 0.1 T. Reproduced from reference 8.

MUV-2 (Fe/Co) (**Figure 5.2.11**) showcases a similar magnetic behaviour, where the $\chi_m T$ product at 300 K is $8.58 \text{ emu}\cdot\text{K}\cdot\text{mol}^{-1}$. This value would be in agreement with a LS configuration for the Co^{II} cation inserted in the trimer cluster, as deduced from the theoretical expected $\chi_m T$ value for the LS and the HS, respectively 9.125 and $10.625 \text{ emu}\cdot\text{K}\cdot\text{mol}^{-1}$. However, the spin configuration of the inserted Co^{II} centre is expected to be HS due to the water molecules coordinated to the cluster. This result would point towards a cluster defect configuration in the framework, as previously suggested in the EDX discussion.

Regarding the magnetization measurements at 2 K, a saturation magnetization value of $3.97 \mu_B$ is obtained at 7 T for MUV-2(Fe/Ni), whereas the material does not present any magnetic ordering characteristics.

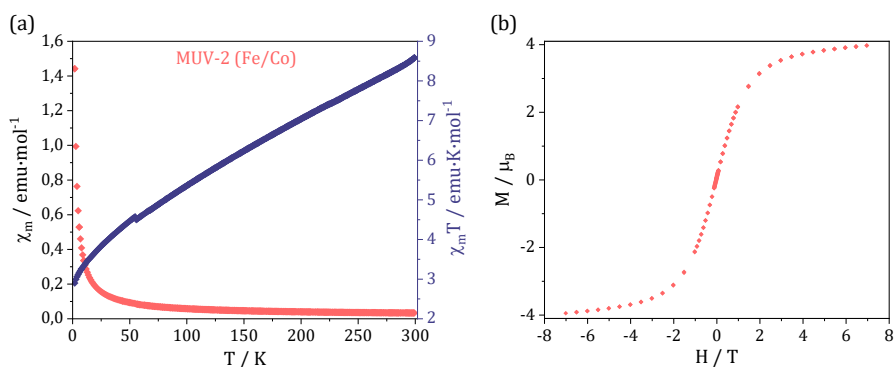


Figure 5.2.11. (a) Magnetic susceptibility χ_m (pink) and $\chi_m T$ (purple) versus temperature variation at 0.1 T and (b) magnetization curves at 2 K of MUV-2(Fe/Co).

MUV-2 (Fe/Ni) magnetic profile (**Figure 5.2.12**) exhibits an even more pronounced paramagnetic behaviour. The $\chi_m T$ product at 300 K of this MM-MUV-2 derivative is 6.41 $\text{emu}\cdot\text{K}\cdot\text{mol}^{-1}$. This value is unexpectedly low, since the theoretical expected result is 9.75 $\text{emu}\cdot\text{K}\cdot\text{mol}^{-1}$, which again points to the presence of cluster defects in the framework and/or the excess of diamagnetic ligands in the sample.

Regarding the magnetization measurements at 2 K, the saturation magnetization value is 3.50 μ_B at 7 T, and analogous to MUV-2(Fe/Co), the nickel derivative does not present any magnetic ordering characteristics.

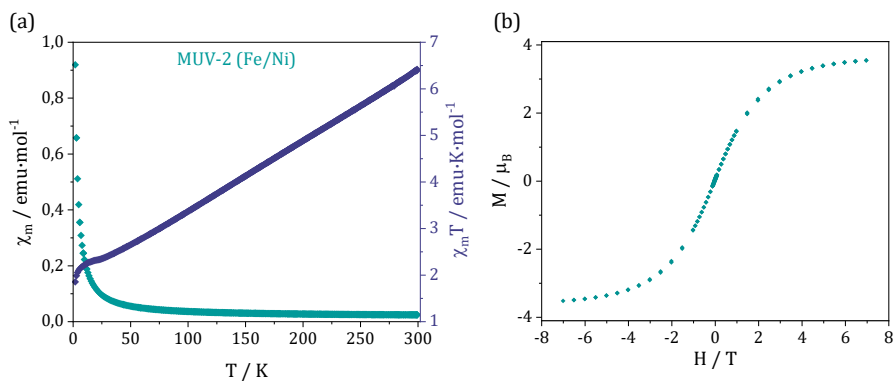


Figure 5.2.12. (a) Magnetic susceptibility χ_m (teal) and $\chi_m T$ (purple) versus temperature variation at 0.1 T and (b) magnetization curves at 2 K of MUV-2(Fe/Ni).

5.2.4. Single-gas sorption studies

Volumetric measurements. Single-gas low pressure sorption studies were performed on MM-MUV-2 as well as on MUV-2(Fe) for comparison. **Figure 5.2.13a** illustrates the N₂ sorption study at 77 K. The porosity of the framework is not compromised after the metal exchange, as the Brunauer-Emmett-Teller (BET) surface area values of the mixed-metal compounds – 1228 and 1249 m²·g⁻¹ for MUV-2(Fe/Co) and MUV-2(Fe/Ni), respectively – maintain a similar sorption behaviour as the iron-based MUV-2 structure (BET surface area: 1176 m²·g⁻¹). The hierarchical porous structure of the compounds is hinted by a slight change in the slope of the 0-0.1 region of relative pressure values. This effect is present in all three materials, and it is more obvious in the logarithmic representation of the N₂ adsorption isotherm (**Figure 5.2.13b**), where three different slopes can be observed in the adsorption profile of all the materials. The particle size decreases with the use of the mixed-metal trimers in the synthetic procedure (as previously discussed in section 5.2.2), and it is also reflected in the N₂ adsorption profile of the MM-MUV-2 derivatives, as an increase in the N₂ uptake is observed in the 0.9-1 region for these materials in comparison with MUV-2(Fe), denoting that the gas is also filling the interparticular space. Taking this effect into account, the maximum N₂ uptake of the mixed-valence materials is determined at 0.9 P/P₀ value, resulting in adsorbed quantities of 16.3 , 16.6 and 14.7 mmol·g⁻¹ for MUV-2(Fe/Co), MUV-2(Fe/Ni) and MUV-2(Fe), respectively.

Pore size distribution analysis of MM-MUV-2 derivatives, as well as MUV-2(Fe) for comparison, was carried out employing the Horvath-Kawazoe method with cylinder pore geometry (Saito-Foley correction)^{18,19} and is showcased in **Figure 5.2.14**. In all cases, 3 PSD centres can be observed with similar attributed widths. **Table 5.2.4** summarizes the sorption capacity of the materials and their pore widths.

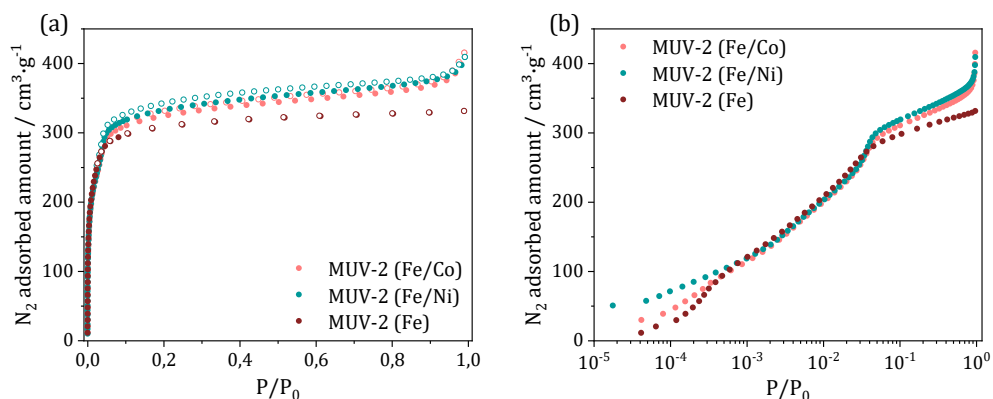


Figure 5.2.13. (a) N_2 volumetric low-pressure single-gas isotherm on MUV-2(Fe) (red), MUV-2(Fe/Co) (pink) and MUV-2(Fe/Ni) (teal) at 77 K (solid symbols for adsorption and open ones for desorption). Activation protocol consists of heating at 393 K under vacuum overnight. (b) Logarithmic representation of the same N_2 adsorption isotherm.

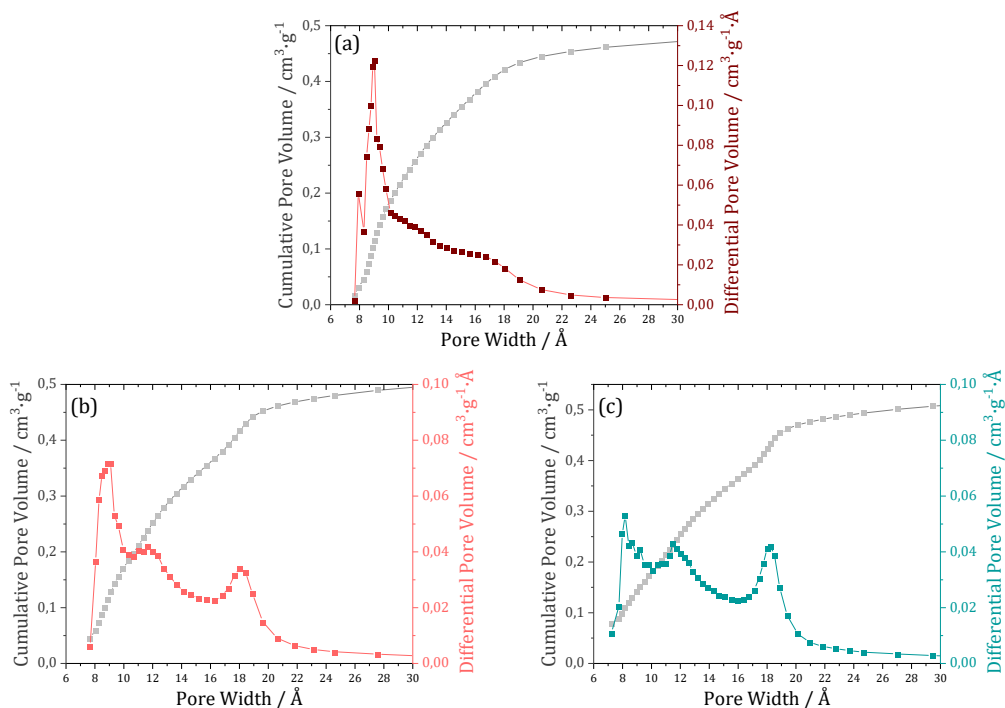
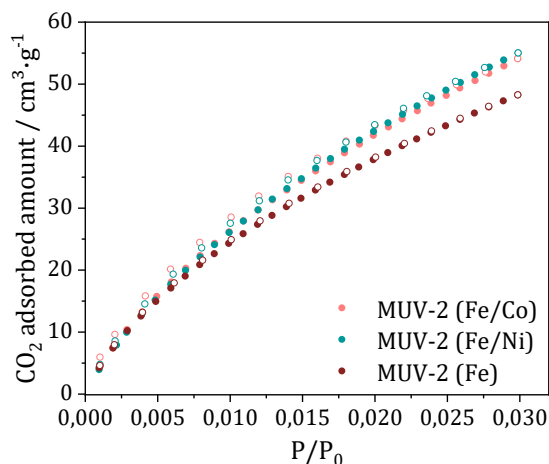


Figure 5.2.14. Pore size distribution analysis of (a) MUV-2(Fe), (b) MUV-2(Fe/Co), and (c) MUV-2(Fe/Ni) employing the Horvath-Kawazoe method.

Table 5.2.4. N₂ sorption capacity and pore size distribution of all the MUV-2 materials.

Material	BET surface / m ² ·g ⁻¹	N ₂ uptake capacity / mmol·g ⁻¹	Pore width / Å
MUV-2(Fe)	1176	14.7	9.1 / 11.9 / 16.2
MUV-2(Fe/Co)	1228	16.3	9.1 / 11.7 / 18.1
MUV-2(Fe/Ni)	1249	16.6	8.2 / 11.5 / 18.3

CO₂ sorption analysis was carried out at 273 K (**Figure 5.2.15**) resulting in this case in a sorption profile with static adsorption capacities of 2.41, 2.45 and 2.15 mmol·g⁻¹ respectively for MUV-2 (Fe/Co), MUV-2 (Fe/Ni), and MUV-2(Fe) at atmospheric pressure. The porous hierarchy of the materials is not observed in these experiments due to the much higher saturation pressure of CO₂ in the experimental conditions (3485.1 kPa at 273 K vs 101.3 kPa at 77 K in the case of N₂).

**Figure 5.2.15.** CO₂ volumetric low-pressure single-gas isotherm on MUV-2(Fe) (red), MUV-2(Fe/Co) (pink) and MUV-2(Fe/Ni) (teal) at 273 K (solid symbols for adsorption and open ones for desorption). Activation protocol consists of heating at 120 °C under vacuum overnight.

Gravimetric measurements. Single-gas gravimetric sorption studies were performed on MM-MUV-2 as well as on MUV-2(Fe), synthesized following the same procedure (**Figure 5.2.16**), at different temperatures (10, 25, 40, 50 °C), up until 10 bar. The three materials present a similar CO₂ sorption profile and capacity. The values of maximum CO₂ adsorption capacity of the materials at 10 °C and 10 bar are 6.61, 4.94 and .67 mmol·g⁻¹ for MUV-2(Fe/Co), MUV-2(Fe/Ni) and reported MUV-2(Fe), respectively.

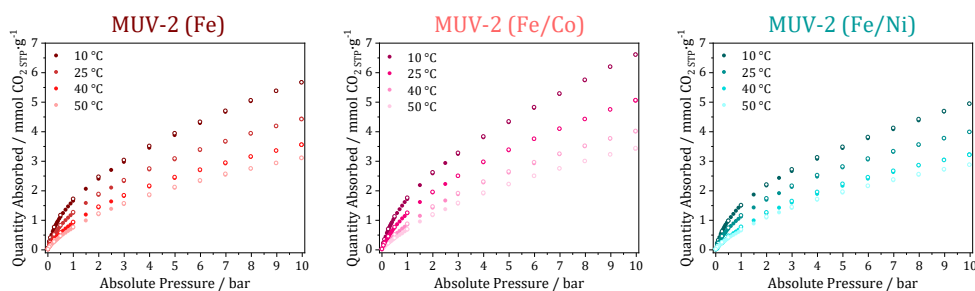


Figure 5.2.16. Gravimetric high-pressure CO₂ sorption isotherms on MUV-2(Fe) (red), MUV-2(Fe/Co) (pink), and MUV-2(Fe/Ni) (teal) at different temperatures up to 10 bar (solid symbols for adsorption and open ones for desorption). Activation protocol consists of heating at 120 °C under vacuum overnight.

Virial approximation is applied for fitting experimental data points from CO₂ isotherms. This approach is a polynomial fitting that provides a precise extrapolation of the adsorption constant at zero coverage (see equation below). A fourth-grade polynomial is able to properly describe the CO₂ isotherms studied at different temperatures (**Figure 5.2.17**).

$$\ln\left(\frac{P}{Q}\right) = a_0 + \frac{a_1}{T} + \left(b_0 + \frac{b_1}{T}\right) \cdot Q + \left(c_0 + \frac{c_1}{T}\right) \cdot Q^2 + \left(d_0 + \frac{d_1}{T}\right) \cdot Q^3 + \dots$$

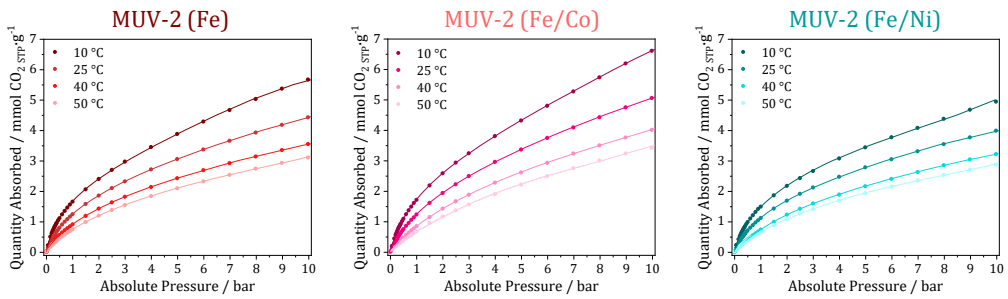


Figure 5.2.17. Virial equation fitting to CO₂ gravimetric single-gas adsorption isotherms of MM-MUV derivatives, compared with MUV-2(Fe) at different temperatures (solid symbols for experimental isotherm points and lines for the simulated isotherm obtained through the virial equation).

In addition, isosteric heat of adsorption for CO₂ was calculated according to the Clausius-Clapeyron equation using adsorption data collected at 283, 298, 313 and 323 K (see equation below).

$$q_{st} = R \cdot T^2 \cdot \left[\frac{\partial(\ln P)}{\partial T} \right]_{Q=cte} \equiv R \cdot \left[- \frac{\partial(\ln P)}{\partial(1/T)} \right]_{Q=cte}$$

The isosteric heat of adsorption at zero coverage was estimated to be 26, 29 and 25 kJ·mol⁻¹ for MUV-2(Fe/Co), MUV-2(Fe/Ni) and MUV-2(Fe), respectively (**Figure 5.2.18**).

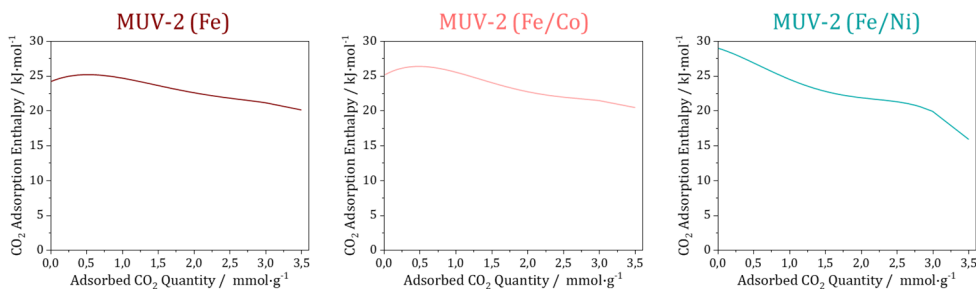


Figure 5.2.18. Isosteric heat of CO₂ adsorption of the materials, according to the Clausius-Clapeyron equation.

The calculated heat of adsorption in the three systems is within the typical range for physisorption of CO₂ on a MOF (see **Table 5.2.5**).²⁰ Thus, the interaction between these materials and the CO₂ molecules is mainly physisorptive in nature, without significant chemical association.

Table 5.2.5. CO₂ isosteric heat of adsorption at zero coverage ($-Q_{st}$) of selected MOFs, showcasing the type of interaction between the framework and the gas molecules. Data extracted from reference 20.

Material	Functionality type	$-Q_{st}$ (kJ·mol ⁻¹)
MIL-100(Cr)		62
MOF-74(Mg)		47
MIL-101(Cr)	Exposed cations	44
MOF-74(Co)		37
MIL-53(Al)		35
HKUST-1		35
MOF-5		34
MAF-2		27
CPL-2	Physisorption	26
NOTT-140		25
MOF-253		23
CuBTTri	Exposed cations	21
IRMOF-3	Amines	19

MUV-2 materials performance in adsorptive gas separation and selective CO₂, CH₄ and C₃H₆/C₃H₈ capture processes was evaluated by Breakthrough (BT) experiments. However, the results obtained for the three MUV-2 derivatives were not significant enough for these materials to be considered as good candidates for this type of applications.

The catalytic activity of MM-MUV-2 derivatives was explored for the aerobic oxidation of dibenzothiophene (DBT), however the poor chemical stability of the materials in the long chain alkanes employed as solvents for the reaction hindered this possible application as well.

In view of these limitations, efforts were focused on the obtention of the three MUV-2 derivatives following a *green* route to be employed in the encapsulation of bioactive macromolecules.

5.2.5. *Green synthesis and Lysozyme encapsulation*

Significant efforts to reproduce the synthesis of MUV-2(Fe) via *green* chemistry, *i.e.* employing less harmful solvents like alcohols, have been undertaken without obtaining the expected results. However, the green synthesis of the MM-MUV-2 derivatives has indeed been achieved by following the *standard* synthetic conditions described in section 5.2.1, but substituting the DMF solvent by isopropanol and lowering the reaction temperature from 105 to 80 °C. With this synthetic protocol, the application of these materials in the encapsulation of biomacromolecules can be carried out following a direct approach, avoiding any additional washing steps.

The performance of the *green* MM-MUV-2 derivatives as macrobiomolecule carriers was evaluated by performing a lysozyme encapsulation. As described in Chapter 3 of this Thesis, lysozyme, is an enzyme obtained from hen egg white with bacteriolytic and bactericidal activities that can be integrated in antimicrobial films for food conservation.^{21,22} In that chapter, lysozyme was *in situ* co-encapsulated with carvacrol to enhance the antibacterial performance of the carvacrol@MIL-100(Fe) composite. Nevertheless, it was observed that the

liberation of lysozyme was hindered by the poor diffusion through the MIL-100(Fe) porous structure due to the small window size of the framework, too small for the protein dimensions. The *in situ* immobilization strategy in that study was by MOF mineralization, *i.e.* growing the framework around the enzyme. After the results yielded by the infiltration methodology through all this Thesis, it was decided to apply this approach to encapsulate lysozyme into the MM-MUV-2 derivatives framework, taking advantage of the large accessible pore windows and superior capacity of the hierarchical mesoporous structure to encapsulate the larger biomolecule *via* impregnation methodology. The mesoporous channels of MM-MUV-2 derivatives (*ca.* 3 nm) along the *c* axis should be able to allocate the lysozyme macromolecule, with a hydrodynamic radius of *ca.* 2 nm.

In a general manner, lysozyme encapsulation was carried out by simply adding a lysozyme aqueous solution to an adequate amount of dry MM-MUV-2 particles and incubating the mixture for a period of time. The influence of the starting lysozyme concentration was evaluated by comparison of the encapsulation kinetic profile of two lysozyme solutions, with concentrations 10 and 50 mg·mL⁻¹. Encapsulation kinetics were followed by means of UV-Vis spectroscopy, following the lysozyme concentration in the encapsulation supernatant employing the BCA assay to quantify the enzyme (**Figure 5.2.19**). For [Ly]₀ = 50 mg·mL⁻¹, at shorter encapsulation times (0.5 to 6 hours) the lysozyme concentration seems to fluctuate, but it stabilizes after 24 h, decreasing in a *ca.* 12 % the lysozyme concentration. For [Ly]₀ = 10 mg·mL⁻¹ the enzyme concentration in the supernatant remains constant at *ca.* 10 mg·mL⁻¹ through all the study.

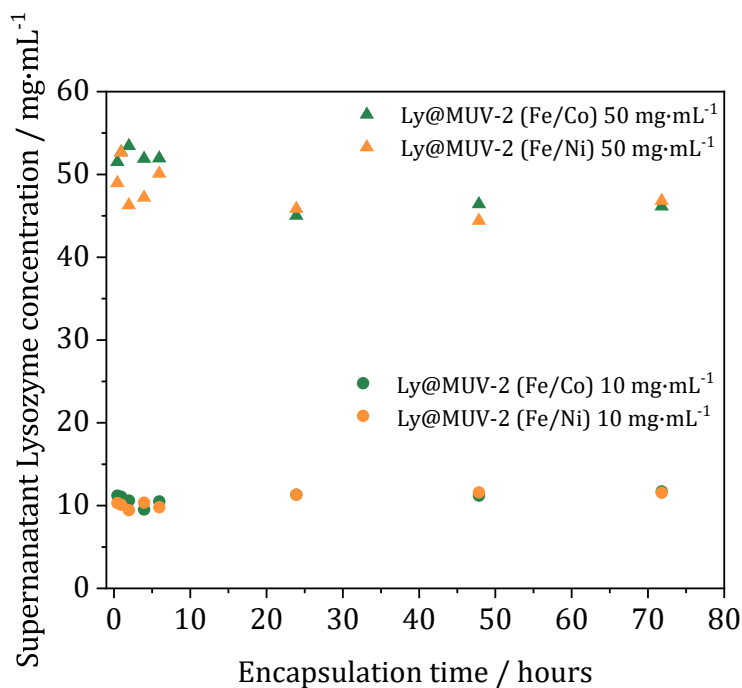


Figure 5.2.19. Evolution of the lysozyme concentration in the supernatant encapsulation media for MUV-2(Fe/Co) (green) and MUV-2(Fe/Ni) (orange) with time. Triangular symbols for starting Ly concentration = 50 mg·mL⁻¹ and round symbols for starting Ly concentration = 10 mg·mL⁻¹.

In view of these results, a blank encapsulation was carried out, adding water to the MM-MUV-2 derivatives, and analysing the supernatant with the BCA assay after 3 days. Both materials presented a violet coloration after adding the BSA reagent and an absorbance signal at $\lambda = 562$ nm, attributed to ligand liberation to the media. It is worth noting that TTFTB linker is removed in the standard protocol with DMF, in which the ligand is highly soluble. However, by employing the *green* synthesis, and thus only using isopropanol as a solvent, remanent TTFTB molecules are present in the MM-MUV-2 materials before the encapsulation process. Essentially, an exchange between this excess linker molecules and the lysozyme present in the encapsulation media would generate a gradual transport process of the enzyme. The proteins could act then as ligands and generate a competitive coordination against pristine linker molecules, a mechanism recently

proposed by Chen and co-workers.²³ This exchange and subsequent TTFTB liberation to the media could explain the higher absorbance values observed in the UV-Vis measurements, overlapping the signal corresponding to the lysozyme molecules present in the supernatant and thus overestimating the remanent enzyme concentration in the encapsulation media.

After discarding the UV-Vis methodology to establish the encapsulation kinetics, TGA measurements of the recovered precipitate aliquots were carried out to estimate the lysozyme concentration and evaluate the success of the encapsulation. The higher lysozyme content is achieved after 24 hours of encapsulation, reaching high estimated loading values (*ca.* 50 %), and presenting a decrease at 72 hours. This may further suggest that the encapsulation takes place following an exchange between the linker excess in the pores and the lysozyme molecules, and after the equilibrium is reached the enzyme can be liberated into the medium.

As expected, employing a starting lysozyme concentration of 50 mg·mL⁻¹ yields higher loading values than the 10 mg·mL⁻¹ concentration, supporting the biomolecule oversaturation conditions exploited in the encapsulation methodology designed throughout this Thesis. **Table 5.2.3** summarises the results.

Table 5.2.3. Lysozyme content estimated by TGA for the two initial lysozyme concentrations employed.

	Inorganic residue (D.B.) / % (w/w)	Encapsulated molecule / % (w/w)
MUV-2(Fe/Co)	18.7	-
MUV-2(Fe/Ni)	19.8	-
[Ly] ₀ = 10 mg·mL ⁻¹		
Ly@MUV-2(Fe/Co) (1h)	17.5	6.3
Ly@MUV-2(Fe/Co) (24h)	16.4	12.3
Ly@MUV-2(Fe/Co) (72h)	16.7	10.6
Ly@MUV-2(Fe/Ni) (1h)	18.6	5.9
Ly@MUV-2(Fe/Ni) (24h)	16.6	16.1
Ly@MUV-2(Fe/Ni) (72h)	17.1	13.7
[Ly] ₀ = 50 mg·mL ⁻¹		
Ly@MUV-2(Fe/Co) (1h)	16.6	11.2
Ly@MUV-2(Fe/Co) (24h)	10.1	45.9
Ly@MUV-2(Fe/Co) (72h)	14.8	20.7
Ly@MUV-2(Fe/Ni) (1h)	16.2	18.0
Ly@MUV-2(Fe/Ni) (24h)	10.3	47.9
Ly@MUV-2(Fe/Ni) (72h)	14.9	24.9

In view of the obtained results, the selected encapsulation parameters to further characterize the encapsulation products were employing 100 mg of MM-MUV-2 derivatives, selecting 50 mg·mL⁻¹ as starting lysozyme concentration, and 24 hours of encapsulation time.

Infrared spectra analysis of the encapsulation media (**Figure 5.2.20**) confirmed the presence of lysozyme in the composite spectra. IR spectrum of free lysozyme shows the most characteristic bands of proteins, namely, amide I at 1643 cm^{-1} , and amide II at 1515 cm^{-1} . These two bands are present in both composites spectra, overlapping with the $\nu_{\text{C=O}}$ related bands of the carboxylate linker at 1608 and 1551 cm^{-1} , as well as the band located at 1686 cm^{-1} , which is directly associated with the previously discussed presence of excess TTFTB linker molecules.

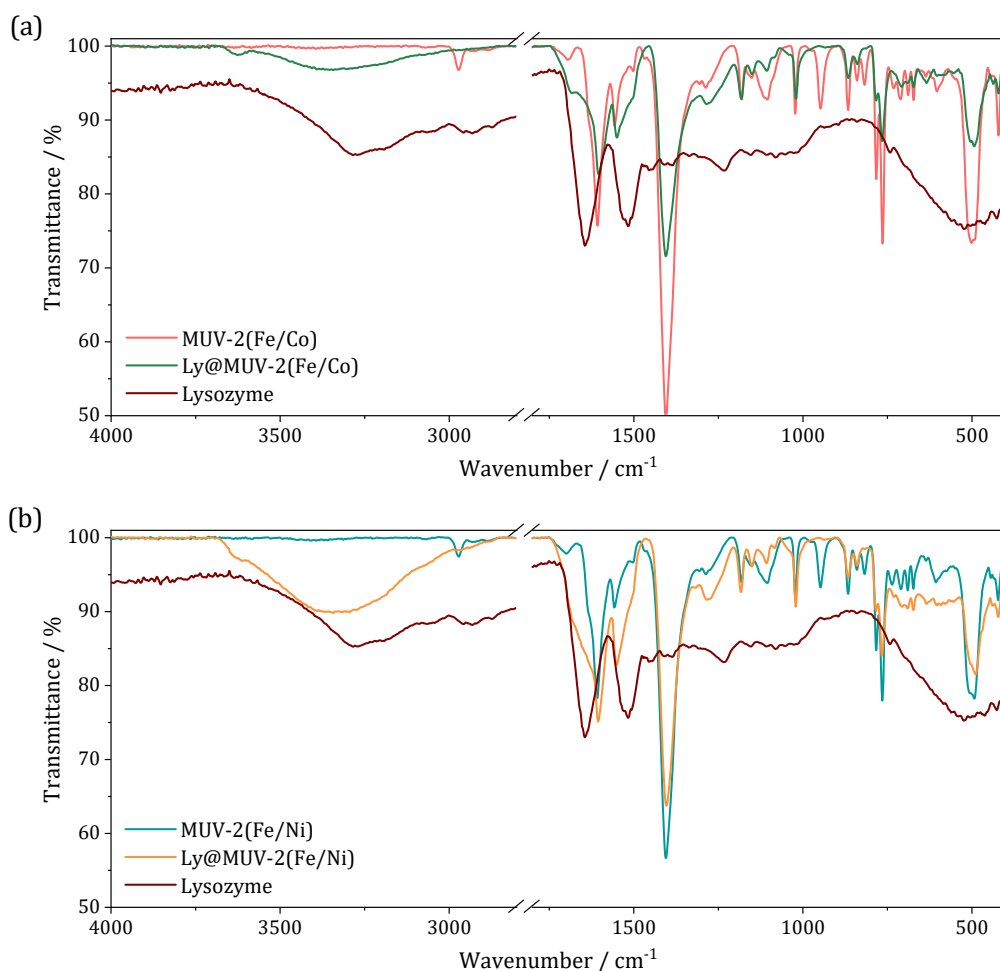


Figure 5.2.20. (a) FTIR spectra Ly@MUV-2(Fe/Co) (green) compared with MUV-2(Fe/Co) (pink) and lysozyme (red). (b) FTIR spectra Ly@MUV-2(Fe/Ni) (orange) compared with MUV-2(Fe/Ni) (teal) and lysozyme (red).

The diffraction pattern of the composites (**Figure 5.2.21**) retains the MM-MUV-2 diffraction peaks, but a sharp decrease in the (1 0 0) associated peak located at $2\theta = 3.4^\circ$ can be observed, directly related with the increase of electronic density due to the lysozyme infiltration into the framework and accommodation into the pores of the structure. The role of water molecules trapped in the porous framework and affecting to this decrease is discarded since the composites were thermally activated at 100°C under vacuum for 3 hours previously to the diffraction measurement. The appearance of a secondary peak at $2\theta = 3.2^\circ$ is directly related to the presence of excess ligand in the MM-MUV-2 derivatives, impeding the total contraction of the pores. This double peak is also present in the composites diffraction pattern, with a decrease in relative intensity of the principal peak. The maintenance of the double peak in the composites diffraction pattern suggests that either the excess ligand trapped into the porous structure could not be completely exchanged by lysozyme molecules, or the linker has been completely removed, and the lysozyme molecules located in the pore are now responsible for hindering the total pore contraction.

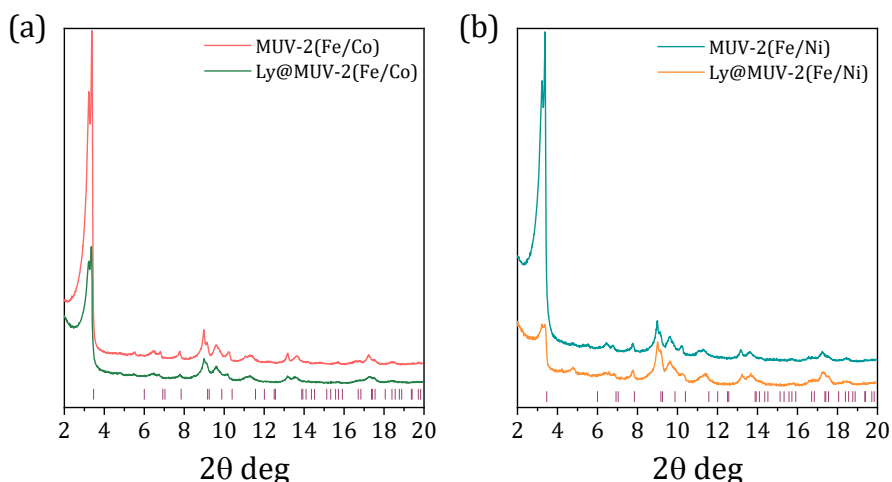


Figure 5.2.21. (a) PXRD pattern of Ly@MUV-2(Fe/Co) (green) compared with MUV-2(Fe/Co) (pink). (b) PXRD pattern of Ly@MUV-2(Fe/Ni) (orange) compared with MUV-2(Fe/Ni) (teal). All samples were thermally activated before measurement.

Thermogravimetric analysis was performed to evaluate the thermal stability of the composite materials and estimate the lysozyme loading into the framework, as well as compare the results with the data extracted from the study of the encapsulation kinetics. **Table 5.2.4** summarizes the inorganic residue content of the composite materials, as compared to their control empty MM-MUV-2 derivative and related theoretical values (theo). In addition, the estimated loaded lysozyme content is provided.

Table 5.2.4. Thermogravimetric analysis summary.

	Solvent / % (w/w)	Ligand decomp. T / °C	Inorganic residue (D.B.) / % (w/w)	Encapsulated molecule / % (w/w)
MUV-2(Fe/Co) theo	-	-	19.0	-
MUV-2(Fe/Co) exp	8.0	325	19.3	-
Ly@MUV-2(Fe/Co)	18.0	320	12.2	37.0
MUV-2(Fe/Ni) theo	-	-	19.0	-
MUV-2(Fe/Ni) exp	8.0	318	20.9	-
Ly@MUV-2(Fe/Ni)	9.0	312	10.6	49.5

In contrast with what has been observed throughout this Thesis, the encapsulation of the biomolecule in this case does not drastically decrease the thermal stability of the framework (**Figure 5.2.22**). The ligand decomposition temperature in both composites decreases only by approximately 5 °C, as a consequence of a gradual lysozyme decomposition instead of an abrupt combustion, due to the absence of a volatile character in the enzyme. The estimated lysozyme loading values are in good agreement with the previously discussed encapsulation aliquots, confirming the

reproducibility of the infiltration process. Interestingly, the mass losses located at around 160 °C in the starting materials thermal profiles that can be attributed to TTFTB molecules trapped in the pores cannot be observed in the composites thermal profiles, which present mass losses at approximately 220 °C, attributed in this case to lysozyme decomposition. Taking into account the hypothesis raised in view of the diffraction pattern, this seems to confirm the exchange of the excess TTFTB molecules by lysozyme during the infiltration process.

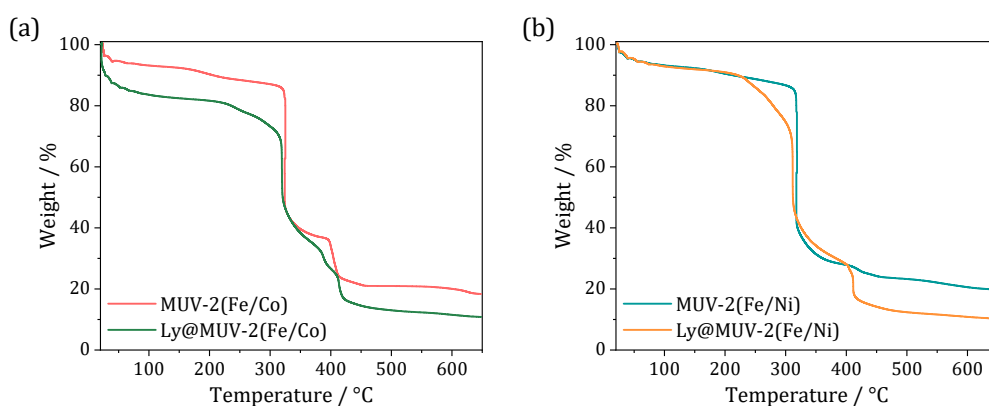


Figure 5.2.22. (a) Thermal profile of Ly@MUV-2(Fe/Co) (green) compared with MUV-2(Fe/Co) (pink). (b) Thermal profile of Ly@MUV-2(Fe/Ni) (orange) compared with MUV-2(Fe/Ni) (teal).

Finally, N₂ sorption studies at 77 K were carried out to identify the impact of lysozyme encapsulation over the porous nature of the MOFs (**Figure 5.2.23**). The starting *green* materials present a lower porosity than their DMF-synthesized counterparts, as expected due to the presence of excess TTFTB linkers trapped in the porous structure, with a 10 % decrease for MUV-2(Fe/Co) and a 30 % decrease for MUV-2(Fe/Ni), confirming the observations discussed in the rest of the characterization techniques.

Regarding the encapsulation products, Ly@MUV-2(Fe/Co) presents a decrease in BET surface of *ca.* 48 % ($S_{\text{BET}} = 1111$ vs. $580 \text{ m}^2 \cdot \text{g}^{-1}$ for MUV-2(Fe/Co) and Ly@MUV-2(Fe/Co), respectively). In the case of

Ly@MUV-2(Fe/Ni), a *ca.* 41 % decrease in the BET surface is observed ($S_{\text{BET}} = 862$ vs. $508 \text{ m}^2 \cdot \text{g}^{-1}$ for MUV-2(Fe/Ni) and Ly@MUV-2(Fe/Ni), respectively). This reduction in porosity is in good agreement with the estimated lysozyme content obtained by thermogravimetric analysis of the composite materials.

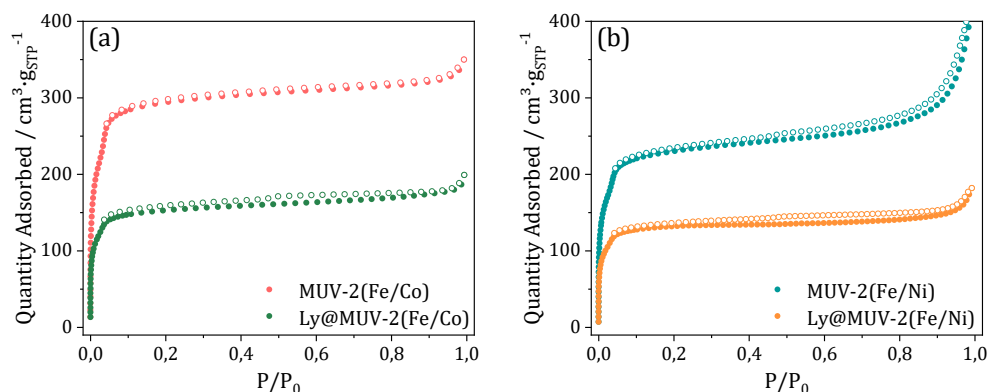


Figure 5.2.23. (a) N₂ sorption isotherms at 77 K of Ly@MUV-2(Fe/Co) (green) compared with MUV-2(Fe/Co) (pink). (b) N₂ sorption isotherms at 77 K of Ly@MUV-2(Fe/Ni) (orange) compared with MUV-2(Fe/Ni) (teal). Solid symbols for adsorption and open ones for desorption. Samples were activated at 100 °C for 3h before measurement.

Pore size distribution analysis of all the materials was also carried out employing the Horvath-Kawazoe method with cylinder pore geometry (Saito-Foley correction) (**Figure 5.2.24**). In all cases, 3 PSD centres can be observed with attributed widths of 9.1, 12.1, and 18.3 Å.

After the encapsulation process, the intensity of the PSD sites of Ly@MUV-2(Fe/Co) at 12.1 and 18.3 Å decreases, but not the one corresponding to the microporous cage at 9.1 Å. This suggests that, as expected due to its larger dimensions, the lysozyme macromolecules are allocated in the mesoporous channels of the structure, whereas the microporous cages remain accessible.

A similar effect can be observed for Ly@MUV-2(Fe/Ni), however the PSD centre corresponding to the microporous cage also presents an intensity

decrease, which could mean that the higher loading in the channels is blocking the accessibility to the microporous channels, since the enzyme is too large to fit them.

Interestingly, there are no changes in the calculated pore width in any of the encapsulation products, confirming the observations after PXRD measurements, where no shifting in the (1 0 0) diffraction peak could be observed in the biocomposite materials diffraction pattern. Essentially, the framework can comfortably accommodate a competitive amount of loaded lysozyme molecules without any distortion in the mesoporous channels, confirming the suitability of these materials as larger biomolecule carriers employing a facile and direct impregnation methodology.

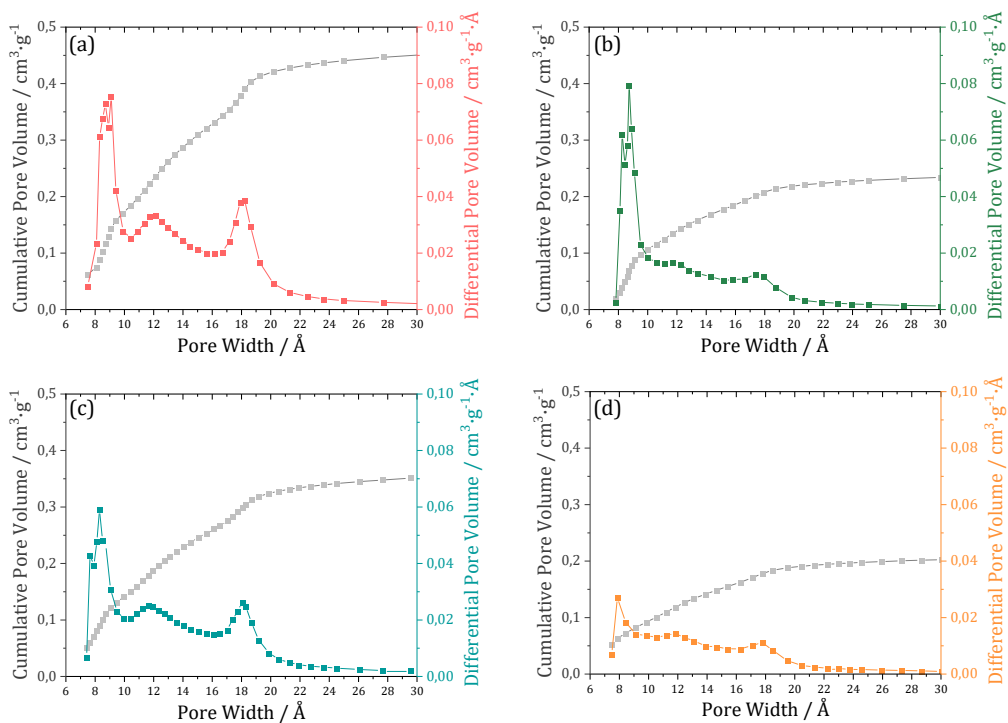


Figure 5.2.24. Pore size distribution analysis of (a) MUV-2(Fe/Co), (b) Ly@MUV-2(Fe/Co), (c) MUV-2(Fe/Ni), and (d) Ly@MUV-2(Fe/Ni).

5.3. Summary and conclusions

Two new Mixed-Metal MOF derivatives of MUV-2(Fe) with empirical formula $(\text{TTFTB})_3[(\text{Fe}_2\text{M}^{\text{II}}\text{O})(\text{H}_2\text{O})_2]_2$ ($\text{M}^{\text{II}} = \text{Co}, \text{Ni}$), have been synthesized. The synthesized materials are isostructural with the crystalline MUV-2 (as confirmed by their diffraction patterns) and present an analogous breathing behaviour upon solvent exposure.

The development of a *green* synthesis approach replaces the harmful DMF solvent preliminary used with the aim to move towards environment friendly methodologies and scalable processes.

Taking advantage of the hierarchical mesoporous nature of the framework, the performance of these materials as larger bioactive molecule carriers was evaluated. Preliminary results showcase composites with high estimated lysozyme loadings (up to 40 %) following an infiltration methodology.

As future work, the lysozyme liberation kinetics and the antimicrobial activity of the obtained composites should be evaluated.

5.4. Methods

Synthesis of Fe₂Ni and Fe₂Co mixed-metal trimer

The first step of the synthesis of heterometallic Fe^{III}₂M^{II} (M^{II} = Ni or Co) acetate unit consisted in the preparation of Fe^{III} acetate, adapting a previously reported protocol.¹⁷ The synthesis of the mixed metal building block Fe^{III}₂M^{II} resulted from the direct mixture of 4g (6 mmol) of Fe^{III} acetate (Fe₃O)(CH₃COO)₆(H₂O)₃[ClO₄]₂·2H₂O and 8 g (32 mmol) of M^{II} acetate tetrahydrate - (Ni(CH₃CO₂)₂·4H₂O or (Co(CH₃CO₂)₂·4H₂O - dissolved in 80 mL of distilled water. The reaction mixture was magnetically stirred at room temperature until a formation of a powder was observed. The crystalline powder obtained was then collected upon filtration, followed by a washing procedure with ethanol.

Standard synthesis of Mixed-Metal MUV-2 (Fe/Ni) and MUV-2 (Fe/Co)

In a general procedure adapted from the synthesis of MUV-2,⁸ pre-formed mixed metal trimer Fe^{III}₂M^{II} (M^{II} = Ni or Co) and H₄TTFTB ligand (prepared following a reported synthetic procedure)²⁴ reacted to form the corresponding Mixed-Metal MUV-2. Specifically, 160 mg (0.24 mmol) of Fe^{III}₂M^{II} and 200 mg (0.30 mmol) of H₄TTFTB were dissolved in 40 mL of DMF, and 12 mL of acetic acid were added to this solution. The reaction mixture was heated in the oven at 105 °C for 72 h. The resulting dark brown powder was collected by filtration and then soaked in DMF for 24 h. The product was filtered again and soaked in hot ethanol (65 °C) for 2 h before being filtered and left to dry at air. Activation of the materials consisted in thermal treatment at 120 °C for 3 hours in the oven.

Green Synthesis of Mixed-Metal MUV-2 (Fe/Ni) and MUV-2 (Fe/Co)

The general *green* procedure to obtain the corresponding Mixed-Metal MUV-2 derivatives was analogous to the *standard* protocol, substituting the

use of DMF as a solvent with isopropanol: 160 mg (0.24 mmol) of $\text{Fe}^{\text{III}}_2\text{M}^{\text{II}}$ and 200 mg (0.30 mmol) of H_4TTFTB were dissolved in 40 mL of isopropanol, and 12 mL of acetic acid were added to this solution. The reaction mixture was heated in the oven at 80 °C for 72 h. The resulting dark brown powder was collected by filtration and then soaked in isopropanol for 24 h, filtered again, and washed one more time with isopropanol before being filtered and left to dry at air. Activation of the materials consisted in thermal treatment at 120 °C for 3 hours in the oven.

Physicochemical characterization of mixed-metal MUV-2 derivatives

Attenuated total reflectance Fourier-transform infrared spectra (ATR-FTIR) were obtained using an ALPHA II FTIR Spectrometer (Bruker) in the 4000-400 cm^{-1} range with a resolution of 4 cm^{-1} in the absence of KBr pellet. Thermogravimetric analyses (TGA) were performed using a TGA 550 (TA Instruments) at a High-Resolution mode from 25 to 700 °C under air. Energy-dispersive X-ray (EDX) measurements and micrographies of the samples were performed in a Hitachi S4800 scanning electron microscope (SEM) with EDX microanalysis system. Inductively Coupled Plasma Mass Spectrometry (ICP-MS) analyses were carried out in a ICPMS7900 spectrometer (Agilent Technologies). Powder X-ray diffraction (PXRD) patterns were obtained using an X-ray diffractometer (PANalytical Empyrean) with copper as a radiation source ($\text{Cu-K}\alpha$, 1.5418 Å) operating at 40 mA and 45 kV. N_2 and CO_2 volumetric isotherms were measured using a Tristar II apparatus (Micromeritics) at -196 °C (77 K) and 0°C (273 K), respectively. Before the analysis, the samples were degassed at 120 °C (393 K) under vacuum overnight. High-pressure adsorption CO_2 isotherms were measured at different temperatures ranging from 10 °C (283 K) to 50 °C (323 K) in an IGA-100 gravimetric gas sorption analyser (Hiden Isochema) using approximately 20 mg of sample. Before each adsorption experiment, the

sample was outgassed at 120 °C (393 K) under vacuum (10^{-5} Pa) for two hours. The samples were then cooled down, still under high vacuum, to the target temperature that was controlled using a recirculating thermostatic bath. Equilibrium conditions corresponded to 600 s. interval, and $0.001 \text{ mg}\cdot\text{min}^{-1}$ tolerance. Virial equations were applied for fitting experimental data points with a fourth-grade polynomial used to properly describe the CO_2 isotherms. The heat of adsorption was calculated according to the Clausius–Clapeyron equation through the data extracted from the experimental isotherms at different temperatures.

Lysozyme quantification by BCA Assay

The BCA assay is a reduction assay of Cu^{II} to Cu^{I} in an alkaline medium by a protein. It mainly involves two steps:

(1) Copper chelation with the protein in an alkaline medium, resulting in the formation of light blue colour. This reaction is called biuret reaction.

(2) The BSA reagent reacts with the reduced cuprous ion formed in the previous step. Purple colour now formed is due to the chelation of two molecules of BCA with one cuprous ion. The complex formed is water soluble and its absorbance can effectively be measured at 562nm.

Two lysozyme water solutions were prepared, with enzyme concentration of 10 and $50 \text{ mg}\cdot\text{mL}^{-1}$, respectively. Parallel encapsulations were carried out by adding 1 mL of lysozyme solution to 5 mg of dry MM-MUV-2 derivative in an Eppendorf tube. Each encapsulation was performed by triplicate. The encapsulations were stopped at different times by centrifugation (13400 rpm, 15 min) and a $10 \mu\text{L}$ aliquot was extracted from each tube, diluted 50 times in water and measured in UV-Vis spectrometer for quantification. The UV-Vis spectra were recorded in a UV-vis microplate spectrophotometer Multiskan Sky (Thermo Scientific) and a Synergy H1M microplate reader (BioTek Instruments, Inc.).

5.5. Supporting Information

Infrared Spectroscopy

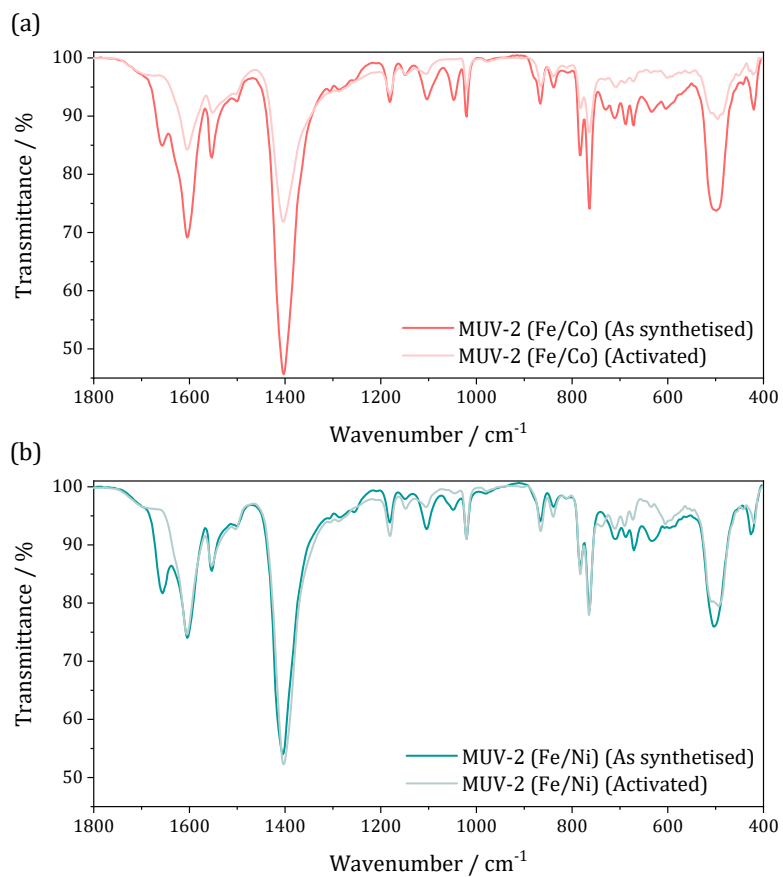


Figure S5.1. FTIR spectra of (a) MUV-2(Fe/Co) and (b) MUV-2(Fe/Ni) before and after washing protocol and thermal treatment.

Thermogravimetric analysis

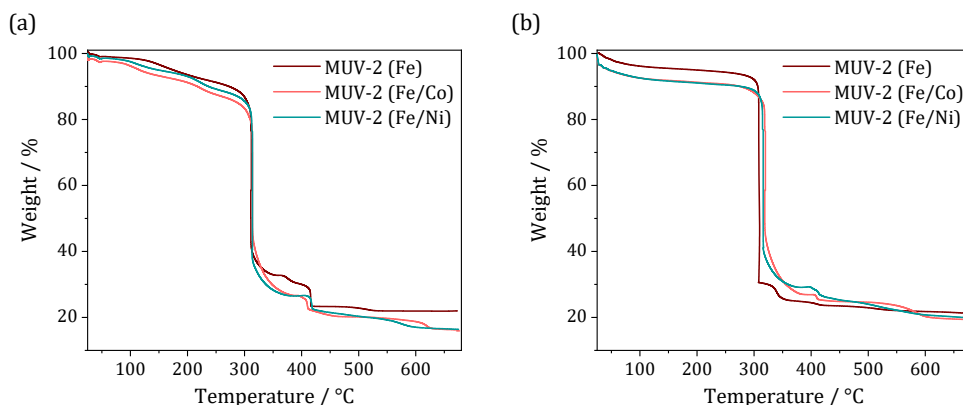


Figure S5.2. Thermal profile of MUV-2(Fe/Co) and MUV-2(Fe/Ni), compared with MUV-2(Fe), before (a) and after (b) washing protocol and thermal treatment.

Magnetic properties

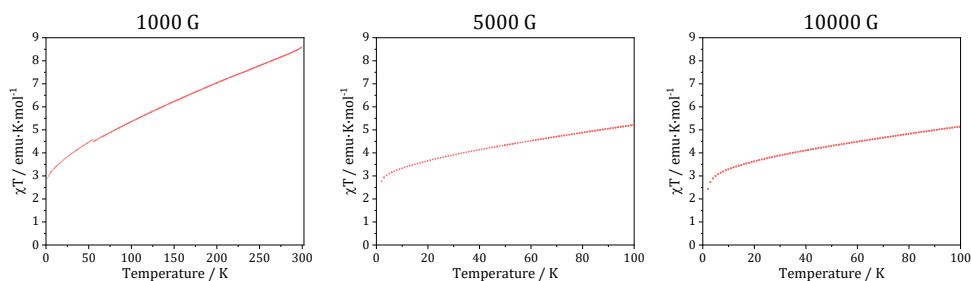


Figure S5.3. Temperature dependence of the magnetic susceptibility upon increasing magnetic fields of MUV-2(Fe/Co).

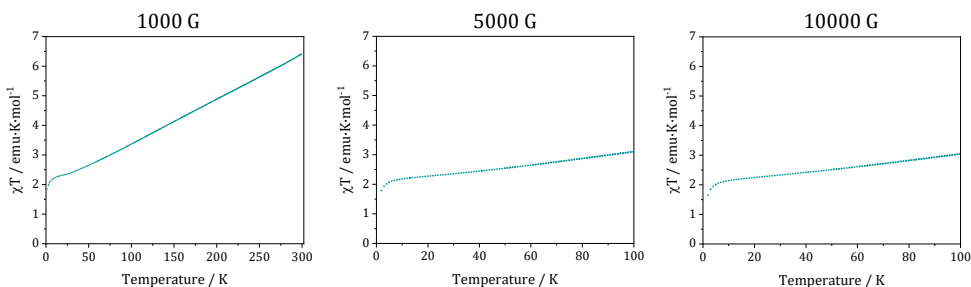


Figure S5.4. Temperature dependence of the magnetic susceptibility upon increasing magnetic fields of MUV-2(Fe/Ni).

5.6. References

- (1) Zhang, X.; Tu, R.; Lu, Z.; Peng, J.; Hou, C.; Wang, Z. Hierarchical Mesoporous Metal–Organic Frameworks Encapsulated Enzymes: Progress and Perspective. *Coord. Chem. Rev.* **2021**, *443*, 214032.
- (2) Chen, Y.; Li, P.; Modica, J. A.; Drout, R. J.; Farha, O. K. Acid-Resistant Mesoporous Metal–Organic Framework toward Oral Insulin Delivery: Protein Encapsulation, Protection, and Release. *J. Am. Chem. Soc.* **2018**, *140* (17), 5678–5681.
- (3) Serre, C.; Millange, F.; Thouvenot, C.; Noguès, M.; Marsolier, G.; Louër, D.; Férey, G. Very Large Breathing Effect in the First Nanoporous Chromium(III)-Based Solids: MIL-53 or CrIII(OH)·{O₂C-C₆H₄-CO₂}·{HO₂C-C₆H₄-CO₂H}_x·H₂O_y. *J. Am. Chem. Soc.* **2002**, *124* (45), 13519–13526.
- (4) Millange, F.; Guillou, N.; Walton, R. I.; Grenèche, J. M.; Margiolaki, I.; Férey, G. Effect of the Nature of the Metal on the Breathing Steps in MOFs with Dynamic Frameworks. *Chem. Commun.* **2008**, No. 39, 4732–4734.
- (5) Qi, F.; He, L.; Cui, L.; Wang, W.; Siddique, K. H. M.; Li, S. Smart Antibacterial Food Packaging Based on MIL-53 (Fe) Functionalized Polylactic Acid Film for PH-Responsive Controlled Release. *J. Polym. Environ.* **2023**, *53* (0123456789).
- (6) Liu, D.; Zou, D.; Zhu, H.; Zhang, J. Mesoporous Metal–Organic Frameworks: Synthetic Strategies and Emerging Applications. *Small* **2018**, *14* (37), 1–40.
- (7) Mao, Y.; Chen, D.; Hu, P.; Guo, Y.; Ying, Y.; Ying, W.; Peng, X. Hierarchical Mesoporous Metal–Organic Frameworks for Enhanced CO₂ Capture. *Chem. - A Eur. J.* **2015**, *21* (43), 15127–15132.
- (8) Souto, M.; Santiago-Portillo, A.; Palomino, M.; Vitórica-Yrezábal, I. J.; Vieira, B. J. C.; Waerenborgh, J. C.; Valencia, S.; Navalón, S.; Rey, F.; García, H.; et al. A Highly Stable and Hierarchical Tetrathiafulvalene-Based Metal–Organic Framework with Improved Performance as a Solid Catalyst. *Chem. Sci.* **2018**, *9* (9), 2413–2418.
- (9) Souto, M.; Romero, J.; Calbo, J.; Vitórica-Yrezábal, I. J.; Zafra, J. L.; Casado, J.; Ortí, E.; Walsh, A.; Mínguez Espallargas, G. Breathing-Dependent Redox Activity in a Tetrathiafulvalene-Based Metal–Organic Framework. *J. Am. Chem. Soc.* **2018**, *140* (33), 10562–10569.

- (10) Das, M. C.; Xiang, S.; Zhang, Z.; Chen, B. Functional Mixed Metal-Organic Frameworks with Metalloligands. *Angew. Chemie - Int. Ed.* **2011**, *50* (45), 10510–10520.
- (11) Masoomi, M. Y.; Morsali, A.; Dhakshinamoorthy, A.; Garcia, H. Mixed-Metal MOFs: Unique Opportunities in Metal–Organic Framework (MOF) Functionality and Design. *Angew. Chemie - Int. Ed.* **2019**, *58* (43), 15188–15205.
- (12) Abednatanzi, S.; Gohari Derakhshandeh, P.; Depauw, H.; Coudert, F. X.; Vrielinck, H.; Van Der Voort, P.; Leus, K. Mixed-Metal Metal-Organic Frameworks. *Chem. Soc. Rev.* **2019**, *48* (9), 2535–2565.
- (13) Zhang, Z.; Xiang, S.; Hong, K.; Das, M. C.; Arman, H. D.; Garcia, M.; Mondal, J. U.; Thomas, K. M.; Chen, B. Triple Framework Interpenetration and Immobilization of Open Metal Sites within a Microporous Mixed Metal-Organic Framework for Highly Selective Gas Adsorption. *Inorg. Chem.* **2012**, *51* (9), 4947–4953.
- (14) Giménez-Marqués, M.; Santiago-Portillo, A.; Navalón, S.; Álvaro, M.; Briois, V.; Nouar, F.; Garcia, H.; Serre, C. Exploring the Catalytic Performance of a Series of Bimetallic MIL-100(Fe, Ni) MOFs. *J. Mater. Chem. A* **2019**, *7* (35), 20285–20292.
- (15) Vaid, K.; Dhiman, J.; Kumar, S.; Kim, K. H.; Kumar, V. Mixed Metal (Cobalt/Molybdenum) Based Metal-Organic Frameworks for Highly Sensitive and Specific Sensing of Arsenic (V): Spectroscopic versus Paper-Based Approaches. *Chem. Eng. J.* **2021**, *426* (March), 131243.
- (16) Jaryal, R.; Kumar, R.; Khullar, S. Mixed Metal-Metal Organic Frameworks (MM-MOFs) and Their Use as Efficient Photocatalysts for Hydrogen Evolution from Water Splitting Reactions. *Coord. Chem. Rev.* **2022**, *464*, 214542.
- (17) Wongsakulphasatch, S.; Nouar, F.; Rodriguez, J.; Scott, L.; Guillouzer, C. Le; Devic, T.; Horcajada, P.; Llewellyn, P. L.; Vimont, A.; Clet, G.; et al. Direct Accessibility of Mixed-Metal (Iii/Ii) Acid Sites through the Rational Synthesis of Porous Metal Carboxylates. *Chem. Commun.* **2015**, No. 51, 10194–10197.
- (18) Saito, A.; Foley, H. C. Curvature and Parametric Sensitivity in Models for Adsorption in Micropores. *AIChE J.* **1991**, *37* (3), 429–436.
- (19) Rege, S. U.; Yang, R. T. Corrected Horvath-Kawazoe Equations for Pore-Size Distribution. **2000**, *46* (4), 734–750.

- (20) Sumida, K.; Rogow, D. L.; Mason, J. A.; McDonald, T. M.; Bloch, E. D.; Herm, Z. R.; Bae, T. H.; Long, J. R. Carbon Dioxide Capture in Metal-Organic Frameworks. *Chem. Rev.* **2012**, *112* (2), 724–781.
- (21) Bayarri, M.; Oulahal, N.; Degraeve, P.; Gharsallaoui, A. Properties of Lysozyme/Low Methoxyl (LM) Pectin Complexes for Antimicrobial Edible Food Packaging. *J. Food Eng.* **2014**, *131*, 18–25.
- (22) Zhang, W.; Rhim, J. W. Functional Edible Films/Coatings Integrated with Lactoperoxidase and Lysozyme and Their Application in Food Preservation. *Food Control* **2022**, *133* (PB), 108670.
- (23) Feng, Y.; Shi, R.; Yang, M.; Zheng, Y.; Zhang, Z.; Chen, Y. A Dynamic Defect Generation Strategy for Efficient Enzyme Immobilization in Robust Metal-Organic Framework for Catalytic Hydrolysis and Chiral Resolution. *Angew. Chemie Int. Ed.* **2023**, *300071*.
- (24) Narayan, T. C.; Miyakai, T.; Seki, S.; Dincă, M. High Charge Mobility in a Tetrathiafulvalene-Based Microporous Metal-Organic Framework. *J. Am. Chem. Soc.* **2012**, *134* (31), 12932–12935.

